Dissertation zur Erlangung des Doktorgrades
der Fakultät für Chemie und Pharmazie
der Ludwig-Maximilians-Universität München

Exploring the structural variety and properties of ternary gallium- and germanium-arsenide semiconductors

Valentin Weippert

aus

Schwäbisch Hall, Deutschland

2021

Erklärung

Diese Dissertation wurde im Sinne von § 7 der Promotionsordnung vom 28. November 2011 von Herrn Prof. Dr. Dirk Johrendt betreut.

Eidesstattliche Versicherung

Diese Dissertation wurde eigenständig und ohne unerlaubte Hilfe erarbeitet.

München, 14.09.2021

Valentin Weippert

Dissertation eingereicht am:	05.07.2021
1. Gutachter:	Prof. Dr. Dirk Johrendt
2. Gutachter:	PD Dr. Constantin Hoch
Mündliche Prüfung am:	11.08.2021

Danksagung

An erster Stelle möchte ich mich bei Prof. Dr. Dirk Johrendt für die hervorragende Betreuung und großen Freiheiten bei der Gestaltung meiner Promotion bedanken. Seine stets offene Tür, der rege Gedankenaustausch und seine vielfältigen Ideen zur Ausarbeitung von Projekten haben diese Arbeit in ihrer Form überhaupt erst ermöglicht.

Ganz besonders möchte ich mich bei PD Dr. Constantin Hoch zum einen für die Übernahme des Zweitgutachtens aber vielmehr für die Begleitung meines ganzen Studiums, angefangen mit meiner Bachelorarbeit über immer wieder erheiternde Gespräche hin zu unzähligen hilfreichen Tipps und fachlichen Unterstützungen bedanken.

Prof Dr. Wolfgang Schnick, Prof. Dr. Oliver Oeckler, Prof. Dr. Thomas Matthias Klapötke und PD Dr. Reiner Lomoth möchte ich herzlich danken für die Teilnahme an meiner Prüfungskommission.

Meinen großen Dank an meine Praktikanten Ana Mateos, Florian Wolf, Thanh Chau und vor allem an den unermüdlichen Kristian Witthaut für eure tollen Ideen und ausdauernde Arbeit.

Danke an alle meine aktuellen und ehemaligen Kollegen: Dr. Simon Peschke, Dr. Juliane Stahl, Dr. Tobias Rackl, Rudolf Schönmann, Dr. Arthur Haffner, Bettina Rendenbach, Marlo Schöneich, Martin Weidemann, Peiqi Chen und natürlich dem AK-Mastermind Catrin Löhnert. Vielen Dank für die tolle Zusammenarbeit, Unterstützung bei zahlreichen Themen, hilfreichen Diskussionen (aka Kaffeepausen) und die freundschaftliche Atmosphäre in den letzten Jahren. Besonders möchte ich Arthur danken für zahllose Einkristall-Tests und -Messungen und seinem nicht enden wollenden Vorrat an Memes.

Vielen Dank an alle aktuelle und ehemaligen Kollegen aus dem AK Schnick und AK Lotsch für den super Zusammenhalt in der Festkörperei und die gemeinsame Zeit. Einen großen Dank dabei an Monika Pointner für ihre Hartnäckigkeit in TEM Angelegenheiten.

Danke an Thomas Miller, Wolfgang Wünschheim, Christian Minke und Dr. Dieter Rau für ihre technische Unterstützung und Problemlösungen.

Bei Arthur Haffner, Bettina Rendenbach, Lucien Eisenburger, Dr. Juliane Stahl und Dr. Tobias Rackl bedanke ich mich für das Korrekturlesen dieser Arbeit.

Danke Niklas, Viktor, Wibke, Edi, Basti, Obi, Schnucki und Felix für eure Freundschaft und dass ihr mich auf diesem langen Weg begleitet und diese Zeit zu einer Unvergesslichen gemacht habt

Ein riesiges Dankeschön geht an Lucien Eisenburger der immer irgendwie dabei war ob nun bei täglichen Gesprächen oder Telefonaten über allerlei Problemchen oder primitivem Gewichte

hochheben und wieder fallen lassen. Du bist für mich in den letzten Jahren ein unschätzbarer Freund geworden der einfach wirklich absolut immer für mich da war.

Ein riesiges Dankeschön geht an meine Familie und insbesondere an meine Eltern Annegret und Albrecht Weippert die es mir ermöglicht haben diesen Weg zu gehen und mir in allen erdenklichen Lebensfragen und –lagen zur Seite standen.

Zu guter Letzt geht ein ganz besonderes Dankeschön an Rahel. Du bist mein Fels. Danke, dass ich mich immer auf dich verlassen kann und mit dir zusammen alles besser ist.

"Das sind nicht die Droiden, die ihr sucht."

– *Miraculix*

Table of Contents

1 Introduction

The advent of the modern information age dawned in 1947 with the discovery of the transistor effect by John Bardeen, William Shockley und Walter Brattain and its subsequent recognition with the noble prize in physics.[1, 2] While this effect has been theoretically established before[3] and prior discoveries like the tip or Schottky diode[4, 5] certainly paved the way, this was the first working device. Initial constructions were based on Germanium, which was deemed superior to silicon due to higher carrier concentration.[6] With silicon on the other hand it was possible to build precise and stable oxide layers. This key feature lead to the development of a groundbreaking device: the metal oxide semiconductor field effect transistor (MOSFET), enabling high performing transistors suitable for mass production.[7] This technology, although refined in multiple ways, is still the foundation of all transistor circuits made today. In 2018 it was estimated that 13 sextillion transistors were manufactured since 1947.[8] Modern daily life would simply be unthinkable without them. They are the basis of everyday items like smartphones, cameras, laptops and even cars up to large-scale server farms and worldwide communication technology. But of course “where there is light, there must be shadow” (Goethe, 1773)[9] and so the global energy consumption has drastically risen, not solely because of information technology but partly. This lead to peculiar side effects like the cryptocurrency bitcoin consuming equal amounts of power like Argentina.[10]

Nevertheless, efforts are made to soften the blow on the environment or even negate the impact and semiconducting materials play a big role in doing just that. The most commonly associated topic with green energy based on semiconductors is solar energy. The majority of solar cells is made from polycrystalline silicon reaching efficiencies up to 20.4 %. For special applications like aerospace, multi-junction GaAs cells can reach up to 31.2 % efficiency.[11] With the advance of GaN based light emitting diodes (LEDs) and new phosphorescent materials, it was possible to produce warm white LEDs, replacing traditional Edison light bulbs and using said energy efficiently since roughly 1/5 of the worldwide energy consumption falls on lighting. [12-14] Another possibility to tackle the increasing carbon dioxide emission is to use alternative fuels, namely hydrogen. Since the vast majority of hydrogen is produced via the natural gas dependent steam reforming process,[15] high hopes are resting on efficient, catalytic driven water splitting.[16, 17] Promising candidates are classical perovskite compounds like $BaTaO_2N$ or tunable solid solutions like GaN:ZnO.[16, 18] A rather sophisticated approach in producing clean energy is to utilize waste heat energy with thermoelectric generators.[19] Alas still a niche application with commercially available devices based on Bi_2Te_3 only reaching conversion efficiencies of ~5 %,[19] continuous advances could allow conversion efficiencies with up to 20 %, painting a promising future.[20]

But what makes a good semiconductor? It is, as always, depending on the use case. Semiconductors can foremost be divided into two main groups: elemental and compound semiconductors. Albeit germanium and selenium had some pertinence as elemental semiconductors in early transistors, they were completely replaced by the readily available and easy to process silicon. As shown in Figure 1.1a silicon crystallizes in the diamond structure type and exhibits an indirect band gap, requiring a change in momentum for an electron to reach the lowest possible exited state. Binary semiconductors with combinations like II-IV (ZnS), II-V (Zn_3As_2), IV-IV (SiC), IV-VI (PbS) and V-VI (Bi_2Te_3) open up a large variety of compounds.[21] However, III-V compounds like GaAs shown in Figure 1.1b possess the most industrial importance. They either crystallize in the sphalerite-, or its hexagonal equivalent, the wurtzite structure type and exhibit mainly direct band gaps. This enables the emittance of a photon upon the recombination of an exited electron and a hole with no change in momentum needed (Figure 1.2d). With the addition of a tunable band gap ranging from 0.17 eV (InSb) to 6.015 eV (AlN) through ternary combinations, it makes them ideal materials for optoelectronics covering everything from infrared (IR) radiation to hard ultraviolet (UV) light. [22-26]

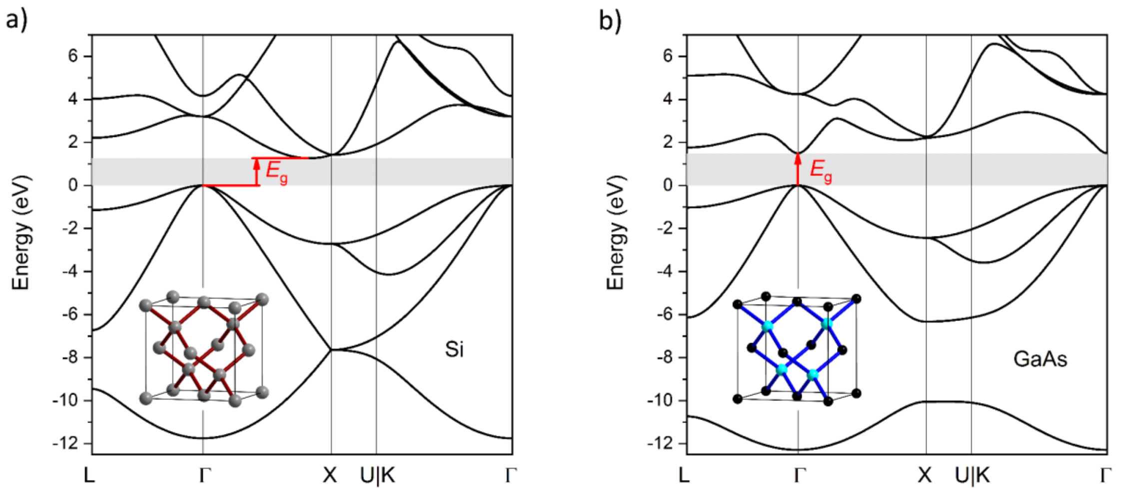

Figure 1.1: Calculated modified Becke-Johnson band structures of (a) silicon and (b) GaAs showing an indirect and a direct band gap respectively.

Another way to classify semiconductors is by their electrical conductivity, delimiting them from metals by a negative temperature coefficient. For the example of silicon, this is evident by the four valence electrons being located in bonded sp^3 hybrid orbitals with none present in the conduction band at $T = 0$ K. Only upon thermal excitation of an electron into the conduction band as shown in Figure 1.2a with step (1), electrical conductivity emerges. The absence of said electron in the valence band leaves a hole, which in turn can be filled by neighboring electrons, thus creating hole conduction. This intrinsic charge carrier density is very low with $1\cdot10^{10}$ cm^{-3} for silicon and

$2.1\cdot10^{6}$ cm^{-3} for GaAs at 300 K and often of no application-related relevance.[27] The *p*- or *n*- nature of the intrinsic electrical conductivity can either be determined directly via Hall effect measurements or indirectly through evaluating the effective masses of holes and electrons. These are accessible from electronic band structures obtained from angle-resolved photoemission spectroscopy (ARPES) or density functional theory (DFT) calculations.[28, 29] The ability to tune the charge carrier density and alter its nature via doping is one of the key aspects of semiconducting material versatility. As shown in Figure 1.2a with steps (2) and (3), the presence of either a *p*- or *n*-dopant inserts an energy level E_A or E_D respectively with very little energy needed for an excited state and therefore increased carrier concentration. For example in silicon doped with phosphorus the E_D-E_C gap is only 45 meV and 67 meV for the E_V-E_A gap upon doping with aluminum.[30] Typical charge carrier concentration achieved are $1\cdot10^{13}$ cm^{-3} for light doping and $1\cdot10^{21}$ cm^{-3} for heavy doping but with the latter often resulting in so called degenerate semiconductors with metal-like behavior.[31]

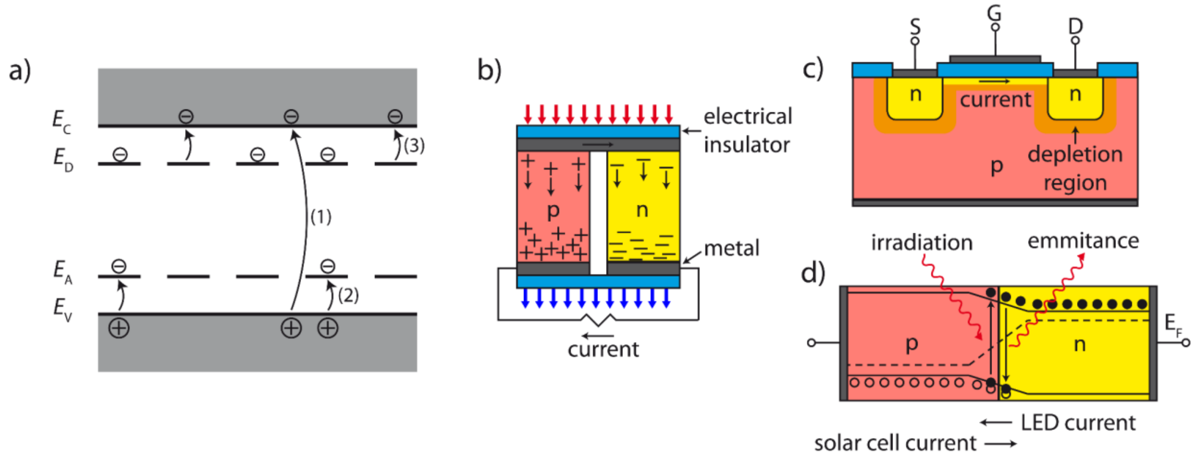

Figure 1.2: (a) Energy scheme for (1) intrinsic, (2) *p*- and (3) *n*-doped samples and their respective excited state mechanism. Schemes of (b) a thermoelectric generator (TEG) utilizing the Seebeck effect, (c) a MOSFET in ohmic mode and (d) an LED or solar cell.

Precise doping enables the construction of efficient MOSFETs with a general scheme depicted in Figure 1.2c. Upon applying a voltage to the gate (G), the field effect permeates the insulating oxide layer and creates a channel, allowing a current to flow from source (S) to drain (D). A *pn*-junction, as shown in Figure 1.2d, is used for LEDs and solar cells to emit light or convert it to electrical energy. Alternating column arrays of *p*- and *n*-semiconductors are used for thermoelectric generators (TEG), depicted in Figure 1.2b. They rely on the Seebeck effect, which was discovered by Johann Seebeck in 1821.[32] The application of a temperature gradient induces a voltage via an electromotive force on both positive and negative charge carriers (Figure 1.2b). The extent is described by the Seebeck coefficient S in Volts per Kelvin. However, a high Seebeck coefficient does not equal a good thermoelectric material. As described in the thermoelectric figure of merit $ZT = \sigma S^2 T/\kappa$, a high electrical conductivity σ and low thermal conductivity κ are just as important.

Unfortunately, this is a somewhat contradictive relation since good electrical conductors are generally good thermal conductors. This is where semiconducting materials can shine by combining reasonable electrical conductivities, through small band gaps and tunable doping levels with low lattice thermal conductivities by introducing scattering centers through complex structures, rattling atoms or impurities.[33-35]

Discovering new semiconducting compounds and investigating intriguing properties remains a challenge up to date. Especially amidst a global shortage of semiconducting devices, even affecting car manufacturers,[36] it is crucial to find new materials to improve upon existing ones. One class of compounds in particular displays an ever-increasing research interest. New Zintl phases show tremendous potential for ion conductivity,[37-39] nano-structuring[40] and foremost thermoelectrics.[41-43] Zintl phases are valence precise compounds with a defined stoichiometry, combining ionic and covalent bonding characteristics. The classical Zintl-Klemm-Busmann concept assumes a complete charge transfer from an electropositive alkaline or alkaline earth metal (A, AE) to an electronegative (semi-)metal of the III-VI main group. The structure and bonding of the resulting polyanionic network follows the $(8-N)$-rule. A basic example is NaTl with the Tl^- anion forming four bonds resulting in a diamond-type structure. An expansion of this concept towards ternary systems and the consideration of electron counting rules like the Wade- and Grimm-Sommerfeld rule leads to a wide variety of compounds with often quite intricate structures. Dependent on differences in electronegativity within the polyanionic network and an emphasis towards some degree of multivalence, an assignment of formal oxidation states instead of homolytic bond splitting according to the 8-N rule is also feasible.[44]

This thesis is an explorative approach towards new Zintl compounds within the ternary system M-Ga/Ge-As (M = Rb, Cs, Sr, Ba, Eu). Research in this field has already produced a multitude of new compounds with numerous structural motifs as exemplary shown in Figure 1.3. They exhibit an increasing structural complexity and network connectivity with decreasing content of the electropositive metal, starting with isolated tetrahedra, over Ge_2As_4 motifs, Ga_2As_6 dumbbells towards interconnected Ge_6As_4 cages. Curiously, compounds with a rather low metal content, as they occur in other related systems like $SrSi_7P_{10}$ or $Ca_3Si_8P_{14}$, have hardly been studied to date.[45, 46] This thesis focuses on the unexplored low-metal-content side of the spectrum depicted in Figure 1.3. By employing solid-state syntheses, it was possible to discover multiple new semiconducting compounds featuring complex polyanionic networks with some surprising relations to known structures and promising indications towards thermoelectric applications.

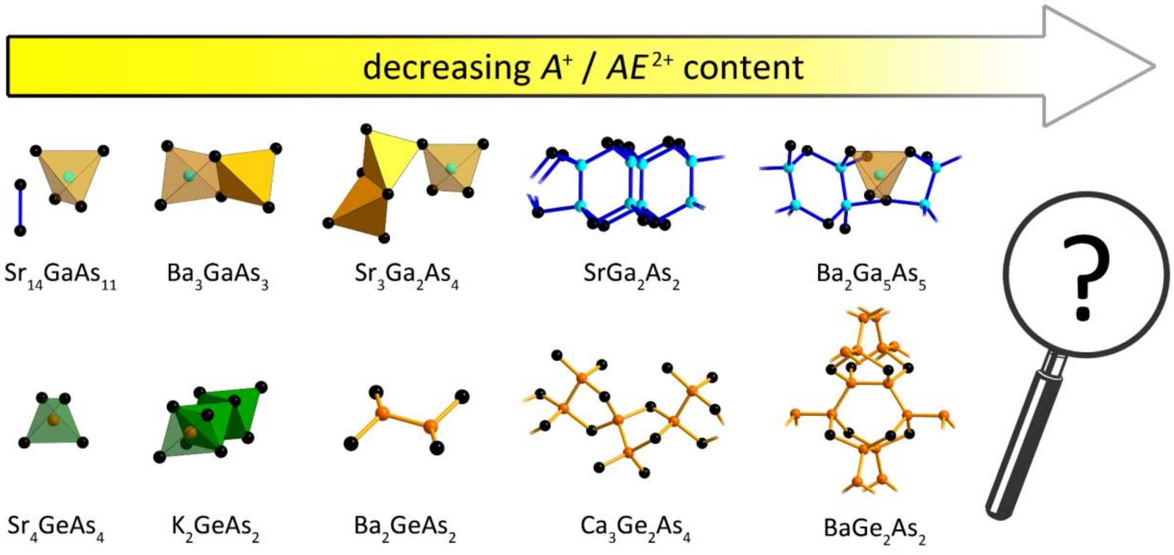

Figure 1.3: Known structural motifs in the *A*/*AE*-Ga/Ge-As system ordered with decreasing *A*/*AE* content.[47-55]

The first part of this thesis mainly focuses on the *M*-Ge-As system with *M* = Rb, Cs, Sr, Ba. For years, Eisenmann *et al*. dominated this field by discovering a multitude of compounds like $BaGe_4As_4$ or $Sr_3Ge_2As_4$.[51, 53-59] Chapter 2.1 presents the new isostructural compounds $SrGe_8As_{10}$ and $BaGe_8As_{10}$. They exhibit an unprecedented structural complexity by combining three different Ge-As motifs and As-As bonds with a remarkable mixed valence germanium with the oxidation states +2, +3 and +4. Similar circumstances are found in the related $BaGe_7P_{12}$, with the addition of an unusual octahedral GeP_6 motif. Chapter 2.2 is about $BaGe_8As_{14}$ as a new representative of the otherwise rare semiconductors with sodalite structure. It shows a static disordered or "rattling" barium atom alongside a mixed Ge/As site. Chapter 2.3 adds the isotypic sodalite-type semiconductors $RbGe_7As_{15}$ and $CsGe_7As_{15}$. DFT calculations of the electrical and thermal transport properties of the new sodalite-type compounds predict high thermoelectric properties. $BaGe_8As_{14}$ reaches efficiencies up to $ZT = 2.7$, which is at the level of current record materials.

The second part is about supertetrahedral structures in the system *M*-Ga-As with additions of indium and silicon. A supertetrahedral entity is a tetrahedrally shaped section of the sphalerite structure type. A "T*n*" denoted supertetrahedron exhibits *n* tetrahedra along the edges and is constituted of t_n tetrahedra with $t_n = n(n+1)(n+2)/6$.[60] Such compounds are used for a multitude of applications ranging from porous materials over well-defined nanoparticles, i.e. in aid of photoelectrode-sensitization, to phosphorescent materials and ion conductivity.[37, 38, 61-63] Since the vast majority of supertetrahedral compounds are chalcogenides with often large bandgaps, the field of *Tr*-As (*Tr* = group 13 elements) based compounds is largely unexplored.[64-66] Chapter 3.1 reports on the new T5 compounds $M_{15}Ga_{22}As_{32}$, and $M_{15}In_{22}As_{32}$ and the so far unprecedented T6 compounds $M_3Ga_6As_8$ with *M* = Sr, Eu. They form saw-tooth like interlocking layers separated by either strontium or europium, which can be described as hierarchical variants of the HgI_2-type structure.[67, 68] The semiconducting properties of all compounds resemble those of GaAs and InAs with direct bandgaps of similar magnitude. Magnetization measurements of the europium compounds indicate low temperature antiferromagnetism. Chapter 3.2 expands this hierarchical family with the supertetrahedral compounds T2-MSiAs$_2$, T3-MGaSiAs$_3$ and polytypic T4-M_4Ga$_5$SiAs$_9$ (M = Sr, Eu), the latter being yet unknown in this series.

The last chapter is based on attempts to achieve even larger supertetrahedral units by utilizing high pressure, yielding the compound SrGa$_4$As$_4$. The chiral compound contains no supertetrahedra, but nevertheless interesting structural motifs, which are discussed in detail.

References

[1] J. Bardeen, W. H. Brattain, *Phys. Rev.* **1948**, *74*, 230-231.

[2] W. Shockley, J. Bardeen, W. H. Brattain, *Nature* **1956**, *178*, 1149-1149.

[3] E. L. Julius, CA272437A, Canada Pat., **1925**.

[4] G. W. Pickard, US836531A, United States Pat., **1906**.

[5] W. Schottky, *Z. Physik* **1939**, *113*, 367-414.

[6] O. Madelung, U. Rössler, M. Schulz, *Semiconductors · Group IV Elements, IV-IV and III-V Compounds. Part b - Electronic, Transport, Optical and Other Properties, Vol. 41A1β*, Springer Materials, Berlin, **2002**.

[7] D. Kahng, in *the Solid State Device Research Conf.*, Pittsburgh, **1960**.

[8] D. Laws, *13 Sextillion & Counting*, https://computerhistory.org/blog/13-sextillion-counting-the-long-winding-road-to-the-most-frequently-manufactured-human-artifact-in-history/, (01.03.2021).

[9] J. W. Goethe, *Götz von Berlichingen mit der eisernen Hand*, Philipp Reclam jun. GmbH & Co. KG, Ditzingen, **2018**.

[10] University of Cambridge, *Cambridge Bitcoin Electricity Consumption Index*, https://cbeci.org/cbeci/comparisons, (01.03.2021).

[11] M. Green, E. Dunlop, J. Hohl-Ebinger, M. Yoshita, N. Kopidakis, X. Hao, *Prog. Photovoltaics* **2021**, *29*, 3-15.

[12] S. Nakamura, T. Mukai, M. Senoh, *Appl. Phys. Lett.* **1994**, *64*, 1687-1689.

[13] P. Pust, P. J. Schmidt, W. Schnick, *Nat. Mater.* **2015**, *14*, 454-458.

[14] G. Zissis, in *Handbook of Advanced Lighting Technology* (Eds.: R. Karlicek, C.-C. Sun, G. Zissis, R. Ma), Springer International Publishing, Cham, **2016**, pp. 1-13.

[15] I. Staffell, D. Scamman, A. Velazquez Abad, P. Balcombe, P. E. Dodds, P. Ekins, N. Shah, K. R. Ward, *Energy Environ. Sci.* **2019**, *12*, 463-491.

[16] K. Maeda, K. Domen, *J. Phys. Chem. Lett.* **2010**, *1*, 2655-2661.

[17] N. Fajrina, M. Tahir, *Int. J. Hydrogen Energy* **2019**, *44*, 540-577.

[18] M. Higashi, R. Abe, K. Teramura, T. Takata, B. Ohtani, K. Domen, *Chem. Phys. Lett.* **2008**, *452*, 120-123.

[19] L. S. Hewawasam, A. S. Jayasena, M. M. M. Afnan, R. A. C. P. Ranasinghe, M. A. Wijewardane, *Energy Rep.* **2020**, *6*, 474-479.

[20] X. Zhang, L.-D. Zhao, *J. Materiomics* **2015**, *1*, 92-105.

[21] W. von Münch, *Werkstoffe der Elektrotechnik*, 6 ed., Vieweg+Teubner Verlag, Wiesbaden, **1989**.

[22] P. Gu, M. Tani, S. Kono, K. Sakai, X. C. Zhang, *J. Appl. Phys.* **2002**, *91*, 5533-5537.

[23] M. Feneberg, R. A. R. Leute, B. Neuschl, K. Thonke, M. Bickermann, *Phys. Rev. B* **2010**, *82*, 075208.

[24] J. Singh, *Semiconductor Optoelectronics: Physics and Technology*, 1 ed., McGraw-Hill, New York, **1995**.

[25] A. Rogalski, *Opto-Electron. Rev.* **2012**, *20*, 279-308.

[26] Y. Taniyasu, M. Kasu, T. Makimoto, *Nature* **2006**, *441*, 325-328.

[27] M. Levinshtein, S. Rumyantsev, M. Shur, *Handbook Series on Semiconductor Parameters, Vol. 1*, 1 ed., World Scientific Pub Co Inc, Singapore, **1996**.

[28] T. C. Chiang, J. A. Knapp, M. Aono, D. E. Eastman, *Phys. Rev. B* **1980**, *21*, 3513-3522.

[29] A. J. Hong, L. Li, R. He, J. J. Gong, Z. B. Yan, K. F. Wang, J. M. Liu, Z. F. Ren, *Sci. Rep.* **2016**, *6*, 22778.

[30] H. Ibach, H. Lüth, *Festkörperphysik*, 7 ed., Springer, Berlin, **2009**.

[31] R. Wittmann, Phd thesis, Technischen Universität Wien (Wien), **2007**.

[32] J. Seebeck, *Abh. Königl. Akad. Wiss. Berlin* **1821**, 265–373.

[33] J. Fulmer, O. I. Lebedev, V. V. Roddatis, D. C. Kaseman, S. Sen, J.-A. Dolyniuk, K. Lee, A. V. Olenev, K. Kovnir, *J. Am. Chem. Soc.* **2013**, *135*, 12313-12323.

[34] T. Tadano, Y. Gohda, S. Tsuneyuki, *Phys. Rev. Lett.* **2015**, *114*, 095501.

[35] G. S. Nolas, J. Poon, M. Kanatzidis, *MRS Bull.* **2006**, *31*, 199-205.

[36] V. S. Debby Wu, Takashi Mochizuki *Chip Shortage Spirals Beyond Cars to Phones and Consoles*, https://www.bloomberg.com/news/articles/2021-02-05/chip-shortage-spirals-beyond-cars-to-phones-and-game-consoles, (09.03.2021).

[37] A. Haffner, T. Bräuniger, D. Johrendt, *Angew. Chem. Int. Ed.* **2016**, *55*, 13585-13588.

[38] A. Haffner, A.-K. Hatz, I. Moudrakovski, B. V. Lotsch, D. Johrendt, *Angew. Chem. Int. Ed.* **2018**, *57*, 6155-6160.

[39] A. Haffner, A.-K. Hatz, O. E. O. Zeman, C. Hoch, B. V. Lotsch, D. Johrendt, *Angew. Chem. Int. Ed.* **2021**, *60*, 13641-13646.

[40] M. Beekman, S. M. Kauzlarich, L. Doherty, G. S. Nolas, *Materials* **2019**, *12*.

[41] S. M. Kauzlarich, S. R. Brown, G. Jeffrey Snyder, *Dalton Trans.* **2007**, 2099-2107.

[42] E. S. Toberer, A. F. May, G. J. Snyder, *Chem. Mater.* **2010**, *22*, 624-634.

[43] G. J. Snyder, E. S. Toberer, *Nat. Mater.* **2008**, *7*, 105-114.

[44] M. Khatun, S. S. Stoyko, A. Mar, *J. Solid State Chem.* **2016**, *238*, 229-235.

[45] A. Haffner, V. Weippert, D. Johrendt, *Z. Anorg. Allg. Chem.* **2021**, *647*, 326-330.

[46] X. Zhang, T. Yu, C. Li, S. Wang, X. Tao, *Z. Anorg. Allg. Chem.* **2015**, *641*, 1545-1549.

[47] K. T. Y. Kauzlarich S.M., *Croat. Chem. Acta* **1991**, *64*, 343-352.

[48] S. Stoyko, L. Voss, H. He, S. Bobev, *Crystals* **2015**, *5*, 433.

[49] H. He, C. Tyson, M. Saito, S. Bobev, *J. Solid State Chem.* **2012**, *188*, 59-65.

[50] H. He, R. Stearrett, E. R. Nowak, S. Bobev, *Eur. J. Inorg. Chem.* **2011**, *2011*, 4025-4036.

[51] B. Eisenmann, H. Jordan, H. Schäfern, *Angew. Chem.* **1981**, *93*, 211-211.

[52] B. Eisenmann, J. Klein, *Journal of the Less Common Metals* **1991**, *175*, 109-117.

[53] B. Eisenmann, H. Jordan, H. Schäfer, *Z. Naturforsch., B: Chem. Sci.* **1982**, *37*, 1221.

[54] B. Eisenmann, H. Schäfer, *Z. Anorg. Allg. Chem.* **1982**, *484*, 142-152.

[55] B. Eisenmann, H. Schäfer, *Z. Naturforsch., B: Chem. Sci.* **1981**, *36*, 415.

[56] B. Eisenmann, H. Schäfer, *Angew. Chem.* **1980**, *92*, 480-481.

[57] B. Eisenmann, H. Jordan, H. Schäfer, *Z. Anorg. Allg. Chem.* **1981**, *475*, 74-80.

[58] B. Eisenmann, H. Jordan, H. Schäfer, *Z. Naturforsch., B: Chem. Sci.* **1982**, *37*, 1564-1568.

[59] B. Eisenmann, H. Jordan, H. Schäfer, *Z. Naturforsch., B: Chem. Sci.* **1984**, *39*, 864-867.

[60] H. Li, J. Kim, T. L. Groy, M. O'Keeffe, O. M. Yaghi, *J. Am. Chem. Soc.* **2001**, *123*, 4867-4868.

[61] H. Li, A. Laine, M. O'Keeffe, O. M. Yaghi, *Science* **1999**, *283*, 1145.

[62] Z.-Q. Li, C.-J. Mo, Y. Guo, N.-N. Xu, Q.-Y. Zhu, J. Dai, *J. Mater. Chem. A* **2017**, *5*, 8519-8525.

[63] P. Wagatha, P. Pust, V. Weiler, A. S. Wochnik, P. J. Schmidt, C. Scheu, W. Schnick, *Chem. Mater.* **2016**, *28*, 1220-1226.

[64] C. Wang, Y. Li, X. Bu, N. Zheng, O. Zivkovic, C.-S. Yang, P. Feng, *J. Am. Chem. Soc.* **2001**, *123*, 11506-11507.

[65] L. Wang, T. Wu, F. Zuo, X. Zhao, X. Bu, J. Wu, P. Feng, *J. Am. Chem. Soc.* **2010**, *132*, 3283-3285.

[66] X. Xu, W. Wang, D. Liu, D. Hu, T. Wu, X. Bu, P. Feng, *J. Am. Chem. Soc.* **2018**, *140*, 888-891.

[67] M. L. Huggins, P. L. Magill, *J. Am. Chem. Soc.* **1927**, *49*, 2357-2367.

[68] M. Hostettler, H. Birkedal, D. Schwarzenbach, *Acta Crystallogr., Sect. B: Struct. Sci.* **2002**, *58*, 903-913.

2 3D networks and sodalite structures in *A*/*AE*-Ge-As

2.1 Mixed Valence and Unusual Germanium Coordination in $SrGe_8As_{10}$, $BaGe_8As_{10}$, and $BaGe_7P_{12}$

Valentin Weippert, Thanh Chau, Kristian Witthaut and Dirk Johrendt

Published in: *Inorganic Chemistry* **2020**, *20*, 15447-15453.

Abstract

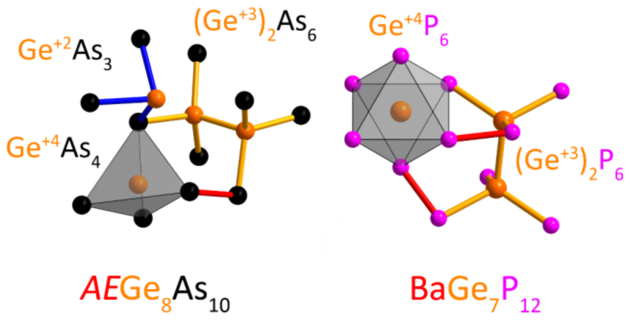

The new Zintl-compounds $AEGe_8As_{10}$ (AE = Sr, Ba) and $BaGe_7P_{12}$ were synthesized via solid-state reactions, and their structures were determined by single crystal and powder X-ray diffraction. $SrGe_8As_{10}$ and $BaGe_8As_{10}$ crystallize in the space group *Cmce* and show complex 3D networks composed of three different Ge–As motifs and As–As bonds with mixed valence of germanium in the oxidation states +2, +3, and +4. Mixed valences of germanium +3 and +4 occur in $BaGe_7P_{12}$, which crystallizes in the space group $R\bar{3}$ with a 3D network built up of Ge_2P_6 dumbbells and P–P bonds. An exceptional 6-fold coordinated germanium resides in the center of a GeP_6 trigonal antiprism. High temperature X-ray diffraction shows thermal stabilities up to 923–953 K. UV–Vis and resistivity measurements reveal a semiconducting nature with small indirect band gaps between 0.02 and 1.6 eV. Electronic band structure calculations confirm the semiconducting state and indicate covalent bonds within the Ge-*Pn* polyanions.

Introduction

Zintl phases are valence precise intermetallic compounds with all atoms achieving closed shell configuration. To satisfy this need of electrons, the anionic part often forms polyanionic units or frameworks instead of simple isolated anions. This enables quite a range of structural possibilities with intriguing properties. Among the use of Zintl ions in batteries[1] or the occurrence of magnetoresistance in $Eu_3In_2P_4$,[2] the main sought after phenomenon is the thermoelectric effect. The complex structures of Zintl phases often result in low thermal conductivity and facilitate various possibilities of tuning their transport properties.[3] $Ba_4In_8Sb_{16}$, $Yb_{14}MnSb_{11}$, $YbMg_2Sb_2$,

$Ba_{1-x}K_xZn_2As_2$, $KGaSb_4$ and $M_{14}MgBi_{11}$ (M = Ca, Sr, Eu) are just a few examples of the numerous Zintl-compounds with promising thermoelectric properties discovered in the recent years.[4-9]

Eisenmann et al. discovered the first alkaline-earth tetrel-pnictides (*AE*-*T*-*Pn*) in the 1980s. The members of the *AE*-*T*-*Pn* family (*AE* = Ca, Sr, Ba; *T* = Si, Ge; *Pn* = P, As) are valence precise Zintl phases with often complex polyanionic $(T,Pn)^{n-}$ networks. Germanium or silicon atoms are mostly in the oxidation state +4 with tetrahedral coordination by four *Pn* atoms. Ge^{+3} with one Ge bond and three *Pn* ligands, or +2 with either two Ge and two *Pn* ligands or with three *Pn* ligands and one lone-pair occur less frequently. Mixed valences of two or even three oxidation states in one compound are rare cases. The compounds $AE_3T_2Pn_4$ crystallize in two structure types with T_2Pn_6 dumbbells.[10-12] The structure of AE_4TPn_4 exhibits isolated TPn_4 tetrahedra,[13-15] while Ba_2GePn_2 (*Pn* = P, As) has the unusual motif of isolated and eclipsed Ge_2Pn_4 dumbbells.[16] $Ba_3Si_4P_6$ is a (Si^{+2}/Si^{+4}) mixed valence compound and has a unique structure with layers of Si-chains interconnected and surrounded by Si_4P_5 clusters.[17] An even more intricate structure has $BaGe_2Pn_2$ (*Pn* = P, As), with a 3D structure built of interconnected Ge_4Pn_4 and Ge_4Pn_5 cages.[18] These early studies mainly focused on the crystal structures, while properties remained undetermined.

The interest in this field was sparked again in 2015 by Zhang et al. with the discovery of $CaSiP_2$, a supertetrahedral compound, and $Ca_3Si_8P_{14}$ featuring a 3D network of vertex sharing SiP_4 tetrahedra and Ca_3SiP_2.[19] The reexamination of $BaGe_2Pn_2$ (*Pn* = P, As)[18] by Chen et al. revealed NLO properties with large second harmonic generation effects in the far IR region.[20] Similar NLO properties occur in $Ba_2Si_3P_6$ with chains of edge and vertex sharing SiP_4 tetrahedra acting as thermal barriers leading to ultralow thermal conductivity.[21] Haffner et al. found two polymorphs of Ba_2SiP_4 with all SiP_4 tetrahedra bridged via P–P bonds.[22, 23] The homologues AE_2SiP_4 (*AE* = Sr, Eu) are isotypic to the low temperature polymorph and exhibit potential as thermoelectrics.[24] Herein, we report the synthesis, crystal structures, and optical and electrical properties as well as electronic structure calculations of the new compounds $AEGe_8As_{10}$ (*AE* = Sr, Ba) and $BaGe_7P_{12}$, which crystallize in new structure types with mixed valence germanium and as yet unknown structural motifs.

Results and Discussion

Crystal Structure. The crystal structures of the isotypic compounds $SrGe_8As_{10}$ and $BaGe_8As_{10}$ were solved from single crystal data by charge flipping and refined in the space group *Cmce* (No. 64). A summary of the crystallographic data is given in Table 2.1. Atomic positions and anisotropic displacement parameters are given in Tables A.1-A.5 (appendix). The crystal structure of $BaGe_7P_{12}$ was determined from powder X-ray data due to the lack of suitable single crystals. It was solved in the space group $R\overline{3}$ (No. 148) with the structural model completed via difference Fourier maps and refined with the Rietveld method leading to the final structure summarized in Table 2.1. Atomic positions and isotropic displacement parameters are given in Tables A.6-A.7.

Table 2.1: Single crystal diffraction data of $SrGe_8As_{10}$ and $BaGe_8As_{10}$ and Powder X-ray diffraction data of $BaGe_7P_{12}$ from Rietveld refinement.

formula	$SrGe_8As_{10}$	$BaGe_8As_{10}$	formula	$BaGe_7P_{12}$
space group	*Cmce* (No. 64)	*Cmce* (No. 64)	space group	$R\overline{3}$ (No. 148)
a / Å	14.5614(7)	14.5799(3)	a / Å	12.630883(32)
b / Å	10.6452(6)	10.7164(2)	b / Å	12.630883(32)
c / Å	11.4283(5)	11.5518(2)	c / Å	9.247182(43)
V_{cell} / Å^3	1771.49(15)	1804.90(6)	V_{cell} / Å^3	1277.637(9)
Z	4	4	Z	3
$\rho_{\text{X-ray}}$ / g cm^{-3}	5.315	5.400	$\rho_{\text{X-ray}}$ / g cm^{-3}	3.967
R_σ / R_{int}	0.0304 / 0.0614	0.0200 / 0.0630	-	-
R_1 ($F^2 > 2\sigma(F^2)$) / all	0.0262 / 0.0372	0.0165 / 0.0230	R_{p} / R_{wp}	2.099 / 2.762
wR_2 ($F^2 > 2\sigma(F^2)$) / all	0.0474 / 0.0503	0.0310 / 0.0335	R_{exp} / R_{Bragg}	2.484 / 0.980
GooF	1.126	1.119	GooF	1.112
$\Delta\rho_{\mathrm{max/min}}$ / eÅ^{-3}	+1.252 / -1.547	+0.846 / -1.029	-	-

The isotypic compounds $SrGe_8As_{10}$ and $BaGe_8As_{10}$ form a new structure type $AEGe_8As_{10}$ with the space group *Cmce* (No. 64). Its complex polyanionic network consists of three different Ge–As units. For a better understanding, we divide the structure into two sections. Figure 2.1a shows the first section in the *ac*-plane with chains of vertex-sharing $Ge^{+4}As_4$ tetrahedra (gray) and $Ge^{+2}As_3$ trigonal pyramids (blue) with its lone pair directed toward the *AE* position. The chains are interconnected by As–As bonds with distances of 2.5144(6) Å (*AE* = Sr) and 2.5296(4) Å (*AE* = Ba), which are close to the sum of the covalence radii (2.40 Å). Figure 2.1b shows the second section in the *ac*-plane with pairs of staggered $(Ge^{+3})_2As_6$ dumbbells and the *AE* position. The dumbbells contain Ge–Ge bonds with distances of 2.4286(6) Å (*AE* = Sr) and 2.4217(4) Å (*AE* = Ba), respectively, again close to sum of the covalent radii (2.36 Å). These two sections are connected via common vertices, resulting in a 3D-network as shown in Figure 2.1c. The connectivity in the polyanion leads to the formula $Ba^{+2}(Ge^{+2})_2(Ge^{+3})_4(Ge^{+4})_2(As^{-2})_4(As^{-3})_6$, thus $BaGe_8As_{10}$ and $SrGe_8As_{10}$ are mixed valence compounds with germanium in three different oxidation states.

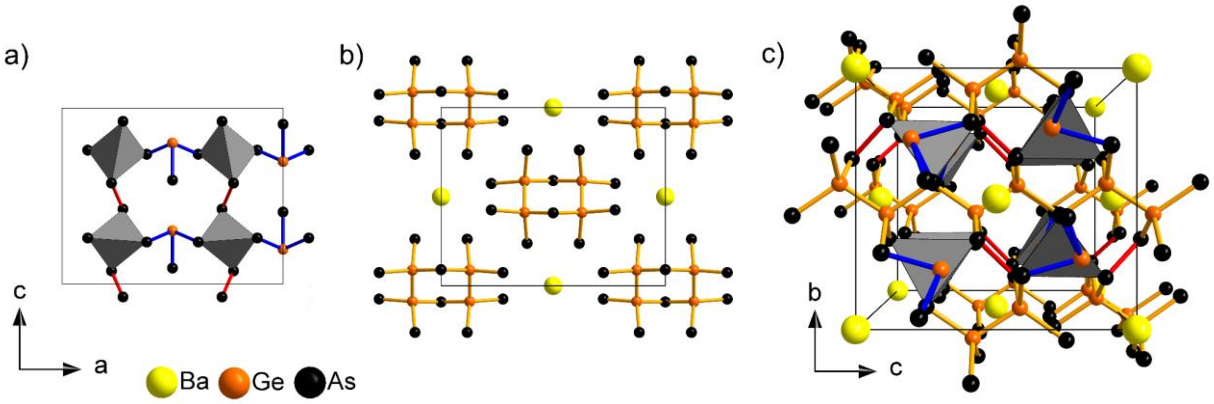

Figure 2.1: Sections of $BaGe_8As_{10}$ in the *ac*-plane with (a) chains of $Ge^{+4}As_4$ tetrahedra (gray) and $Ge^{+2}As_3$ trigonal pyramids (blue) interconnected by As–As bonds (red), (b) pairs of $(Ge^{+3})_2As_6$ dumbbells (orange) with Ba located in between and (c) the unit cell viewed along the *a*-axis with the sections connected via common vertices forming an interconnected 3D-network.

The AE^{+2} cations are embedded in this framework and coordinated by distorted $As_{10}Ge_2$ icosahedra (Figure 2.2). The 12 AE–As/Ge bonds subdivide into six shorter (3.2335(7)–3.3172(4) Å) forming a distorted trigonal antiprism, and six longer (3.6793(7)–3.8237(5) Å) located above the equatorial planes. Due to the rigid polyanionic network, the AE–As/Ge distances are similar, as the difference of the unit cell volumes of the two compounds is only 1.9 % (Table A.8, appendix). These values are lower compared to what one might expect from the difference in ionic radii of Sr^{+2} (1.18 Å) and Ba^{+2} (1.35 Å) with $\Delta = 14.4$ %.[25] These circumstances result in a significantly smaller thermal displacement ellipsoid for the larger Ba^{+2} cation (U_{eq} = 0.01841(9) Å^2) compared to the Sr^{+2} cation (U_{eq} = 0.0302(2) Å^2).

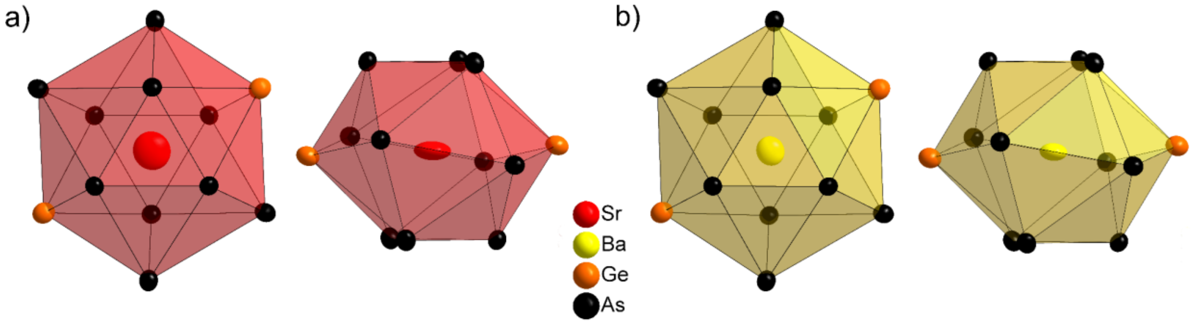

Figure 2.2: Distorted icosahedral coordination sphere of Sr^{+2} and Ba^{+2} in (a) $SrGe_8As_{10}$ and (b) $BaGe_8As_{10}$, respectively. Thermal displacement ellipsoids are drawn at the 95 % probability level.

The compound $BaGe_7P_{12}$ crystallizes likewise in a new structure type in the space group $R\bar{3}$ (No. 148) with comparable structural motifs and a polyanionic 3D network like $AEGe_8As_{10}$. Figure 2.3a shows the building units of $BaGe_7P_{12}$. Columns of alternately stacked face-sharing $Ge^{+4}P_6$ trigonal antiprisms and BaP_{12} icosahedra run along the *c*-axis. The high coordination number 12 is again realized by six shorter (3.493(2) Å) and six longer (3.679(3) Å) Ba–P bonds. The 6-fold coordinated germanium atoms with six identical bonds (2.551(3) Å Ge–P) are quite unusual and unprecedented so far. The high pressure phase of GeP_3 contains germanium likewise in a trigonal antiprism but shifted off the center with three short (2.50 Å) and three longer (2.85 Å) Ge–P distances.[26] Here, the germanium atom is in the center of the trigonal antiprism. We assume that the elongation of the octahedron toward trigonal symmetry relies on the fact that the coordinating phosphorus atoms are part of a rigid covalent network (Figure 2.3c).

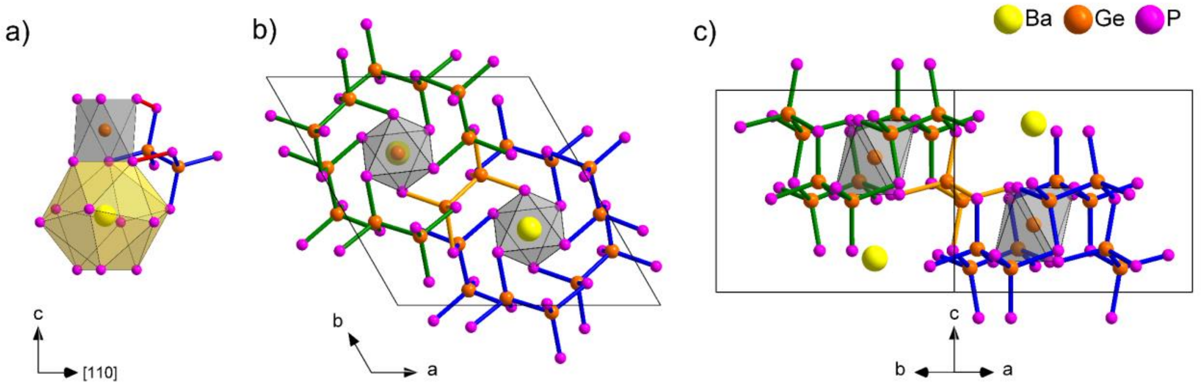

Figure 2.3: (a) Building units of $BaGe_7P_{12}$ with $Ge^{+4}P_6$ trigonal antiprisms (gray), BaP_{12} icosahedra (yellow), P–P bonds (red) and $(Ge^{+3})_2P_6$ dumbbells (blue). (b) Two 12er ring motifs (green/blue) built of six Ge_2P_6 unit connected via a common Ge_2P_6 unit (orange) and (c) view along (110).

The columns of BaP_{12} icosahedra and GeP_6 antiprisms are connected to staggered $(Ge^{+3})_2P_6$ dumbbells via common vertices or P–P bonds with a distance of 2.202(4) Å. $BaGe_7P_{12}$ has two independent P-positions, and both form this P–P bond, resulting in P^{-2} for the whole compound. These motifs and connections result in the mixed valence formula $Ba^{+2}(Ge^{+3})_6Ge^{+4}(P^{-2})_{12}$. The Ge_2P_6 dumbbells (2.444(2) Å Ge–Ge) are connected to each other via common vertices, forming 12er rings (Figure 2.3b, green/blue) surrounding the $Ge^{+4}P_6$ unit. These rings are linked through common Ge_2P_6 dumbbells (orange). Figure 2.3c shows the alternately stacked arrangement of the 12er rings. A more expanded view of this motif shows Figure A.1 (see appendix).

Powder X-ray Diffraction. X-ray powder diffraction data for $SrGe_8As_{10}$, $BaGe_8As_{10}$, and $BaGe_7P_{12}$ and the respective Rietveld refinements are shown in Figures A.2-A.4 (see appendix). The calculated patterns are in excellent agreement with the measured ones. The samples contain minor impurities (< 8 wt.-%) of GeAs, Ge, and $SrAs_3$. High temperature X-ray powder diffraction patterns of $SrGe_8As_{10}$, $BaGe_8As_{10}$, and $BaGe_7P_{12}$ (Figures A.5-A.7, appendix) indicate thermal stability up to temperatures of 923, 943, and 953 K, respectively.

EDX Measurements. Table 2.2 shows the EDX results of $SrGe_8As_{10}$, $BaGe_8As_{10}$, and $BaGe_7P_{12}$. The experimental values agree with the theoretical ones within the typical error of the method.

UV-Vis Spectroscopy. Figure 2.4a shows the diffuse reflectance spectra of $BaGe_7P_{12}$ converted to a Tauc plot. It reveals an indirect optical band gap of approximately 1.6 eV. Although the optical band gaps of $SrGe_8As_{10}$ and $BaGe_8As_{10}$ were too small to be detected, their respective Tauc plots indicate indirect band gaps as well.

Table 2.2: EDX results of $SrGe_8As_{10}$, $BaGe_8As_{10}$ and $BaGe_7P_{12}$.

Formula	*AE* (at-%)	Ge (at-%)	*Pn* (at-%)
AEGe_8As_{10} (calc.)	5.3	42.1	52.6
$SrGe_8As_{10}$	5.3(6)	42.5(5)	52.2(7)
$BaGe_8As_{10}$	5.3(2)	41.0(5)	53.7(6)
$BaGe_7P_{12}$ (calc.)	5	35	60
$BaGe_7P_{12}$	5.3(2)	37.2(7)	57.5(7)

Table 2.3: Resistivity and bandgaps of $SrGe_8As_{10}$, $BaGe_8As_{10}$ and $BaGe_7P_{12}$.

formula	resistivity (Ωcm) 300 K	bandgap E_g (eV)		
		electrical	optical	calculated
$SrGe_8As_{10}$	43	0.20	-	0.43
$BaGe_8As_{10}$	56	0.13	-	0.57
$BaGe_7P_{12}$	8	0.02	1.6	1.47

Resistivity Measurements. To determine the bandgaps of $SrGe_8As_{10}$ and $BaGe_8As_{10}$, electrical resistivity measurements were conducted between 250 and 300 K. In this temperature range, they exhibit semiconducting behavior (Figure 2.4b) with rather high resistivities (Table 2.3). The band gaps were determined from Arrhenius plots (Figure 2.4c) to values of 0.20 and 0.13 eV, respectively. $BaGe_7P_{12}$ most likely shows extrinsic semiconducting behavior caused by defects or impurity doping, which leads to a lower resistivity of 7.7 Ωcm at 300 K and a negligible band gap of 0.02 eV (Figure A.8, appendix). The intrinsic region at higher temperatures (see Figure A.9a, appendix) is not accessible due to device limitations. Larger band gaps have been reported for the related compounds $BaGe_2As_2$ (1.26 eV) or $BaGe_2P_2$ (1.32 eV).[20] We suggest that this comes from the higher charge of the Ge*Pn*-Polyanions in the latter compounds, which enhances the ionic character.

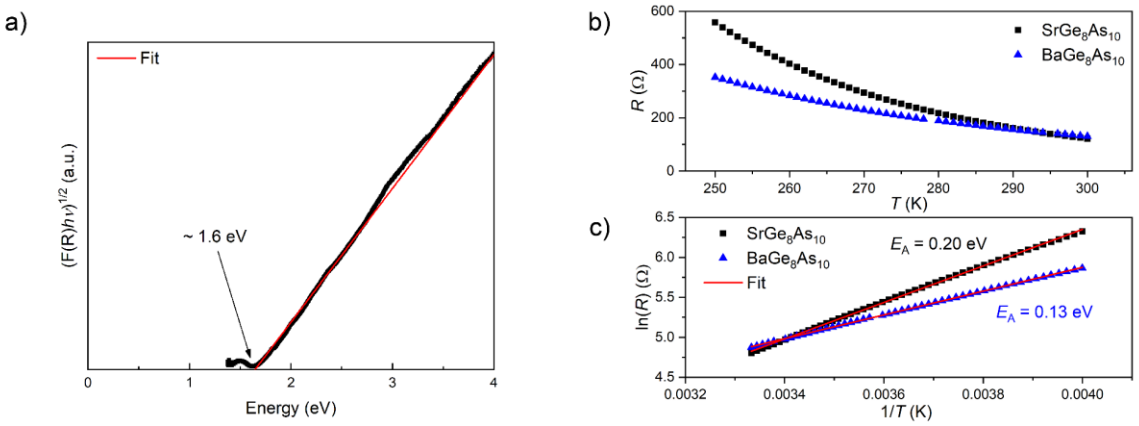

Figure 2.4: (a) Tauc Plot of a Kubelka–Munk converted diffuse reflectance UV–Vis spectra of $BaGe_7P_{12}$. (b) Resistivity of $SrGe_8As_{10}$ and $BaGe_8As_{10}$ and (c) the respective Arrhenius plots.

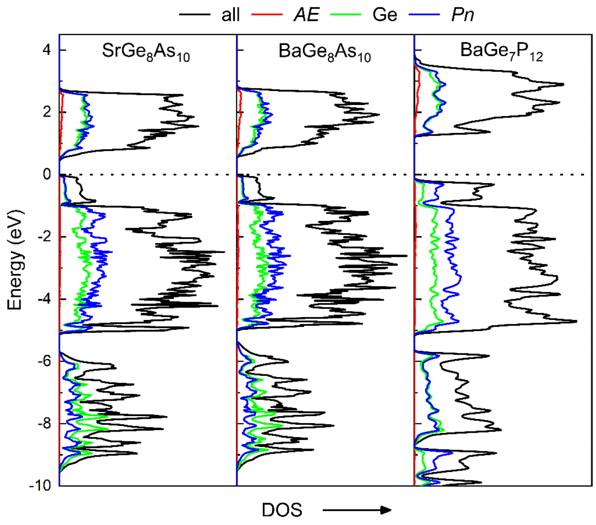

Figure 2.5: Total and atom resolved density of states (DOS) for $SrGe_8As_{10}$ (left), $BaGe_8As_{10}$ (middle) and $BaGe_7P_{12}$ (right). The Fermi level E_F (dotted line) is the energy reference at 0 eV.

Electronic structure. DFT calculations were conducted to support the experimental band gap values and their nature. Band structure calculations confirm indirect band gaps for all compounds (Figures A.9b-A.10, appendix). The mBJ hybrid functional gives gaps of 0.43 eV ($SrGe_8As_{10}$), 0.57 eV ($BaGe_8As_{10}$), and 1.47 eV ($BaGe_7P_{12}$) (Table 2.3). These values are in the same order of magnitude as the experimental values; however, the smaller values of the electrical gap indicate extrinsic conductivity to some degree. Figure 2.5 shows the density of state plots (DOS). $SrGe_8As_{10}$ and $BaGe_8As_{10}$ show almost identical patterns. The states below the Fermi level are almost exclusively constituted from Ge and As states. Being down to −5 eV, the more electronegative As shows a higher contribution whereas states between −5 and −10 eV show a higher proportion of Ge states. The conduction band shows a certain contribution of Sr and Ba states, but due to the stoichiometric proportions of *AE* to Ge/As, it is still dominated by Ge and As states. The DOS of $BaGe_7P_{12}$ shows similar features, but due to P instead of As, a wider band gap and the states below the Fermi level are dominated by P states.

Table 2.4: Oxidation states (OS) and Bader charges of $SrGe_8As_{10}$, $BaGe_8As_{10}$ and $BaGe_7P_{12}$.

atom site	Oxidation state		Bader charges	
		$SrGe_8As_{10}$	$SrGe_8As_{10}$	$SrGe_8As_{10}$
AE	+2	+1.45	+1.34	+1.44
Ge	+2	+0.21	+0.21	
Ge	+3	+0.30	+0.29	+0.48
Ge	+4	+0.38	+0.37	+0.70
As (P)	−2	−0.24	−0.23	−0.42
As	−3	−0.48	−0.46	

To evaluate the bonding character of the compounds, we calculated Bader charges. The results are summarized in Table 2.4. A more detailed list is given in Tables A.9-A.10 (see appendix). The Bader charges of the *AE* ions are +1.34 and +1.45 and indicate ionic bonds. The charges of germanium and arsenic in the polyanionic networks differ greatly from their oxidation states, which indicates mainly covalent character. The results for $BaGe_7P_{12}$ show an overall increased ionic character as can be expected from the more electronegative P instead of As. However, the values are still far off from the oxidation states, thus also supporting a major covalent character of the polyanionic network. All charges follow the trend according to the different oxidation states of Ge, As, and P. The relatively high Bader charge of the 6-fold coordinated germanium in $BaGe_7P_{12}$ indicates a stronger ionic character of the six Ge–P bonds.

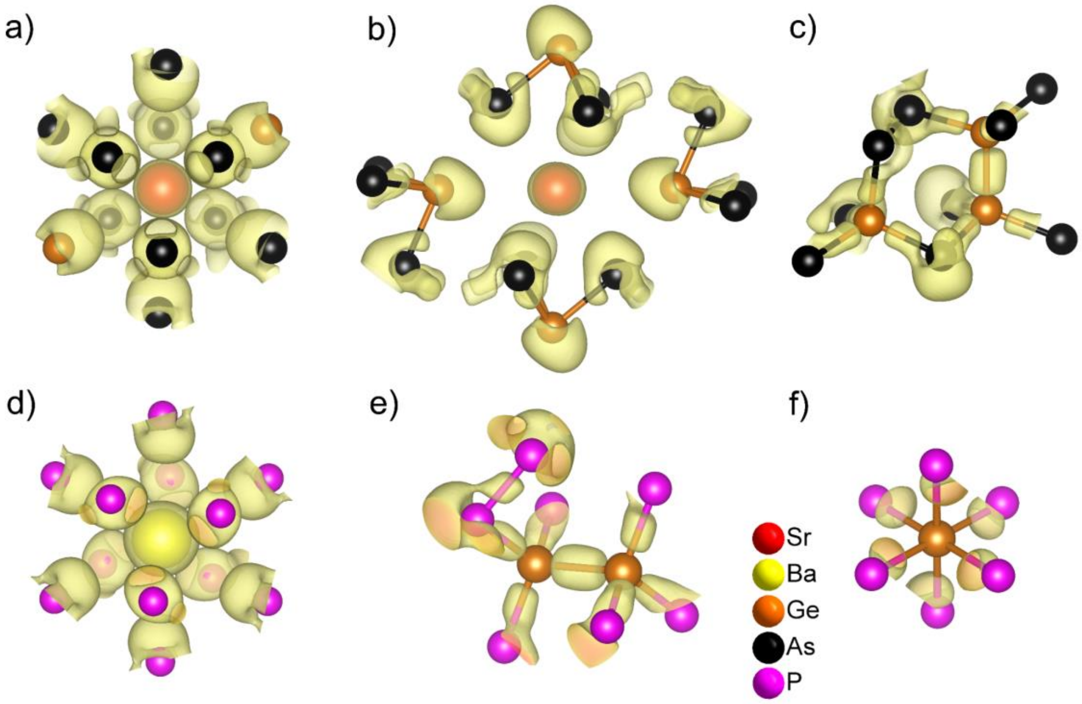

Figure 2.6: Electron location function (ELF) of $SrGe_8As_{10}$ (Isosurfaces at ELF = 0.8) with the (a) $SrAs_{10}Ge_2$ icosahedron, (b) a section of said icosahedra with $GeAs_3$ trigonal pyramids and respective lone pairs and (c) the $GeAs_4$ and Ge_2As_6 units with the As–As bond. The ELF of $BaGe_7P_{12}$ with (d) the BaP_{12} icosahedron, (e) the Ge_2P_6 dumbbell and P–P bond and (f) the GeP_6 trigonal antiprism.

To visualize the electronic environments and bonding conditions, electron localization functions (ELF) were calculated for all compounds. Figure 2.6 shows the structural motifs of $SrGe_8As_{10}$ and $BaGe_7P_{12}$. The respective motifs of $BaGe_8As_{10}$ are shown in Figure A.11 (see appendix). The icosahedra of $SrGe_8As_{10}$ and $BaGe_7P_{12}$ show no localization between the alkaline earth central atom and the respective ligand atoms, supporting their ionic character as calculated from Bader charges (Figure 2.6a,d). Figure 2.6b shows the $GeAs_3$ motif of $SrGe_8As_{10}$ with a clearly visible lone pair according to the oxidation state of Ge^{+2}. The $GeAs_4$ and Ge_2As_6 motifs and As–As and Ge–Ge bonds of $SrGe_8As_{10}$ in Figure 2.6c display electron density along all drawn bonds, which is in line with a covalently bound polyanionic network. The Ge_2P_6 dumbbell and P–P bond of $BaGe_7P_{12}$ are shown in Figure 2.6e. Similar to $SrGe_8As_{10}$, electron density can be found on all drawn bonds underlining its covalent character. Figure 2.6f shows the GeP_6 trigonal antiprism with electron density directed to the central Ge atom but lacking discrete covalent bonds.

Conclusion

$SrGe_8As_{10}$ and $BaGe_8As_{10}$ are isotypic Zintl phases and crystallize in a new structure type in the space group *Cmce*. They exhibit a complex polyanionic network with a 3D structure comprised of $Ge^{+2}As_3$ trigonal pyramids, $Ge^{+4}As_4$ tetrahedra, and ethane-like $(Ge^{+3})_2As_6$ motifs, including As–As bonds and mixed valence germanium +2, +3, and +4. $BaGe_7P_{12}$ crystallizes in a new structure type in the space group $R\overline{3}$. It features exceptional 6-fold coordinated germanium in $Ge^{+4}P_6$ trigonal antiprisms, and an arrangement of $(Ge^{+3})_2P_6$ dumbbells into interconnected 12er rings forming a 3D network. UV–Vis spectroscopy and resistivity measurements reveal semiconducting behavior for all compounds and indirect bandgaps between 0.02 and 1.6 eV. DFT band structure calculations support the semiconducting state. ELF calculations and Bader charge analysis indicate a highly covalent character of the polyanionic networks.

Experimental Section

Synthesis. All compounds were synthesized by heating stoichiometric mixtures of the elements (Sr, 99.95 %, Sigma-Aldrich; Ba, 99.99 % Sigma-Aldrich; Ge, 99.999 %, Sigma-Aldrich; As, 99.99999+ %, Alfa Aesar; P_{red}, 99.999 %, Chempur) with typical batch sizes of 300 mg. All reaction steps were performed in alumina crucibles sealed in silica ampules under an atmosphere of purified argon. To grow single crystals of the arsenide compounds, the mixtures were heated to 1123 K at a rate of 25 Kh^{-1}, kept at this temperature for 20 h, and cooled to 673 K at a rate of 10 Kh^{-1}; after that, the furnace was switched off. Single-phase samples emerged if the mixtures were heated to 893 and 913 K for 60 h for $AEGe_8As_{10}$ and $BaGe_7P_{12}$, respectively, with heating and cooling rates of 25 Kh^{-1}. The samples were thoroughly homogenized in an argon-filled glovebox, pressed into pellets, and heated at the same temperatures at rates of 50 Kh^{-1}. The latter step was repeated five times. Due to a certain evaporation of P in $BaGe_7P_{12}$ samples, the weight loss was compensated by adding small amounts of phosphorus (~20 mg) after each step. This procedure yielded black powders, which are stable at air.

Single Crystal X-ray Diffraction. Single crystal data were collected using a Bruker D8 Quest diffractometer (Mo Kα, Photon-II detector). Intensity integration, data reduction, and absorption corrections were done with APEX3[27] and SADABS;[28] the space groups were determined from systematic absences using XPREP.[29] The crystal structures were solved with the Superflip[30] package and refined with the SHELXL[31] package.

Powder X-ray Diffraction. Samples were filled and sealed in glass capillaries of 0.2 or 0.1 mm in diameter (Hilgenberg GmbH). The X-ray powder patterns were measured using a Stoe Stadi-P diffractometer (Cu Kα1, Ge(111)-monochromator, Mythen 1k detector) and fitted with the TOPAS package.[32] Peaks were indexed with the SVG-algorithm, and a suitable space group was chosen based on systematic extinctions.[33] Intensities were gathered using the Pawley method, and the structure solution was performed via charge-flipping.[34-36] The structure models were refined with the Rietveld method.

The deposition numbers 2010143 ($SrGe_8As_{10}$), 2010144 ($BaGe_8As_{10}$), 2010142 ($BaGe_7P_{12}$) contain the crystallographic data. These are provided free of charge by the joint Cambridge Crystallographic Data Centre and Fachinformationszentrum Karlsruhe Access Structures service www.ccdc.cam.ac.uk/structures.

High Temperature Powder X-ray Diffraction. Samples were filled in silica capillaries of 0.4 mm in diameter (Hilgenberg GmbH) sealed by grease to compensate increasing pressure. Diffraction data were collected under argon atmosphere with a Stoe Stadi P diffractometer (Mo Kα1, Ge(111)-monochromator, IP-PSD detector) equipped with a graphite furnace. The samples were heated with 2 K min^{-1}. The data were visualized with WinXPOW.[37]

EDX Measurements. Scanning electron microscopy was performed on a Carl Zeiss EVO-MA 10 with SE and BSE detectors controlled by the SmartSEM[38] software. The microscope was equipped with a Bruker Nano EDX detector (X-Flash detector 410-M) for EDX investigations using the QUANTAX 200[39] software to collect and evaluate the spectra. Elements contained in the sample holder and adhesive carbon pads were disregarded.

UV-Vis Spectroscopy. Diffuse reflectance spectra of powder samples were measured with a Jasco V-650 UV–Vis spectrometer with detectible radiation between 240 to 900 nm. Data were converted according to the Kubelka–Munk theory[40] and plotted as Tauc graphs.

Resistivity Measurements. Samples were pressed into pellets and sintered at 823 K for 40 h in corundum crucibles that were sealed in silica ampules under an atmosphere of purified argon. Resistivity measurements were conducted with a Quantum Design Inc. PPMS (physical property measurement system), equipped with a resistivity option, between 250 and 300 K. The samples were contacted with a four point Van der Pauw press contact by Wimbush. Data were collected with the PPMS MultiVu software package.[41]

DFT Calculations. First-principles electronic structure calculations were performed using the Vienna ab initio simulation package (VASP),[42, 43] which is based on density functional theory (DFT) and plane wave basis sets. Projector-augmented waves (PAW)[44] were used and contributions of correlation and exchange were treated in the generalized-gradient approximation (GGA).[45] The electron location function (ELF) was used to illustrate atomic bonds.[46] We used the modified Becke-Johnson exchange potential (mBJ)[47] which yields band gaps close to experimental values. The Bader analysis[48] implemented by Henkelman et al.[49] was used to extract charges from the electron density distribution.

2.2 $BaGe_8As_{14}$: a semiconducting sodalite type compound

Valentin Weippert, Thanh Chau, Kristian Witthaut, Lucien Eisenburger and Dirk Johrendt

Published in: *Chemical Communications* **2021**, *57*, 1332-1335

Reproduced from reference with permission from the Royal Society of Chemistry.

Abstract

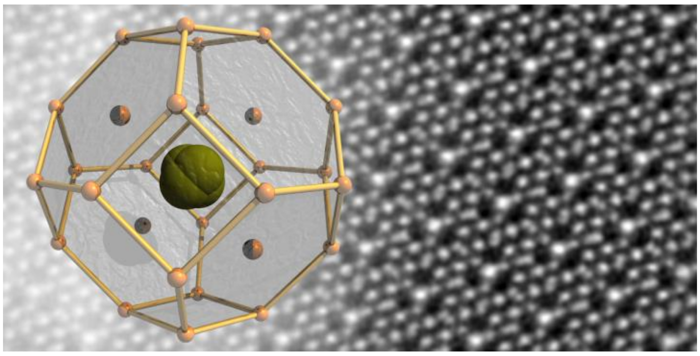

A new sodalite-type compound, namely $BaGe_8As_{14}$ was synthesized via solid-state reactions and structurally characterized with single crystal X-ray diffraction (space group $I\bar{4}3m$). Vertex-sharing $GeAs_4$-tetrahedra form β-cages with additional Ge/As-mixed sites located slightly above or below the six-membered rings. The structure is similar to the borate mineral rhodizite. Barium atoms are disordered due to a slight shift off the centers of large β-cages. This partially disordered structure together with a narrow bandgap of 0.43 eV in line with low resistivity (2×10^{-2} Ωcm), and a high carrier concentration (1.6×10^{20} cm^{-3})at 300 K qualifies$BaGe_8As_{14}$ as a potential thermo-electric material.

Introduction

Cage compounds represent a fascinating class of solids and attract considerable interest.[50] The group of zeolites, although first mentioned in 1756, is one of the most intensely researched fields in chemistry, with an increasing tendency. According to *SciFinder*, it has produced over 900 publications annually since 2016. Zeolites allow a multitude of applications ranging from ion-exchange or -absorption, energy storage, thermoelectric materials to catalysts in petrochemical cracking.[51-55] The variety of zeolite frameworks is based on the variations of the Al/Si ratio, substitution of framework atoms, and different ways to connect cages and other structural motifs. As of today, the Database of Zeolite Structures lists 252 types of different frameworks.[56] A base motif of many zeolites is the sodalite cage, originating from the equally named $Na_8(Al_6Si_6O_{24})Cl_2$ mineral.[57] Combined with other cages, it occurs in many frameworks.[50] The sodalite framework (SOD) itself is composed of all-face-sharing β-cages packed in a bcc arrangement. The different coordinations of cage positions and the incorporation of guest atoms lead to a large variety of sodalite-type compounds.[50, 58] Almost all are oxides, such as $Zn_4O(BO_2)_6$, $[GaGe_5O_{12}]^-$ or $Na_8(Si_9Be_3O_{24})Cl_2$,[59-61] whereas non-oxide sodalite frameworks such as $Cu_{12}Sb_4S_{13}$, $Zn_7(P_{12}N_{24})Cl_2$,[62-65] and $[Cu_2Zn_{10}Cl_{24}]$ are rare.[51, 66] Consequently, semiconducting intermetallic compounds with sodalite cages are largely unexplored. But just these compounds can be of particular interest for high performing thermoelectric materials as they offer the possibility to incorporate so-called "rattling atoms" in the large void of the sodalite cage. This concept already leads to promising results in skutterudite compounds such as Fe_3CoSb_{12}, doped $CoSb_3$ and $IrSb_3$, or $Ba_8Ga_{16}T_{30}$ (T = Si and Ge) for clathrates.[67-70] Herein, we present $BaGe_8As_{14}$, the first Ge–As-based sodalite-type compound. It features a disordered Ba position in an unusually large coordination sphere with promising semiconducting properties.

Results and Discussion

Crystal structure. The crystal structure of $BaGe_8As_{14}$ was analyzed using single-crystal X-ray data via charge flipping and refining in the $I\bar{4}3m$ space group (no. 217). Table 2.5 summarizes main results, with detailed crystallographic data tabulated in Tables A.11 – A.14 (see appendix).

Table 2.5: Single crystal diffraction data of $BaGe_8As_{14}$.

formula	$BaGe_8As_{14}$
space group	$I\bar{4}3m$ (No. 217)
a / Å	10.3145(2)
V_{cell} / Å^3	1097.35(6)
Z	2
$\rho_{X\text{-ray}}$ / g cm^{-3}	5.35
R_σ / R_{int}	0.0113 / 0.0408
R_1 ($F^2 > 2\sigma(F^2)$) / all	0.0123 / 0.0132
wR_2 ($F^2 > 2\sigma(F^2)$) / all	0.0301 / 0.0303
GooF	1.33
$\Delta\rho_{max/min}$ / eÅ^{-3}	+0.597 / -0.598

The $BaGe_8As_{14}$ compound crystallizes in a sodalite-type structure with the typical β-cage, as shown in Figure 2.7a (without arsenic atoms) and Figure 2.7b (with $GeAs_4$ tetrahedra). Barium atoms located near the centers of Ge_{24} cages are slightly shifted off the high symmetry $2a$ ($\bar{4}3m$) site by 0.358 Å along [111] to the $8c$ (3m) site. Figure 2.7b shows $GeAs_4$ tetrahedra at cage positions sharing common vertices. The $Ge_{0.5}As_{0.5}$ mixed site is slightly above or below the centers of the 6er rings of the Ge_{24} cage unlike in the related structure of rhodizite with a Be atom centered in its 6er ring.[71] The mixed site forms $(Ge/As)As_3$ trigonal pyramids (Figure 2.8) with the (Ge/As)–As bond length of 2.504(2) Å, which are in the range of typical Ge–As or As–As bonds. This arrangement allows the $Ba^{+2}(Ge^{+4})_6(Ge^{+2})_2(As^0)_2(As^{-2})_6(As^{-3})_6$ charge-neutral

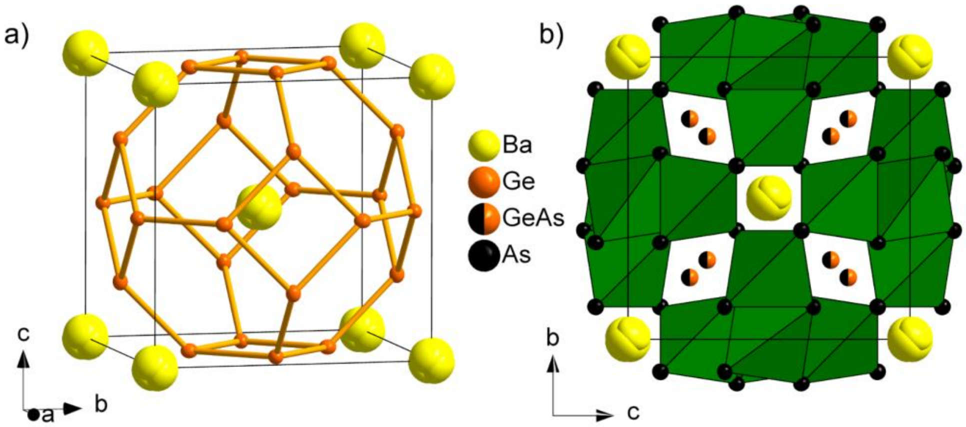

Figure 2.7: (a) Ge_{24} cage with a disordered Ba-position and (b) the complete cage with vertex sharing $GeAs_4$ tetrahedra with a mixed Ge/As position. Thermal displacement ellipsoids show the 95 % probability level.

Figure 2.8 shows the environment of the disordered Ba position. The $\bar{4}3m$ symmetry at the center results in a tetrahedral array of Ba atoms (each occupying 25 %). The coordination is a pseudo-Frank–Kasper polyhedron with CN = 9 + 7, comprising four Ge/As and twelve As with two sets of distances: $d_{(\mathrm{CN}\,9)}$ = 3.607(2)–3.869(2) Å and $d_{(\mathrm{CN}\,7)}$ = 4.113(2)–4.271(2) Å (Figure 2.8)

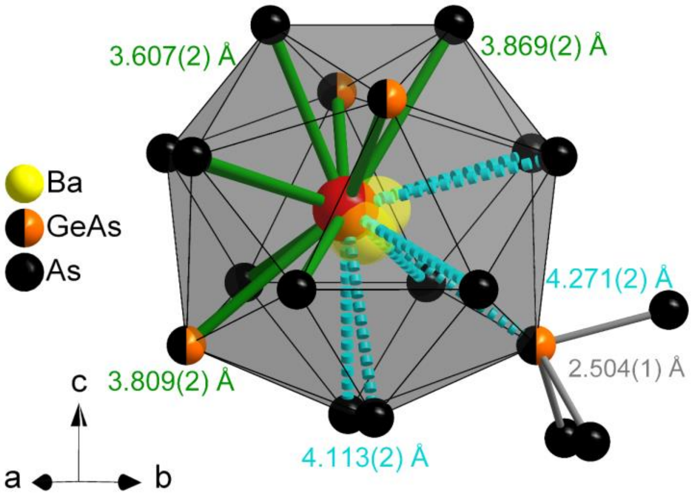

Figure 2.8: The Ba coordination sphere with a CN = 9 + 7 pseudo-Frank–Kasper polyhedra (selected the central Ba atom in red) and the (Ge/As)As_3 trigonal pyramid motif (grey).

Low-temperature single-crystal X-ray experiments demonstrate that the displacement of Ba atoms is static. The corresponding crystallographic data, atomic positions, and anisotropic displacement parameters are tabulated in Tables A.15 – A.23 (see appendix). Only the disordered Ba position yielded excellent results with small residuals. Refinements with Ba at the center (2a) position result in large displacement parameters, which do not extrapolate to zero at low temperatures (Figure 2.9).

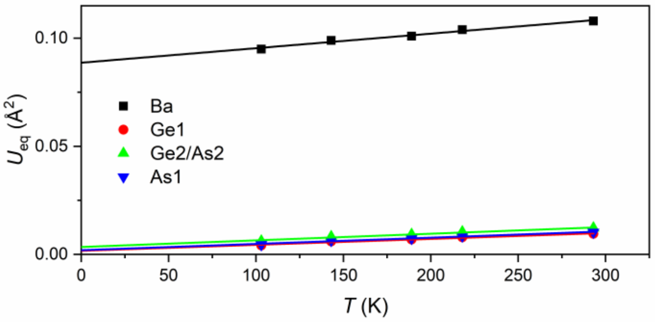

Figure 2.9: The U_{eq} of an ordered Ba position at 2a (0, 0, 0), and Ge and As positions in $BaGe_8As_{14}$ at 293, 218, 189, 143, and 103 K with regression lines.

Since Ge and As are indistinguishable through laboratory-scale X-ray diffraction, we checked a possible ordering of the Ge/As site with selected area electron diffraction (SAED) experiments. SAED simulations with the ordered structure in the $P\bar{4}3m$ space group with As and Ge on different 4e sites show additional weak spots (with $h + k + l \neq 2n$), which are not visible in measured patterns (Figure A.12, appendix). Thus, the body-centred space group is correct. Further, STEM-HAADF images (Figure 2.10 and Figure A.13, appendix) perfectly coincide with the structure overlay, which further supports the structure.

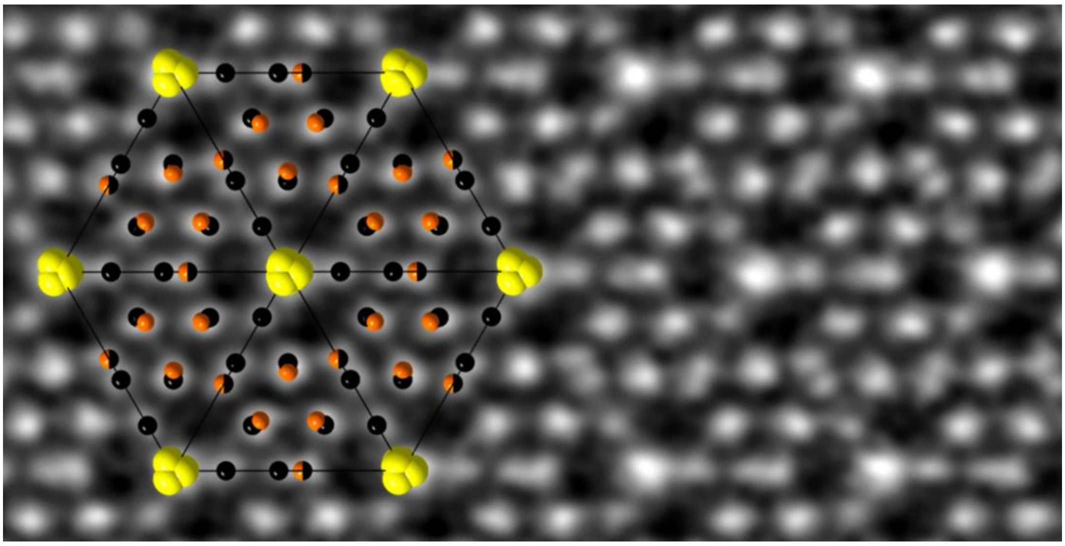

Figure 2.10: The crystal structure of $BaGe_8As_{14}$ in the [111] direction combined with a projection of one-unit cell from the STEM HAADF image in Figure A.13 (see appendix) (Ba: yellow, Ge: brown and As: black).

Given the charge-neutral formula, we expected semiconducting properties. The optical bandgap from UV-Vis-NIR measurements assuming indirect or direct transitions in the Kubelka–Munk function is 0.43 eV or 0.45 eV, respectively (Figure 2.11a). The resistivity of a compacted and sintered $BaGe_8As_{14}$ pellet is 2.2×10^{-2} Ω cm at 300 K, and increases with a decreasing temperature (Figure A.14a, appendix). From the fit of the Arrhenius-plot (Figure A.14b, appendix), we obtain very small activation energies of 0.01 to 0.03 eV, similar to the observation in related compounds.[72] This indicates extrinsic conductivity through dopant levels close to the conduction band. The small amounts of impurities hardly contribute to the optical absorption; thus, the optical band gap is much larger and closer to the intrinsic value. Hall effect measurements indicate the p-type nature of the $BaGe_8As_{14}$ compound (Figure A.15, appendix) and yield the carrier concentrations of 1.6×10^{20} cm^{-3} (300 K) and 2.3×10^{20} cm^{-3} (400 K), which are typical for a doped semiconductor (p-type GaAs: 8×10^{18} cm^{-3})[73] with low mobility values of ≈ 2 cm^{2} V^{-1} s^{-1}.

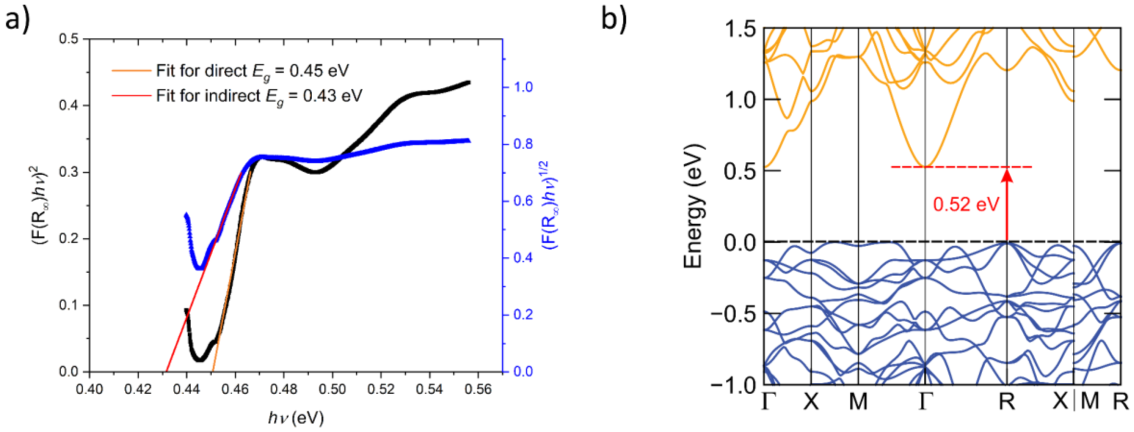

Figure 2.11: (a) The Tauc plots of a diffuse reflectance spectrum of the $BaGe_8As_{14}$ compound for direct and indirect band gap transitions. (b) The PBE band structure of the $BaGe_8As_{14}$ compound indicating an indirect band gap.

DFT band structure calculations reveal the indirect band gaps of 0.36 eV, 0.52 eV, and 0.88 eV (Figure 2.11b) using PBEsol,[74] PBE,[45] and SCAN[75] functionals, respectively. We did not expect an accurately calculated band gap because we cannot treat the disorder and thus have used an ordered structure in the $P\bar{4}3m$ space group. However, calculations indicate that the measured optical gap of 0.43 eV was that of the indirect band gap. The density of states plot (DOS, Figure A.16, appendix) shows the significant contributions of Ge and As states below the Fermi level, while Ba states are in the conduction band.The Bader analysis yields the charge-neutral formula as $Ba^{1.47+}(Ge^{0.38+})_6(Ge^{0.13+})_2(As^{0.05-})_2(As^{0.26-})_6(As^{0.39-})_6$. The Ba position has a high charge while the charges of the polyanionic network are significantly smaller than the formal oxidation states in $Ba^{+2}(Ge^{+4})_6(Ge^{+2})_2(As^{0})_2(As^{-2})_6(As^{-3})_6$. This indicates a strong covalent character of the Ge/As network.

The Rietveld refinements of X-ray powder diffraction data (Figure 2.12) support the single-crystal structure (Table A.25, appendix). The sample consists of 96 wt% $BaGe_8As_{14}$ with 3 % $GeAs_2$ and 1 % Ge impurity phases. High temperature powder X-ray diffraction patterns (Figure A.18, appendix) reveal that the $BaGe_8As_{14}$ compound is stable up to 873 K.

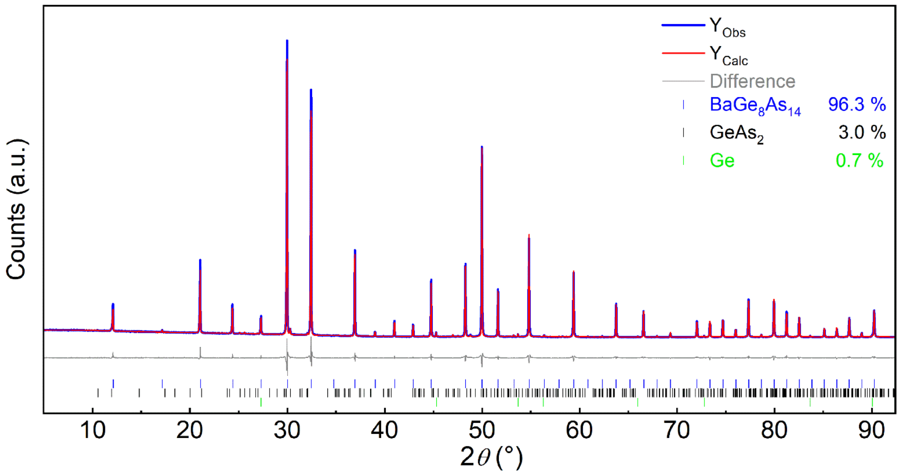

Figure 2.12: The powder X-ray diffraction pattern and Rietveld refinement of the $BaGe_8As_{14}$ compound with the minor impurities of $GeAs_2$ and Ge.

EDX measurements confirm the composition of the $BaGe_8As_{14}$ compound within 5 %, which is the typical error of the method: Ba 4.4(3) at% [4.3], Ge 33.0(7) at% [34.8], and As 62.6(8) at% [60.9]. The values given in square brackets were calculated from the formula.

Conclusion

$BaGe_8As_{14}$, to the best of our knowledge, is the first Ge/As-based sodalite-type compound. Barium atoms are too small to fit into the large sodalite framework, and are therefore disordered around the center. A $Ge_{0.5}As_{0.5}$-mixed site introduces additional disorder; such structural disorders act as phonon scattering centers, which typically reduce the thermal conductivity κ. However, the $BaGe_8As_{14}$ compound is a relatively good electronic conductor, with low resistivity ($\rho_{300\,K}$ = 2.2×10^{-2} Ω cm). Both properties together are promising prerequisites for a thermoelectric material, where the product $\rho \cdot \kappa$ needs to be small for high efficiency, while being difficult to optimize.

Experimental

Synthesis. $BaGe_8As_{14}$ was synthesized via high temperature solid-state reactions. Stochiometric mixtures of Ba (99.99 % Sigma Aldrich), Ge (99.999 %, Sigma Aldrich) and As (99.99999+ %, Alfa Aesar) were filled in a corundum crucible (l = 40 mm, $Ø_o$ = 10 mm, $Ø_i$ = 6 mm) and sealed in silica ampoules (l = 60 mm, $Ø_o$ = 14 mm, $Ø_i$ = 11 mm) under an atmosphere of purified argon. To obtain suitable single crystals, the mixture was heated to 1123 K with a rate of 25 Kh^{-1}, kept at this temperature for 20 h and cooled to 673 K with a rate of 10 Kh^{-1} after which the furnace was switched off. For the synthesis of phase pure samples the mixture was heated to 873 K for 60 h with heating and cooling rates of 25 Kh^{-1}. After that the samples were thoroughly ground, pressed into pellets and treated with the same temperature program. This procedure was repeated twice.

The reactions yielded either silver shards or black powder respectively. The compound is stable in air and water.

Single Crystal X-ray Diffraction. A suitable single crystal was isolated in paraffin oil and inserted and sealed into a glass capillary (Hilgenberg GmbH) of 0.2 mm in diameter. Single crystal data at room temperature was collected with a Bruker D8 Quest diffractometer (Mo Kα, Photon-II detector). Low temperature single crystal data was collected between 293 and 105 K with a Bruker D8 Venture (Mo Kα, Photon-II detector) equipped with a Kryoflex II cooling unit. Integration and absorption correction were performed with APEX3 and SADABS.[27, 28] The space group was determined with XPREP based on systematically absent reflections.[29] The phase problem was solved with Superflip and the model was refined with the SHELXL package.[30, 31]

The deposition numbers 2015241 (293 K), 2017129 (218 K), 2017128 (189 K), 2017127 (143 K) and 2017126 (103 K) contain the crystallographic data for this paper. These data are provided free of charge by the joint Cambridge Crystallographic Data Centre and Fachinformationszentrum Karlsruhe Access Structures service www.ccdc.cam.ac.uk/structures.

Powder X-ray Diffraction. A powdered sample was filled and sealed in a glass capillary (Hilgenberg GmbH) of 0.2 mm in diameter. The X-ray powder pattern was obtained with a Stoe Stadi-P diffractometer (Cu Kα1, Ge(111)-monochromator, Mythen 1k detector). The Topas software package[32] was used for data analysis and Rietveld refinement of the model obtained from single crystal data.

High Temperature Powder X-ray Diffraction. A powdered sample was filled and sealed with grease in a silica capillary (Hilgenberg GmbH) of 0.4 mm in diameter. Data were collected between 298 and 1273 K with a Stoe Stadi P diffractometer (Mo Kα1, Ge(111)-monochromator, IP-PSD detector) equipped with a graphite furnace. The data was analyzed with WinXPOW.[37]

EDX Measurements. A Carl Zeiss EVO-MA 10 with SE and BSE detectors controlled by the SmartSEM[38] software was used for scanning electron microscopy. EDX measurements were performed with the attached Bruker Nano EDX detector (X-Flash detector 410-M). Data evaluation was performed with the QUANTAX 200 software.[39] Signals from the aluminum sample holder and adhesive carbon tabs were disregarded.

UV-Vis-NIR Measurements. A diffuse reflectance spectrum of a powdered sample was measured with a VARIAN Cary 500 UV-Vis-NIR spectrophotometer equipped with a DRA-CA-5500 integrating sphere between 400 and 2000 nm. To account for the black color of $BaGe_8As_{14}$, the sample was mixed with $BaSO_4$. To determine optical bandgaps the data was converted based on the Kubelka-Munk theory.[40]

Resistivity and Hall Effect Measurements. A Sample was pressed into a pellet and sintered at 853 K for 60 h with heating and cooling rates of 50 Kh^{-1} in a corundum crucible sealed in a silica ampule under an atmosphere of purified argon. Resistivity and Hall Effect measurements were performed with a Quantum Design Inc. PPMS (physical property measurement system) equipped with a resistivity option. The pellet was contacted with four point Van der Pauw press contact by Wimbush. Data were collected with the MultiVu software between 150 and 300 K with field strengths of ±50 kOe.[41]

TEM and STEM investigations. $BaGe_8As_{14}$ was ground in an agate mortar, suspended in pure ethanol and drop-cast on a TEM Grid with holey carbon film (Plano GmbH, Germany). The grid was mounted on a double-tilt holder and transferred into a Cs DCOR probe-corrected Titan Themis 300 (FEI, USA) TEM equipped with X-FEG, post-column filter (Enfinium ER-799), US1000XP/FT camera system (Gatan, Germany) and a windowless, 4-quadrant Super-X EDX detector. TEM images were recorded using a 4k × 4k FEI Ceta CMOS camera. The microscope was operated at 300 kV accelerating voltage for SAED and STEM-HAADF (convergence angle of 16.6 mrad, 50 µm aperture, detector inner half angle 33 mrad for 245 mm camera length). For evaluation of the TEM data, the following software was used: Digital Micrograph (Fourier filtering of STEM images), ProcessDiffraction7 (geometric calculations for SAED), JEMS (SAED simulations).[76-78]

DFT Calculations. We performed first principle electronic structure calculations with the Vienna Ab initio Simulation Package (VASP),[42, 43] based on density functional theory (DFT) and plane wave basis sets. Projector-augmented waves (PAW)[44] were applied and contributions of correlation and exchange were treated in the generalized-gradient approximation (GGA) using PBE,[45] PBEsol,[74] or SCAN[75] functionals. The Brillouin-zone was sampled with a 10×10×10 k-mesh. The structure parameters have been optimized until the energy changes are below 10^{-8} eV and forces between atoms below 10^{-3} eV/Å. To extract charges from the electron density we used the Bader analysis[48] implemented by Henkelman *et al.*[49] Mixed and fractional occupancies cannot be treated with VASP. Therefore, we reduced the symmetry of the structure to the subgroup $P\bar{4}3m$ (No. 215), which allows ordering of the mixed Ge/As site (8*c* to 2×4*e*). The split Ba position was idealized as fully occupied position (2*a*). The results of the structure relaxations are shown in Table A.24 and Figure A.17. The DOS and band structure were plotted using the sumo tools.[79]

2.3 High thermoelectric properties in the sodalite compounds $BaGe_8As_{14}$ and AGe_7As_{15} (A = Rb, Cs)

Valentin Weippert, Kristian Witthaut, Monika Pointner, Lucien Eisenburger and Dirk Johrendt

submitted

Abstract

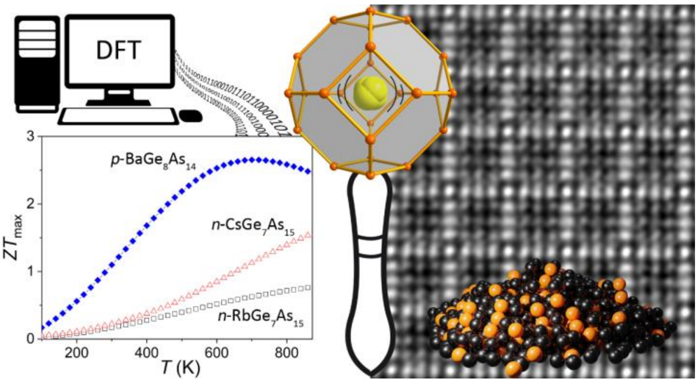

$RbGe_7As_{15}$ and $CsGe_7As_{15}$ have been synthesized and their structures determined by single-crystal X-ray diffraction and STEM-HAADF/EDX. They crystallize with a cubic sodalite-type structure in the space group $I\bar{4}3m$ isotypic to $BaGe_8As_{14}$. Rubidium and caesium are highly coordinated by 16 arsenic or germanium atoms and perfectly fit into the sodalite-cage due to their bigger ionic radii compared to barium, which is displaced from the center. The compounds are narrow-band p-type semiconductors with electrical conductivities of $1.2\text{-}3 \cdot 10^4$ S/m at 300 K and carrier densities of $1\text{-}2 \cdot 10^{20}$ cm^{-1}. First principles DFT calculations give clear evidence of ultralow lattice thermal conductivity around 0.5 Wm^{-1}K^{-1} in $BaGe_8As_{14}$ due to the position disorder of the barium atoms and the anharmonicity of its thermal movement. Frozen phonon calculations indicate that rattling probably decreases the lattice thermal conductivity of $BaGe_8As_{14}$ even further. These effects are chemically switched off in $RbGa_7As_{15}$ with a parabolic potential and no signs of rattling, leading to a four times higher lattice thermal conductivity. The calculated transport properties agree with the measured data, and their combination predicts a thermoelectric efficiency ZT up to 2.7 for $BaGe_8As_{14}$, reaching the value of current record materials.

Introduction

Thermoelectric materials directly convert thermal energy into electricity and enable the harnessing of heat from any source including otherwise unused waste heat. Compact thermoelectric devices rank among the smartest ways of energy-conversion thanks to neither moving parts nor any emissions.[80, 81] The key to cost-effective applications is a high conversion efficiency of thermoelectric materials, defined as $ZT = \sigma S^2 T/(\kappa_{\mathrm{el}}+\kappa_{\mathrm{L}})$. A good performance requires a high electrical conductivity σ, a large Seebeck coefficient S and low thermal conductivity $\kappa = \kappa_{\mathrm{el}}+\kappa_{\mathrm{L}}$. Since the electrical conductivity σ inevitably enforces a high electronic thermal conductivity κ_{el}, a lot of effort is put into minimizing the charge carrier-independent lattice thermal conductivity κ_{L}. Lowering κ_{L} is possible by nano-structuring techniques,[82, 83] introducing disorder through heteroatoms, point defects[84] or grain-boundary engineering.[85] Another approach are compounds with intrinsically low κ_{L}. Prerequisites found so far are complex structures like Ag_9TlTe_5,[86] or the valence precise Zintl phase $Yb_{14}MnSb_{11}$[5, 87] as well as the "phonon glass-electron crystal" (PGEC) concept by combining glass-like low thermal conductivity and good electrical conductivity.[88] This situation is favored by high crystal symmetry, heavy elements with small electronegativity difference and narrow band gaps.[89] Framework structures have further advantages enabling the incorporation of loosely bonded atoms in cage-like structures. This has been realized in skutterudite- and clathrate-type compounds where so-called "rattling" atoms act as phonon scattering centers.[67-70, 90-92] Possible new candidates fulfilling this concept may be found amongst the large family of zeolite-like structures.[51-53, 55, 56, 93-95] Their underlying sodalite framework itself offers a unique playground. It consists of a *bcc* arrangement of β-cages built up from *vierer*- and *sechser*-rings ($4^6 6^8$) with guest atom sites in the *sechser*-rings and the cage centers. Apart from very few exceptions,[62-66] the majority of the sodalite materials are oxides and electrical insulators.[96] However, related cage compounds with networks made of heavier main group elements offer beneficial conditions for thermoelectric materials. Following this idea, we recently reported on the synthesis and crystal structure of the sodalite compound $BaGe_8As_{14}$ and its possible thermoelectric properties.[97] Indeed, it exhibits all of the aforementioned conditions favoring a low lattice thermal conductivity κ_{L}.

The β-cages in $BaGe_8As_{14}$ are apparently too large for the barium atoms, which are displaced from the center in a disordered manner. A therefore presumably low lattice thermal conductivity together with a good electrical conductivity and favorable charge carrier density are good prerequisites for thermoelectric properties. To chemically control the disorder in the β-cage, we replaced barium in $BaGe_8As_{14}$ by larger rubidium or caesium atoms. Here we report on the crystal structures of the isotypic compounds $RbGe_7As_{15}$ and $CsGe_7As_{15}$. We demonstrate that the disorder in the cage is absent in these compounds, and from first principle DFT calculations[98] we predict ultralow thermal conductivity only in $BaGe_8As_{14}$ due to static disorder combined with anharmonic effects, which are both switched off in $RbGe_7As_{15}$ and $CsGe_7As_{15}$. The calculated thermoelectric efficiency for $BaGe_8As_{14}$ of ZT = 2.7 is at the level of today's record materials.

Results and Discussion

Crystal Structure. The crystal structures of the isotypic compounds $RbGe_7As_{15}$ and $CsGe_7As_{15}$ were determined from X-ray single crystal data using charge flipping to solve the phase problem followed by refinement in the space group $I\bar{4}3m$ (no. 217). Table 2.6 shows the main results. Detailed crystallographic data including atomic positions, anisotropic displacement parameters and selected interatomic distances are given in Tables A.26-A.31, low temperature data in Tables A.32-49 (see appendix).

Table 2.6: Single crystal diffraction data of $RbGe_7As_{15}$ and $CsGe_7As_{15}$.

formula	$RbGe_7As_{15}$	$CsGe_7As_{15}$
space group	$I\bar{4}3m$ (no. 217)	
a / Å	10.3642(2)	10.38170(10)
V_{cell} / Å^3	1113.29(6)	1118.94(3)
Z	2	
$\rho_{X\text{-ray}}$ / g cm^{-3}	5.123	5.238
R_σ / R_{int}	0.0104 / 0.0467	0.0074 / 0.0385
R_1 ($F^2 > 2\sigma(F^2)$) / all	0.0128 / 0.0134	0.0069 / 0.0078
wR_2 ($F^2 > 2\sigma(F^2)$) / all	0.0284 / 0.0285	0.0144 / 0.0147
GooF	1.269	1.221
$\Delta\rho_{max/min}$ / eÅ^{-3}	+0.643 / -0.800	+0.411 / -0.286

The new compounds crystallize with a sodalite-type structure isotypic to $BaGe_8As_{14}$.[97] A Ge_{24} β-cage (Figure 2.13a), is the core structure of the polyanionic network of vertex sharing $GeAs_4$ tetrahedra (Figure 2.13b). This network can be described as over-collapsed with large tilt angles of $\varphi \approx 54$ ° and little change upon cooling (Figure A.19, appendix). A comparative explanation of different degrees of network expansions is shown in Figure A.20 (see appendix). The rubidium or caesium cations at the centers of the β-cage (Figure 2.13a).

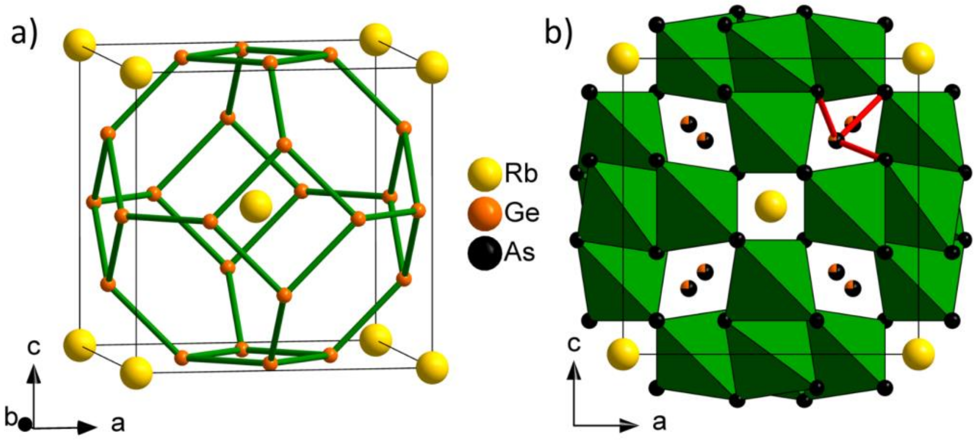

Figure 2.13: (a) Ge_{24} β-cage of $RbGe_7As_{15}$ and (b) vertex sharing tetrahedra network with a statistically occupied $(Ge_{0.25}As_{0.75})As_3$ trigonal pyramid (red).

To check for disorder as known from BaGe$_8$As$_{14}$, we measured the crystal structures of RbGe$_7$As$_{15}$ and CsGe$_7$As$_{15}$ at low temperatures. Figure 2.14 shows the thermal displacement parameters versus temperature of the new compounds and those of BaGe$_8$As$_{14}$ for comparison. The latter exhibits a static disorder by displacing the barium atoms off the high symmetry ($\bar{4}3m$) site at the cage centers. This is evident from a non-zero extrapolation of the thermal displacement parameter U_{eq} to about 0.89 at $T = 0$.[97] The effect is absent in RbGe$_7$As$_{15}$ and CsGe$_7$As$_{15}$, where the U_{eq} extrapolate to 0.01 and 0.005, respectively (Figure 2.14). Thus the rubidium and caesium atoms remain at the cage centers due to their bigger ionic radii compared with (Ba^{2+}: 1.35 Å, Rb^{1+}: 1.52 Å, Cs^{1+}: 1.67 Å).[25] This leads to highly coordinated Rb/Cs atoms surrounded by 16 As/Ge atoms at almost identical distances which vary by 1% only. Thus, the heavy alkaline atoms perfectly fit into the sodalite cage.

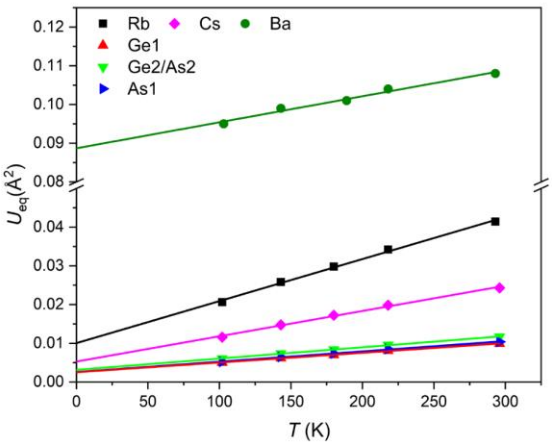

Figure 2.14: U_{eq} of RbGe$_7$As$_{15}$, CsGe$_7$As$_{15}$ and BaGe$_8$As$_{14}$[97] with regression lines indicating static disorder in BaGe$_8$As$_{14}$.

In contrast, the distances to the 16 As/Ge around the off-center barium atoms in BaGe$_8$As$_{14}$ vary by 12% because the Ba^{+2} ions are too small to fill the cage. The Ge$_{0.5}$As$_{0.5}$ mixed site in BaGe$_8$As$_{14}$ generates (Ge$_{0.5}$As$_{0.5}$)As$_3$ trigonal pyramids.[97] The lower charge of Rb$^+$ and Cs$^+$ changes this site to Ge$_{0.25}$As$_{0.75}$ in order to achieve the charge neutral formula A^+(Ge^{+4})$_6$Ge^{+2}(As^0)$_3$(As^{-2})$_6$(As^{-3})$_6$ (A = Rb, Cs). The resulting (Ge$_{0.25}$As$_{0.75}$)As$_3$ trigonal pyramids are shown in Figure 2.13a. EDX measurements (Table 2.7) confirm the compositions RbGe$_7$As$_{15}$ and CsGe$_7$As$_{15}$.

Table 2.7: EDX results of RbGe$_7$As$_{15}$ and CsGe$_7$As$_{15}$.

formula	A	Ge	As
AGe$_7$As$_{15}$ (calc.)	4.4	30.4	65.2
RbGe$_7$As$_{15}$	4.8(4)	28(1)	66(1)
CsGe$_7$As$_{15}$	4.8(3)	28.6(7)	66.6(8)

Structure models for $RbGe_7As_{15}$ and $CsGe_7As_{15}$ with Ge/As ordering arise from symmetry reduction from the space group $I\bar{4}3m$ to the *translationsgleiche* subgroup $R3m$ (no. 160). Refinements of high- resolution single crystal data ($d > 0.58$ Å) yielded lower R-values for the disordered ($I\bar{4}3m$) than for the ordered structure ($R3m$) as shown in Table 2.8. Considering the Ge/As disorder in $BaGe_8As_{14}$ confirmed by SAED,[97] we assume likewise Ge/As disorder at the 8*c* sites in $RbGe_7As_{15}$ and $CsGe_7As_{15}$.

Table 2.8: R-values for the disordered ($I\bar{4}3m$) and ordered structures ($R3m$) of $RbGe_7As_{15}$ and $CsGe_7As_{15}$.

compound	R_1 ($I\bar{4}3m$)	R_1 ($R3m$)	wR_2 ($I\bar{4}3m$)	wR_2 ($R3m$)
$RbGe_7As_{15}$	0.0134	0.0189	0.0285	0.0336
$CsGe_7As_{15}$	0.0078	0.0116	0.0147	0.0209

STEM-HAADF images of $RbGe_7As_{15}$ perfectly agree with the structure overlays (Figure 2.15 and A.21). Atomic positions are verified with STEM-EDX mapping as shown in Figure 2.15 and Figures A.22-A.23 (see appendix). Regions rich of respective element are clearly separable.

Rietveld refinements (Figures A.40-A.41 and Table A.55 in the appendix) revealed a minor (3 wt-%) germanium impurity in $CsGe_7As_{15}$ while the $RbGe_7As_{15}$ sample was single phase.

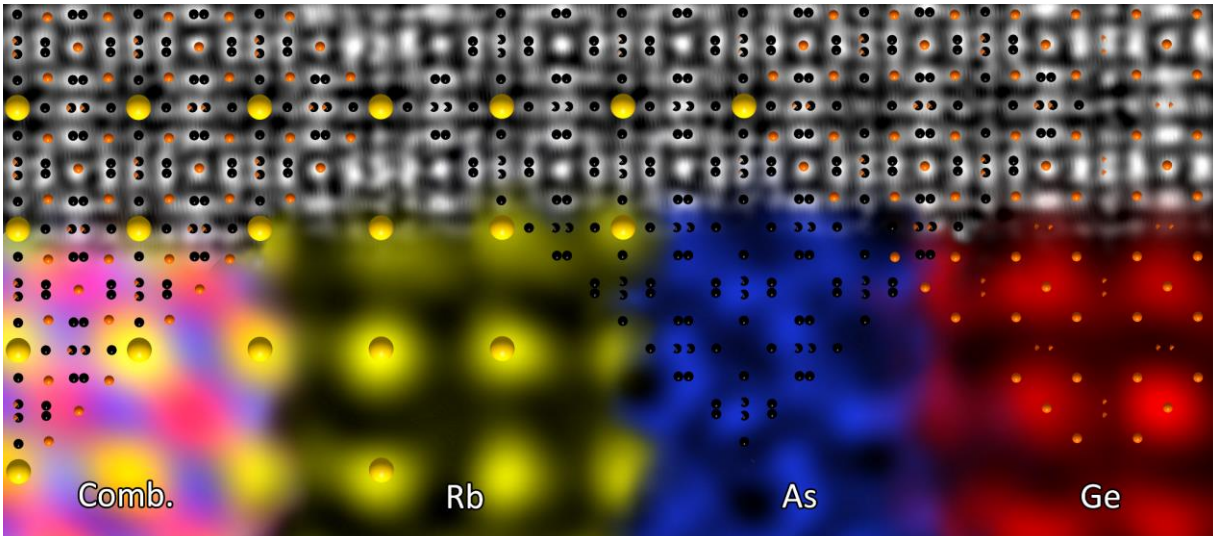

Figure 2.15: STEM-HAADF image and high resolution STEM-EDX maps of $RbGe_7As_{15}$ along [100] with structural overlays.

Optical Properties. The Tauc plots of Kubelka Munk converted diffuse reflectance spectra of $RbGe_7As_{15}$ (Figure 2.16a) and $CsGe_7As_{15}$ (Figure A.24, appendix) both indicate indirect band gaps with 0.44 and 0.43 eV, respectively, and direct transitions at 0.46 eV. These results are almost identical to the values we found for $BaGe_8As_{14}$ with 0.43 and 0.45 eV for indirect and direct band gaps.[97]

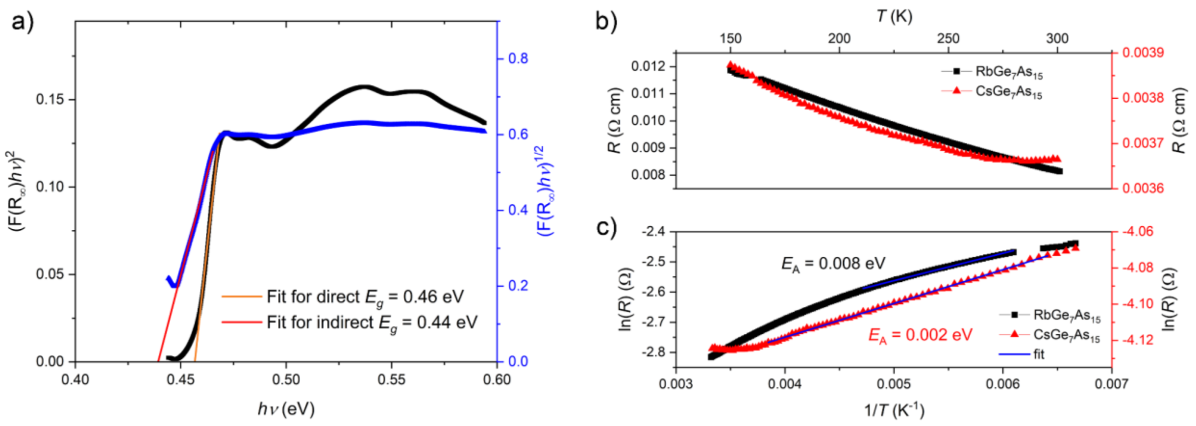

Figure 2.16: (a) Tauc plots of a Kubelka Munk converted diffuse reflectance spectra of $RbGe_7As_{15}$ exhibiting an indirect band gap of 0.44 eV and a direct band gap of 0.46 eV. Resistivity of $RbGe_7As_{15}$ and $CsGe_7As_{15}$ (b) and their respective Arrhenius plots (c).

Electronic Properties. $RbGe_7As_{15}$ and $CsGe_7As_{15}$ are semiconductors. Figure 2.16b shows increasing resistivities at lower temperatures. The electronic bandgaps extracted from Arrhenius plots give very small activation energies of 0.008 and 0.002 eV for $RbGe_7As_{15}$ and $CsGe_7As_{15}$, respectively (Figure 2.16c). This indicates extrinsic behavior through dopant (impurity) levels close to the valence band, similar to $BaGe_8As_{14}$ and other related compounds.[72, 97] Hall effect data at 300 K (Figure A.25, appendix) reveal a *p*-type nature of $RbGe_7As_{15}$ and $CsGe_7As_{15}$ with carrier concentrations of $1.3\cdot10^{20}$ cm^{-3} and $8.2\cdot10^{19}$ cm^{-3} and mobilities μ of 5.8 $cm^2V^{-1}s^{-1}$ and 21 $cm^2V^{-1}s^{-1}$, respectively, similar to $BaGe_8As_{14}$ with $p = 2.3\cdot10^{20}$ cm^{-3} and $\mu = 2$ $cm^2V^{-1}s^{-1}$.[97]

Electronic Structure. DFT is not able to handle the Ge/As- mixed atom sites. We have used an ordered structure model of $RbGe_7As_{15}$ and $CsGe_7As_{15}$ in the space group $R3m$. The $Ge_{0.5}As_{0.5}$ site in $BaGe_8As_{14}$ allows two ordered variants in the space group $R3m$, and one each in the space groups $P\bar{4}2_1m$ and $Fmm2$. We denote these ordered structure models as *hR*-1-, *hR*-2-, *tP*- and *oF*-$BaGe_8As_{14}$. The results of the ionic relaxations are shown in Figures A.26-A.27 and Tables A.50-A.52 in the appendix. While the alkaline metals in $RbGe_7As_{15}$ and $CsGe_7As_{15}$ retains its position at the center of the sodalite cage, barium is shifted off this position in *oF*- and *tP*-$BaGe_8As_{14}$ in perfect agreement with the crystal structure data.[97] However, relaxations of *hR*-1- and *hR*-2-$BaGe_8As_{14}$ did not fully converge. The electronic band structures shown in Figure 2.17 reveal indirect band gaps of 0.42, 0.58, and 0.48 eV for $RbGe_7As_{15}$, $CeGe_7As_{15}$, and *tP*-$BaGe_8As_{14}$, respectively. *oF*-$BaGe_8As_{14}$ has a smaller direct gap of 0.28 eV. Values with other GGA potentials are given in Table A.53 (appendix). The density of states (DOS) shows only small contributions of Rb, Cs or Ba in the conduction bands. Thus, the band gaps are in the 4*p*-bands of the GeAs-frameworks as in binary semiconductors like GaAs. Bader charge analysis indicate a ionic character with $Rb^{0.82+}$ and $Cs^{0.77+}$ ions, and a covalently bonded polyanionic network $Ge^{0.23+}(Ge^{0.37+})_6(As^{0.04-})_3(As^{0.22-})_8(As^{0.37-})_4$. This covalence is visualized by the electron location function (ELF) in Figure A.28 (see appendix).

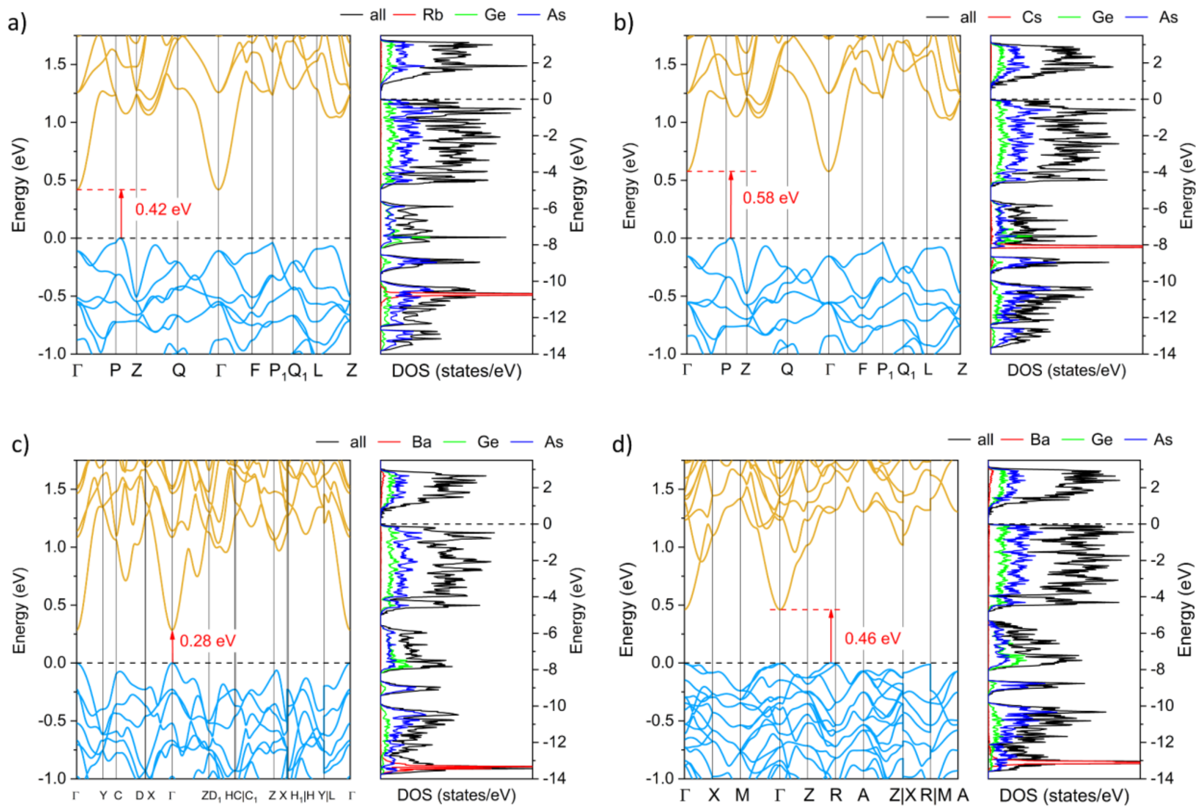

Figure 2.17: Band structures of (a) $RbGe_7As_{15}$ (PBE) (b) $CsGe_7As_{15}$ (PBEsol) (c) *oF*-$BaGe_8As_{14}$ (PBEsol) and (d) *tP*-$BaGe_8As_{14}$ (PBEsol) with indirect and direct band gaps indicated by red arrows and respective total and atom projected density of states (DOS) calculated with PBE. The energy zeros are taken at the Fermi level E_F (dashed line).

Electronic transport. To calculate the Seebeck coefficient S, the electrical conductivity σ and the electronic thermal conductivity κ_{el} it is necessary to determine the relaxation times τ for both holes and electrons., which is based on the deformation potential constant V_{DP}, the effective masses of holes and electrons m^* and elastic constants c_{11} (Table 2.9). Figures A.29-A.30 show the band edge energy E_{edge} of the VBM and CBM as a function of the relative shift in lattice parameters. The resulting V_{DP} values are linear with slightly lower values for holes than for electrons for *oF*-/*tP*-$BaGe_8As_{14}$. The effective masses of the holes (0.51-0.81 m_e) are roughly 2 to 3 times larger than the effective masses of the electrons (0.19-0.24 m_e, Table 4), which is due to different band dispersions. This results in 9 to 22 times higher mobility values and 3 to 6 times longer lifetimes for electrons compared to holes (Table 2.9).

A summary of the calculated thermoelectric properties at 300 K is given in Figure 2.18. Detailed temperature and dopant dependent data are in Figures A.31-38 (appendix). The Seebeck coefficient is rather low with ~90 and ~-50 μVK^{-1} for low *p*- and *n*-doping levels, respectively. The higher values for *p*-doping can be explained with the proportional relation of the Seebeck coefficient and the effective mass.[99] The values for σ and κ_{el} follow the typical counteracting relationship to S. The calculated values for σ are in good agreement with the experimental ones at similar carrier concentration (Table A.54, appendix), thus supporting the validity of our calculations. Since *PF* is defined as $S^2\sigma$ it reaches its maximum at doping concentrations between $1\cdot10^{20}$ and $4\cdot10^{20}$ cm^{-3}, which is in the range of doping levels we measured for our samples ($8.2\cdot10^{19}$ – $2.3\cdot10^{20}$ cm^{-3}).[97]

Table 2.9: Deformation potential constant V_{DP} effective mass m^* (m_e is the free electron mass) and exemplary values for mobility μ and relaxation time τ at 300 K of electrons and holes of AGe$_7$As$_{15}$ and BaGe$_8$As$_{14}$ as well as elastic moduli c_{11}.

compound	carrier	V_{DP} (eV)	m^* (m_e)	μ_{300K} (cm^{2}V^{-1}s^{-1})	τ_{300K} (fs)	c_{11} (GPa)
RbGe$_7$As$_{15}$	*n*	-27.05	0.23	494	64	148
	p	-27.70	0.78	22	10	
CsGe$_7$As$_{15}$	*n*	-26.43	0.24	457	63	150
	p	-26.95	0.81	21	10	
oF-BaGe$_8$As$_{14}$	*n*	-28.58	0.19	666	73	143
	p	-25.84	0.51	71.7	21	
tP-BaGe$_8$As$_{14}$	*n*	-28.28	0.20	648	72	144
	p	-25.31	0.56	58.4	19	

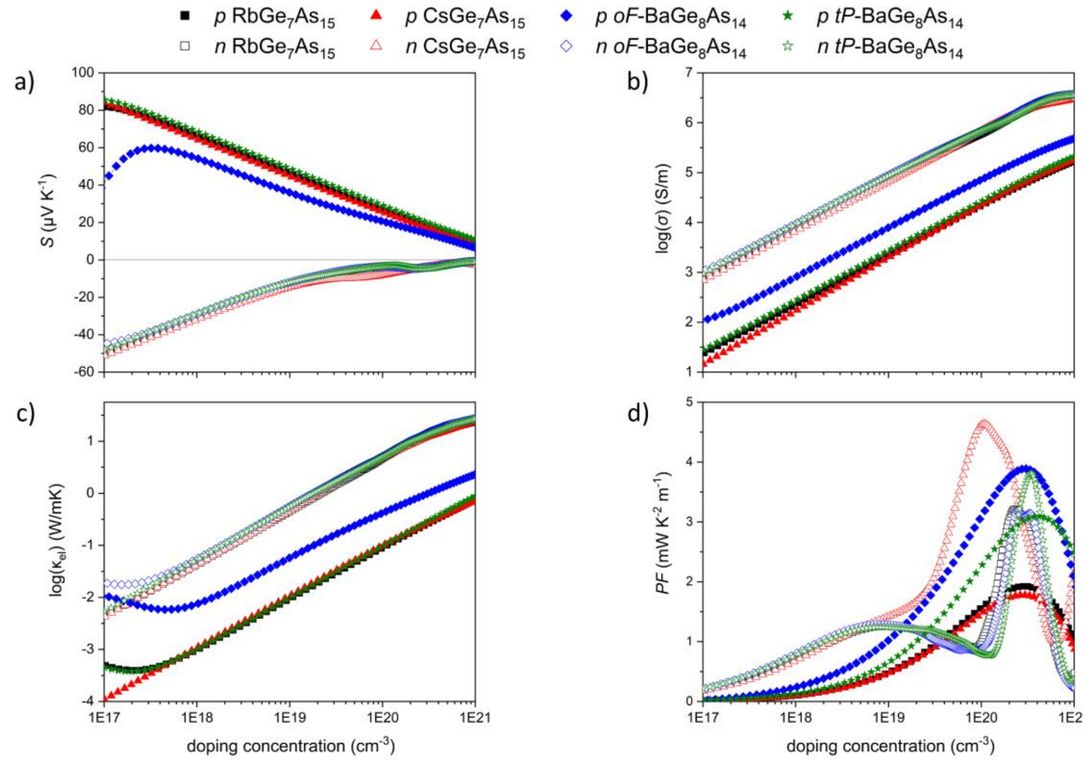

Figure 2.18: (a) Seebeck coefficient *S*, (b) electrical conductivity log(σ), (c) electronic thermal conductivity log(κ_{el}) and (d) Power Factor *PF* of all compounds with *p*-type and *n*-type doping at 300 K and increasing dopant concentration.

Lattice thermal transport. Figure 2.19 shows the calculated phonon spectra and their respective pDOS. There are no imaginary frequencies present, indicating mechanical stability of the ordered variants. All of them exhibit acoustic bands at frequencies $\omega < \sim1.2$ THz with a threefold degeneracy at the Γ-point. The optical bands show very little dispersion for AGe$_7$As$_{15}$ (Figure 2.19a,b) and slightly more for both ordered variants of BaGe$_8$As$_{14}$ (Figure 2.19c,d). The pDOS can be divided into four sections. For states at $\omega > 7$ THz and 2 THz - 4 THz both Ge and As are present, whereas for 5 - 7 THz the states are dominated by As and for $\omega < 2$ THz by Rb, Cs or Ba. The distribution of Rb and Cs states is very narrow but less so for Ba, which is most likely due to its shifted position mentioned earlier.

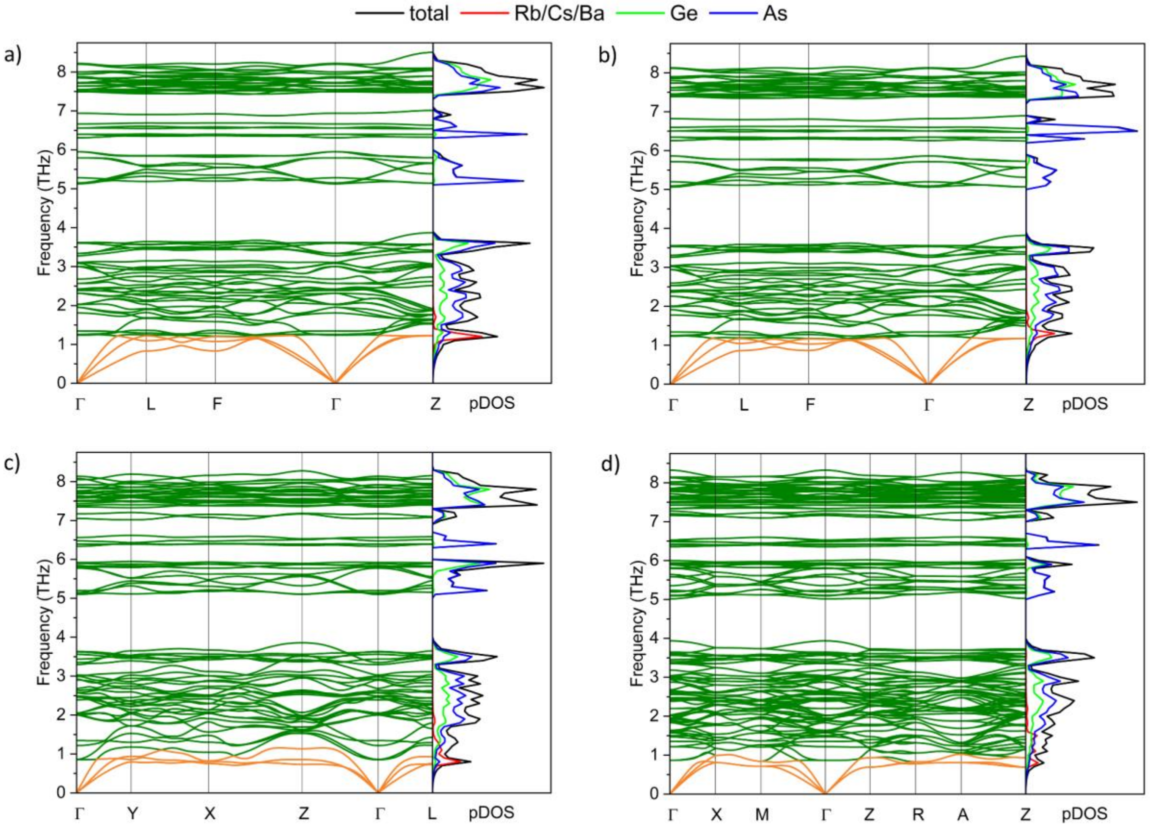

Figure 2.19: Calculated phonon spectra with optical (green) and acoustic (orange) bands of (a) RbGe$_7$As$_{15}$ (b) CsGe$_7$As$_{15}$ (c) *oF*-BaGe$_8$As$_{14}$ and (d) *tP*-BaGe$_8$As$_{14}$ and their projected phonon DOS.

The calculated values for the lattice thermal conductivity κ_L are shown in Figure 2.20. RbGe$_7$As$_{15}$ and CsGe$_7$As$_{15}$ exhibit nearly identical values with ~1.9 Wm^{-1}K^{-1} at 300 K, which is slightly higher than other cage compounds like A_8Al$_8$Si$_{128}$ (A = Rb, Cs; ~1 Wm^{-1}K^{-1}),[100] AE_8Ga$_{16}$Ge$_{30}$ (AE = Sr, Ba; 0.9-1.1 Wm^{-1}K^{-1})[101, 102] or Cs$_8$Zn$_4$Sn$_{42}$ (1.1 Wm^{-1}K^{-1}).[103] BaGe$_8$As$_{14}$ on the other hand shows ultralow values ranging from 0.43 to 0.53 Wm^{-1}K^{-1} for the orthorhombic and tetragonal variant respectively. This almost rivals some of the lowest values reported so far like Gd$_{117}$Co$_{56}$Sn$_{112}$ (0.28 Wm^{-1}K^{-1}),[88] Ag$_9$TlTe$_5$ (0.22 Wm^{-1}K^{-1})[86] and Ba$_8$Au$_{16}$P$_{30}$ (0.18 Wm^{-1}K^{-1}).[104]

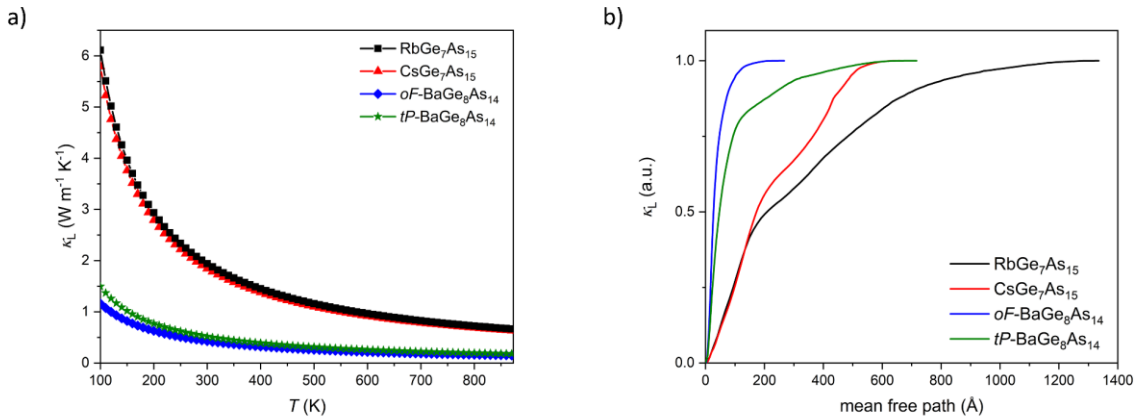

Figure 2.20: (a) Lattice thermal conductivity κ_L as a function of the temperature and (b) relative cumulative lattice thermal conductivity κ_L at 300 K as a function of the mean free path of $RbGe_7As_{15}$ (black) $CsGe_7As_{15}$ (red) *oF*-$BaGe_8As_{14}$ (blue) and *tP*-$BaGe_8As_{14}$ (green).

As mentioned above, lattice thermal conduction can be reduced by disorder and/or rattling. The latter is a dynamic effect that requires a flat energy curve as a function of the atomic position. Since the Ge/As disorder is present in all compounds, the large difference in lattice thermal conductivity between Rb/$CsGe_7As_{15}$ and $BaGe_8As_{14}$ is probably due to the misorientation of the barium atoms in the cage. To investigate this, we have performed frozen-phonon calculations. The structures were first relaxed with rubidium or barium atoms fixed at the cage centres. These atoms were then displaced from their positions and the respective energies were calculated. The results are shown in Figure 2.21a.

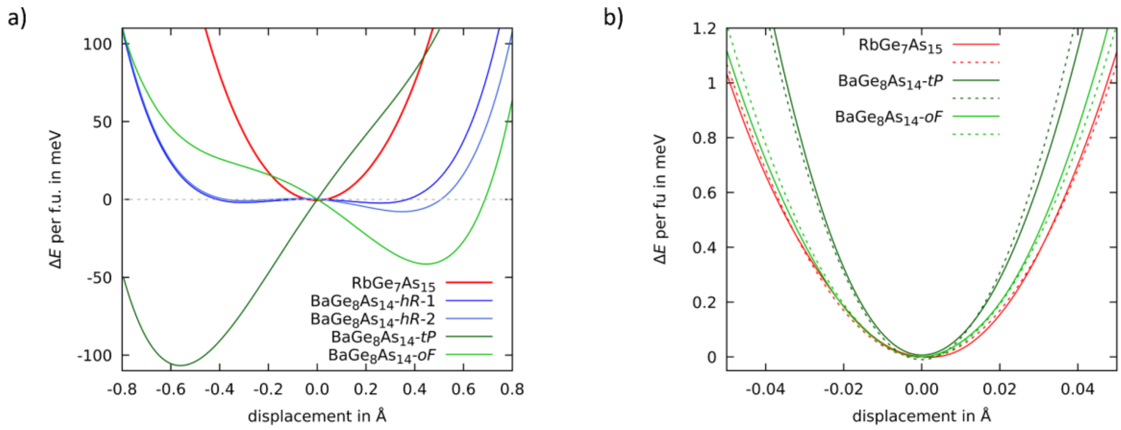

Figure 2.21: (a) Energy changes versus the displacement of the rubidium or barium atoms from the cage center for different ordered structure variants. (b) Energy changes at small displacements from the minima in (a) and in the range of typical thermal movement. Dashed lines are parabolic fits to the data.

The rubidium atoms perfectly fill the cages, consequently we find a symmetric parabolic potential. The energy minima of *tP*- and *oF*-$BaGe_8As_{14}$ are significantly shifted away from the cage centers in agreement with the crystallographic data and the full relaxation of the structures. This full relaxation failed for the rhombohedral variants of $BaGe_8As_{14}$, and the reason becomes clear from the blue curves in Figure 2.21a. We find a very flat double-well potential with a tiny energy barrier of only 5 meV between the two minima. Thus, the barium atoms in the *hR*-1 and *hR*-2 structures can move in the cage without significant energy change, tantamount to the rattling effect. Unfortunately, we were unable to calculate the thermoelectric parameters of these variants due to the poor convergence of the structural relaxations, which is clearly a consequence of this flat potential. However, phonon dispersions of the *hR*-1 structure show imaginary modes originating from the barium atoms, as expected (Figure A.39 in the appendix).

Figure 2.21b shows the energy changes at small displacements from the minima in Figure 2.21a, respectively, in the range of realistic thermal movement. Deviations from the parabolic fits (dashed lines) indicate anharmonic contributions in *tP*- and *oF*-$BaGe_8As_{14}$, while the fit is much better for $RbGe_7As_{15}$. From this we conclude that the ultralow lattice thermal conductivity of $BaGe_8As_{14}$ comes from the static off-center disorder of the barium atoms and from anharmonic contributions in its thermal motion. Our calculations give clear evidence for a rattling effect, which we could not consider in the calculations of the thermoelectric properties. However, it cannot be ruled out that the actual lattice thermal conductivity will be reduced even further by the rattling effect.

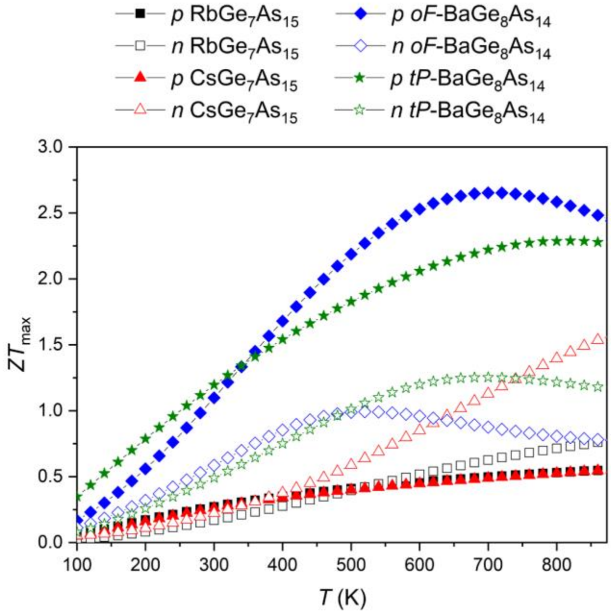

Figure 2.22: Maximum figure of merit ZT_{max} of all compounds as a function of the temperature.

Figure of merit. The figure of merit ZT of all compounds as function of temperature and doping is shown in Figures A.31e-A.38e (see appendix). For each temperature, ZT reaches a maximum at a certain doping concentration. These ZT_{max} are shown in Figure 2.22. The maximum values achieved for *p*- and *n*-doped AGe_7As_{15} and *n*-doped $BaGe_8As_{14}$ range from ZT_{max} = 0.55-1.53, which is in line with known values of clathrates like $Ba_8Cu_{14}Zn_2P_{30}$ (ZT = 0.62)[105], $Ba_8Ga_{16}Ge_{30}$ (ZT = 1.1)[106] or $(K,Ba)_{24}(Ga,Sn)_{136}$ (ZT = 1.19).[107] *p*-doped $BaGe_8As_{14}$ on the other hand exhibits large *ZT* values of $ZT_{\max}$ = 2.3-2.7 depending on the ordering of the Ge/As-sites. Comparable *ZT* values are only found so far in Bi_2Te_3/Sb_2Te_3 superlattices (*ZT* = 2.4)[108] or for SnSe single crystals along the *b*-axis (*ZT* = 2.6).[109]

Conclusion

$RbGe_7As_{15}$ and $CsGe_7As_{15}$ are new narrow-gap semiconductors with the sodalite-type structure isotypic to $BaGe_8As_{14}$. Rubidium and caesium perfectly fit into the sodalite-cage due to their bigger ionic radii compared to barium, which is displaced from the center. First principles DFT calculations give clear evidence of ultralow lattice thermal conductivity around 0.5 $Wm^{-1}K^{-1}$ in $BaGe_8As_{14}$ which is a consequence of both the disordered position of the barium atoms and the anharmonicity of its thermal movement. Frozen phonon calculations indicate that rattling may further decrease the lattice thermal conductivity of $BaGe_8As_{14}$. These effects are chemically switched off in Rb/$CsGa_7As_{15}$ which shows a parabolic potential and no signs of rattling, leading to a four times higher lattice thermal conductivity. The predicted thermoelectric efficiency *ZT* is up to 2.7 for $BaGe_8As_{14}$, reaching the value of current record materials.

Experimental Section

Synthesis. $RbGe_7As_{15}$ and $CsGe_7As_{15}$ were synthesized via high temperature solid-state reactions. Starting materials were stoichiometric mixtures of RbAs or CsAs, Ge (99.999 %, Sigma Aldrich) and As (99.99999+ %, Alfa Aesar). The precursors RbAs and CsAs were synthesized by heating the elements Rb (99.75 %, Alfa Aesar) or Cs (99.98 %, smart elements) and As for 15 h at 973 K in alumina crucibles in sealed steel ampules sealed in silica ampules under purified argon. Mixtures of the starting compounds were thoroughly homogenized, filled in alumina crucibles and sealed in silica ampules under argon atmosphere. The samples were heated to 873 K with 25 Kh^{-1} for 60 h and cooled down to room temperature with 25 Kh^{-1}. Suitable single crystals were isolated from these polycrystalline samples. Single phase materials resulted after homogenizing, pressing to pellets and heating at 873 K for 250 h. The compounds are black powders stable in air and water. Phase purity was confirmed with PXRD. All manipulations were conducted in an argon filled Glovebox.

Single Crystal X-ray Diffraction. Single Crystal Data were collected with a Bruker D8 Venture (Mo Kα, Photon II-Detector, Kryoflex II cooling unit). APEX 3[27] and SADABS[28] were used for intensity integration and absorption correction. The space group was chosen with XPREP[29] based on systematic absences. The phase problem was solved with the SUPERFLIP[30] package and refinement of the structure was performed with the SHELXL[31] package.

The deposition numbers 2078533-2078542 (detailed in Table A.85; appendix) contain the crystallographic data for this paper. These data are provided free of charge by the joint Cambridge Crystallographic Data Centre and Fachinformationszentrum Karlsruhe Access Structures service www.ccdc.cam.ac.uk/structures.

Powder X-ray Diffraction. Powdered samples were filled and sealed in glass capillaries of 0.2 mm diameter (Hilgenberg GmbH). Data were collected with a STOE Stadi-P diffractometer (Cu $K\alpha1$, Ge(111) monochromator, Myhten 1k detector) and fitted with the TOPAS[110] package based on single crystal data.

TEM and STEM Investigations. $RbGe_7As_{15}$ was ground thoroughly, distributed on a Cu grid covered with a carbon film (Plano GmbH, Germany) and mounted on a double tilt holder. Experiments were realized with a Titan Themis 300 (FEI, USA) TEM equipped with an X-FEG electron source, a Cs DCOR probe-corrector, a US1000XP/FT camera system (Gatan, Germany) and a windowless 4-quadrant Super-X EDX detector. The system was operated at an acceleration voltage of 300 kV. A 4k × 4k FEI Ceta CMOS camera (FEI, USA) was used for TEM images. Data processing and Fourier filtering were performed with JEMS (SAED simulations)[78] and Velox v3.0 (STEM images, EDX maps).[111]

EDX Measurements. EDX spectra were measured using a Carl Zeiss EVO-MA 10 scanning electron microscopy with SE and BSE detectors and equipped with a Bruker Nano EDX detector (X-Flash detector 410-M). Data were collected and processed with the SmartSEM[38] and QUANTAX 200[39] software. Elements contained in the sample holder and adhesive carbon tabs were disregarded.

UV-Vis-NIR Spectroscopy. A VARIAN Cary 500 UV-Vis-NIR spectrophotometer with a DRA-CA-5500 integrating sphere was used to collect diffuse reflectance spectra between 2000 and 3000 nm. To account for a strong absorption, the samples were diluted with $BaSO_4$. The data were converted according to the Kubelka-Munk theory[40] and plotted as Tauc graphs.

Resistivity and Hall-Effect Measurements. Powdered samples were pressed into pellets of 4 mm in diameter and 0.5 mm in thickness. They were put into alumina crucibles, sealed in silica ampules under an atmosphere of purified argon and sintered at 853 K for 60 h with heating and cooling rates of 50 Kh^{-1}. Resistivity and Hall-Effect measurements were conducted with a Quantum Design Inc. PPMS (physical property measurement system) equipped with a DC resistivity option. The pellet was contacted using Wimbush four-point Van der Pauw press contacts. Data were collected between 150 and 300 K and field strengths of ±50 kOe with the MultiVu software package.[41]

DFT Calculations. The progress of theoretical approaches for thermoelectrics enables predictions in excellent agreement with experimental values,[98] and screening of thousands of compounds accelerates research in this field rapidly.[112-114] First principle electronic structure calculations were performed based on density functional theory (DFT) and plane wave basis sets using the Vienna ab initio simulation package (VASP).[42, 43] Projector augmented waves (PAW)[44] were used and contributions of correlation and exchange were treated in the generalized-gradient approximation (GGA).[45] Depending on the accordance with experimental lattice parameters, PBE,[45] PBEsol[74] or SCAN[75] potentials were used. The Brillouin-zones were sampled with 10×10×10 ($A\mathrm{Ge}_7\mathrm{As}_{15}$, oF-$\mathrm{BaGe}_8\mathrm{As}_{14}$) and 8×8×8 ($tP$- and hR-$\mathrm{BaGe}_8\mathrm{As}_{14}$) Monkhorst Pack k-point meshes and a plane wave energy cutoff of 500 eV. Structure parameters were optimized until interatomic forces are below 10^{-4} $\mathrm{eV\AA^{-1}}$.

Phonon dispersions and lattice thermal conductivities κ_L were calculated from interatomic force constants (IFC) using the supercell approach (2×2×2) implemented in phonopy and phono3py codes.[115, 116] Respective electronic relaxation calculations of supercell structures were performed at the Γ-point only with a 4 Å cutoff for third-order force constants to keep computational costs within limits. Sampling of the phonon lifetimes were performed with Γ-centered 11×11×11 ($A\mathrm{Ge}_7\mathrm{As}_{15}$, oF-$\mathrm{BaGe}_8\mathrm{As}_{14}$) or 9×9×9 ($tP$-$\mathrm{BaGe}_8\mathrm{As}_{14}$) q-meshes. The Seebeck coefficient S, electrical conductivity σ and electronic thermal conductivity κ_el were calculated using the Boltzmann transport theory with the BoltzTraP2 package.[117] The necessary relaxation time values for this approach were calculated based on the deformation potential (DP) theory.[118] The respective effective masses were obtained with the EMC package.[119] Further detail are in the ESI. The electron location function (ELF)[46] was calculated to visualize chemical bonding and the Bader analysis[49] to extract charges from the electron density.

References

[1] Y.-S. Choi, Y.-W. Byeon, J.-P. Ahn, J.-C. Lee, *Nano Lett.* **2017**, *17*, 679-686.

[2] J. Jiang, M. M. Olmstead, S. M. Kauzlarich, H.-O. Lee, P. Klavins, Z. Fisk, *Inorg. Chem.* **2005**, *44*, 5322-5327.

[3] E. S. Toberer, A. F. May, G. J. Snyder, *Chem. Mater.* **2010**, *22*, 624-634.

[4] S.-J. Kim, S. Hu, C. Uher, M. G. Kanatzidis, *Chem. Mater.* **1999**, *11*, 3154-3159.

[5] S. R. Brown, S. M. Kauzlarich, F. Gascoin, G. J. Snyder, *Chem. Mater.* **2006**, *18*, 1873-1877.

[6] T. Zhou, Z. Feng, J. Mao, J. Jiang, H. Zhu, D. J. Singh, C. Wang, Z. Ren, *Chem. Mater.* **2020**, *32*, 776-784.

[7] K. Kihou, H. Nishiate, A. Yamamoto, C.-H. Lee, *Inorg. Chem.* **2017**, *56*, 3709-3712.

[8] B. R. Ortiz, P. Gorai, V. Stevanović, E. S. Toberer, *Chem. Mater.* **2017**, *29*, 4523-4534.

[9] W. Tan, Z. Wu, M. Zhu, J. Shen, T. Zhu, X. Zhao, B. Huang, X.-t. Tao, S.-q. Xia, *Inorg. Chem.* **2017**, *56*, 10576-10583.

[10] B. Eisenmann, H. Schäfer, *Angew. Chem.* **1980**, *92*, 480-481.

[11] B. Eisenmann, H. Schäfer, *Z. Anorg. Allg. Chem.* **1982**, *484*, 142-152.

[12] B. Eisenmann, H. Jordan, H. Schäfer, *Z. Naturforsch., B: Chem. Sci.* **1982**, *37*, 1564-1568.

[13] B. Eisenmann, H. Jordan, H. Schäfern, *Angew. Chem.* **1981**, *93*, 211-211.

[14] B. Eisenmann, H. Jordan, H. Schäfer, *Z. Anorg. Allg. Chem.* **1981**, *475*, 74-80.

[15] B. Eisenmann, H. Jordan, H. Schäfer, *Mater. Res. Bull.* **1982**, *17*, 95-99.

[16] B. Eisenmann, H. Jordan, H. Schäfer, *Z. Naturforsch., B: Chem. Sci.* **1982**, *37*, 1221.

[17] B. Eisenmann, H. Jordan, H. Schäfer, *Z. Naturforsch., B: Chem. Sci.* **1984**, *39*, 864-867.

[18] B. Eisenmann, H. Schäfer, *Z. Naturforsch., B: Chem. Sci.* **1981**, *36*, 415.

[19] X. Zhang, T. Yu, C. Li, S. Wang, X. Tao, *Z. Anorg. Allg. Chem.* **2015**, *641*, 1545-1549.

[20] J. Chen, C. Lin, G. Peng, F. Xu, M. Luo, S. Yang, S. Shi, Y. Sun, T. Yan, B. Li, N. Ye, *Chem. Mater.* **2019**, *31*, 10170-10177.

[21] J. Mark, J. Wang, K. Wu, J. G. Lo, S. Lee, K. Kovnir, *J. Am. Chem. Soc.* **2019**, *141*, 11976-11983.

[22] A. Haffner, D. Johrendt, *Z. Anorg. Allg. Chem.* **2017**, *643*, 1717-1720.

[23] A. Haffner, V. Weippert, D. Johrendt, *Z. Anorg. Allg. Chem.* **2020**, *646*, 120-124.

[24] J. Mark, J.-A. Dolyniuk, N. Tran, K. Kovnir, *Z. Anorg. Allg. Chem.* **2019**, *645*, 242-247.

[25] R. D. Shannon, *Acta Crystallogr. Sect. A: Found. Crystallogr.* **1976**, *32*, 751-767.

[26] J. Gullman, O. Olofsson, *J. Solid State Chem.* **1972**, *5*, 441-445.

[27] v2016.5-0 ed., Bruker AXS Inc., Madison, USA, **2016**.

[28] G. M. Sheldrick, Version 2012/1 ed., Bruker AXS Inc., Madison,USA, **2001**.

[29] G. M. Sheldrick, Version 2008/2 ed., Bruker AXS Inc., Madison, USA, **2008**.

[30] L. Palatinus, G. Chapuis, *J. Appl. Crystallogr.* **2007**, *40*, 786-790.

[31] G. Sheldrick, *Acta Crystallogr., Sect. C: Struct. Chem.* **2015**, *71*, 3-8.

[32] A. Coelho, 6 ed., Coelho Software, Brisbane, Australia, **2016**.

[33] A. Coelho, *J. Appl. Crystallogr.* **2003**, *36*, 86-95.

[34] G. Pawley, *J. Appl. Crystallogr.* **1981**, *14*, 357-361.

[35] A. Coelho, *Acta Crystallographica Section A* **2007**, *63*, 400-406.

[36] G. Oszlanyi, A. Suto, *Acta Crystallographica Section A* **2008**, *64*, 123-134.

[37] Version 3.0.2.5 ed., STOE & Cie GmbH, Darmstadt, Germany, **2011**.

[38] Version 5.07 Beta ed., Carl Zeiss Microscopy Ltd., Cambridge, UK, **2014**.

[39] Version 1.9.4.3448 ed., Bruker Nano GmbH, Berlin, Germany, **2013**.

[40] P. Kubelka, F. Munk, *Z. Tech. Phys.* **1931**, *12*, 593-601.

[41] Version 1.5.11 ed., Quantum Design Inc., San Diego, USA, **2013**.

[42] G. Kresse, J. Hafner, *Phys. Rev. B* **1994**, *49*, 14251-14269.

[43] G. Kresse, J. Furthmüller, *Comput. Mater. Sci.* **1996**, *6*, 15-50.

[44] P. E. Blöchl, *Phys. Rev. B* **1994**, *50*, 17953-17979.

[45] J. P. Perdew, K. Burke, M. Ernzerhof, *Phys. Rev. Lett.* **1996**, *77*, 3865-3868.

[46] B. Silvi, A. Savin, *Nature* **1994**, *371*, 683-686.

[47] F. Tran, P. Blaha, *Phys. Rev. Lett.* **2009**, *102*, 226401.

[48] R. F. W. Bader, *Atoms in Molecules - A Quantum Theory*, Oxford University Press, London, **1990**.

[49] G. Henkelman, A. Arnaldsson, H. Jónsson, *Comput. Mater. Sci.* **2006**, *36*, 354-360.

[50] W. Depmeier, *Reviews in Mineralogy and Geochemistry* **2005**, *57*, 203-240.

[51] H. S. Sherry, *J. Phys. Chem.* **1966**, *70*, 1158-1168.

[52] N. Savage, M. S. Diallo, *J. Nanopart. Res.* **2005**, *7*, 331-342.

[53] R. A. Shigeishi, C. H. Langford, B. R. Hollebone, *Sol. Energy* **1979**, *23*, 489-495.

[54] G. S. Nolas, J. Poon, M. Kanatzidis, *MRS Bull.* **2006**, *31*, 199-205.

[55] E. T. C. Vogt, B. M. Weckhuysen, *Chem. Soc. Rev.* **2015**, *44*, 7342-7370.

[56] Ch. Baerlocher, L. B. McCusker, *Database of Zeolite Structures*, https://europe.iza-structure.org/IZA-SC/ftc_table.php,

[57] I. Hassan, H. D. Grundy, *Acta Crystallographica Section B* **1984**, *40*, 6-13.

[58] X. F. Reinhard, W. H. Baur, *Z. Kristallogr. Cryst. Mater* **2009**, *224*, 185-197.

[59] P. Smith-Verdier, S. Garcia-Blanco, *Z. Kristallogr. Cryst. Mater* **1980**, *151*, 175-177.

[60] X. Bu, P. Feng, T. E. Gier, D. Zhao, G. D. Stucky, *J. Am. Chem. Soc.* **1998**, *120*, 13389-13397.

[61] J. A. Armstrong, M. T. Weller, *Dalton Trans.* **2006**, 2998-3005.

[62] B. J. Wuensch, *Z. Kristallogr. Cryst. Mater* **1964**, *119*, 437-453.

[63] W. Schnick, J. Lücke, *Angew. Chem. Int. Ed.* **1992**, *31*, 213-215.

[64] F. Wester, W. Schnick, *Z. Anorg. Allg. Chem.* **1996**, *622*, 1281-1286.

[65] F. J. Pucher, C. Frhr. von Schirnding, F. Hummel, V. R. Celinski, J. Schmedt auf der Günne, B. Gerke, R. Pöttgen, W. Schnick, *Eur. J. Inorg. Chem.* **2015**, *2015*, 382-388.

[66] J. D. Martin, K. B. Greenwood, *Angew. Chem. Int. Ed.* **1997**, *36*, 2072-2075.

[67] B. C. Sales, D. Mandrus, R. K. Williams, *Science* **1996**, *272*, 1325.

[68] X. Tang, Q. Zhang, L. Chen, T. Goto, T. Hirai, *J. Appl. Phys.* **2005**, *97*, 093712.

[69] G. A. Slack, V. G. Tsoukala, *J. Appl. Phys.* **1994**, *76*, 1665-1671.

[70] V. L. Kuznetsov, L. A. Kuznetsova, A. E. Kaliazin, D. M. Rowe, *J. Appl. Phys.* **2000**, *87*, 7871-7875.

[71] M. J. Buerger, K. Taxer, *Science* **1966**, *152*, 500.

[72] V. Weippert, T. Chau, K. Witthaut, D. Johrendt, *Inorg. Chem.* **2020**, *59*, 15447-15453.

[73] M. Sharmin, S. Choudhury, N. Akhtar, T. Begum, *J. Bangladesh Acad. Sci.* **2012**, *36*, 97-107.

[74] J. P. Perdew, A. Ruzsinszky, G. I. Csonka, O. A. Vydrov, G. E. Scuseria, L. A. Constantin, X. Zhou, K. Burke, *Phys. Rev. Lett.* **2008**, *100*, 136406.

[75] J. Sun, A. Ruzsinszky, J. P. Perdew, *Phys. Rev. Lett.* **2015**, *115*, 036402.

[76] 3.6.1 ed., Gatan Software Team, **1999**.

[77] J. L. Lábár, 7.3.2 Q ed., **2012**.

[78] P. A. Stadelmann, 3.3425 ed., **2008**.

[79] A. M. Ganose, A. J. Jackson, D. O. Scanlon, *Journal of Open Source Software* **2018**, *3*, 717.

[80] G. J. Snyder, E. S. Toberer, *Nat. Mater.* **2008**, *7*, 105-114.

[81] L. S. Hewawasam, A. S. Jayasena, M. M. M. Afnan, R. A. C. P. Ranasinghe, M. A. Wijewardane, *Energy Rep.* **2020**, *6*, 474-479.

[82] K. F. Hsu, S. Loo, F. Guo, W. Chen, J. S. Dyck, C. Uher, T. Hogan, E. K. Polychroniadis, M. G. Kanatzidis, *Science* **2004**, *303*, 818.

[83] P. F. P. Poudeu, J. D'Angelo, A. D. Downey, J. L. Short, T. P. Hogan, M. G. Kanatzidis, *Angew. Chem. Int. Ed.* **2006**, *45*, 3835-3839.

[84] J. He, L.-D. Zhao, J.-C. Zheng, J. W. Doak, H. Wu, H.-Q. Wang, Y. Lee, C. Wolverton, M. G. Kanatzidis, V. P. Dravid, *J. Am. Chem. Soc.* **2013**, *135*, 4624-4627.

[85] R. Moshwan, X.-L. Shi, W.-D. Liu, Y. Wang, S. Xu, J. Zou, Z.-G. Chen, *ACS Appl. Energy Mater.* **2019**, *2*, 2965-2971.

[86] K. Kurosaki, A. Kosuga, H. Muta, M. Uno, S. Yamanaka, *Appl. Phys. Lett.* **2005**, *87*, 061919.

[87] S. M. Kauzlarich, S. R. Brown, G. Jeffrey Snyder, *Dalton Trans.* **2007**, 2099-2107.

[88] D. C. Schmitt, N. Haldolaarachchige, Y. Xiong, D. P. Young, R. Jin, J. Y. Chan, *J. Am. Chem. Soc.* **2012**, *134*, 5965-5973.

[89] G. S. Nolas, J. Sharp, H. J. Goldsmid, *The Phonon—Glass Electron-Crystal Approach to Thermoelectric Materials Research*, Springer, Berlin, **2001**.

[90] D. J. Voneshen, K. Refson, E. Borissenko, M. Krisch, A. Bosak, A. Piovano, E. Cemal, M. Enderle, M. J. Gutmann, M. Hoesch, M. Roger, L. Gannon, A. T. Boothroyd, S. Uthayakumar, D. G. Porter, J. P. Goff, *Nat. Mater.* **2013**, *12*, 1028-1032.

[91] G. S. Nolas, J. L. Cohn, G. A. Slack, *Phys. Rev. B* **1998**, *58*, 164-170.

[92] G. S. Nolas, J. L. Cohn, G. A. Slack, S. B. Schujman, *Appl. Phys. Lett.* **1998**, *73*, 178-180.

[93] A. Marchuk, W. Schnick, *Angew. Chem. Int. Ed.* **2015**, *54*, 2383-2387.

[94] A. Marchuk, S. Wendl, N. Imamovic, F. Tambornino, D. Wiechert, P. J. Schmidt, W. Schnick, *Chem. Mater.* **2015**, *27*, 6432-6441.

[95] W. Hölderich, M. Hesse, F. Näumann, *Angew. Chem. Int. Ed.* **1988**, *27*, 226-246.

[96] J. V. Smith, *Chem. Rev.* **1988**, *88*, 149-182.

[97] V. Weippert, T. Chau, K. Witthaut, L. Eisenburger, D. Johrendt, *Chem. Commun.* **2021**, *57*, 1332 -1335.

[98] W. Chen, J.-H. Pöhls, G. Hautier, D. Broberg, S. Bajaj, U. Aydemir, Z. M. Gibbs, H. Zhu, M. Asta, G. J. Snyder, *Journal of Materials Chemistry C* **2016**, *4*, 4414-4426.

[99] Y. Pei, X. Shi, A. LaLonde, H. Wang, L. Chen, G. J. Snyder, *Nature* **2011**, *473*, 66-69.

[100] D. Xue, C. W. Myles, *Appl. Sci.* **2019**, *9*.

[101] S. B. Schujman, G. S. Nolas, R. A. Young, C. Lind, A. P. Wilkinson, G. A. Slack, R. Patschke, M. G. Kanatzidis, M. Ulutagay, S. J. Hwu, *J. Appl. Phys.* **2000**, *87*, 1529-1533.

[102] J. L. Cohn, G. S. Nolas, V. Fessatidis, T. H. Metcalf, G. A. Slack, *Phys. Rev. Lett.* **1999**, *82*, 779-782.

[103] G. S. Nolas, T. J. R. Weakley, J. L. Cohn, *Chem. Mater.* **1999**, *11*, 2470-2473.

[104] J. Fulmer, O. I. Lebedev, V. V. Roddatis, D. C. Kaseman, S. Sen, J.-A. Dolyniuk, K. Lee, A. V. Olenev, K. Kovnir, *J. Am. Chem. Soc.* **2013**, *135*, 12313-12323.

[105] J.-A. Dolyniuk, J. Wang, M. A. T. Marple, S. Sen, Y. Cheng, A. J. Ramirez-Cuesta, K. Kovnir, *Chem. Mater.* **2018**, *30*, 3419-3428.

[106] L.-H. Wang, L.-S. Chang, *J. Alloys Compd.* **2017**, *722*, 644-650.

[107] K. Kishimoto, S. Koda, K. Akai, T. Koyanagi, *J. Appl. Phys.* **2015**, *118*, 125103.

[108] R. Venkatasubramanian, E. Siivola, T. Colpitts, B. O'Quinn, *Nature* **2001**, *413*, 597-602.

[109] L.-D. Zhao, S.-H. Lo, Y. Zhang, H. Sun, G. Tan, C. Uher, C. Wolverton, V. P. Dravid, M. G. Kanatzidis, *Nature* **2014**, *508*, 373-377.

[110] A. Coelho, 4.1 ed., Coelho Software, Brisbane, Australia, **2007**.

[111] 3.0.0.815 ed., Thermo Fisher Scientific, **2021**.

[112] K. Choudhary, K. F. Garrity, F. Tavazza, *J. Phys.: Condens. Matter* **2020**, *32*, 475501.

[113] F. Ricci, W. Chen, U. Aydemir, G. J. Snyder, G.-M. Rignanese, A. Jain, G. Hautier, *Sci. Data* **2017**, *4*, 170085.

[114] K. F. Garrity, *Phys. Rev. B* **2016**, *94*, 045122.

[115] A. Togo, I. Tanaka, *Scripta Mater.* **2015**, *108*, 1-5.

[116] A. Togo, L. Chaput, I. Tanaka, *Phys. Rev. B* **2015**, *91*, 094306.

[117] G. K. H. Madsen, J. Carrete, M. J. Verstraete, *Comput. Phys. Commun.* **2018**, *231*, 140-145.

[118] J. Bardeen, W. Shockley, *Phys. Rev.* **1950**, *80*, 72-80.

[119] C. S. A. Fonari, **2012**.

3 Layered supertetrahedral compounds: a hierarchical family

3.1 Supertetrahedral Layers Based on GaAs or InAs

Valentin Weippert, Arthur Haffner, Alexis Stamatopoulos and Dirk Johrendt

Published in: *Journal of the American Chemical Society* **2019**, *141*, 11245-11252.

Abstract

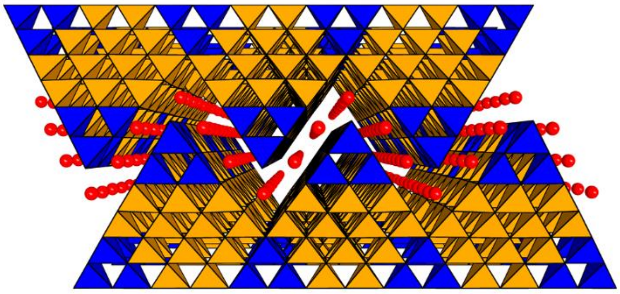

The solid-state compounds $M_{15}Tr_{22}As_{32}$ and $M_3Ga_6As_8$ (M = Sr, Eu; Tr = Ga, In) were synthesized by heating the elements, and their crystal structures were determined by single-crystal and powder X-ray diffraction (space group $C2/c$). The structures are hierarchical variants of the HgI_2 type and consist of layers of polymeric T5 ($M_{15}Tr_{22}As_{32}$) or T6 supertetrahedra ($M_3Ga_6As_8$), separated by strontium or europium cations. These compounds constitute hitherto unknown GaAs- or InAs-based supertetrahedral structures and represent the first binary vacancy-free T5 and T6 supertetrahedra. Vacancies or mixed-metal strategies for charge compensation, as known from related chalcogenides, are not required for supertetrahedra based on charge-neutral GaAs or InAs. Optical band gap, resistivity, and Hall-effect measurements together with DFT calculations reveal that the supertetrahedral compounds are direct band gap semiconductors similar to binary GaAs or InAs. Magnetic susceptibility measurements confirm Eu^{2+} in $Eu_{15}Ga_{22}As_{32}$, $Eu_{15}In_{22}As_{32}$, and $Eu_3Ga_6As_8$ and indicate antiferromagnetic ordering below 10 K.

Introduction

Crystalline supertetrahedral structures have attracted increasing attention since they combine well-defined sizes and compositions with properties of nanoparticles and quantum dots.[1, 2] Supertetrahedra also offer unique structural building blocks for porous networks, metal-organic frameworks with huge pores, or discrete nanoclusters.[3-5] These fields are dominated by main-group and transition-metal chalcogenide compounds which usually rely on organic spacers and capping agents.[6-9] With the introduction of group III and IV pnictides of the alkaline and alkaline-earth metals, their application possibilities expanded even further. Utilizing the supertetrahedral network as host matrix, Wagatha et al. presented $Ca_{18.75}Li_{10.5}[Al_{39}N_{55}]:Eu^{2+}$ as a highly efficient red-emitting luminescent phosphor.[10] With Li_2SiP_2, $LiSi_2P_3$, $Na_{19}Si_{13}P_{25}$, $Na_{23}Si_{19}P_{33}$, $Na_{23}Si_{28}P_{45}$, $Na_{23}Si_{37}P_{57}$, and $NaSi_2P_3$ Haffner et al. synthesized a family of fast solid-state Li^+ and Na^+ ion conductors.[11, 12] One of the main endeavors of this research is creating ever-larger supertetrahedral building blocks. In 2002 the first T5 cluster based on InS was presented.[7] Only in 2018 did Xu et al. synthesize a T6 ZnInS cluster with organic spacer through combinations of aliovalent metals for charge compensation.[13] In the ternary systems Sr-*Tr*-As and Eu-*Tr*-As (*Tr* = Ga, In) a variety of compounds have been synthesized.[14-19] Their structures contain isolated tetrahedra, chains, or layers with corner- and edge-sharing tetrahedra. However, as of today, no III-V supertetrahedral systems based on either GaAs or InAs are known. Since supertetrahedra can be seen as sections of cubic GaAs (sphalerite type), such compounds may exhibit interesting properties that differ from either individual clusters or the bulk. Pure GaAs is used in the semiconductor industry for many purposes. Although it has some drawbacks to conventional Si semiconductor materials such as high costs and difficulties in manufacturing, it has advantages in certain areas. In contrast to Si, GaAs features a direct band gap, making it an ideal material for highly efficient solar cells.[20] With a higher intrinsic electron mobility in comparison to Si it allows higher frequency processors and 5G modules in smartphones.[21, 22] Combining it with other triel elements leads to quantum dot systems such as InGaAs/GaAs with photoluminescent properties.[23] In this paper, we present the first supertetrahedral structures based on GaAs and InAs. Our approach to large supertetrahedra circumvents the problem of charge compensation simply by underlying charge-neutral binaries GaAs and InAs, which can principally form supertetrahedral clusters of any size without defects caused by charge imbalance. The new compounds $Sr_{15}Ga_{22}As_{32}$, $Eu_{15}Ga_{22}As_{32}$, $Sr_{15}In_{22}As_{32}$, and $Eu_{15}In_{22}As_{32}$ exhibit T5 supertetrahedra consisting of 35 $TrAs_4$ tetrahedra. With $Sr_3Ga_6As_8$ and $Eu_3Ga_6As_8$, we introduce the first binary T6 supertetrahedra without the aid of organic spacers or mixed-metal strategies. These contain 56 $GaAs_4$ tetrahedra with an unprecedented fusion of the supertetrahedra via T2 units. To compare the new supertetrahedral compounds with binary GaAs or InAs, we have measured basic semiconductor properties and performed electronic structure calculations.

Results and Discussion

Crystal Structure. The crystal structures of all compounds were solved from X-ray single-crystal data by charge flipping and refined in the monoclinic space group $C2/c$ (No. 15). Crystallographic data are summarized in Table 3.1, and detailed data, atomic positions, and anisotropic displacement parameters are given in Tables A.56–A.66 in the appendix.

Table 3.1: Crystallographic Data of $Sr_{15}Ga_{22}As_{32}$, $Eu_{15}Ga_{22}As_{32}$, $Sr_{15}In_{22}As_{32}$, $Eu_{15}In_{22}As_{32}$, $Sr_3Ga_6As_8$, and $Eu_3Ga_6As_8$.

Formula	$Sr_{15}Ga_{22}As_{32}$	$Eu_{15}Ga_{22}As_{32}$	$Sr_{15}In_{22}As_{32}$	$Eu_{15}In_{22}As_{32}$	$Sr_3Ga_6As_8$	$Eu_3Ga_6As_8$
Space group	*C*2/*c* (No. 15)	*C*2/*c* (No. 15)	*C*2/*c* (No. 15)	*C*2/*c* (No. 15)	*C*2/*c* (No. 15)	*C*2/*c* (No. 15)
a / Å	22.9660 (4)	22.8204 (7)	23.838 (5)	23.703 (2)	22.8363 (13)	22.740 (3)
b / Å	22.9639 (3)	22.8257 (7)	23.818 (4)	23.702 (2)	22.8335 (13)	22.747 (3)
c / Å	19.8929 (3)	19.7972 (6)	20.763 (4)	22.337 (2)	26.8169 (15)	25.505 (3)
β / °	98.2290 (10)	98.2370 (10)	98.244 (6)	113.473 (2)	108.613 (2)	96.393 (2)
V_{cell} / Å^3	10383.3 (3)	10205.8 (5)	11667 (4)	11511 (2)	13251.8 (13)	13111 (3)
Z	6	6	6	6	32	32
$\rho_{X\text{-}Ray}$ / g·cm^{-3}	5.033	6.063	5.327	6.235	5.135	5.972
R_1 ($F^2 > 2\sigma(F^2)$) / all	0.0365/0.0793	0.0724/0.0926	0.0403/0.0535	0.0553/0.0749	0.1159/0.1884	0.1306/0.1663
wR_2 ($F^2 > 2\sigma(F^2)$) / all	0.0642/0.0765	0.1573/0.1674	0.0853/0.0912	0.1499/0.1640	0.3198/0.3773	0.2890/0.3120
GooF	1.011	1.085	1.044	1.059	1.067	1.177
$\Delta\rho_{max/min}$ / eÅ^{-3}	+1.594/-1.877	+4.783/-4.542	+7.071/-3.141	+6.113/-4.099	+16.374/-5.380	+9.028/-9.518

The new structure types consist of layers of T5 or T6 supertetrahedra, fused by common T1 or T2 tetrahedra as shown in Figure 3.1.These motifs represent hierarchical variants of the tetragonal structure of red HgI_2, which exhibits analogous layers of $HgI_{4/2}$ tetrahedra (T1).[24] The orange modification of HgI_2 forms tetragonal polymorphs which contain layers of corner-sharing Hg_4I_{10} supertetrahedra (T2).[25] Filling of cations between charged layers of this topology leads to the large family of compounds with the $TlGaSe_2$-type structure, which crystallize in the space group *C*2/*c*.[26-33]

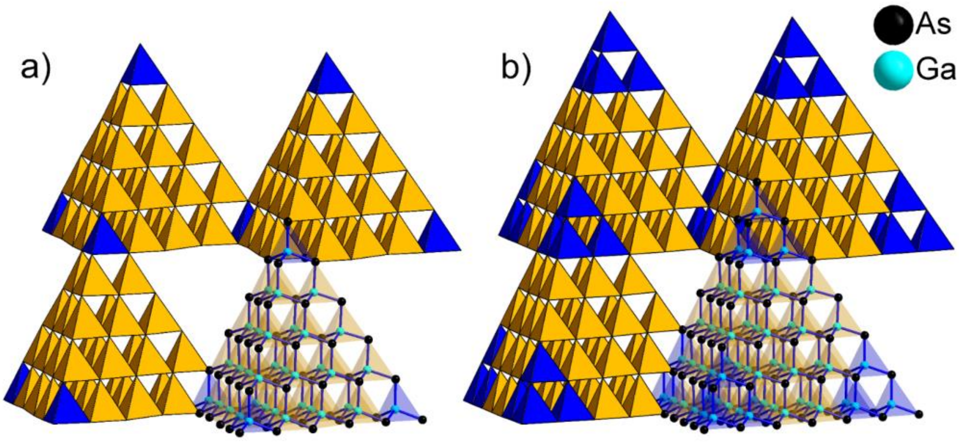

Figure 3.1: Supertetrahedra of (a) $M_{15}Tr_{22}As_{32}$ (T5) sharing one common $TrAs_4$ tetrahedron (blue) and (b) $M_3Ga_6As_8$ (T6) sharing a T2 supertetrahedron (blue).

The next hierarchic level represents the structure of $CsMnInTe_3$ with $[Mn_4In_6Te_{20}]^{14-}$ supertetrahedra (T3), fused by one common $InTe_4$ tetrahedron.[34] While an analogous T4 structure is currently unknown, the new gallium and indium arsenides presented here consequently expand this hierarchical series by T5 and T6 supertetrahedra. We do not observe cation vacancies inside the supertetrahedra as found in SiP^+- or InS^+-based compounds.[12, 13] This is because the new compounds derive from GaAs or InAs charge-neutral binaries; therefore, no charge compensation is necessary as the supertetrahedra sizes increase and the atomic ratios approach 1:1. *Tr*As-based T6 supertetrahedra have a lower negative charge on the surface in comparison to T5 or smaller supertetrahedra, which is dampened further by sharing a T2 unit (Figure 3.1b).

The supertetrahedral layers are stacked along the crystallographic *c* axis in a sawtooth-like manner. This is exemplarily shown in Figure 3.2a, where 56 $GaAs_4$ tetrahedra are combined to one tetrahedron which represents a T6 supertetrahedron, respectively. This general structure motif of stacked layers of supertetrahedra is known from the orange modification of HgI_2 with edge-sharing T2 units of Hg_4I_{10}.[25] Therein, stacking variants generate different polytypes of orange HgI_2 and stacking faults occur. The $TlGaSe_2$-type compounds are likewise strongly affected by stacking disorder.[28, 29] However, the layers of the larger T5 and T6 supertetrahedra partially interpenetrate into each other, which allows translational degrees of freedom of the layers only perpendicular to the direction of the sawtooth interlocking (Figure 3.2a). As a consequence of different stacking motifs, the new compounds $M_{15}Tr_{22}As_{32}$ and $M_3Ga_6As_8$ form two polytypes, respectively, distinguishable by the monoclinic angles (T5: ~98 or ~113 °; T6: ~96 or ~108 °; see Table 3.1). The stacking variants result from different shifts of the adjacent supertetrahedral layers along [110] and $[1\bar{1}0]$, as depicted in Figure 3.2.

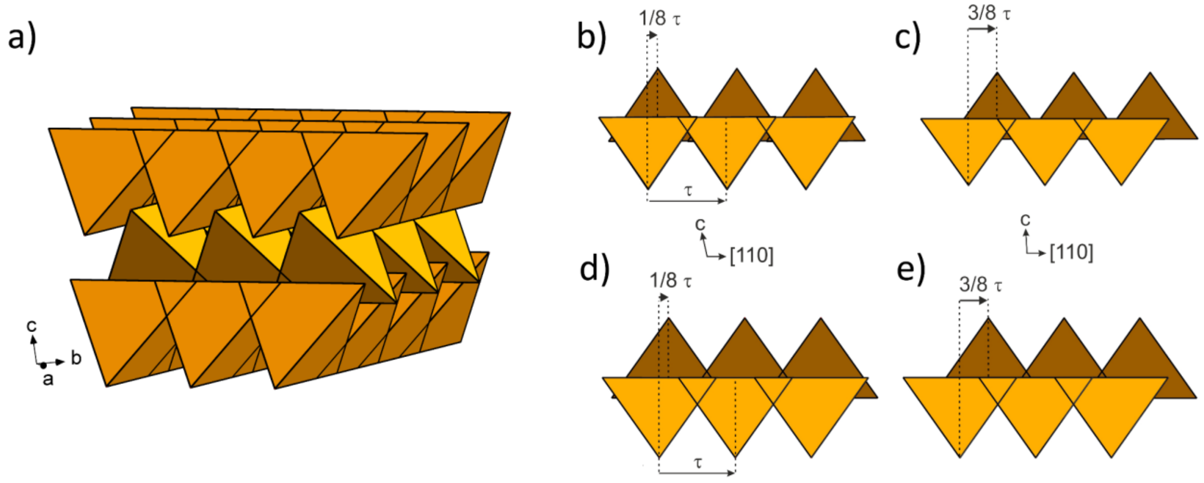

Figure 3.2: (a) Sawtooth-like stacking of supertetrahedral layers in $Sr_3Ga_6As_8$. Each tetrahedron represents a T6 unit. [110] shifts of adjacent supertetrahedral layers: (b) T5-$Eu_{15}In_{22}As_{32}$; (c) T5-$Sr_{15}Ga_{22}As_{32}$, $Eu_{15}Ga_{22}As_{32}$, and $Sr_{15}In_{22}As_{32}$; (d) T6-$Sr_3Ga_6As_8$; (e) T6-$Eu_3Ga_6As_8$.

In the first case with a larger β angle, the centers of the supertetrahedra nearly coincide in the [110] direction (Figure 3.2b,d); their relative shift is exactly 1/8 of the translation period τ, where τ corresponds to half of the *a,b* face diagonal. The other polymorph emerges if the [110] shift is 3/8 τ (Figure 3.2c,e), which means that their centers are almost at the gaps of the other. The same shift principle applies for the $[1\bar{1}0]$ direction. The shifts of the T5 and T6 supertetrahedra are identical, because in both cases one [110] translation comprises eight $TrAs_4$ tetrahedra, respectively. Since the larger T6 units share two common $TrAs_4$ tetrahedra, the same period τ emerges for the T5 units, which share only one $TrAs_4$ tetrahedron (Figure 3.2).

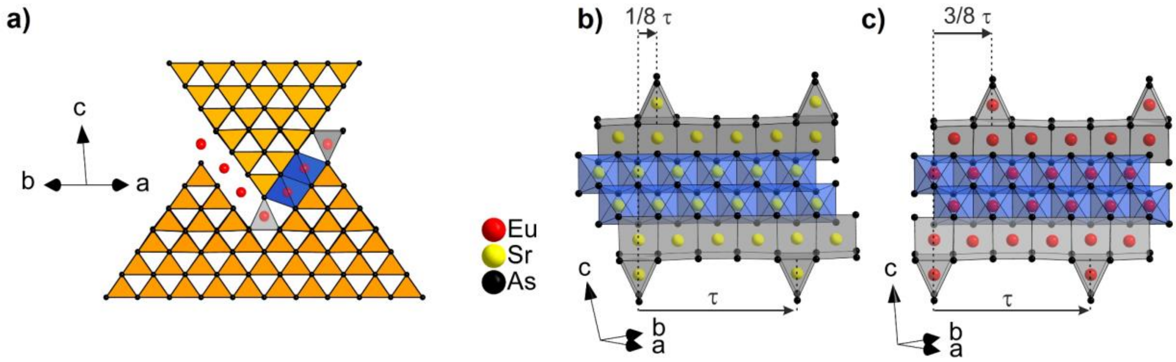

Figure 3.3: (a) Coordination of the Eu^{2+} ions between the T6 supertetrahedra in $Eu_3Ga_6As_8$. $EuAs_6$ octahedra are blue, and $EuAs_6$ trigonal prisms are gray. (b, c) Arrangements of the cation polyhedral in $Sr_3Ga_6As_8$ and $Eu_3Ga_6As_8$. Trigonal prisms perpendicular to the translation τ mark the positions of adjacent supertetrahedral layers, which are shifted by 1/8 τ or 3/8 τ relative to each other.

The relative shifts of the layers are not arbitrary because of the coordination requirements of the interjacent strontium or europium atoms, respectively. The surfaces of the supertetrahedra exhibit triangular nets of arsenic atoms, and the next surface is aligned in a way that its triangles are rotated by 180 °, thus forming octahedra of arsenide ions, which are filled with Sr^{2+} or Eu^{2+} ions (Figure 3.3a). The smallest possible distance between neighboring octahedra along [110] is 1/4 τ; thus, no offsets other than 1/8 τ or 3/8 τ between the supertetrahedra can occur. Two double chains of face-sharing $SrAs_6$ octahedra are over the surfaces of the T5 and T6 supertetrahedra (blue polyhedra in Figure 3.3). Chains of MAs_6 trigonal prisms run along the edges in the T6 compounds (gray polyhedra in Figure 3.3b,c). The perpendicular trigonal prisms mark the position of the next supertetrahedral layers and exhibit the same 1/8 or 3/8 shifts. Since the two rows of octahedra require a shift of 1/8, it becomes clear why the layers cannot coincide with zero shift.

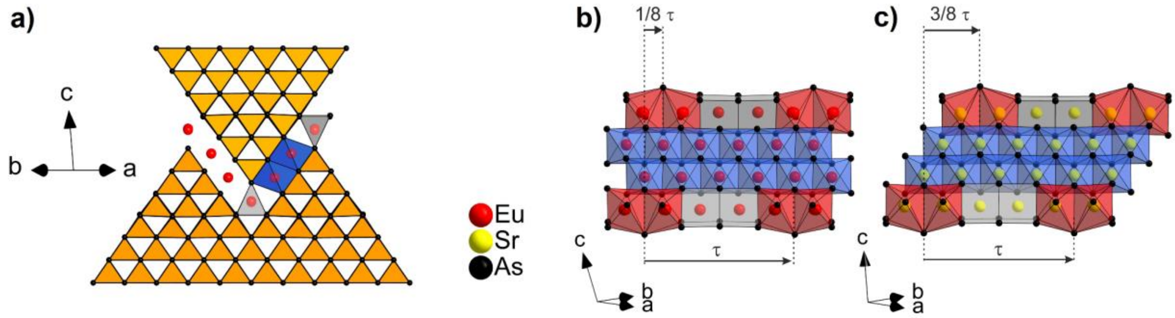

Figure 3.4: (a) Coordination of the Eu^{2+} ions between the T5 supertetrahedra in $Eu_{15}In_{22}As_{32}$. $EuAs_6$ octahedra are blue, $EuAs_6$ trigonal prisms are gray, and $EuAs_7$ pentagonal bipyramids are red. (b, c) Arrangements of the cation polyhedra in $Eu_{15}In_{22}As_{32}$ and $Sr_{15}Ga_{22}As_{32}$. Pairs of pentagonal bipyramids mark the positions of adjacent supertetrahedral layers, which are shifted by 1/8 τ or 3/8 τ relative to each other.

The voids at the crossing points of the supertetrahedral layers are larger in the T5 than in the T6 compounds. For this reason the rows of identical trigonal prisms in Figure 3.3b,c (T6) become rows of two trigonal prisms alternating with two distorted-pentagonal prisms (Figure 3.4a). The latter mark the crossings of the adjacent layers and underlie the same [110] shift principle as discussed above (Figure 3.4b,c). Figure 3.5 emphasizes the coordination of the disordered Sr(Eu) atoms in the polyhedra at the crossing voids in the T5 structures.

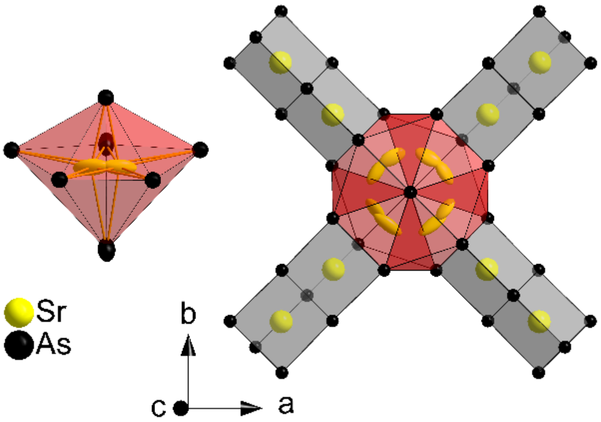

Figure 3.5: Sr coordination in $Sr_{15}Ga_{22}As_{32}$ at the cross-section of two perpendicular rows with trigonal prisms (gray) and pentagonal bipyramids (red). Ellipsoids are drawn with 66 % probability.

Since the correlation between a supertetrahedral layer and the adjacent layer is weak, the stacking along the *c* axis may not comply with ideal periodicity, and stacking faults can occur. Figure 3.6 shows reconstructed diffraction patterns of the 1*kl*, *h*1*l*, and *hl*1 layers of a $Eu_3Ga_6As_8$ crystal. The spots are smeared to streaks along *c**, while they are sharp in the *a** and *b** directions. This smearing is caused by stacking faults of the layers, and these are the reason for the poor *R* values of the single-crystal refinements with high residual electron densities (Table 3.1). This problem occurs only in the T6 structures. We suggest that the different coordination of the Sr/Eu atoms at the crossing points in the T5 structures (Figure 3.3 and Figure 3.4) as mentioned above act as fixation points between the layers, which makes stacking faults less probable.

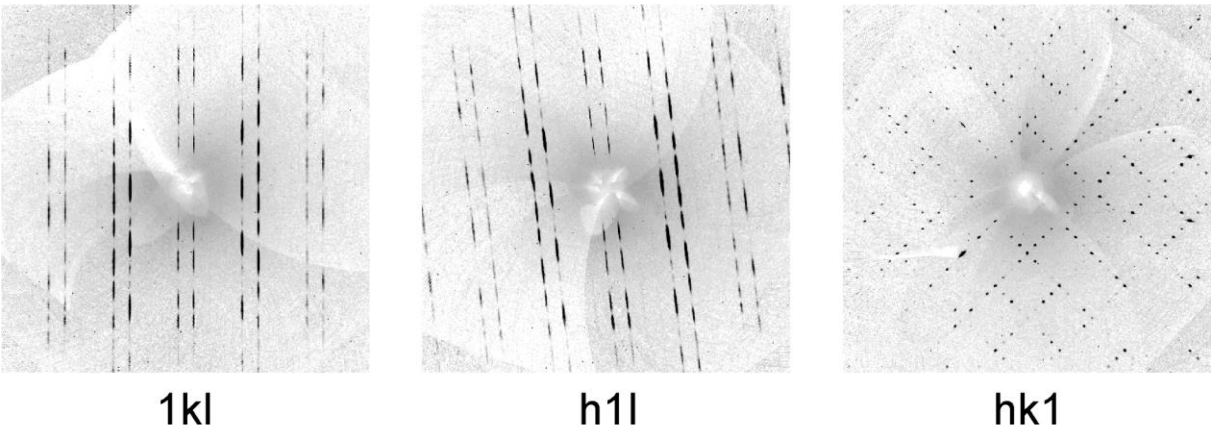

Figure 3.6: Diffraction patterns of the 1*kl*, *h*1*l* and *hk*1 sections of $Eu_3Ga_6As_8$.

$Sr_3Ga_6As_8$ and $Eu_3Ga_6As_8$ are the first examples of binary T6 supertetrahedra. As mentioned above, mixed cation strategies as in the recently reported T6 ZnInS structure[13] are not necessary because the charge of the GaAs- or InAs-based supertetrahedra decreases with increasing size, in contrast to known compounds that derive from formally charged binaries such as InS^+ or SiP^+. For this reason, we believe that the III-V based compounds have the potential to form supertetrahedra even larger than T6.

X-ray Powder Diffraction. Rietveld refinements of X-ray powder diffraction patterns based on single-crystal structure data are given in the Figures A.43–A.48 in the appendix. The refinements show acceptable accordance with the observed patterns. However, all of them show intensity problems to different extents, most likely caused by the discussed stacking faults. This problem also occurs for the T5 compounds, which show no diffuse diffraction in the measured single crystals. It is therefore probable that the T5 bulk samples exhibit stacking faults to some extent as well. No or few phase impurities (1 wt-% GaAs in $Sr_3Ga_6As_8$) were detected.

EDX Measurements. EDX data are in excellent agreement with the expected values within the typical error of the method and confirm the compositions obtained from single-crystal data. The results are shown in Table A.67.

Table 3.2: Optical Band Gap E_g, Electrical Resistivity ρ, Charge Carrier Density N, and Hall Mobility μ of $M_{15}Tr_{22}As_{32}$, $M_3Ga_6As_8$, GaAs,[35-39] and InAs.[38, 40-42]

Formula	E_g (eV)	ρ_{300K} (Ωcm)	N_{300K} (cm^{-3})	μ_{300K} (cm^{2}V^{-1}s^{-1})
$Sr_{15}Ga_{22}As_{32}$	1.2	1.6	1.6×10^{18}	2.6
$Eu_{15}Ga_{22}As_{32}$	1.0	1.7	1.8×10^{19}	0.2
$Sr_{15}In_{22}As_{32}$	1.0	1.1×10^{-2}	1.3×10^{18}	453
$Eu_{15}In_{22}As_{32}$	0.8	3.4	1.1×10^{18}	1.7
$Sr_3Ga_6As_8$	1.2	5.0	1.3×10^{18}	0.9
$Eu_3Ga_6As_8$	1.2	2.2	1.2×10^{18}	2.4
$GaAs_{intr.}$	1.42	3.3×10^{8}	2.1×10^{6}	400
$GaAs_{doped}$	1.2 – 1.7	5.6×10^{-3}	8.12×10^{18}	131
$InAs_{intr.}$	0.36	0.13	1×10^{15}	500
$InAs_{doped}$	0.29 – 0.57	$1 \cdot 10^{-3}$	1×10^{18}	10000

UV−Vis−NIR Spectroscopy. The absorption spectra were converted to Tauc plots (Figures A.49-51) and revealed direct optical band gaps of 1.0−1.2 eV for the gallium arsenides and 0.8−1.0 eV for the indium arsenides (Table 3.2). Room-temperature band gaps of GaAs between 1.2 and 1.7 eV have been reported;[35, 37] thus, our GaAs-based supertetrahedral materials have band gaps similar to those of the binary. In contrast, the gaps of our InAs-based compounds are significantly greater than expected, since the room-temperature band gap of cubic InAs is 0.36 eV.[36] However, band gaps depend strongly on tiny amounts of impurities and crystal defects. Our synthesis methods yield purities of 99 % at best, which is far from an intrinsic semiconductor.

In order to get an idea of this, we have synthesized GaAs in a fashion similar to that for our new compounds and found an optical band gap of 1.2 eV (Figure A.52 in the appendix).

Resistivity and Hall-Effect Measurements. The samples are p-type semiconductors with relatively high resistivities up to 5 Ωcm at 300 K (Table 3.2; additional data for 400 K are given in Table A.68). We ascribe this mainly to grain boundary effects in the compacted polycrystalline pellets. The carrier densities in the range of $4.8 \times 10^{16} - 1.8 \times 10^{19}$ cm^{-3} are comparable with those of doped GaAs or InAs. In contrast, the Hall mobilities are much smaller except for $Sr_{15}In_{22}As_{32}$. This may be a consequence of the high sample resistivity values or is caused by specific band structure features of the supertetrahedral compounds. We note that semiconductor data often span ranges of several magnitudes depending on the sample purity. However, our synthesis preparation methods are not intended to produce samples, which allow measurements of intrinsic properties. We have control neither of the doping level nor of crystallite sizes or grain boundaries. Therefore, the results in Table 3.2 should be considered as orienting values, which nevertheless clearly support that the supertetrahedral compounds exhibit semiconducting properties similar to those of GaAs or InAs.

Table 3.3: Effective Magnetic Moments μ_{eff} and Weiss Temperatures Θ of $Eu_{15}Tr_{22}As_{32}$ and $Eu_3Ga_6As_8$.

Formula	$Eu_{15}Ga_{22}As_{32}$	$Eu_{15}In_{22}As_{32}$	$Eu_3Ga_6As_8$
μ_{eff} / μ_B	7.871(1)	7.934(1)	7.7870(8)
Θ / K	7.45(6)	5.04(6)	8.60(4)

Magnetization Measurements. The Eu-containing compounds are paramagnetic and obey the Curie-Weiss law down to ≈ 10 K as is exemplarily shown in Figure 3.7a for $Eu_{15}In_{22}As_{32}$. The inverse magnetic susceptibilities of $Eu_{15}Ga_{22}As_{32}$ and $Eu_3Ga_6As_8$ are similar (Figure A.53). The resulting effective magnetic moments are close to the theoretical value of Eu^{2+}, which is $\mu_{eff} = 7.94\ \mu_B$[43] (Table 3.3). Magnetization isotherms at 2 K show values lower than an ideal paramagnetic state, indicating antiferromagnetic ordering (Figure A.54–A.14) despite small positive Weiss constants Θ.

Electronic Structure. The electronic band structure of the T6 compound $Sr_3Ga_6As_8$ was calculated as an example and compared with that of cubic GaAs. The T5 structures were not treatable due to the disordered Sr(Eu) positions. Figure 3.7b shows the total and atom-resolved density of states (DOS, pDOS). The DOS distributions of both compounds are remarkably similar; especially, the gallium and arsenic contributions of $Sr_3Ga_6As_8$ and cubic GaAs largely coincide. Moreover, the band gaps of both compounds are direct (at Γ) with identical calculated values of 1.57 eV using the modified Becke-Johnson potential.[44] This is in excellent agreement (+3 %) with the experimental value of 1.52 eV for cubic GaAs at absolute zero.[37]

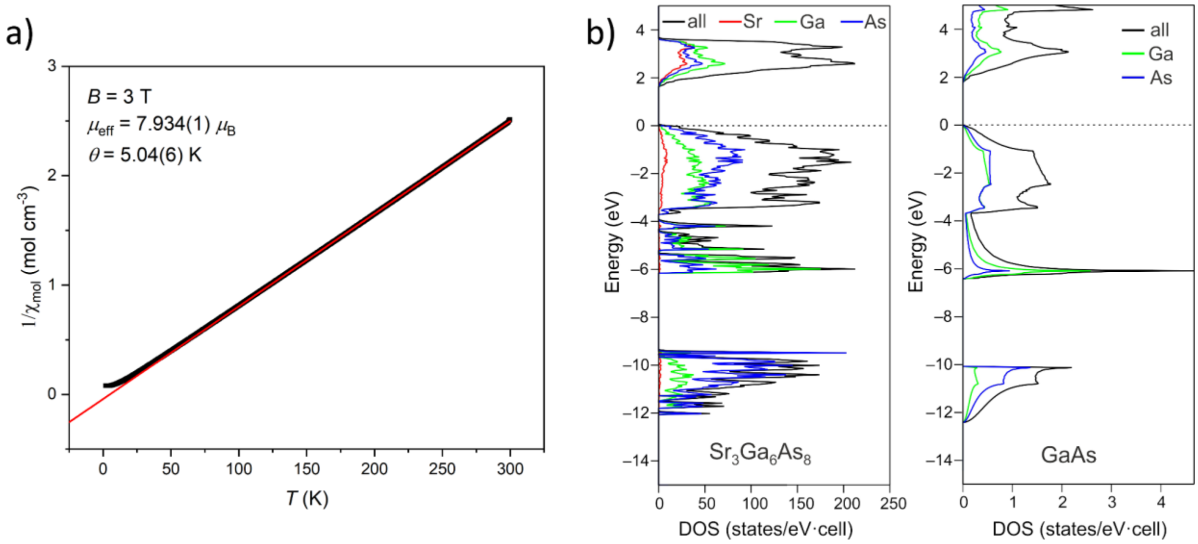

Figure 3.7: (a) Inverse magnetic susceptibility of $Eu_{15}In_{22}As_{32}$ with Curie-Weiss fit (red). (b) Total and atom-resolved electronic density of states for $Sr_3Ga_6As_8$ and for GaAs with the cubic sphalerite-type structure. The energy zeros are taken at the Fermi levels.

One may actually expect a larger gap for $Sr_3Ga_6As_8$, which has a higher ionic character due to the less electronegative strontium atoms. However, one must consider that in $Sr_3Ga_6As_8$ some of the $GaAs_4$ tetrahedra are inside the T6 supertetrahedra without contacts to the strontium atoms. These inner "GaAs-like" tetrahedra should have a charge similar to that in cubic GaAs, while the tetrahedra at the surface with contacts to the strontium atoms are expected to have higher negative charges. In order to compare these species, we have calculated the Bader charges for $Sr_3Ga_6As_8$ and cubic GaAs. The results are summarized in Table 3.4.

Table 3.4: Bader Charges in $Sr_3Ge_6As_8$ and Cubic GaAs^a.

Compound	Sr	Ga	As(i)	As(s)
$Sr_3Ga_6As_8$	+1.38	+0.57	−0.57	−1.03
GaAs		+0.57	−0.57	

^{a}As(i) and As(s) denote arsenic atoms inside (i) or at the surface (s)of the supertetrahedra. Values for $Sr_3Ga_6As_8$ are averages of theequivalent positions.

The primitive unit cell of $Sr_3Ga_6As_8$ contains 128 arsenic toms; 24 of them are inside the supertetrahedra and are solely bonded to gallium, and 104 of them are at the surface and are bonded to gallium and strontium. The Bader charges of the latter (As(s) in Table 3.4) are much larger because of the higher iconicity of a Sr−As bond in comparison with a Ga−As bond. The charge of the inner arsenic atoms (As(i) in Table 3.4) is identical with that of arsenic in cubic GaAs; thus, the inner $GaAs_4$ tetrahedra in the supertetrahedra have indeed the same charge distribution as in the binary GaAs. However, the gap is concretely determined by the splitting between the valence band with mainly As character and the conduction band with combined Sr and Ga character. Figure 3.7b shows that the contribution of the Sr atoms to the conduction band (red line) is in the same energy range as that for the Ga atoms (green line); thus, the lower electronegativity of Sr does not increase the gap. For comparison we have calculated the band gaps of the Sr-richer compounds $Sr_3Ga_2As_4$ and Sr_3GaAs_3, which are 1.37 and 1.35 eV, respectively. Also in these cases the gap does not increase relative to GaAs, in spite of the high content of weakly electronegative Sr. It appears that the ternary Sr compounds with $GaAs_4$ tetrahedra have bandgaps similar to that of GaAs. This means that the gap is mainly determined through the band splitting caused by the strong covalent Ga–As bonds, which are largely the same as in binary GaAs.

Conclusion

We have reported the first supertetrahedral compounds based on GaAs or InAs. $Sr_{15}Ga_{22}As_{32}$, $Eu_{15}Ga_{22}As_{32}$, $Sr_{15}In_{22}As_{32}$, and $Eu_{15}In_{22}As_{32}$ exhibit layers of T5 supertetrahedra sharing one common $TrAs_4$ tetrahedron. With $Sr_3Ga_6As_8$ and $Eu_3Ga_6As_8$ we have discovered T6 supertetrahedral structures without mixed-metal strategies, vacancies, or organic spacers. They likewise form a layered structure with T6 supertetrahedra sharing T2 units. The new structures are hierarchical extensions of the tetragonal HgI_2-type structure. All GaAs based compounds show direct optical band gaps similar to those of cubic GaAs, which was exemplarily confirmed by DFT calculations on $Sr_3Ga_6As_8$. The InAs-based compounds show a slightly higher optical band gap in comparison to pure InAs. Our samples are p-type semiconductors with carrier concentrations in the range of 10^{16} – 10^{19} cm^{-3} similar to those of doped GaAs and InAs. Magnetization measurements confirm Eu^{2+} for all Eu-containing compounds and indicate a possible antiferromagnetic ground state at temperatures below 10 K. These new compounds represent a unique way to confine the semiconductors GaAs and InAs, which may yield interesting properties in the future.

Experimental Section

Synthesis. The compounds were synthesized by heating stoichiometric mixtures of the respective elements in alumina crucibles sealed in silica ampules under an atmosphere of purified argon. Single-phase samples of $M_3Ga_6As_8$ (M = Sr, Eu) were obtained in a one-step synthesis. The mixtures were heated to 1323 K at a rate of 25 K h^{-1}, kept at this temperature for 60 h, and cooled to 1123 K at a rate of 3 K h^{-1} followed by switching off the furnace. To obtain $M_{15}Tr_{22}As_{32}$ (Tr = Ga, In), the mixtures were heated to 1223 K and cooled to 1023 K at the same rates. The multi-phase samples were ground and heated at 1323 K for 60 h. The reactions yielded silver to black plate-like crystals, which are stable in air (see appendix Figure A.42).

Single-Crystal X-ray Diffraction. Single-crystal data were collected using a Bruker D8 Quest diffractometer (Mo Kα1, Photon-II detector). Intensity integration, data reduction, and absorption corrections were done with APEX3[45] and SADABS.[46] The crystal structures were solved with the Superflip[47, 48] package and refined with the SHELXL[49] package.

Powder X-ray Diffraction. The X-ray powder patterns were obtained with either a Stoe Stadi-P (Mo Kα1/Cu Kα1, Ge(111) monochromator, Mythen 1k detector) or Huber G670 (Co Kα1, Ge(111) monochromator, image plate detector) diffractometer and fitted using TOPAS.[50]

EDX Measurements. Scanning electron microscopy of singlecrystalline and polycrystalline samples was performed on a Carl Zeiss EVO-MA 10 instrument with SE and BSE detectors, which were controlled by the SmartSEM[51] software. The microscope was equipped with a Bruker Nano EDX detector (X-Flash detector 410-M) for EDX investigations using the QUANTAX 200[52] software to collect and evaluate the spectra. Elements contained in the sample holder and adhesive carbon pads were disregarded.

Resistivity and Hall-Effect Measurements. Samples were pressed into pellets and sintered at 1073 K for 12 h in glassy-carbon crucibles sealed in silica ampules under an atmosphere of purified argon. Resistivity and Hall-Effect measurements were conducted with a Quantum Design Inc. PPMS (physical property measurement system) apparatus at 300 and 400 K with field strengths of ±30 kOe. The samples were contacted with a four-point Van der Pauw press contact by Wimbush. Data were collected with the PPMS MultiVu software package.[53]

Magnetization Measurements. Magnetization isotherms and susceptibility measurements of powder samples were performed with a Quantum Design Inc. PPMS apparatus with field strengths of ±50 kOe and between temperatures of 1.9 and 300 K. Data were collected with the PPMS MultiVu software package.[53]

UV–Vis–NIR Spectroscopy. Diffuse reflectance spectra of powder samples were measured with an Agilent Technologies Cary 5000 UV–Vis–NIR spectrophotometer (200–2000 nm). The spectra were converted on the basis of the Kubelka-Munk[54] theory to determine optical bandgaps.

DFT Calculations. First-principles electronic structure calculations were performed using the Vienna ab initio simulation package (VASP),[55, 56] which is based on density functional theory (DFT) and plane wave basis sets. Projector-augmented waves (PAW)[57] were used, and contributions of correlation and exchange were treated in the generalized-gradient approximation (GGA).[58] We used the modified Becke-Johnson exchange potential (mBJ),[44] which yields band gaps close to experimental values. The Bader analysis[59] implemented by Henkelman et al.[60] was used to extract charges from the electron density distribution.

3.2 New layered supertetrahedral compounds T2-MSiAs$_2$, T3-MGaSiAs$_3$ and polytypic T4-M_4Ga$_5$SiAs$_9$ (M = Sr, Eu)

Valentin Weippert, Arthur Haffner and Dirk Johrendt

Published in: *Zeitschrift für Naturforschung B* **2020**, *75*, 983-989.

Reproduced from reference with permission from De Gruyter.

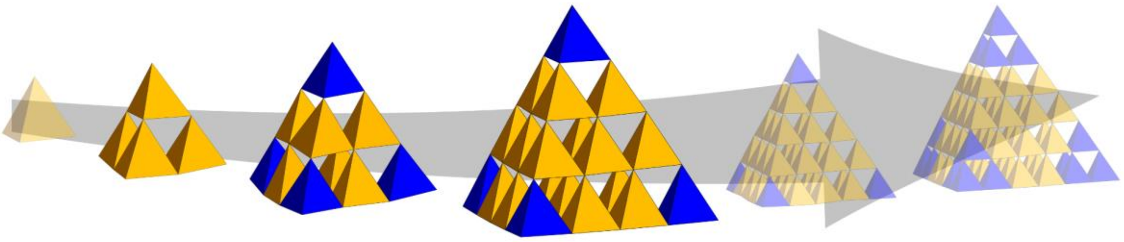

Abstract

The new supertetrahedral compounds MSiAs$_2$, MGaSiAs$_3$ and mC/tI-M_4Ga$_5$SiAs$_9$ (M = Sr, Eu) have been synthesized by solid-state reactions at high temperatures. The structures were determined by single crystal or powder X-ray diffraction. MSiAs$_2$ and MGaSiAs$_3$ crystallize in the monoclinic TlGaSe$_2$- and RbCuSnS$_3$-type structures, respectively (space group $C2/c$). These are topologically hierarchical variants of the tetragonal HgI$_2$-type structure with stacked layers of T2 or T3 supertetrahedra. The T4 compounds M_4Ga$_5$SiAs$_9$ are dimorphic and form new structure types in the space groups $C2/c$ and $I4_1/amd$, respectively. The latter exhibits coinciding layer stacking as known from tetragonal HgI$_2$. The T4 compounds close the gap between the longer known T2 types and the recently reported compounds with T5 and T6 supertetrahedra. Measurements of the optical band gap, electrical resistivity and Hall Effect support the semiconducting nature of M_4Ga$_5$SiAs$_9$. Magnetization measurements confirm Eu^{2+} in Eu$_4$Ga$_5$SiAs$_9$ and indicate ferromagnetism below T = 2 K.

Introduction

Supertetrahedral compounds exhibit a large structural variety thanks to the different sizes and connectivity motifs of the supertetrahedral units.[3, 7-9, 61-63] The size of the supertetrahedra currently ranges from the smallest T2[11, 29] up to large T6 units, which consist of 56 base tetrahedra. [13, 64] Supertetrahedra occur isolated,[5, 65] connected via common vertices,[3, 7-10, 62] sharing common base tetrahedra[11, 64] or combining the latter two cases.[12] This often results in complex 3D networks with giant cavities,[62] pathways for fast ion conductivity[11, 12] or ion exchange properties.[66] On the other hand, supertetrahedral compounds surprisingly often exhibit layered structures with $C2/c$ space group symmetry. These represent hierarchical variants of tetragonal HgI_2 polymorphs. The red modification contains layers of corner-sharing $HgI_{4/2}$ tetrahedra (T1)[24] and the orange polymorph layers of corner-sharing T2 supertetrahedra.[25] The $TlGaSe_2$-type structure has analogous layers of corner-sharing T2 supertetrahedra with cations in between. The stacked layers of supertetrahedra are often shifted, resulting in the monoclinic space group $C2/c$.[34] Numerous $ATrX_2$ compounds crystallize with the $TlGaSe_2$-type structure (A = Li, Na, K, Rb, Cs, Tl; Tr = Al, Ga, In; X = S, Se, Te).[26-33] Frequently occurring stacking faults cause diffuse scattering, which often makes structure refinements of these compounds difficult. In 2004, Kienle et al. gained insights into the nature of these stacking faults via high-resolution transmission electron microscopy. They observed statistically disordered stacking sequences but also ordered variants.[29] The next step in this hierarchy is the $RbCuSnS_3$-type structure type with layers of T3 supertetrahedra fused by one common base tetrahedron.[34, 67-69] Some members of this family are discussed as possible materials for X-ray and γ-ray radiation detection.[68, 69] While a corresponding T4 structure was unknown so far, we recently found the T5 compounds $M_{15}Tr_{22}As_{32}$ and the T6 compounds $M_3Ga_6As_8$ (M = Sr, Eu; Tr = Ga, In) which have expanded the structural hierarchy.[64] These compounds have $C2/c$ symmetry and form two polymorphs. In the course of our systematic synthesis attempts in the system M-(Ga/Si)-As (M = Sr, Eu) we came across the six new compounds MSiAs$_2$, MGaSiAs$_3$ and $M_4Ga_5SiAs_9$ (M = Sr, Eu). The latter close the gap existing owing to the hitherto missing T4 compound in the hierarchical sequence of HgI_2-type derivatives.

Results and Discussion

Crystal Structure. The crystal structures of $SrSiAs_2$, $EuSiAs_2$, $SrGaSiAs_3$, and $EuGaSiAs_3$ were determined from powder X-ray diffraction data based on the isotypic monoclinic ($C2/c$) structures of $RbGaS_2$ and $CsMnInTe_3$, respectively.[31, 34] The structures of tI-$Sr_4Ga_5SiAs_9$ and mC-$Eu_4Ga_5SiAs_9$ were determined from powder and single-crystal data. Resulting crystallographic data from the Rietveld refinements are compiled in Table 3.5, atomic positions and isotropic displacement parameters are given in Tables A.69-A.72 (see appendix). Due to serious stacking faults, which frequently occur in such compounds,[29, 64] all strontium based compounds show mediocre R values. Samples of the T2 and T3 structures contain significant fractions of other phases (Figures A.57-A.60; appendix), which make the refinements even more difficult. Samples of the T4 structures are always mixtures of the two polymorphs without impurity phases (Figures A.61-A.62; appendix). However, since the problematic structures are either additionally refined from single crystal data (T4) or known from the literature (T2, T3), we assume that the assignments and structural data are correct.

Table 3.5: Powder X-ray diffraction data of $SrSiAs_2$, $EuSiAs_2$, $SrGaSiAs_3$, $EuGaSiAs_3$, mC-$Sr_4Ga_5SiAs_9$, and tI-$Eu_4Ga_5SiAs_9$ from Rietveld refinements.

formula	$SrSiAs_2$	$EuSiAs_2$	$SrGaSiAs_3$	$EuGaSiAs_3$	mC-$Sr_4Ga_5SiAs_9$	tI-$Eu_4Ga_5SiAs_9$
space group	$C2/c$ (No. 15)	$C2/c$ (No. 15)	$C2/c$ (No. 15)	$C2/c$ (No. 15)	$C2/c$ (No. 15)	$I4_1/amd$ (No. 141)
a / Å	10.68318(14)	10.6369(3)	10.8992(2)	10.8783(12)	16.9442(7)	11.9167(6)
b / Å	10.6832(2)	10.6371(4)	10.9089(2)	10.8766(9)	16.9333(10)	11.9167(6)
c / Å	14.3500(3)	14.2022(4)	19.8354(3)	19.6704(9)	19.938837(2)	39.260(5)
β / °	100.7272(9)	100.7923(13)	97.900(3)	97.957(9)	98.143(4)	90
V_{cell} / Å^3	1609.16(5)	1578.49(9)	2336.02(8)	2305.0(3)	5663.2(4)	5575.2(9)
Z	16	16	16	16	12	12
$\rho_{\text{X-ray}}$ / g cm^{-3}	4.384	5.553	4.665	5.471	4.914	5.935
R_p	12.997	1.999	6.027	1.818	14.379	3.777
R_{wp}	16.498	2.688	8.367	2.442	18.126	5.224
GooF	1.463	2.760	5.337	1.853	1.584	2.010

Table 3.6: Single crystal data of tI-$Sr_4Ga_5SiAs_9$ and mC-$Eu_4Ga_5SiAs_9$.

formula	tI-$Sr_4Ga_5SiAs_9$	mC-$Eu_4Ga_5SiAs_9$
space group	$I4_1/amd$ (No. 141)	$C2/c$ (No. 15)
a / Å	11.9653(13)	16.8498(3)
b / Å	11.9653(13)	16.8496(3)
c / Å	39.458(4)	19.8216(3)
β / °	90	98.1550(10)
V_{cell} / Å^3	5649.1(14)	5570.69(16)
Z	12	12
$\rho_{\text{X-ray}}$ / g cm^{-3}	4.943	5.934
μ / mm^{-1}	34.007	36.381
Θ-range / °	6.184 – 61.058	5.116 – 76.644
refl. measured	54449	100625
independent refl.	2249	9680
parameters	83	262
R_σ	0.0512	0.0186
R_{int}	0.1021	0.0369
R_1 ($F^2 > 2\sigma(F^2)$) / all	0.0758 / 0.0938	0.0241 / 0.0356
wR_2 ($F^2 > 2\sigma(F^2)$) / all	0.2072 / 0.2238	0.0485 / 0.0532

The single crystal data of the T4 compounds tI-$Sr_4Ga_5SiAs_9$ and mC-$Eu_4Ga_5SiAs_9$ are compiled in Table 3.6, and atomic positions and anisotropic displacement parameters are given in Tables A.73-A.76 (appendix). Both T4 compounds form new structure types. Monoclinic mC-$Eu_4Ga_5SiAs_9$ crystallizes in the space group $C2/c$ following the aforementioned hierarchy. Tetragonal tI-$Sr_4Ga_5SiAs_9$ crystallizes in the space group $I4_1/amd$ and differs from all other compounds by a coinciding (not shifted) stacking sequence of the layers similar to the orange modification of HgI_2.[25] The high residual electron density and the rather poor R values are again caused by stacking faults, manifesting in diffuse scattering. Based on single crystal data, the structures of $Sr_4Ga_5SiAs_9$ and $Eu_4Ga_5SiAs_9$ were additionally refined from powder X-ray diffraction data, which revealed that both form the monoclinic and tetragonal polymorphs, respectively (see Tables A.77-A.78; appendix).

Figure 3.8 shows the supertetrahedral building blocks of the different structure types. The compounds $M\text{SiAs}_2$ contain T2 supertetrahedra connected via common vertices, leaving voids in the layers with edge lengths of two base tetrahedra (Figure 3.8a). $M\text{GaSiAs}_3$ consists of T3 supertetrahedra, which are fused by one common base tetrahedron, creating voids with edge lengths of only one tetrahedron (Figure 3.8b). The T4 supertetrahedra in $M_4\text{Ga}_5\text{SiAs}_9$ are fused by one common tetrahedron as well. This creates voids in the layers with edge lengths of two tetrahedra as in $M\text{SiAs}_2$ (Figure 3.8c).

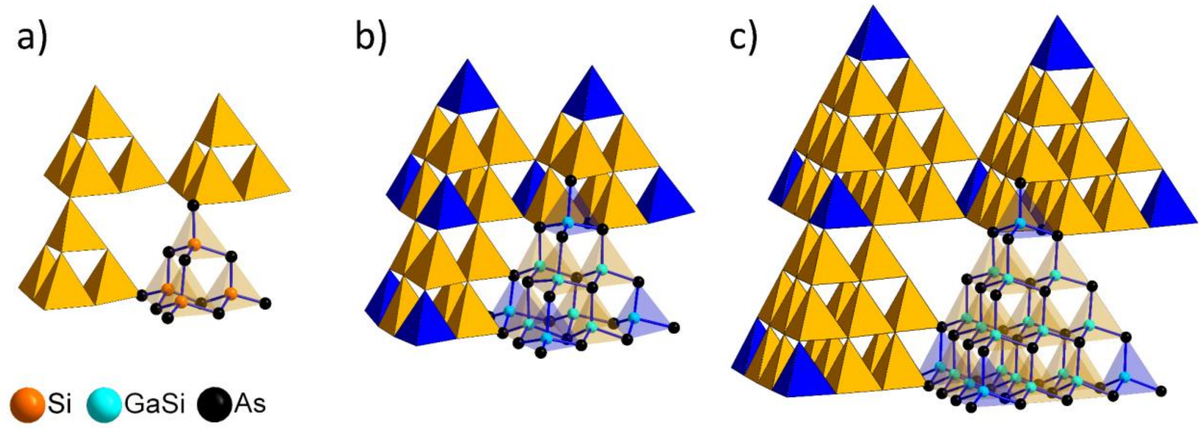

Figure 3.8: Supertetrahedral units of (a) T2-$M\text{SiAs}_2$ connected by common vertices, (b) T3-$M\text{GaSiAs}_3$ and (c) T4-$M_4\text{Ga}_5\text{SiAs}_9$ sharing one common tetrahedron (blue).

The layer stacking of *tI*-$M_4\text{Ga}_5\text{SiAs}_9$ is exemplarily shown in Figure 3.9a. The similar stacking sequences of $M\text{SiAs}_2$, $M\text{GaSiAs}_3$ and *mC*-$M_4\text{Ga}_5\text{SiAs}_9$ are shown in Figure A.56 (appendix). Both polytypes of $M_4\text{Ga}_5\text{SiAs}_9$ feature an interlocked saw-tooth like stacking of the supertetrahedral layers. $M\text{SiAs}_2$ and $M\text{GaSiAs}_3$ follow this stacking principle as well, but the layers do not interlock.

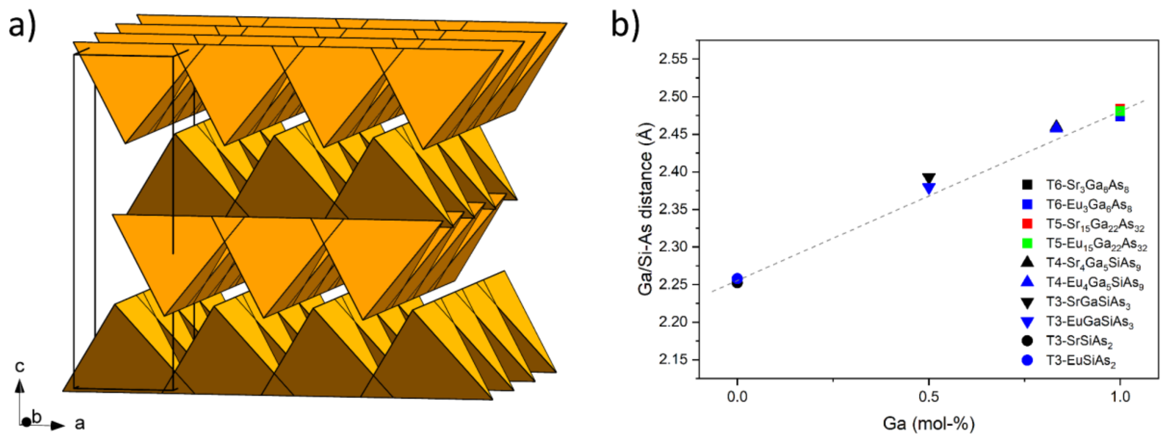

Figure 3.9: (a) Layered structure of *tI*-$M_4\text{Ga}_5\text{SiAs}_9$ with a saw tooth-like arrangement. Each tetrahedron represents one T4 supertetrahedron. (b) Distances (Å) found in (Ga/Si)As_4 tetrahedra of $M\text{SiAs}_2$, $M\text{GaSiAs}_3$, $M_4\text{Ga}_5\text{SiAs}_9$, $M_{15}\text{Ga}_{22}\text{As}_{32}$, and $M_3\text{Ga}_6\text{As}_8$[64] (dashed line as a guide to the eye).

With decreasing supertetrahedron size, the surface to volume ratio increases, leaving an increasing negative charge. This is compensated by a certain degree of fusion of the supertetrahedra. Because this approach has practical limits, and inevitably results in cubic GaAs, silicon was introduced to compensate the negative charge. This results in a Ga to Si ratio of 5:1 for $M_4\mathrm{Ga_5SiAs_9}$, 1:1 for $M\mathrm{GaSiAs_3}$ and 0:1 for $M\mathrm{SiAs_2}$. Different silicon contents lead to slightly changed Ga/Si–As distances in (Ga/Si)$\mathrm{As_4}$ base tetrahedra as shown in Figure 3.9b. No Ga/Si ordering was detected in single crystal refinements of $M_4\mathrm{Ga_5SiAs_9}$. This is different in $M\mathrm{GaSiAs_3}$. The highest Si contents are found in the fused tetrahedra, followed by the positions situated along the edges running parallel to (001) (Figure 3.10). $\mathrm{CsMnInTe_3}$ has a similar distribution but forms an ordered variant with $\mathrm{In^{3+}}$ exclusively occupying the positions of the higher $\mathrm{Si^{4+}}$ content and $\mathrm{Mn^{2+}}$ in place of the positions of the higher $\mathrm{Ga^{3+}}$ content when compared to $M\mathrm{GaSiAs_3}$.[34]

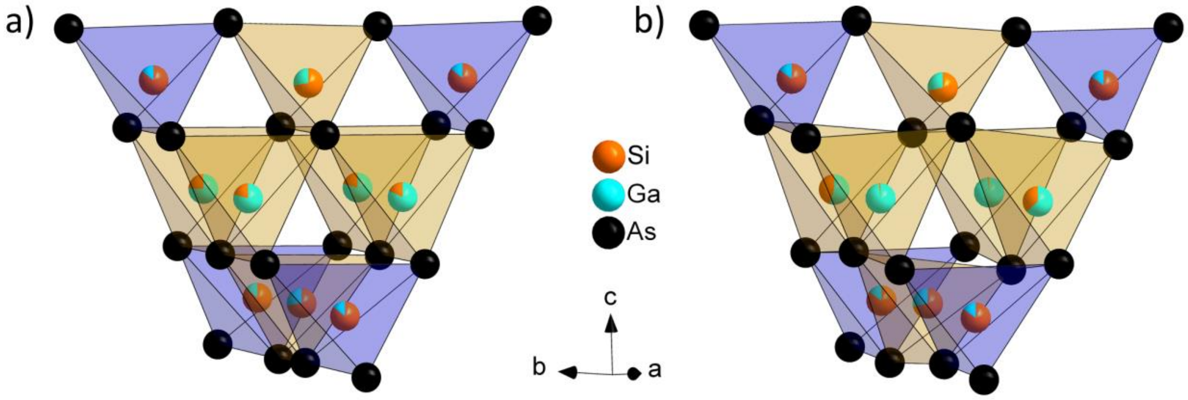

Figure 3.10: T3 supertetrahedral units with Ga (turquoise)/Si (orange) distribution of (a) $\mathrm{SrGaSiAs_3}$ and (b) $\mathrm{EuGaSiAs_3}$.

In our recent work about T5 and T6 supertetrahedral compounds, we described the shifts of adjacent layers and the formation of polytypes with different monoclinic angles.[64] Adjacent supertetrahedral layers are shifted relative to each other by fractions of the a,b diagonal (τ). These shifts occur along [110] and [1^{-}10]. The same description applies to $M\mathrm{SiAs_2}$, $M\mathrm{GaSiAs_3}$ and *mC*-$M_4\mathrm{Ga_5SiAs_9}$. Figure 3.11a-c shows the respective supertetrahedral layers and their shifts τ, which is zero in the tetragonal polytype *tI*-$M_4\mathrm{Ga_5SiAs_9}$ (Figure 3.11d).

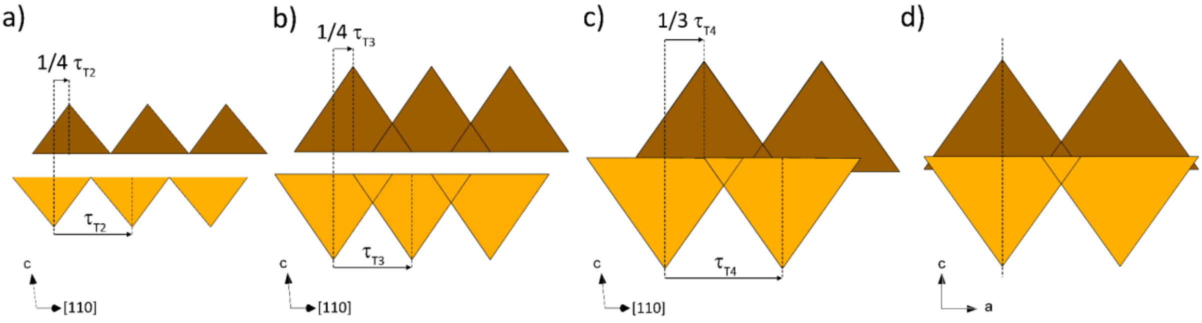

Figure 3.11: Fractional (110) shifts of the supertetrahedral layers relative to the translational period τ for (a) $M\mathrm{SiAs_2}$, (b) $M\mathrm{GaSiAs_3}$, (c) *mC*-$M_4\mathrm{Ga_5SiAs_9}$ and the lack thereof in (d) *tI*-$M_4\mathrm{Ga_5SiAs_9}$.

These concrete shifts are caused by the respective coordination of the Sr/Eu cations. The trigonal prisms of the adjacent layers (violet) are in the voids of the supertetrahedral layers (Figure 3.8). MSiAs$_2$ exhibits two separated rows of face-sharing MAs$_6$ trigonal prisms for each supertetrahedral layer (Figure 3.12a). MGaSiAs$_3$ shows the same motif, but due to the reduced size of the void with an edge length of only one tetrahedron (Figure 3.8b), the rows of adjacent layers do not share common faces (Figure 3.12b). The T4 compounds *mC*-M_4Ga$_5$SiAs$_9$ and *tI*-M_4Ga$_5$SiAs$_9$ feature two rows of face-sharing MAs$_6$ trigonal prisms, which are connected via common vertices through one row of edge-sharing MAs$_6$ octahedra (Figure 3.12c-d). This arrangement enables one tilted and one coinciding arrangement of the supertetrahedral layers without unfavorable electrostatic interactions.

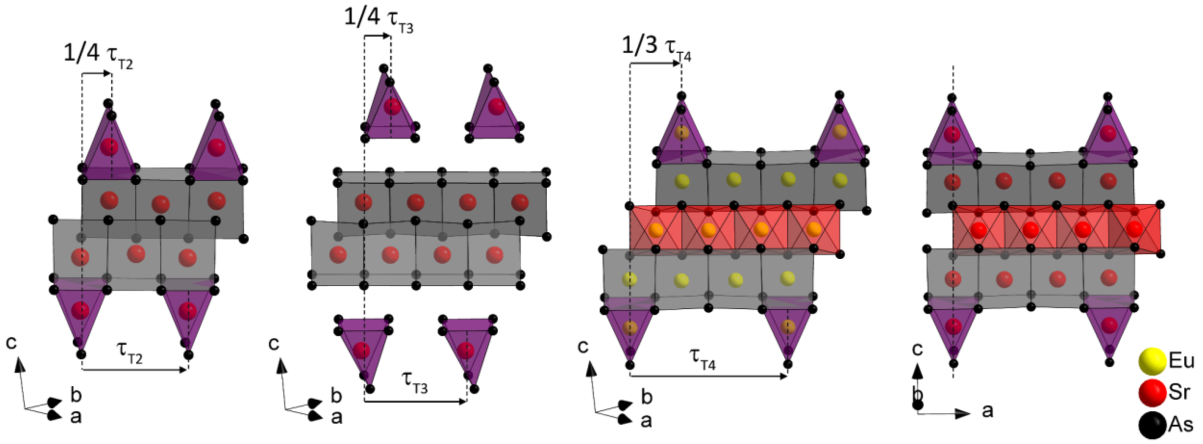

Figure 3.12: Coordination of the Sr/Eu positions and fractional (110) shifts of (a) SrSiAs$_2$, (b) SrGaSiAs$_3$, (c) *mC*-Eu$_4$Ga$_5$SiAs$_9$, and (d) *tI*-Sr$_4$Ga$_5$SiAs$_9$ with chains of face-sharing trigonal prisms (grey) and trigonal prisms (violet) of the adjacent supertetrahedral layer as well as chains of edge-sharing chains of octahedra (red).

EDX measurements. Table 3.7 shows EDX results of MSiAs$_2$, MGaSiAs$_3$ and M_4Ga$_5$SiAs$_9$. Within the typical error of the method, the experimental values are in good agreement with the theoretical values.

Table 3.7: EDX results of MSiAs$_2$, MGaSiAs$_3$ and M_4Ga$_5$SiAs$_9$.

Formula	*M* (at-%)	Ga (at-%)	Si (at-%)	As (at-%)
MSiAs$_2$ (calc.)	25	-	25	50
SrSiAs$_2$	24(1)	-	24(1)	52.6(8)
EuSiAs$_2$	26.0(8)	-	24(1)	50(1)
MGaSiAs$_3$ (calc.)	16.7	16.7	16.7	50
SrGaSiAs$_3$	18(1)	16(1)	16(1)	50(2)
EuGaSiAs$_3$	17.8(6)	18.4(9)	15.0(9)	49(2)
M_4Ga$_5$SiAs$_9$ (calc.)	21.1	26.3	5.3	47.4
Sr$_4$Ga$_5$SiAs$_9$	21(1)	26(1)	4(1)	49(2)
Eu$_4$Ga$_5$SiAs$_9$	22(1)	27(1)	4.5(3)	47(2)

UV/Vis spectroscopy. Only the samples of $M_4Ga_5SiAs_9$ allowed measurements of physical properties. We do not expect a significant impact of the polymorphism on the properties, because the modifications only differ by small shifts of the layers. Tauc plots of $Sr_4Ga_5SiAs_9$ and $Eu_4Ga_5SiAs_9$ are given in Figure A.63 (appendix). Using the Kubelka-Munk function $F(R)$, $h\nu$ was plotted versus $(F[R]\ h\nu)^{1/n}$ with $n = 1/2$ for a direct band gap and $n = 2$ for an indirect band gap. As the better results were obtained with $n = 2$, $Sr_4Ga_5SiAs_9$ and $Eu_4Ga_5SiAs_9$ are assumed to be indirect band gap semiconductors with optical band gaps of 1.6 and 1.7 eV, respectively. These values are slightly higher than those for T5-$M_{15}Ga_{22}As_{32}$ (E_g = 1.0–1.2 eV) and T6-$M_3Ga_6As_8$ (E_g = 1.2 eV)[64], which is as expected due to the partial substitution of Ga^{3+} with the more highly charged Si^{4+}. Because of the mixed Ga/Si occupancy of the supertetrahedra, we were not able to support these results with electronic structure calculations.

Resistivity and Hall Effect measurements. To investigate the semiconducting nature of $Sr_4Ga_5SiAs_9$ and $Eu_4Ga_5SiAs_9$, electrical resistivity and Hall Effect were measured. At T = 300 K, the compounds show dc electrical resistivities of 5.7 and 0.74 Ω cm, charge carrier densities of 1.7×10^{18} and 6.1×10^{18} cm^{-3} and Hall mobilities of 0.66 and 1.4 $cm^2V^{-1}\ s^{-1}$, respectively. These are in the order of doped GaAs, which resembles the silicon substituted supertetrahedral network.[39] Additional values at T = 400 K are given in Table A.79 (appendix). Even though these values clearly support the semiconducting nature of the new compounds, our synthesis method is not suitable to produce samples pure enough for measurements of intrinsic properties. Therefore, these results are considered as estimates.

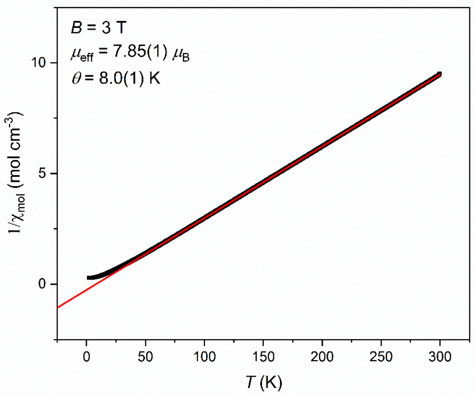

Figure 3.13: Inverse magnetic susceptibility of $Eu_4Ga_5SiAs_9$ with Curie-Weiss fit (red).

Magnetization measurements. Figure 3.13 shows the inverse magnetic susceptibility of $Eu_4Ga_5SiAs_9$ with a linear paramagnetic behavior according to the Curie-Weiss law down to T~20 K. The fit reveals an effective magnetic moment of μ_{eff} = 7.85(1) μ_B which is in agreement with the theoretical value of μ_{eff} = 7.94 μ_B for Eu^{2+}.[43] Magnetization isotherms for T = 2 and 300 K are shown in Figure A.64a (appendix). At 2 K the magnetization tends to saturate against 28 μ_B

per formula unit ($4 \times g_J J[\mathrm{Eu}^{2+}]$) with a small hysteresis (Figure A.64; appendix), indicating ferromagnetism at low temperatures in line with the positive Weiss temperature $\Theta = 8.0(1)$ K.

Conclusion

The new compounds $\mathrm{SrSiAs_2}$, $\mathrm{EuSiAs_2}$, $\mathrm{SrGaSiAs_3}$, $\mathrm{EuGaSiAs_3}$, *mC*/*tI*-$\mathrm{Sr_4Ga_5SiAs_9}$, and *mC*/*tI*-$\mathrm{Eu_4Ga_5SiAs_9}$ contain T2-T4 supertetrahedra and expand the series of topologically hierarchical variants of the tetragonal $\mathrm{HgI_2}$ structure type. While $M\mathrm{SiAs_2}$ (T2) and $M\mathrm{GaSiAs_3}$ (T3) crystallize in the known $\mathrm{TlGaSe_2}$- and $\mathrm{RbCuSnS_3}$-type structures, respectively, the T4 compounds *mC*/*tI*-$M_4\mathrm{Ga_5SiAs_9}$ form new structure types. Their interlocking layered structures contain T4 supertetrahedra fused by one common tetrahedron. The two polytypes differ by their respective shifts of the adjacent supertetrahedral layers. The monoclinic type is shifted by $\tau = 1/3$ along (110), whereas the tetragonal type shows coinciding stacking of the layers with $\tau = 0$. The syntheses yielded mixtures of both polytypes. $\mathrm{Sr_4Ga_5SiAs_9}$ and $\mathrm{Eu_4Ga_5SiAs_9}$ exhibit indirect optical band gaps between 1.6 and 1.7 eV. Resistivity and Hall Effect measurements support their semiconducting nature with resistivity and charge carrier densities in the order of doped GaAs. Magnetization measurements confirm $\mathrm{Eu^{2+}}$ in $\mathrm{Eu_4Ga_5SiAs_9}$ and indicate weak ferromagnetism below $T = 2$ K.

Experimental section

Synthesis. The title compounds were obtained from stoichiometric mixtures of either SrAs/EuAs, Si and As for $M\mathrm{SiAs_2}$ or the respective elements for $M\mathrm{GaSiAs_3}$ and $M_4\mathrm{Ga_5SiAs_9}$ in alumina crucibles sealed in silica ampoules under an atmosphere of purified argon. The samples $M\mathrm{SiAs_2}$, $M\mathrm{GaSiAs_3}$ and $M_4\mathrm{Ga_5SiAs_9}$ were heated to $T = 1173$, 1223 and 1323 K, respectively, with a rate of 25 K h^{-1}, kept at this temperature for 60 h and cooled down to 973, 1023 and 1123 K, respectively, with a rate of 3 K h^{-1} after which the furnace was switched off. The reactions yielded deep red, for $M\mathrm{SiAs_2}$, and black, for $M\mathrm{GaSiAs_3}$ and $M_4\mathrm{Ga_5SiAs_9}$, lustre metallic shards. With increasing Si content, the compounds were increasingly sensitive to air and moisture. Therefore, all manipulations were conducted in an argon-filled glovebox.

Single crystal X-ray diffraction. Single crystal data were collected using a Bruker D8 Quest diffractometer (Mo Kα radiation, Photon-II detector). Intensity integration, data reduction, and absorption corrections were done with the programs APEX3[45] and SADABS.[46] Based on systemically absent reflections the space groups were determined with XPREP.[70] The crystal structures were solved with the Superflip package,[47, 48] and refined with the SHELXL package.[49]

Powder X-ray diffraction. Samples were filled and sealed in glass capillaries of 0.2 and 0.3 mm diameter (Hilgenberg GmbH) to avoid hydrolysis. The X-ray powder patterns were obtained with a STOE Stadi-P diffractometer (Mo Kα1/Cu Kα1 radiation, Ge(111)-monochromator, Mythen 1K detector) and were indexed and refined with models obtained from single-crystal data and database entries[71] using TOPAS.[72]

The deposition numbers CSD-1971148 ($SrSiAs_2$), 1971149 (*mC*-$Sr_4Ga_5SiAs_9$), 1971150 ($EuSiAs_2$), 1971151 ($SrGaSiAs_3$), 1971152 (*mC*-$Eu_4Ga_5SiAs_9$, SC), 1971153 (*tI*-$Eu_4Ga_5SiAs_9$), 1971154 ($EuGaSiAs_3$), and 1971155 (*tI*-$Sr_4Ga_5SiAs_9$, SC) contain the supplementary crystallographic data for this paper. These data are provided free of charge by the joint Cambridge Crystallographic Data Centre and Fachinformationszentrum Karlsruhe Access Structures service www.ccdc.cam.ac.uk/structures.

EDX measurements. Scanning electron microscopy was performed on a Carl Zeiss EVO-MA 10 instrument with SE and BSE detectors, which were controlled by the SmartSEM[51] software. The microscope was equipped with a Bruker Nano EDX detector (X-Flash detector 410-M) for EDX investigations using the QUANTAX 200[52] software to collect and evaluate the spectra. Elements contained in the sample holder, oxygen from partial hydrolysis and adhesive carbon pads were disregarded.

UV/Vis spectroscopy. Diffuse reflectance spectra of powder samples were measured with a Jasco V-650 UV/Vis spectrometer with radiation between 240 and 900 nm. Data were converted based on the Kubelka–Munk theory[54] and plotted as Tauc graphs.

Resistivity and Hall Effect measurements. Samples were pressed into pellets and sintered at $T = 1073$ K for 12 h in glassy carbon crucibles sealed in silica ampoules under an atmosphere of purified argon. Resistivity and Hall Effect measurements were conducted with a Quantum Design Inc. PPMS (physical property measurement system), equipped with a resistivity option, at $T = 300$ and 400 K with field strengths of ±30 kOe (1 kOe = 7.96×10^4 A m^{-1}). The samples were contacted with a four point Van der Pauw press contact by Wimbush. Data were collected with the PPMS MultiVu software package.[53]

Magnetization measurements. Magnetization isotherms and susceptibility measurements of powder samples were performed with a Quantum Design Inc. PPMS, equipped with a VSM (vibrating sample magnetometer) option, with field strengths of ±90 kOe and temperatures of 2-300 K. Data were collected with the PPMS MultiVu software package.[53]

References

[1] V. N. Soloviev, A. Eichhöfer, D. Fenske, U. Banin, *J. Am. Chem. Soc.* **2001**, *123*, 2354-2364.

[2] J. F. Corrigan, O. Fuhr, D. Fenske, *Adv. Mater.* **2009**, *21*, 1867-1871.

[3] H. Li, A. Laine, M. O'Keeffe, O. M. Yaghi, *Science* **1999**, *283*, 1145.

[4] P. Vaqueiro, S. Makin, Y. Tong, S. J. Ewing, *Dalton Trans.* **2017**, *46*, 3816-3819.

[5] Z.-Q. Li, C.-J. Mo, Y. Guo, N.-N. Xu, Q.-Y. Zhu, J. Dai, *J. Mater. Chem. A* **2017**, *5*, 8519-8525.

[6] C. Wang, Y. Li, X. Bu, N. Zheng, O. Zivkovic, C.-S. Yang, P. Feng, *J. Am. Chem. Soc.* **2001**, *123*, 11506-11507.

[7] C. Wang, X. Bu, N. Zheng, P. Feng, *J. Am. Chem. Soc.* **2002**, *124*, 10268-10269.

[8] L. Wang, T. Wu, F. Zuo, X. Zhao, X. Bu, J. Wu, P. Feng, *J. Am. Chem. Soc.* **2010**, *132*, 3283-3285.

[9] L. Wang, T. Wu, X. Bu, X. Zhao, F. Zuo, P. Feng, *Inorg. Chem.* **2013**, *52*, 2259-2261.

[10] P. Wagatha, P. Pust, V. Weiler, A. S. Wochnik, P. J. Schmidt, C. Scheu, W. Schnick, *Chem. Mater.* **2016**, *28*, 1220-1226.

[11] A. Haffner, T. Bräuniger, D. Johrendt, *Angew. Chem. Int. Ed.* **2016**, *55*, 13585-13588.

[12] A. Haffner, A.-K. Hatz, I. Moudrakovski, B. V. Lotsch, D. Johrendt, *Angew. Chem. Int. Ed.* **2018**, *57*, 6155-6160.

[13] X. Xu, W. Wang, D. Liu, D. Hu, T. Wu, X. Bu, P. Feng, *J. Am. Chem. Soc.* **2018**, *140*, 888-891.

[14] K. T. Y. Kauzlarich S.M., *Croat. Chem. Acta* **1991**, *64*, 343-352.

[15] J. Mathieu, R. Achey, J.-H. Park, K. M. Purcell, S. W. Tozer, S. E. Latturner, *Chem. Mater.* **2008**, *20*, 5675-5681.

[16] A. M. Goforth, H. Hope, C. L. Condron, S. M. Kauzlarich, N. Jensen, P. Klavins, S. MaQuilon, Z. Fisk, *Chem. Mater.* **2009**, *21*, 4480-4489.

[17] H. He, R. Stearrett, E. R. Nowak, S. Bobev, *Eur. J. Inorg. Chem.* **2011**, *2011*, 4025-4036.

[18] H. He, C. Tyson, M. Saito, S. Bobev, *J. Solid State Chem.* **2012**, *188*, 59-65.

[19] S. Stoyko, L. Voss, H. He, S. Bobev, *Crystals* **2015**, *5*, 433.

[20] E. Yablonovitch, O. D. Miller, S. R. Kurtz, in *2012 38th IEEE Photovoltaic Specialists Conference*, **2012**, pp. 001556-001559.

[21] K. K. N. Simon M. Sze, *Physics of Semiconductor Devices, Vol. 3*, John Wiley & Sons, Inc., New Jersey, **2006**.

[22] G. Varrall, *5G and Satellite Spectrum, Standards, and Scale*, Artech House, London, **2018**.

[23] D. Leonard, M. Krishnamurthy, C. M. Reaves, S. P. Denbaars, P. M. Petroff, *Appl. Phys. Lett.* **1993**, *63*, 3203-3205.

[24] M. L. Huggins, P. L. Magill, *J. Am. Chem. Soc.* **1927**, *49*, 2357-2367.

[25] M. Hostettler, H. Birkedal, D. Schwarzenbach, *Acta Crystallogr., Sect. B: Struct. Sci.* **2002**, *58*, 903-913.

[26] D. Müller, H. Hahn, *Z. Anorg. Allg. Chem.* **1978**, *438*, 258-272.

[27] B. Eisenmann, A. Hoffmann, *Z. Kristallogr.* **1991**, *195*, 318.

[28] J. Kim, T. Hughbanks, *J. Solid State Chem.* **2000**, *149*, 242-251.

[29] L. Kienle, V. Duppel, A. Simon, M. Schlosser, O. Jarchow, *J. Solid State Chem.* **2004**, *177*, 6-16.

[30] F. Q. Huang, B. Deng, D. E. Ellis, J. A. Ibers, *J. Solid State Chem.* **2005**, *178*, 2128-2132.

[31] A. Kumari, K. Vidyasagar, *Acta Crystallogr. Sect. E: Struct. Rep. Online* **2005**, *61*, i193-i195.

[32] D. Friedrich, M. Schlosser, A. Pfitzner, *Cryst. Growth Des.* **2016**, *16*, 3983-3992.

[33] D. Friedrich, M. Schlosser, A. Pfitzner, *Z. Anorg. Allg. Chem.* **2017**, *643*, 1589-1592.

[34] H. Lin, J.-N. Shen, L. Chen, L.-M. Wu, *Inorg. Chem.* **2013**, *52*, 10726-10728.

[35] H. C. Casey, D. D. Sell, K. W. Wecht, *J. Appl. Phys.* **1975**, *46*, 250-257.

[36] R. Bhat, P. S. Dutta, S. Guha, *J. Cryst. Growth* **2008**, *310*, 1910-1916.

[37] Y. I. Diakite, S. D. Traore, Y. Malozovsky, B. Khamala, L. Franklin, D. Bagayoko, *J. Mod. Phys.* **2016**, *8*, 531-546.

[38] M. Levinshtein, S. Rumyantsev, M. Shur, *Handbook Series on Semiconductor Parameters, Vol. 1*, 1 ed., World Scientific Pub Co Inc, Singapore, **1996**.

[39] M. Sharmin, S. Choudhury, N. Akhtar, T. Begum, *J. Bangladesh Acad. Sci.* **2012**, *36*, 97-107.

[40] T. C. Harman, H. L. Goering, A. C. Beer, *Phys. Rev.* **1956**, *104*, 1562-1564.

[41] F. Oswald, in *Z. Naturforsch., A: Phys. Sci., Vol. 10*, **1955**, p. 927.

[42] F. Stern, R. M. Talley, *Phys. Rev.* **1955**, *100*, 1638-1643.

[43] H. Lueken, *Magnetochemie*, Teubner, Wiebaden, Germany, **1999**.

[44] F. Tran, P. Blaha, *Phys. Rev. Lett.* **2009**, *102*, 226401.

[45] v2016.5-0 ed., Bruker AXS Inc., Madison, USA, **2016**.

[46] G. M. Sheldrick, Version 2012/1 ed., Bruker AXS Inc., Madison,USA, **2001**.

[47] L. Palatinus, G. Chapuis, *J. Appl. Crystallogr.* **2007**, *40*, 786-790.

[48] L. Palatinus, S. J. Prathapa, S. van Smaalen, *J. Appl. Crystallogr.* **2012**, *45*, 575-580.

[49] G. Sheldrick, *Acta Crystallogr., Sect. C: Struct. Chem.* **2015**, *71*, 3-8.

[50] A. Coelho, 4.1 ed., Coelho Software, Brisbane, Australia, **2007**.

[51] Version 5.07 Beta ed., Carl Zeiss Microscopy Ltd., Cambridge, UK, **2014**.

[52] Version 1.9.4.3448 ed., Bruker Nano GmbH, Berlin, Germany, **2013**.

[53] Version 1.5.11 ed., Quantum Design Inc., San Diego, USA, **2013**.

[54] P. Kubelka, F. Munk, *Z. Tech. Phys.* **1931**, *12*, 593-601.

[55] G. Kresse, J. Hafner, *Phys. Rev. B* **1994**, *49*, 14251-14269.

[56] G. Kresse, J. Furthmüller, *Comput. Mater. Sci.* **1996**, *6*, 15-50.

[57] P. E. Blöchl, *Phys. Rev. B* **1994**, *50*, 17953-17979.

[58] J. P. Perdew, K. Burke, M. Ernzerhof, *Phys. Rev. Lett.* **1996**, *77*, 3865-3868.

[59] R. F. W. Bader, *Atoms in Molecules - A Quantum Theory*, Oxford University Press, London, **1990**.

[60] G. Henkelman, A. Arnaldsson, H. Jónsson, *Comput. Mater. Sci.* **2006**, *36*, 354-360.

[61] M. O'Keeffe, M. Eddaoudi, H. Li, T. Reineke, O. M. Yaghi, *J. Solid State Chem.* **2000**, *152*, 3-20.

[62] H. Li, J. Kim, T. L. Groy, M. O'Keeffe, O. M. Yaghi, *J. Am. Chem. Soc.* **2001**, *123*, 4867-4868.

[63] G. Férey, *Angew. Chem. Int. Ed.* **2003**, *42*, 2576-2579.

[64] V. Weippert, A. Haffner, A. Stamatopoulos, D. Johrendt, *J. Am. Chem. Soc.* **2019**, *141*, 11245-11252.

[65] M. Döch, A. Hammerschmidt, S. Pütz, B. Krebs, *Phosphorus, Sulfur Silicon Relat. Elem.* **2004**, *179*, 933-935.

[66] M. Manos, R. Iyer, E. Quarez, J. Liao, M. Kanatzidis, *Angew. Chem. Int. Ed.* **2005**, *44*, 3552-3555.

[67] J. H. Liao, M. G. Kanatzidis, *Chem. Mater.* **1993**, *5*, 1561-1569.

[68] H. Li, C. D. Malliakas, Z. Liu, J. A. Peters, H. Jin, C. D. Morris, L. Zhao, B. W. Wessels, A. J. Freeman, M. G. Kanatzidis, *Chem. Mater.* **2012**, *24*, 4434-4441.

[69] H. Li, C. D. Malliakas, J. A. Peters, Z. Liu, J. Im, H. Jin, C. D. Morris, L.-D. Zhao, B. W. Wessels, A. J. Freeman, M. G. Kanatzidis, *Chem. Mater.* **2013**, *25*, 2089-2099.

[70] G. M. Sheldrick, Version 2008/2 ed., Bruker AXS Inc., Madison, USA, **2008**.

[71] P. Villars, K. Cenzual, *Pearson's Crystal Data - Crystal Structure Database for Inorganic Compounds*, ASM International, Ohio, USA, **2016/17**.

[72] A. Coelho, 6 ed., Coelho Software, Brisbane, Australia, **2016**.

4 High-pressure synthesis and crystal structure of $SrGa_4As_4$

Valentin Weippert and Dirk Johrendt

Published in: *Acta Crysallographica Section E* **2019**, *75*, 1643-1645.

Abstract

Strontium tetragallate(II,III) tetraarsenide, $SrGa_4As_4$, was synthesized in a Walker-type multianvil apparatus under high-pressure/high-temperature conditions of 8 GPa and 1573 K. The compound crystallizes in a new structure type ($P3_221$, $Z = 3$) as a three-dimensional (3D) framework of corner-sharing $SrAs_8$ quadratic antiprisms with strontium situated on a twofold rotation axis (Wyckoff position 3*b*). This arrangement is surrounded by a 3D framework which can be described as alternately stacked layers of either condensed $Ga^{III}As_4$ tetrahedra or honeycomb-like layers built up from distorted ethane-like $Ga^{II}_2As_6$ units comprising Ga–Ga bonds.

Chemical context

The ternary systems *A*–*Tr*–As (*A* = Ca, Sr or Ba; *Tr* = Ga or In) contain numerous compounds with different crystal structures based on $TrAs_4$ tetrahedra which occur isolated,[1] as dimers, as chains,[2, 3] condensed to ethane-like Tr_2As_6 groups[4-6] or as large supertetrahedral units.[7] $SrGa_4As_4$ is the first high-pressure compound in this system and contains an unprecedented layer-like framework, thus expanding the structural variety of the *A*–*Tr*–As family.

Structural Commentary

$SrGa_4As_4$ crystallizes in the space group $P3_221$ (No. 154) and constitutes a new structure type. Strontium is coordinated in a quadratic antiprismatic manner by eight As atoms (Figure 4.1a). The antiprisms are slightly distorted, with their quadratic planes twisted by ~34° relative to each other instead of 45° for an ideal quadratic antiprism. Sr–As distances range from 3.2665(4) to 3.4560(4) Å. The $SrAs_8$ polyhedra are connected through common corners, each As atom shared by two quadratic antiprisms, building up a three-dimensional (3D) framework. A similar structural motif is known for $RbAg_2SbS_4$, which crystallizes in the space group $P3_121$.[8] The surrounding construct in the two crystal structures differs however.

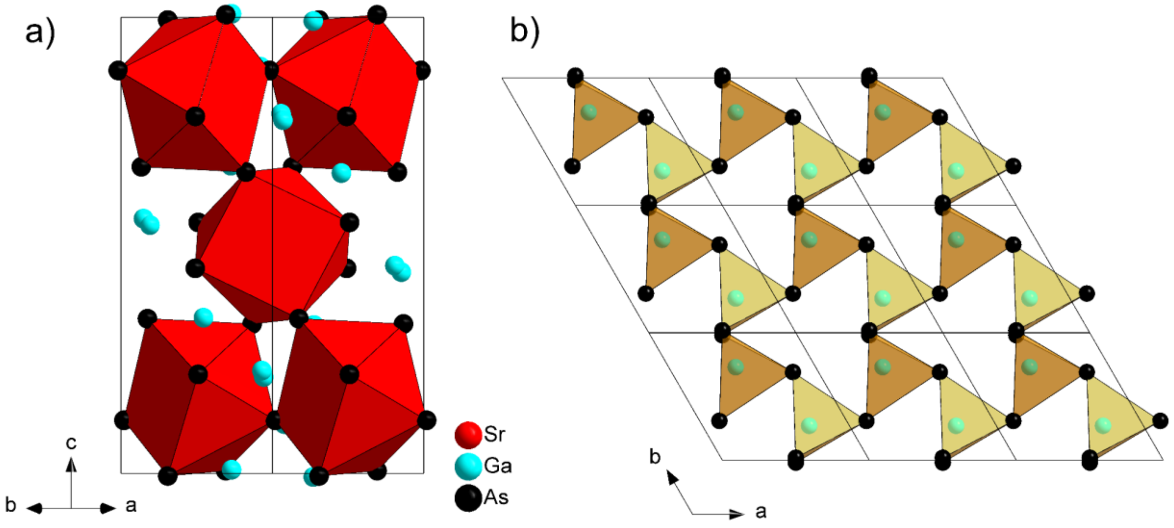

Figure 4.1: (a) The unit cell of $SrGa_4As_4$, viewed along $[\bar{1}\bar{1}0]$, with the quadratic antiprismatic strontium coordination spheres shown as red polyhedra. (b) Edge- and corner-sharing $GaAs_4$ tetrahedra forming a layer with triangular voids viewed along [001].

$SrGa_4As_4$ contains a 3D Ga/As framework that can be subdivided into two types of layers with an *AB* stacking sequence along the *c* axis. The first type is built up from corner- and edge-sharing $GaAs_4$ tetrahedra forming sheets with triangular voids (Figure 4.1b). The tetrahedra are distorted, with angles in the range of 100.790(19)–127.996(19)°, and have typical Ga–As distances of 2.4384(5)–2.5470(5) Å. The second layer type consists of distorted ethane-like Ga_2As_6 groups with nearly eclipsed conformations. The Ga_2As_6 groups are connected *via* common corners, forming a honeycomb-like sheet (Figure 4.2a).

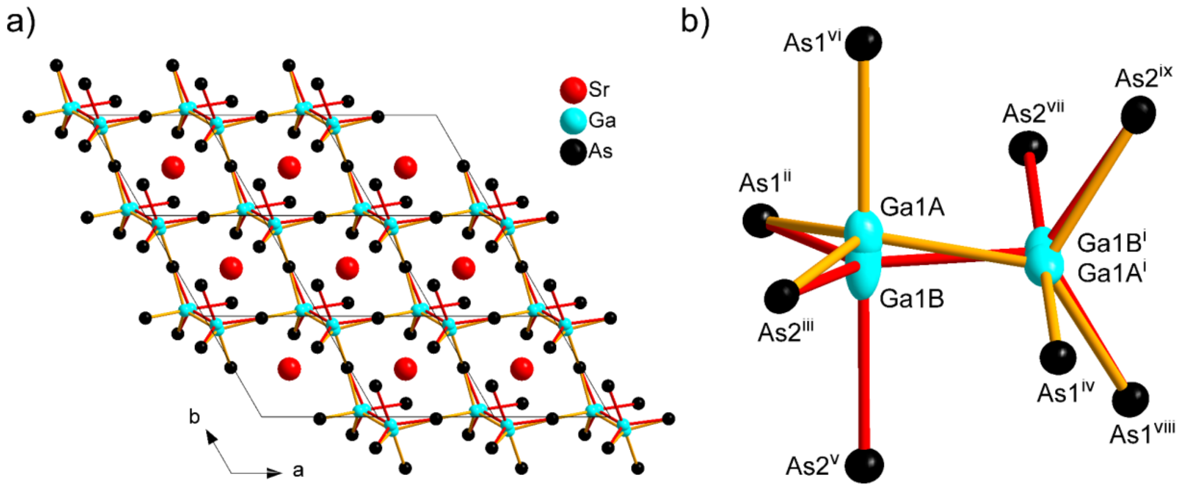

Figure 4.2: (a) Corner-sharing Ga_2As_6 dumbbells with disordered Ga positions forming a honeycomb-like layer viewed along [001]. (b) Ga_2As_6 groups with disordered Ga positions having an occupancy of 50%. Displacement ellipsoids are drawn at the 95 % probability level. [Symmetry codes: (i) $-x+2, -x+y+1, -z+\frac{5}{3}$; (ii) $y, x, -z+1$; (iii) $x, y+1, z+1$; (iv) $y+1, x+1, -z+1$; (v) $y+1, x, -z+1$; (vi) $-y+1, x-y+1\ z+\frac{2}{3}$; (vii) $-y+1, x-y, z+\frac{2}{3}$; (viii) $-y+2, x-y+1, z+\frac{2}{3}$; (ix) $-x+2, -x+y+2, -z+\frac{2}{3}$.]

The Ga1*A* and Ga1*B* positions of the Ga–Ga dumbbell are disordered and were treated with split positions having an occupancy of 50 % each (Figure 4.2b). The coordination of each of these Ga sites consists of three As atoms and one Ga atom forming trigonal pyramids, showing torsion angles of 114.5(1)° for As1^{vi}–Ga1*A*–Ga1*A*^{i}–As1^{iv} and 119.3(1)° for As2^{v}–Ga1*B*–Ga1*B*^{i}–As2^{vii} (for symmetry codes, see Figure 4.2b). The Ga–Ga distances range between 2.542(8) and 2.572(8) Å and are considered as Ga–Ga bonds, which is consistent with a charge-neutral compound. Ga–As distances between 2.477(4) and 2.694(2) Å for Ga1*A* are near to the covalent radii sum of 2.46 Å.[9] In comparison, the trigonal pyramid around Ga1*B* is elongated, with Ga–As distances of 2.415(4)–2.845(2) Å.

Synthesis and Crystallization

The starting material SrAs was synthesized by heating stoichiometric amounts of Sr (Sigma–Aldrich, 99.95 %) and As (Alfa Aesar, 99.99999+ %) in an alumina crucible, sealed in a silica ampule under an atmosphere of purified argon for 20 h at 1223 K. The title compound was obtained *via* high-pressure synthesis using a modified Walker-type multianvil set-up driven by a 1000 t hydraulic press (Voggenreiter, Mainleus, Germany). A Cr_2O_3-substituted (6 %) MgO octahedron (Ceramic Substrates & Components, Isle of Wight, UK) with an edge length of 18 mm, housing a ZrO_2 sleeve with graphite sleeves (Schunk, Heuchelheim, Germany) for heating and a h-BN crucible (Henze, Kempten, Germany), was compressed with tungsten carbide cubes (Hawedia, Marklkofen, Germany) with an edge length of 11 mm. The starting materials SrAs (73.4 mg, 0.452 mmol), Ga (66.5 mg, 0.953 mmol, Alfa Aesar, 99.999%) and As (60.1 mg, 0.802 mmol) were mixed in a glove-box (H_2O, O_2 <1 ppm) and filled into the octahedron assembly. The reaction was carried out at 8 GPa and 1573 K, with a dwell time of 3 h. The temperature was increased and decreased over a period of 1 h. The assembly was opened in a glove-box, revealing crystals with a metallic luster.

The composition of $SrGa_4As_4$ was verified by EDX measurements using a Carl Zeiss EVO-MA 10 instrument with a Bruker Nano EDX detector. The experimental values [Sr 12(1) at%, Ga 44(2) at% and As 45 (1) at%] are in excellent agreement with the expected values (Sr 11.1 at%, Ga 44.4 at% and As 44.4 at%) within the typical error of the method, and confirm the composition obtained from single-crystal X-ray diffraction data.

Refinement

Crystal data, data collection and structure refinement details are summarized in Table 4.1. Detailed data, atomic positions, anisotropic displacement parameters as well as geometric parameters are given in the appendix (Tables A.81-A.84). The Ga1*A* and Ga1*B* positions were introduced as half-occupied split positions since one fully occupied position with a prolate ellipsoid caused residual densities in the order of 2.2 eÅ^{-3}. Upon exclusion of the Ga1*A*/Ga1*B* positions, the contour difference map in PLATON[10] shows two clearly separated maxima justifying this approach. Structural data were standardized with STRUCTURE-TIDY.[11]

Table 4.1: Single crystal data of $SrGa_4As_4$.

Formula	$SrGa_4As_4$
space group	$P3_221$ (No. 154)
a / Å	6.3615(1)
c / Å	16.5792(2)
V_{cell} / Å^3	581.05(2)
Z	3
$\rho_{X\text{-}Ray}$ / g·cm^{-3}	5.711
R_σ / R_{int}	0.0135 / 0.0337
R_1 ($F^2 > 2\sigma(F^2)$) / all	0.0116 / 0.0120
wR_2 ($F^2 > 2\sigma(F^2)$) / all	0.0253 / 0.0254
GooF	1.172
$\Delta\rho_{max/min}$ / eÅ^{-3}	+0.51 / -0.69

References

[1] K. T. Y. Kauzlarich S.M., *Croat. Chem. Acta* **1991**, *64*, 343-352.

[2] S. Stoyko, L. Voss, H. He, S. Bobev, *Crystals* **2015**, *5*, 433.

[3] H. He, C. Tyson, M. Saito, S. Bobev, *J. Solid State Chem.* **2012**, *188*, 59-65.

[4] J. Mathieu, R. Achey, J.-H. Park, K. M. Purcell, S. W. Tozer, S. E. Latturner, *Chem. Mater.* **2008**, *20*, 5675-5681.

[5] A. M. Goforth, H. Hope, C. L. Condron, S. M. Kauzlarich, N. Jensen, P. Klavins, S. MaQuilon, Z. Fisk, *Chem. Mater.* **2009**, *21*, 4480-4489.

[6] H. He, R. Stearrett, E. R. Nowak, S. Bobev, *Eur. J. Inorg. Chem.* **2011**, *2011*, 4025-4036.

[7] V. Weippert, A. Haffner, A. Stamatopoulos, D. Johrendt, *J. Am. Chem. Soc.* **2019**, *141*, 11245-11252.

[8] G. L. Schimek, W. T. Pennington, P. T. Wood, J. W. Kolis, *J. Solid State Chem.* **1996**, *123*, 277-284.

[9] L. Pauling, *The Nature of the Chemical Bond, Vol. 260*, Cornell university press, Ithaca, NY, **1960**.

[10] A. Spek, *Acta Crystallogr. Sect. D. Biol. Crystallogr.* **2009**, *65*, 148-155.

[11] L. M. Gelato, E. Parthe, *J. Appl. Crystallogr.* **1987**, *20*, 139-143.

5 Summary

This thesis adds numerous new compounds to the system *M*-Ga/Ge-As (*M* = Rb, Cs, Sr, Ba, Eu), which has not been comprehensively studied to date. A special focus was on compounds with low metal contents, resulting in unprecedented structure types or advancing into fields largely dominated by chalcogenides, with only sparse examples of small band gap semiconductors like the ones presented here. The determination of the intricate structures through single crystal X-ray diffraction presented multiple challenges arising from occupational- and static-disorder, similar atom scattering factors or stacking faults. They were solved with the assistance of SAED and elemental analysis. A wide range of analytical methods like high temperature PXRD, UV-Vis-NIR spectroscopy, resistivity-, Hall-effect- and susceptibility-measurements was utilized. DFT calculations were employed to support these findings, as well as explore electronic structures and transport properties. Altogether they revealed small bandgap semiconductors as well as favorable properties for thermoelectric applications in some compounds.

Mixed Valence and Unusual Germanium Coordination in $SrGe_8As_{10}$, $BaGe_8As_{10}$, and $BaGe_7P_{12}$

The isotypic $SrGe_8As_{10}$ and $BaGe_8As_{10}$ crystallize in a new structure type in the space group *Cmce*. They were obtained from a multi-step solid-state synthesis with only minor impurities. The structure was determined by single crystal X-ray diffraction and consists of $Ge^{+2}As_3$ trigonal pyramids, $(Ge^{+3})_2As_6$ dumbbells and $Ge^{+4}As_4$ tetrahedra. Linked via common vertices and As-As bonds they form a 3D network, thus icosahedrally enclosing strontium or barium. $BaGe_7P_{12}$ crystallizes in the space group $R\overline{3}$ and was obtained from multi-step solid-state synthesis, however small amounts of phosphorus needed to be added after each step. DFT calculations predicted indirect band gaps of 0.43 and 0.57 eV for the strongly covalent $SrGe_8As_{10}$ and $BaGe_8As_{10}$ and 1.47 eV for $BaGe_7P_{12}$ with a more ionic character. Their respective bonding situation was evaluated with Bader charge and ELF calculations. Either resistivity or UV-Vis measurements confirmed those values.

$BaGe_8As_{14}$: a semiconducting sodalite type compound

$BaGe_8As_{14}$ represents the first Ge-As based sodalite type compound. It is easily obtained as a phase pure sample from the elements at 873 K through multiple sintering steps. The sodalite cage is comprised of $GeAs_4$ tetrahedra with a statistically occupied $Ge_{0.5}/As_{0.5}$ position residing in the 6er rings of the cage. This disorder was supported through SAED, with none of the required reflections present for an ordered variant. Temperature dependent single crystal X-ray diffraction revealed a static disorder or “rattling” of the central barium atom. A semiconducting nature of $BaGe_8As_{14}$

was determined from optical and electrical properties with a small indirect band gap (0.43 eV), low resistivity ($2.2 \cdot 10^{-2}$ Ω cm) and high carrier concentration ($1.6 \cdot 10^{20}$ cm^{-3}) at 300 K. These results were supported via DFT calculations, which also indicated a strong covalent character of the sodalite framework.

High thermoelectric properties in the sodalite compounds $BaGe_8As_{14}$ and AGe$_7$As$_{15}$ (A = Rb, Cs)

$RbGe_7As_{15}$ and $CsGe_7As_{15}$ have been synthesized and their structures determined by single-crystal X-ray diffraction and STEM-HAADF/EDX. They crystallize with a cubic sodalite-type structure in the space group $I\bar{4}3m$ isotypic to $BaGe_8As_{14}$. Rubidium and caesium are highly coordinated by 16 arsenic or germanium atoms and perfectly fit into the sodalite-cage due to their bigger ionic radii compared to barium, which is displaced from the center. The compounds are narrow-band p-type semiconductors with electrical conductivities of $1.2\text{-}3 \cdot 10^4$ S/m at 300 K and carrier densities of $1\text{-}2 \cdot 10^{20}$ cm^{-1}. First principles DFT calculations give clear evidence of ultralow lattice thermal conductivity around 0.5 Wm^{-1}K^{-1} in $BaGe_8As_{14}$ due to the position disorder of the barium atoms and the anharmonicity of its thermal movement. Frozen phonon calculations indicate that rattling probably decreases the lattice thermal conductivity of $BaGe_8As_{14}$ even further. These effects are chemically switched off in $RbGa_7As_{15}$ with a parabolic potential and no signs of rattling, leading to a four times higher lattice thermal conductivity. The calculated transport properties agree with the measured data, and their combination predicts a thermoelectric efficiency ZT up to 2.7 for $BaGe_8As_{14}$, reaching the value of current record materials.

Supertetrahedral Layers Based on GaAs or InAs

Several new supertetrahedral compounds based on either GaAs or InAs were discovered. They are hierarchical extensions of tetragonal HgI_2 and crystallize in the space group $C2/c$ with saw-tooth like interlocking layers. With $M_3Ga_6As_8$ (M = Sr, Eu), the first T6 supertetrahedral compounds were presented, requiring neither mixed metal strategies for charge compensation nor organic spacers for stabilization. The T6 supertetrahedra units of each layer are fused via common T2 supertetrahedra. Stacking with different shifts of the layers relative to each other results in two different polymorphs with different monoclinic angles. Similar circumstances were found for the T5 compounds $M_{15}Tr_{22}As_{32}$ (M = Sr, Eu; Tr = Ga, In). Their T5 supertetrahedra are fused via common tetrahedra and form two polymorphs as well. This polymorphism is the source of some serious stacking faults in the T6 compounds but less for the T5 compounds. All compounds exhibit direct bandgaps of similar magnitude compared to GaAs or InAs, which was exemplary confirmed with DFT calculations for $Sr_3Ga_6As_8$. All compounds displayed low electrical resistivities between 1.3-5.0 Ω cm and Hall effect measurements indicated p-type semiconducting behavior with carrier concentrations between 10^{16}-10^{19} cm^{-3}. Magnetization measurements indicate an antiferromagnetic ordering below $T = 10$ K and confirm Eu^{2+} in all europium-containing compounds.

New layered supertetrahedral compounds T2-$MSiAs_2$, T3-$MGaSiAs_3$ and polytypic T4-$M_4Ga_5SiAs_9$ (M = Sr, Eu)

Through systematic synthesis attempts based on the T5 and T6 compounds in Chapter 3.1, the compounds T2-$MSiAs_2$, T3-$MGaSiAs_3$ and T4-*mC*-/*tI*-$M_4Ga_5SiAs_9$ (M = Sr, Eu) were discovered. Together they form a hierarchical family of layered supertetrahedral compounds ranging from small vertex sharing T2 units up to large fused T6 entities. Owed to the increased surface to volume ratio and subsequent increased negative charge density of smaller supertetrahedra, Ga^{3+} had to be replaced incrementally with Si^{4+}. The compounds T2-$MSiAs_2$ and T3-$MGaSiAs_3$ are isotypic to known structure types and thus were refined from powder X-ray diffraction data. Due to their small size and therefore limited possibilities to shift adjacent supertetrahedral layers relative to each other, they do not form polymorphs. T4-$M_4Ga_5SiAs_9$ on the other hand forms two new structure types with a tilted monoclinic polymorph and a tetragonal polymorph with coinciding layers. Contrary to the T5 and T6 compounds, they exhibit indirect optical bandgaps of 1.6-1.7 eV and magnetization measurements for $EuGa_5SiAs_9$ indicate a weak ferromagnetic ordering below T = 2 K.

High-pressure synthesis and crystal structure of $SrGa_4As_4$

The attempt to expand the aforementioned supertetrahedral family by adding high pressure to the equation and creating even larger T7 supertetrahedra, resulted in the compound $SrGa_4As_4$. The synthesis at 1573 K and 8 GPa in a modified Walker-type multianvil press yielded black crystals with a metallic luster. $SrGa_4As_4$ crystallizes in the chiral space group $P3_221$ with a 3D network comprised of $GaAs_4$ tetrahedra, Ga_2As_6 dumbbells with a disordered Ga position and corner sharing $SrAs_8$ quadratic antiprisms. The structure was determined through single crystal X-ray diffraction and the chemical composition confirmed with EDX.

6 Conclusion

This thesis shows that explorative research in a rather neglected system, namely M-Ga/Ge-As, can yield an astonishing variety of new compounds with intriguing properties. A new branch in this field was found by using lower fractions of alkaline or alkaline earth metals as in earlier studies with elements known to form polyanionic networks, like Ga/Ge-As.

Intricate 3D networks were found in $AE\mathrm{Ge}_8\mathrm{As}_{10}$ (AE = Sr, Ba) and $\mathrm{BaGe}_7\mathrm{P}_{12}$ with the first example of germanium in three different oxidation states and sixfold coordinated in an unusual GeP_6 motif. Upon utilizing other elements like alkaline metals or lighter and heavier elemental homologues like silicon or antimony, this field could yield a large number of new compounds.

The sodalite compounds $\mathrm{BaGe}_8\mathrm{As}_{14}$ and $A\mathrm{Ge}_7\mathrm{As}_{15}$ (A = Rb, Cs) on the other hand demonstrated that it is not of the utmost importance to provide new structure-types but rather revisit well established ones, albeit with different elements. DFT studies were performed on the notion that the underlying structural features of these compounds, disorder, anharmonicity, and rattling along with low electrical resistivities, are in favor of good thermoelectric properties. Indeed the calculations resulted in overwhelming predictions like ultralow lattice thermal conductivity and up to $ZT = 2.7$ in $\mathrm{BaGe}_8\mathrm{As}_{14}$. Of course these results need to be experimentally verified in future studies, but a well established DFT procedure can be used as a good indicator and helps through a better understanding of underlying mechanisms.

The supertetrahedral hierarchical family ranging from T2 to T6 supertetrahedra is a unique way to confine GaAs or a hypothetical SiAs to well defined nanocluster-like units. Although almost all these supertetrahedral compounds suffer from stacking faults making the structure determination rather difficult, this disorder could also have some merit for possible thermoelectric properties by acting as scattering centers to phonons or invoke quantum dot effects. Future studies are necessary to determine this possibility.

In the end, the exploration of the system M-Ga/Ge-As yielded a multitude of compounds with a lot of potential for real world application and a lot more potential to explore.

A Appendix

A.1 Mixed Valence and Unusual Germanium Coordination in $SrGe_8As_{10}$, $BaGe_8As_{10}$, and $BaGe_7P_{12}$

Table A.1: Detailed single crystal diffraction data of $SrGe_8As_{10}$ and $BaGe_8As_{10}$.

formula	$SrGe_8As_{10}$	$BaGe_8As_{10}$
space group	*Cmce* (No. 64)	*Cmce* (No. 64)
a / Å	14.5614(7)	14.5799(3)
b / Å	10.6452(6)	10.7164(2)
c / Å	11.4283(5)	11.5518(2)
V_{cell} / $Å^3$	1771.49(15)	1804.90(6)
Z	4	4
$\rho_{X\text{-ray}}$ / g cm^{-3}	5.315	5.400
crystal size / mm	0.064 x 0.048 x 0.018	0.141 x 0.047 x 0.033
diffractometer	Bruker D8 QUEST	
radiation type (λ / nm)	Mo Kα (0.71073)	
T / K	293	
μ / mm^{-1}	34.872	33.440
F(000)	2496	2568
Θ-range / °	5.931 – 61.076	5.890 – 60.980
hkl range	$-20 \leq h \leq 19$; $k \leq \pm15$; $l \leq \pm16$	$h \leq \pm19$; $k \leq \pm15$; $l \leq \pm16$
refl. measured	16410	29495
independent refl.	1402	1373
parameters	49	50
R_σ / R_{int}	0.0304 / 0.0614	0.0200 / 0.0630
R_1 ($F^2 > 2\sigma(F^2)$) / all	0.0262 / 0.0372	0.0165 / 0.0230
wR_2 ($F^2 > 2\sigma(F^2)$) / all	0.0474 / 0.0503	0.0310 / 0.0335
GooF	1.126	1.119
$\Delta\rho_{max/min}$ / $eÅ^{-3}$	+1.252 / -1.547	+0.846 / -1.029

Table A.2: Atomic coordinates and equivalent displacement parameters ($Å^2$) $SrGe_8As_{10}$ from single crystal data.

atom	Wyckoff	*x*	*y*	*z*	U_{eq}
Sr1	4a	0	0	0	0.0302(2)
Ge1	16g	0.12748(3)	0.43658(4)	0.08832(4)	0.00986(10)
Ge2	8f	0	0.22784(6)	0.30155(6)	0.01243(14)
Ge3	8e	0.25	0.19641(6)	0.25	0.00978(13)
As1	16g	0.11490(3)	0.06440(4)	0.23495(4)	0.01120(10)
As2	16g	0.27674(3)	0.32871(4)	0.07460(4)	0.01103(10)
As3	8f	0	0.28889(6)	0.08742(5)	0.01048(12)

Table A.3: Anisotropic displacement parameters (Å^2) of $SrGe_8As_{10}$ from single crystal data.

atom	U_{11}	U_{22}	U_{33}	U_{23}	U_{13}	U_{12}
Sr1	0.0421(6)	0.0295(6)	0.0189(5)	-0.0133(4)	0	0
Ge1	0.0102(2)	0.0088(2)	0.0106(2)	0.00062(16)	0.00097(15)	0.00055(15)
Ge2	0.0120(3)	0.0149(3)	0.0105(3)	0.0014(2)	0	0
Ge3	0.0088(3)	0.0109(3)	0.0096(3)	0	-0.0003(2)	0
As1	0.0100(2)	0.0119(2)	0.0117(2)	0.00137(17)	-0.00185(14)	-0.00103(16)
As2	0.0119(2)	0.0108(2)	0.0104(2)	-0.00029(15)	-0.00055(15)	0.00142(15)
As3	0.0109(3)	0.0090(3)	0.0115(3)	0.0005(2)	0	0

Table A.4: Atomic coordinates and equivalent displacement parameters (Å^2) $BaGe_8As_{10}$ from single crystal data.

atom	Wyckoff	x	y	z	U_{eq}
Ba1	4a	0	0	0	0.01841(9)
Ge1	16g	0.12780(2)	0.43885(3)	0.08814(2)	0.00972(7)
Ge2	8f	0	0.22897(4)	0.30256(4)	0.01284(10)
Ge3	8e	0.25	0.20017(4)	0.25	0.00972(9)
As1	16g	0.11637(2)	0.06748(3)	0.23842(2)	0.01079(7)
As2	16g	0.27598(2)	0.32922(3)	0.07424(2)	0.01110(7)
As3	8f	0	0.29373(4)	0.09062(3)	0.01017(8)

Table A.5: Anisotropic displacement parameters (Å^2) of $BaGe_8As_{10}$ from single crystal data.

atom	U_{11}	U_{22}	U_{33}	U_{23}	U_{13}	U_{12}
Ba1	0.0248(2)	0.01806(17)	0.01242(17)	-0.00575(13)	0	0
Ge1	0.01008(14)	0.00915(14)	0.00992(14)	0.00052(10)	0.00104(10)	0.00039(10)
Ge2	0.0118(2)	0.0148(2)	0.0118(2)	0.00127(15)	0	0
Ge3	0.00807(19)	0.01156(19)	0.00953(19)	0	-0.00034(14)	0
As1	0.00935(14)	0.01231(14)	0.01070(14)	0.00107(10)	-0.00196(10)	-0.00146(10)
As2	0.01121(14)	0.01131(13)	0.01079(14)	-0.00010(10)	-0.00040(10)	0.00125(10)
As3	0.01030(18)	0.00877(17)	0.01144(19)	-0.00012(14)	0	0

Table A.6: Detailed powder X-ray diffraction data of $BaGe_7P_{12}$ from Rietveld refinement.

formula	$BaGe_7P_{12}$
space group	$R\overline{3}$ (No. 148)
a / Å	12.630883(32)
c / Å	9.247182(43)
V_{cell} / Å^3	1277.637(9)
Z	3
$\rho_{X\text{-}ray}$ / g cm^{-3}	3.96729
diffractometer	Stoe Stadi P
radiation type (λ / nm)	Cu Kα1 (1.54056)
T / K	293
μ / mm^{-1}	41.672729
F(000)	1380
2Θ-range / °	5.000 - 92.420
refl. measured	251

parameters	23
background parameter	14
R_p / R_{wp}	2.099 / 2.762
R_{exp} / R_{Bragg}	2.484 / 0.980
GooF	1.112

Table A.7: Atomic coordinates and isotropic displacement parameters B_{iso} (Å^2; $B_{iso} = 8*\pi^2*U_{iso}$) of $BaGe_7P_{12}$ from Rietveld refinement.

atom	Wyckoff	x	y	z	B_{iso}
Ba1	3b	0	0	0.5	2.09(5)
Ge1	18f	0.30323(12)	0.06508(10)	0.11946(11)	1.13(3)
Ge2	3a	0	0	0	1.20(7)
P1	18f	0.06724(30)	0.17276(23)	0.18339(24)	1.10(8)
P2	18f	0.23796(20)	0.34108(22)	0.12833(23)	1.18(8)

Table A.8: *AE*-As and *AE*-Ge distances of the $AEAs_{10}Ge_2$ icosahedra, cell volume, ionic radii and their respective differences of $AEGe_8As_{10}$.

	count	$d_{Sr\text{-}As/Ge}$ (Å) / volume (Å^3) / $r_{Sr(II)}$ (pm)	$d_{Ba\text{-}As/Ge}$ (Å) / volume (Å^3) / $r_{Ba(II)}$ (pm)	Δ (%)
As1	4x	3.2371(5)	3.3147(3)	2.4
As2	4x	3.8237(5)	3.8410(3)	0.5
As3	2x	3.2335(7)	3.3172(4)	2.6
Ge2	2x	3.6793(7)	3.6930(4)	0.4
volume		1771.49(15)	1804.90(6)	1.9
AE		118	135	14.4

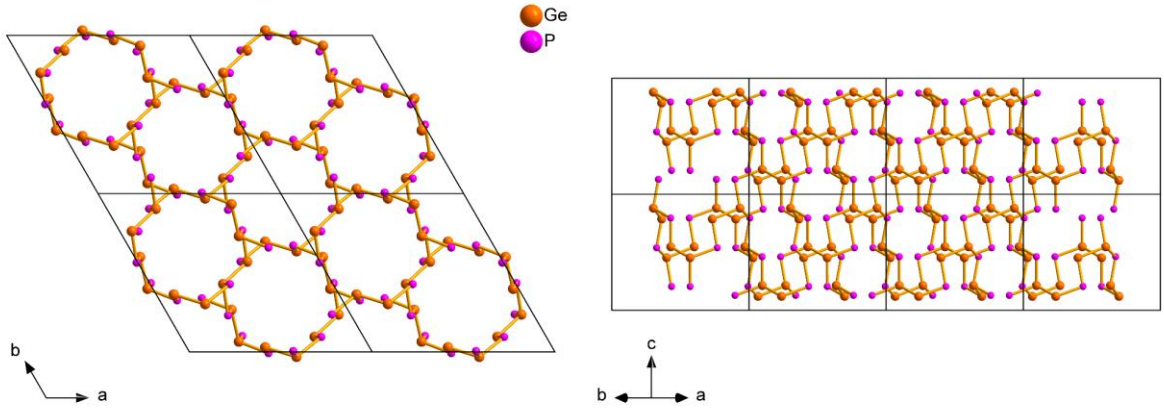

Figure A.1: 2x2x2 supercell of $BaGe_7P_{12}$ showing the interconnected 12er ring arrangements composed of Ge_2P_6 dumbbells along the *c*-axis (left) and along (110) (right).

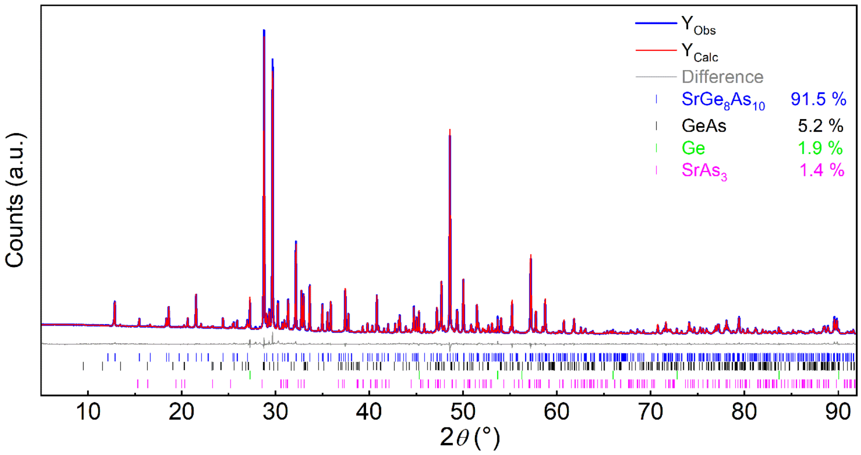

Figure A.2: X-ray powder diffraction pattern (Y_{obs}, Cu Kα1), Rietveld fit (Y_{calc}) and difference curve (grey) of $SrGe_8As_{10}$ and GeAs, Ge and $SrAs_3$ as minor side phases.

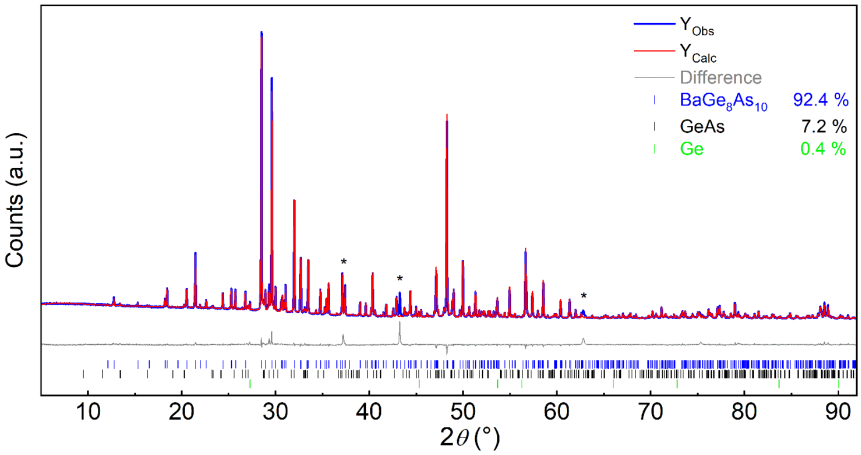

Figure A.3: X-ray powder diffraction pattern (Y_{obs}, Cu Kα1), Rietveld fit (Y_{calc}) and difference curve (grey) of $BaGe_8As_{10}$ and GeAs and Ge as minor side phases. An unknown phase is marked with asterisks.

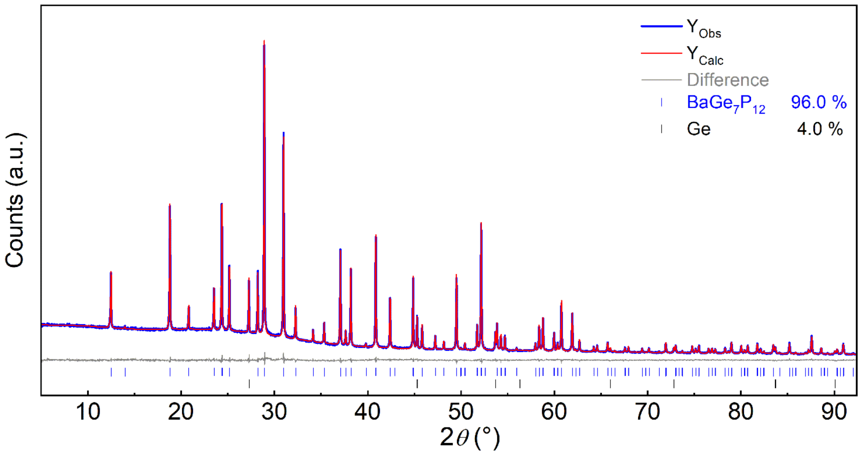

Figure A.4: X-ray powder diffraction pattern (Y_{obs}, Cu Kα1), Rietveld fit (Y_{calc}) and difference curve (grey) of $BaGe_7P_{12}$ and Ge as a minor side phase.

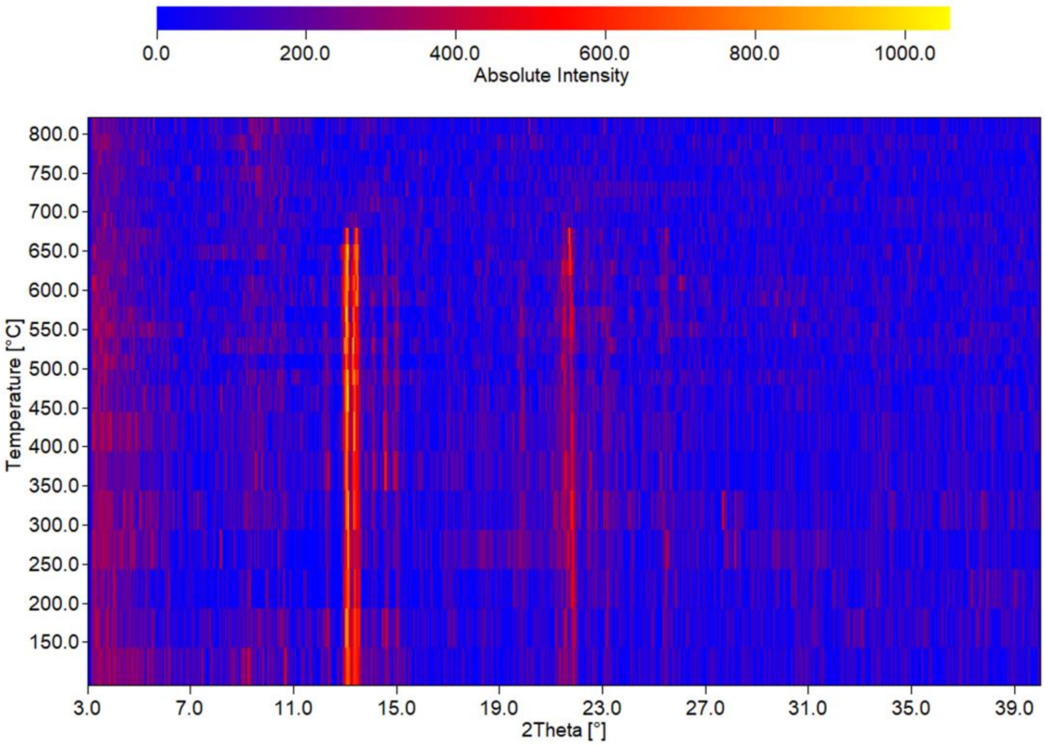

Figure A.5: High Temperature X-ray powder diffraction patterns (Mo Kα1) of $SrGe_8As_{10}$ between 393 K and 1083 K with steps of 50 K for 393 K ≤ T ≤ 773 K and 20 K for 773 K ≤ T ≤ 1083 K. Intensities of $SrGe_8As_{10}$ decreasing for T ≥ 923 K. The overall low intensities are owed to the strong fluorescence of Sr, Ge and As in Mo Kα1 radiation.

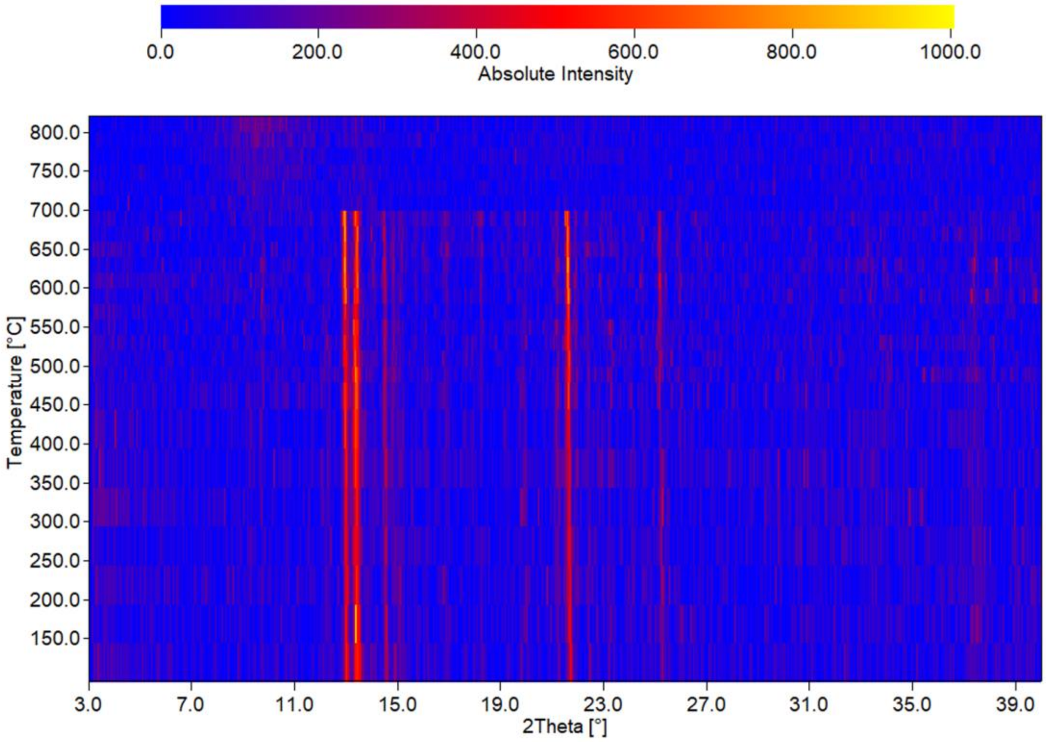

Figure A.6: High Temperature X-ray powder diffraction patterns (Mo Kα1) of $BaGe_8As_{10}$ between 393 K and 1173 K with steps of 50 K for 393 K ≤ T ≤ 1083 K and 20 K for 773 K ≤ T ≤ 1083 K. Intensities of $BaGe_8As_{10}$decreasing for T ≥ 943 K. The overall low intensities are owed to the strong fluorescence of Ba, Ge and As in Mo Kα1 radiation.

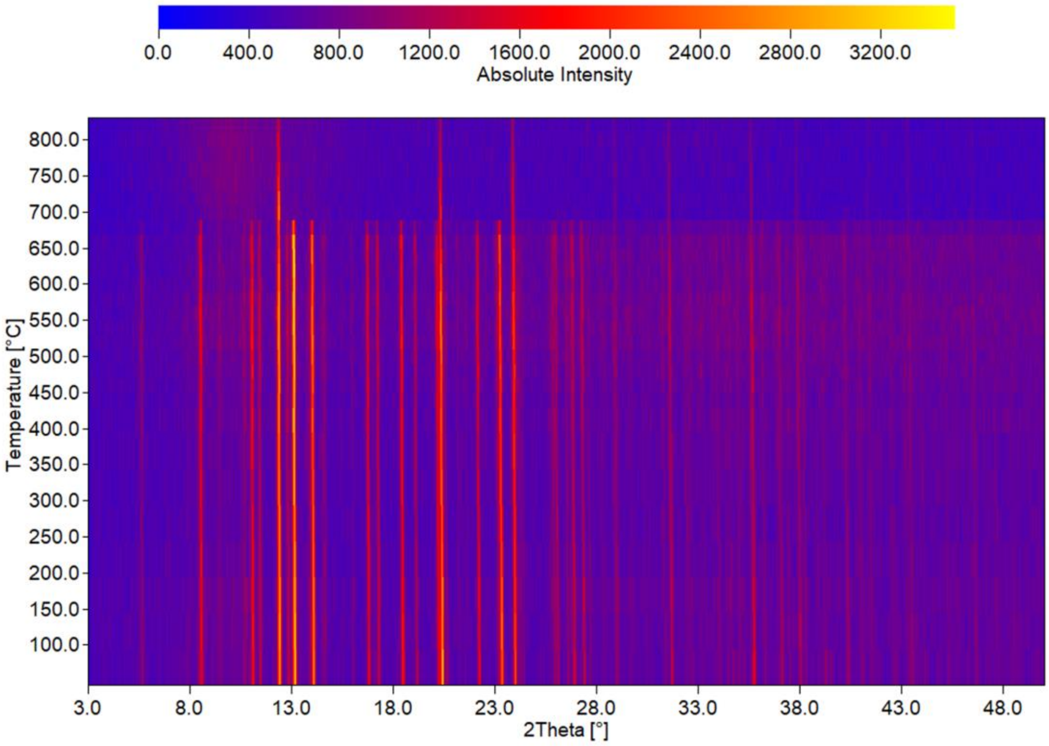

Figure A.7: High Temperature X-ray powder diffraction patterns (Mo Kα1) of $BaGe_7P_{12}$ between 343 K and 1173 K with steps of 50 K for 343 K ≤ T ≤ 773 K and 20 K for 773 K ≤ T ≤ 1173 K. Intensities of $BaGe_7P_{12}$ decreasing for T ≥ 953 K.

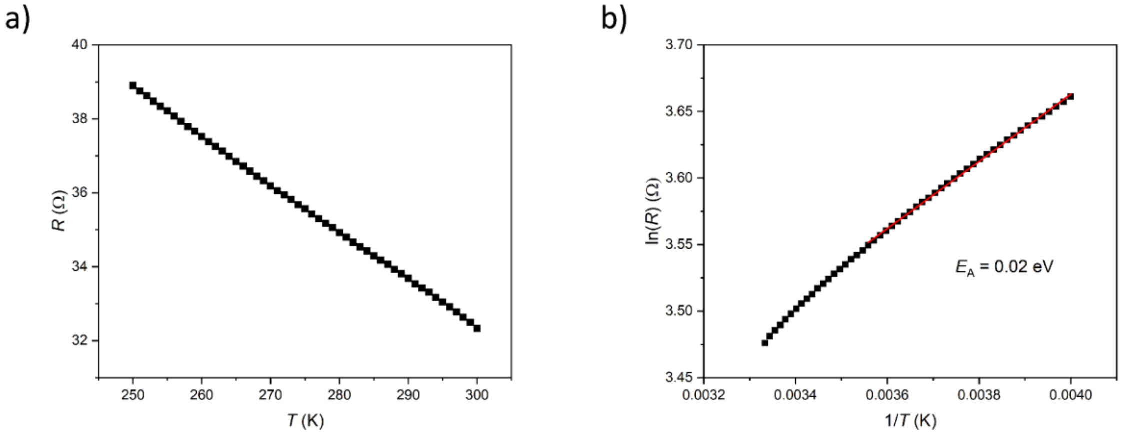

Figure A.8: (a) Resistivity of $BaGe_7P_{12}$ between 250 K and 300 K showing extrinsic semiconducting behaviour. (b) Arrhenius plot of the resistivity of $BaGe_7P_{12}$ showing a band gap of 0.02 eV.

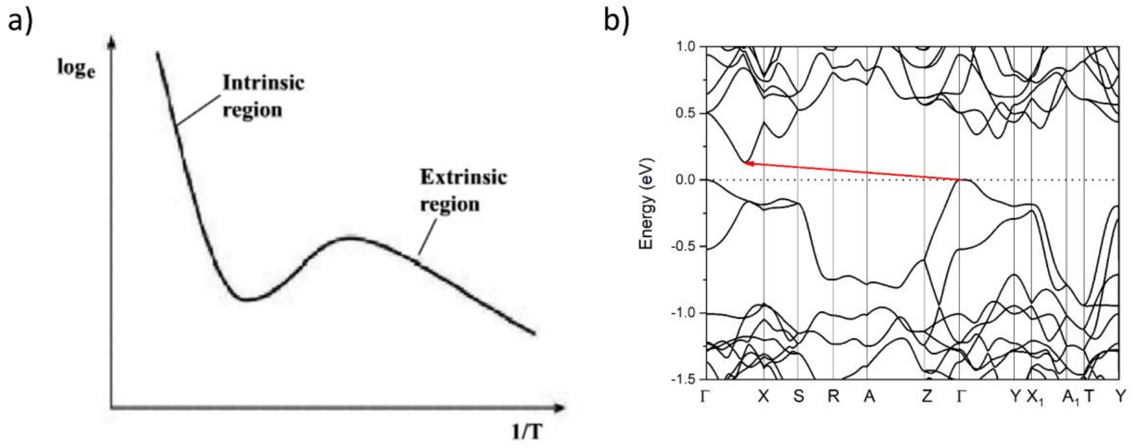

Figure A.9: (a) Intrinsic region and extrinsic region of a semiconductor.[1] (b) Band structure of $SrGe_8As_{10}$ indicating an indirect band gap (red arrow).

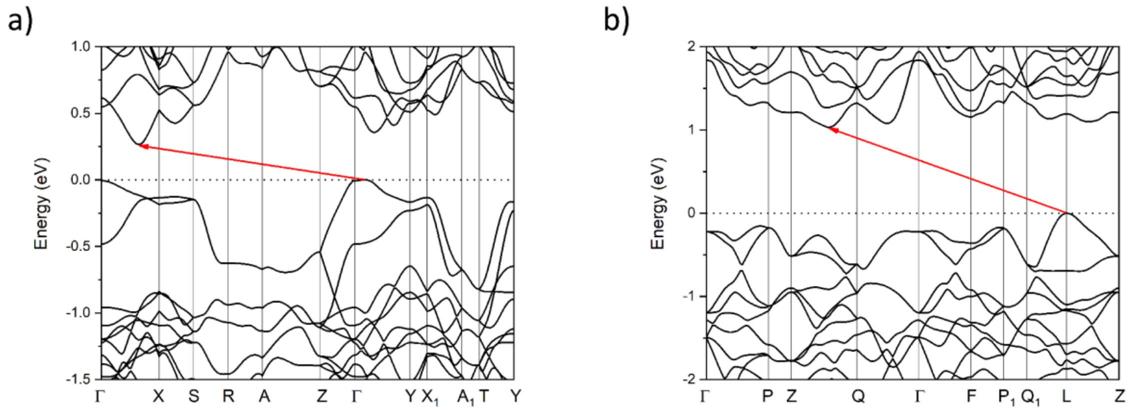

Figure A.10: Band structures of (a) $BaGe_8As_{10}$ and (b) $BaGe_7P_{12}$. Both indicate an indirect band gap (red arrow).

Table A.9: Oxidation states (OS) and Bader charges of $SrGe_8As_{10}$ and $BaGe_8As_{10}$.

atom site	Oxidation state	Bader charge	
		$SrGe_8As_{10}$	$BaGe_8As_{10}$.
AE	+2	+1.45	+1.34
Ge2	+2	+0.21	+0.21
Ge1	+3	+0.30	+0.29
Ge3	+4	+0.38	+0.37
As2	-2	-0.24	-0.23
As1	-3	-0.47	-0.46
As3	-3	-0.48	-0.46

Table A.10: Oxidation states (OS) and Bader charges of $BaGe_7P_{12}$.

atom site	Oxidation state	Bader charge
Ba	+2	+1.44
Ge1	+3	+0.48
Ge2	+4	+0.70
P1	-2	-0.44
P2	-2	-0.40

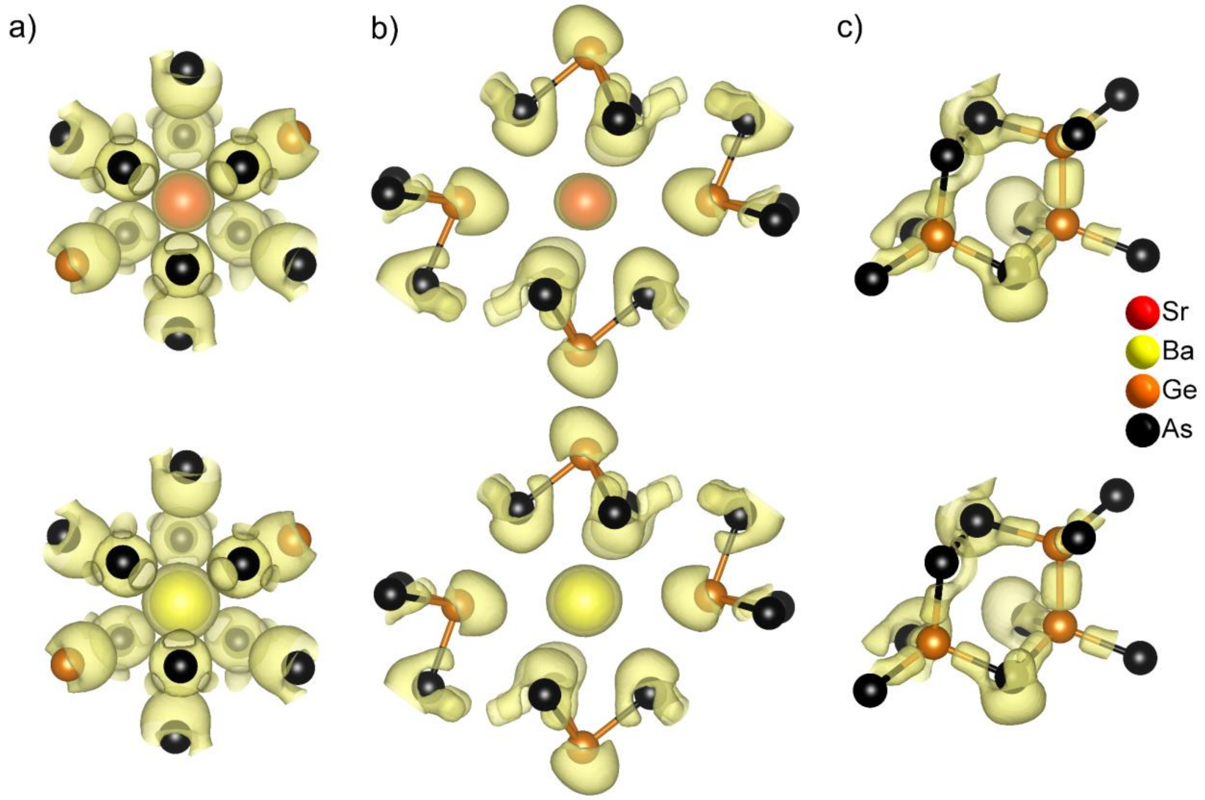

Figure A.11: Calculated electron location function (ELF) of $SrGe_8As_{10}$ (left) and $BaGe_8As_{10}$ (right) (Isosurfaces at ELF = 0.8) with the a) $AEAs_{10}Ge_2$ icosahedra, b) a section of said icosahedra with $GeAs_3$ trigonal pyramids and respective lone pairs and c) the $GeAs_4$ and Ge_2As_6 units with the As-As bond.

A.2 BaGe$_8$As$_{14}$: a semiconducting sodalite type compound

Table A.11: Detailed single crystal diffraction data of BaGe$_8$As$_{14}$

formula	BaGe$_8$As$_{14}$
space group	$I\bar{4}3m$ (No. 217)
a / Å	10.3145(2)
V_{cell} / Å^3	1097.35(6)
Z	2
$\rho_{\text{X-ray}}$ / g cm^{-3}	5.348
crystal size / mm	0.134 x 0.087 x 0.054
diffractometer	Bruker D8 QUEST
radiation type (λ / nm)	Mo Kα (0.71073)
T / K	293
μ / mm^{-1}	33.493
F(000)	1548
Θ-range / °	5.586 – 71.848
hkl range	$-13 \leq h \leq 14$; $k \leq \pm14$; $-13 \leq l \leq +14$
refl. measured	8373
independent refl.	329
parameters	16
R_σ / R_{int}	0.0113 / 0.0408
R_1 ($F^2 > 2\sigma(F^2)$) / all	0.0123 / 0.0132
wR_2 ($F^2 > 2\sigma(F^2)$) / all	0.0301 / 0.0303
GooF	1.330
$\Delta\rho_{\text{max/min}}$ / eÅ^{-3}	+0.597 / -0.598
constraints	5

Table A.12: Atomic coordinates, equivalent displacement parameters (Å^2) and site occupancy factor (s.o.f.) of BaGe$_8$As$_{14}$ from single crystal data.

atom	Wyckoff	x	y	z	U_{eq}	s.o.f.
Ba1	8 *c*	0.47998(18)	0.47998(18)	0.47998(18)	0.0503(13)	0.25
Ge1	12 *d*	¼	½	0	0.01077(15)	1
Ge2	8 *c*	0.21902(5)	0.21902(5)	0.21902(5)	0.01339(18)	0.5
As1	24 *g*	0.38499(3)	0.38499(3)	0.15708(5)	0.01151(13)	1
As2	8 *c*	0.21902(5)	0.21902(5)	0.21902(5)	0.01339(18)	0.5

Table A.13: Anisotropic displacement parameters (Å^2) of BaGe$_8$As$_{14}$ from single crystal data.

atom	U_{11}	U_{22}	U_{33}	U_{23}	U_{13}	U_{12}
Ba1	0.0503(13)	0.0503(13)	0.0503(13)	-0.0092(7)	-0.0092(7)	-0.0092(7)
Ge1	0.0129(3)	0.00973(18)	0.00973(18)	0	0	0
Ge2	0.01339(18)	0.01339(18)	0.01339(18)	0.00172(19)	0.00172(19)	0.00172(19)
As1	0.01216(16)	0.01216(16)	0.0102(2)	0.00053(12)	0.00053(12)	0.00034(16)
As2	0.01339(18)	0.01339(18)	0.01339(18)	0.00172(19)	0.00172(19)	0.00172(19)

Table A.14: Selected distances (Å) of $BaGe_8As_{14}$.

atoms	distance	atoms	distance
Ba1 — As1	3.6073(19)	Ba1 — As1	4.1126(19)
Ba1 — As1	3.6073(19)	Ba1 — As1	4.1126(19)
Ba1 — As1	3.6073(19)	Ba1 — Ge2|As2	4.2705(19)
Ba1 — Ge2|As2	3.8086(19)	Ge1 — As1	2.4436(4)
Ba1 — Ge2|As2	3.8086(19)	Ge1 — As1	2.4436(4)
Ba1 — Ge2|As2	3.8086(19)	Ge1 — As1	2.4436(4)
Ba1 — As1	3.8694(19)	Ge1 — As1	2.4436(4)
Ba1 — As1	3.8694(19)	Ge2|As2 — As1	2.5039(7)
Ba1 — As1	3.8694(19)	Ge2|As2 — As1	2.5039(7)
Ba1 — As1	4.1126(19)	Ge2|As2 — As1	2.5039(6)
Ba1 — As1	4.1126(19)	As1 — Ge1	2.4436(4)
Ba1 — As1	4.1126(19)	As1 — Ge1	2.4436(4)
Ba1 — As1	4.1126(19)	As1 — Ge2|As2	2.5039(6)

Table A.15: Detailed single crystal diffraction data of $BaGe_8As_{14}$ at 218, 189, 143 and 103 K.

formula	$BaGe_8As_{14}$			
space group	$I\bar{4}3m$ (No. 217)			
a / Å	10.3060(2)	10.3052(2)	10.3018(2)	10.2967(2)
V_{cell} / Å^3	1094.64(6)	1094.38(6)	1093.30(6)	1091.68(6)
Z	2			
$\rho_{X\text{-ray}}$ / g cm^{-3}	5.361	5.362	5.367	5.375
crystal size / mm	0.059 x 0.111 x 0.119			
diffractometer	Bruker D8 VENTURE			
radiation type (λ / nm)	Mo Kα (0.71073)			
T / K	218	189	143	103
μ / mm^{-1}	33.576	33.584	33.617	33.667
F(000)	1548			
Θ-range / °	5.590 – 89.110	5.591 – 89.118	5.592 – 90.793	5.595 – 89.211
hkl range	± 17			
refl. measured	17101	17257	17366	17494
independent refl.	540	541	542	547
parameters	16			
R_σ / R_{int}	0.0098 / 0.0355	0.0100 / 0.0373	0.0100 / 0.0358	0.0105 / 0.0395
R_1 ($F^2 > 2\sigma(F^2)$) / all	0.0116 / 0.0120	0.0119 / 0.0119	0.0117 / 0.0119	0.0119 / 0.0121
wR_2 ($F^2 > 2\sigma(F^2)$) / all	0.0373 / 0.0374	0.0366 / 0.0366	0.0364 / 0.0364	0.0345 / 0.0346
GooF	1.418	1.431	1.468	1.351
$\Delta\rho_{max/min}$ / eÅ^{-3}	+0.870 / -0.436	+1.105 / -0.741	+0.840 / -0.688	+1.266 / -0.524
constraints	5			

Table A.16: Atomic coordinates*, equivalent displacement parameters (Å^2) and site occupancy factor (s.o.f.) of $BaGe_8As_{14}$ from single crystal data at 218 K.

atom	Wyckoff	*x*	*y*	*z*	U_{eq}	s.o.f.
Ba1	8 c	0.01986(18)	0.01986(18)	0.01986(18)	0.0446(12)	0.25
Ge1	12 d	¼	½	0	0.00792(11)	1
Ge2	8 c	0.28102(5)	0.28102(5)	0.28102(5)	0.01021(15)	0.5
As1	24 g	0.11512(4)	0.11512(4)	0.34292(5)	0.00855(9)	1
As2	8 c	0.28102(5)	0.28102(5)	0.28102(5)	0.01021(15)	0.5

*Inverted structure compared to Table S4 due to Flack parameter requirements.

Table A.17: Anisotropic displacement parameters (Å^2) of $BaGe_8As_{14}$ from single crystal data at 218 K.

atom	U_{11}	U_{22}	U_{33}	U_{23}	U_{13}	U_{12}
Ba1	0.0446(12)	0.0446(12)	0.0446(12)	-0.0092(6)	-0.0092(6)	-0.0092(6)
Ge1	0.0098(3)	0.00699(15)	0.00699(15)	0	0	0
Ge2	0.01021(15)	0.01021(15)	0.01021(15)	0.00186(17)	0.00186(17)	0.00186(17)
As1	0.00894(12)	0.00894(12)	0.00776(18)	0.00054(10)	0.00054(10)	0.00035(14)
As2	0.01021(15)	0.01021(15)	0.01021(15)	0.00186(17)	0.00186(17)	0.00186(17)

Table A.18: Atomic coordinates, equivalent displacement parameters (Å^2) and site occupancy factor (s.o.f.) of $BaGe_8As_{14}$ from single crystal data at 189 K.

atom	Wyckoff	*x*	*y*	*z*	U_{eq}	s.o.f.
Ba1	8 c	0.01981(17)	0.01981(17)	0.01981(17)	0.0417(12)	0.25
Ge1	12 d	¼	½	0	0.00687(11)	1
Ge2	8 c	0.28105(5)	0.28105(5)	0.28105(5)	0.00895(15)	0.5
As1	24 g	0.11513(4)	0.11513(4)	0.34287(5)	0.00742(9)	1
As2	8 c	0.28105(5)	0.28105(5)	0.28105(5)	0.00895(15)	0.5

Table A.19: Anisotropic displacement parameters (Å^2) of $BaGe_8As_{14}$ from single crystal data at 189 K.

atom	U_{11}	U_{22}	U_{33}	U_{23}	U_{13}	U_{12}
Ba1	0.0417(12)	0.0417(12)	0.0417(12)	-0.0091(6)	-0.0091(6)	-0.0091(6)
Ge1	0.0085(2)	0.00603(15)	0.00603(15)	0	0	0
Ge2	0.00895(15)	0.00895(15)	0.00895(15)	0.00170(16)	0.00170(16)	0.00170(16)
As1	0.00781(12)	0.00781(12)	0.00662(18)	0.00045(10)	0.00045(10)	0.00030(13)
As2	0.00895(15)	0.00895(15)	0.00895(15)	0.00170(16)	0.00170(16)	0.00170(16)

Table A.20: Atomic coordinates, equivalent displacement parameters (Å^2) and site occupancy factor (s.o.f.) of $BaGe_8As_{14}$ from single crystal data at 143 K.

atom	Wyckoff	*x*	*y*	*z*	U_{eq}	s.o.f.
Ba1	8 c	0.01979(16)	0.01979(16)	0.01979(16)	0.0388(11)	0.25
Ge1	12 d	¼	½	0	0.00598(11)	1
Ge2	8 c	0.28107(5)	0.28107(5)	0.28107(5)	0.00799(14)	0.5
As1	24 g	0.11513(3)	0.11513(3)	0.34287(5)	0.00649(9)	1
As2	8 c	0.28107(5)	0.28107(5)	0.28107(5)	0.00799(14)	0.5

Table A.21: Anisotropic displacement parameters (Å^2) of $BaGe_8As_{14}$ from single crystal data at 143 K.

atom	U_{11}	U_{22}	U_{33}	U_{23}	U_{13}	U_{12}
Ba1	0.0388(11)	0.0388(11)	0.0388(11)	-0.0092(5)	-0.0092(5)	-0.0092(5)
Ge1	0.0075(2)	0.00524(15)	0.00524(15)	0	0	0
Ge2	0.00799(14)	0.00799(14)	0.00799(14)	0.00174(16)	0.00174(16)	0.00174(16)
As1	0.00677(12)	0.00677(12)	0.00593(17)	0.00044(10)	0.00044(10)	0.00032(13)
As2	0.00799(14)	0.00799(14)	0.00799(14)	0.00174(16)	0.00174(16)	0.00174(16)

Table A.22: Atomic coordinates, equivalent displacement parameters (Å^2) and site occupancy factor (s.o.f.) of $BaGe_8As_{14}$ from single crystal data at 103 K.

atom	Wyckoff	x	y	z	U_{eq}	s.o.f.
Ba1	8 c	0.01987(15)	0.01987(15)	0.01987(15)	0.0340(10)	0.25
Ge1	12 d	¼	½	0	0.00409(10)	1
Ge2	8 c	0.28112(5)	0.28112(5)	0.28112(5)	0.00593(14)	0.5
As1	24 g	0.11514(3)	0.11514(3)	0.34284(5)	0.00459(8)	1
As2	8 c	0.28112(5)	0.28112(5)	0.28112(5)	0.00593(14)	0.5

Table A.23: Anisotropic displacement parameters (Å^2) of $BaGe_8As_{14}$ from single crystal data at 103 K.

atom	U_{11}	U_{22}	U_{33}	U_{23}	U_{13}	U_{12}
Ba1	0.0340(10)	0.0340(10)	0.0340(10)	-0.0089(5)	-0.0089(5)	-0.0089(5)
Ge1	0.0054(2)	0.00345(14)	0.00345(14)	0	0	0
Ge2	0.00593(14)	0.00593(14)	0.00593(14)	0.00172(15)	0.00172(15)	0.00172(15)
As1	0.00481(11)	0.00481(11)	0.00413(17)	0.00043(10)	0.00043(10)	0.00028(13)
As2	0.00593(14)	0.00593(14)	0.00593(14)	0.00172(15)	0.00172(15)	0.00172(15)

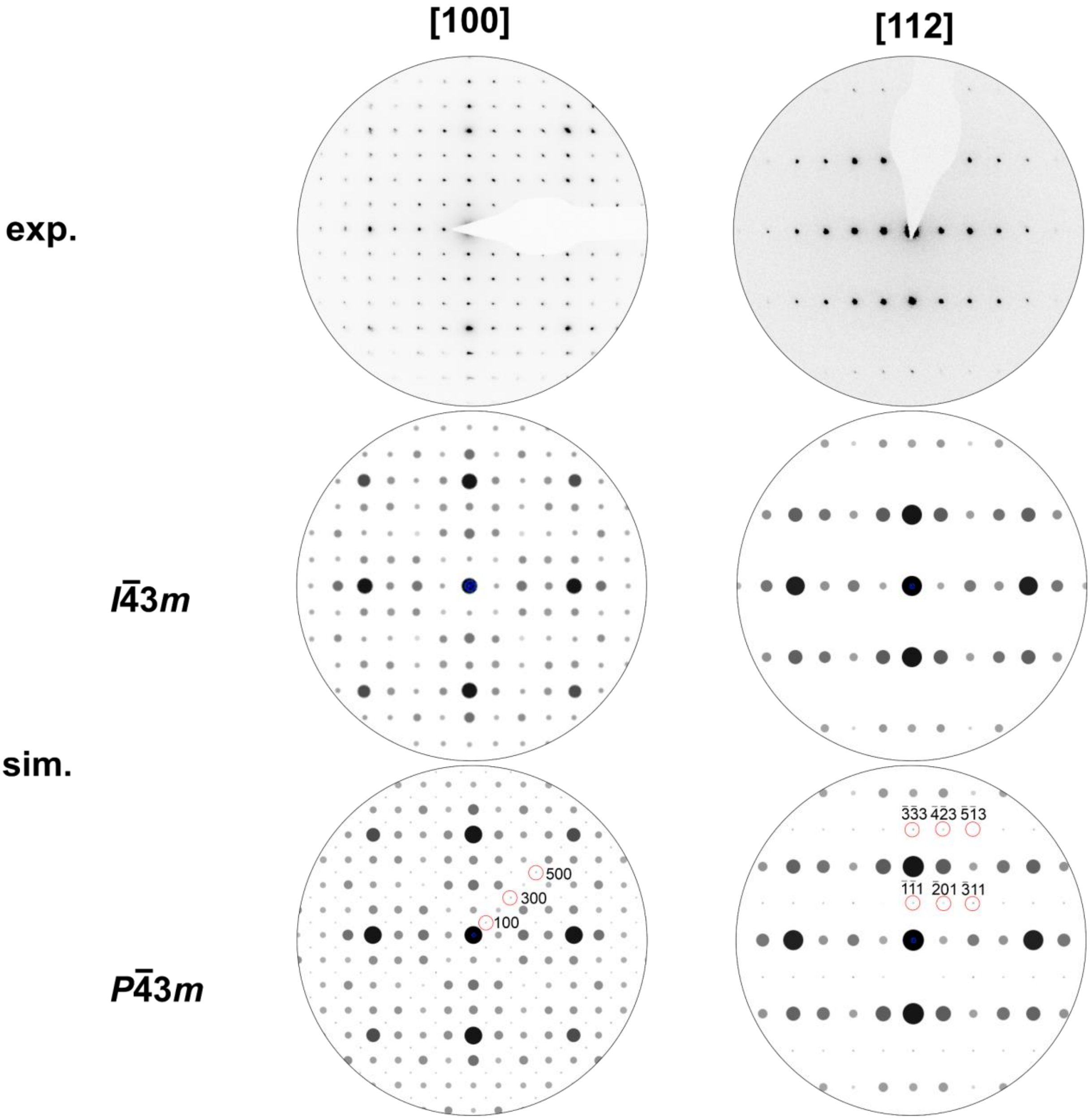

Figure A.12: Top: SAED pattern of $BaGe_8As_{14}$ in [100] and [112] direction on thick crystals to enhance the effects of dynamical diffraction (enable violation of systematical absences due to multiple scattering). Middle: Simulated SAED patterns of $BaGe_8As_{14}$ with the space group $I\bar{4}3m$ (No. 217) as obtained from single crystal X-ray diffraction with a mixed occupied Ge/As position (8c). Bottom: Simulated SAED pattern of $BaGe_8As_{14}$ in the klassengleiche subgroup $P\bar{4}3m$ (No. 215) with ordered Ge (4e) and As (4e) positions. Selected additional reflexes are highlighted (red) and indexed. These do not appear in the experimental pattern.

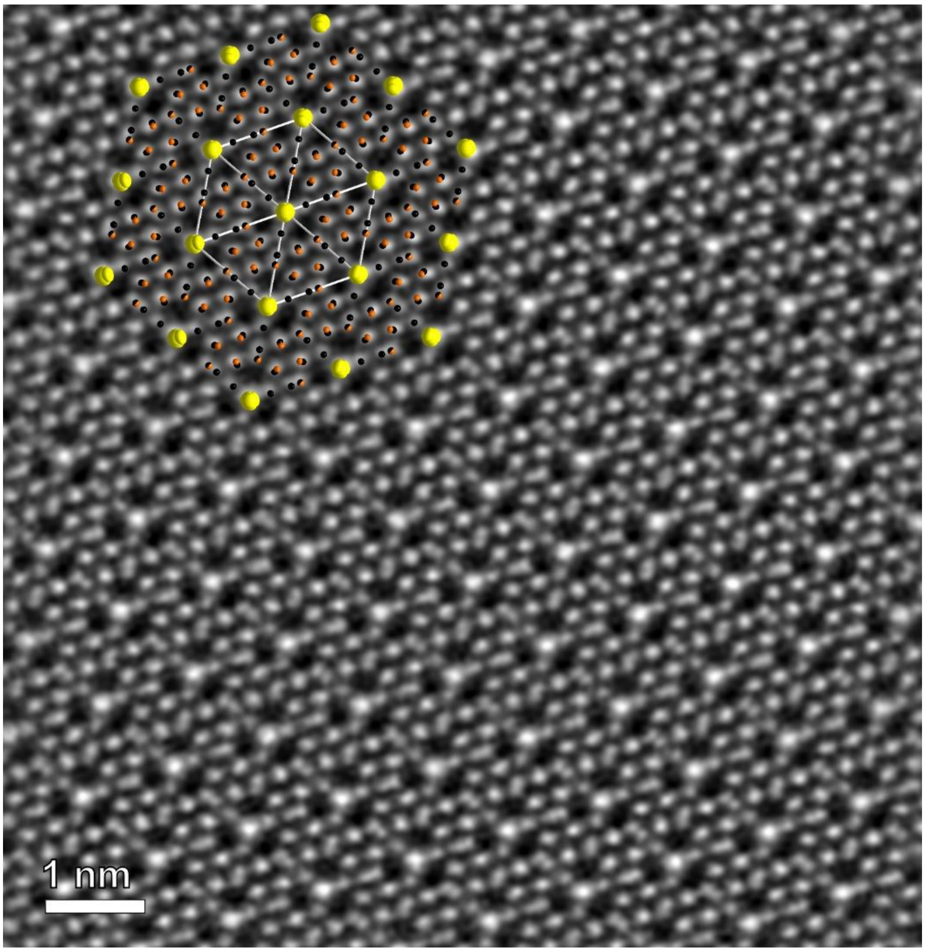

Figure A.13: STEM HAADF image of BaGe$_8$As$_{14}$ in [111] direction with overlay (Ba: yellow, Ge: brown, As: black).

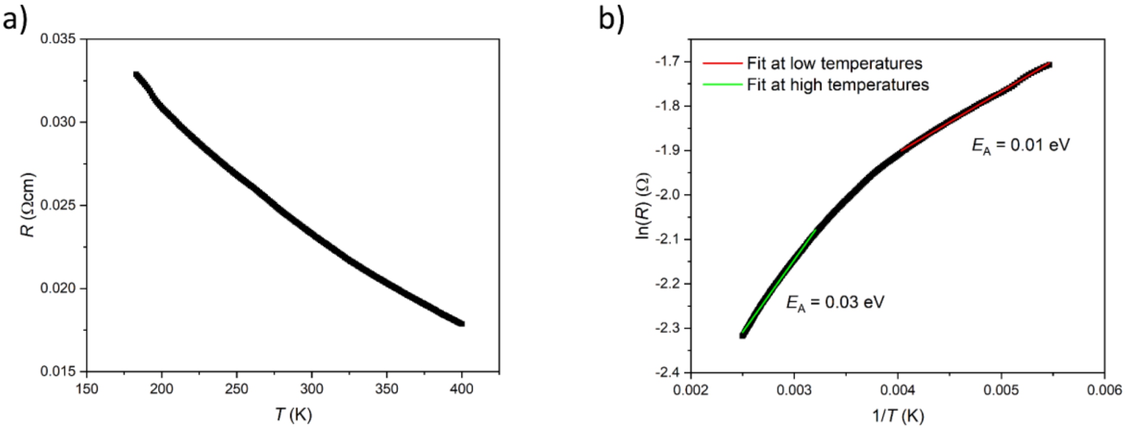

Figure A.14: (a) Resistivity of BaGe$_8$As$_{14}$ between 400 K and 180 K. (b) Arrhenius plot of the resistivity of BaGe$_8$As$_{14}$ showing a band gap of 0.03 eV at high temperatures and a band gap of 0.01 eV at low temperatures.

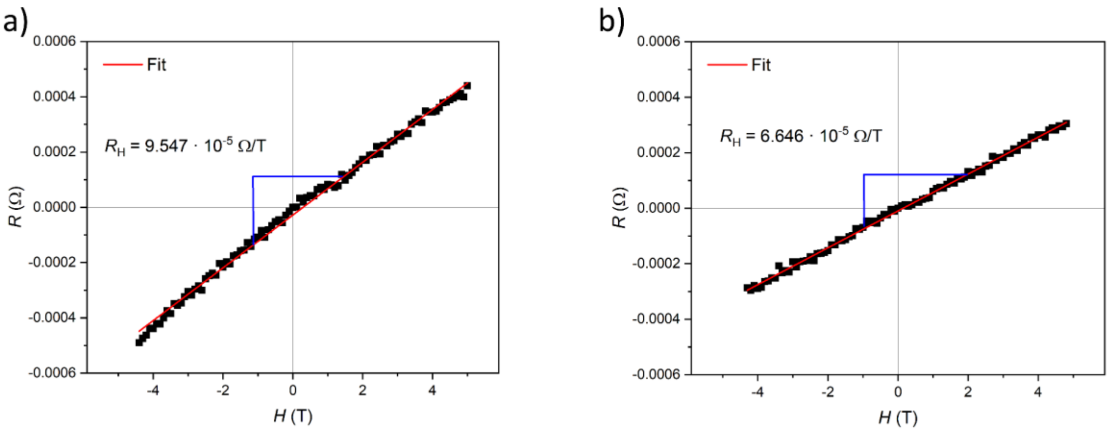

Figure A.15: (a) Hall Effect measurement of $BaGe_8As_{14}$ at 300 K yielding a positive Hall resistance of $9.547 \cdot 10^{-5}$ Ω/T. This results in a carrier concentration of $1.6 \cdot 10^{20}$ cm^{-3} and a mobility μ of 1.6 cm^{2}V^{-1}s^{-1}. (b) Hall Effect measurement of $BaGe_8As_{14}$ at 400 K yielding a positive Hall resistance of $6.646 \cdot 10^{-5}$ Ω/T. This results in a carrier concentration of $2.3 \cdot 10^{20}$ cm^{-3} and a mobility μ of 1.5 cm^{2}V^{-1}s^{-1}.

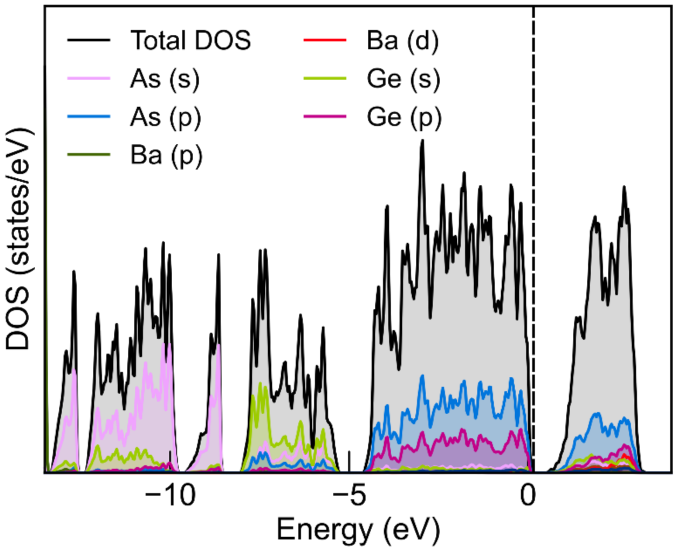

Figure A.16: Total and atom projected density of states (DOS) of $BaGe_8As_{14}$ calculated with PBE functional. The energy zero is taken at the Fermi level Fermi (dashed line).

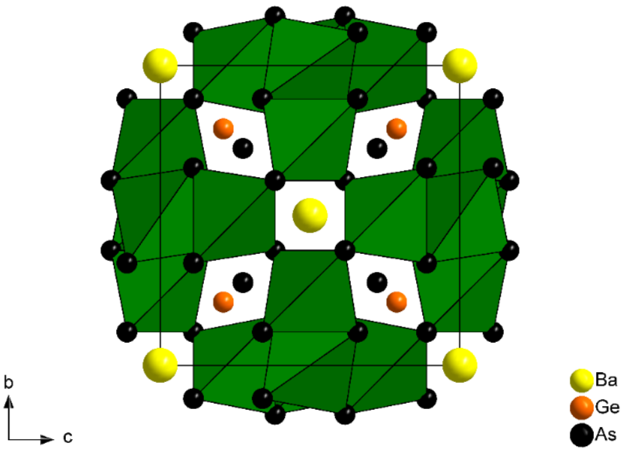

Figure A.17: Unit cell of $BaGe_8As_{14}$ in the subgroup $P\bar{4}3m$ with ordered Ge and As positions.

Table A.24: Calculated parameters for $BaGe_8As_{14}$ (VASP, PBE)

Lattice parameter a = 10.487 Å, space group $P\bar{4}3m$				
Atom	Wyckoff	x	y	z
Ba1	1*a*	0	0	0
Ba2	1*b*	½	½	½
Ge1	12*h*	0.2543	½	½
Ge2	4e	0.7177	x	x
As1	4*e*	0.2252	x	x
As2	12*i*	0.3873	x	0.1554
As3	12*i*	0.8813	x	0.6601

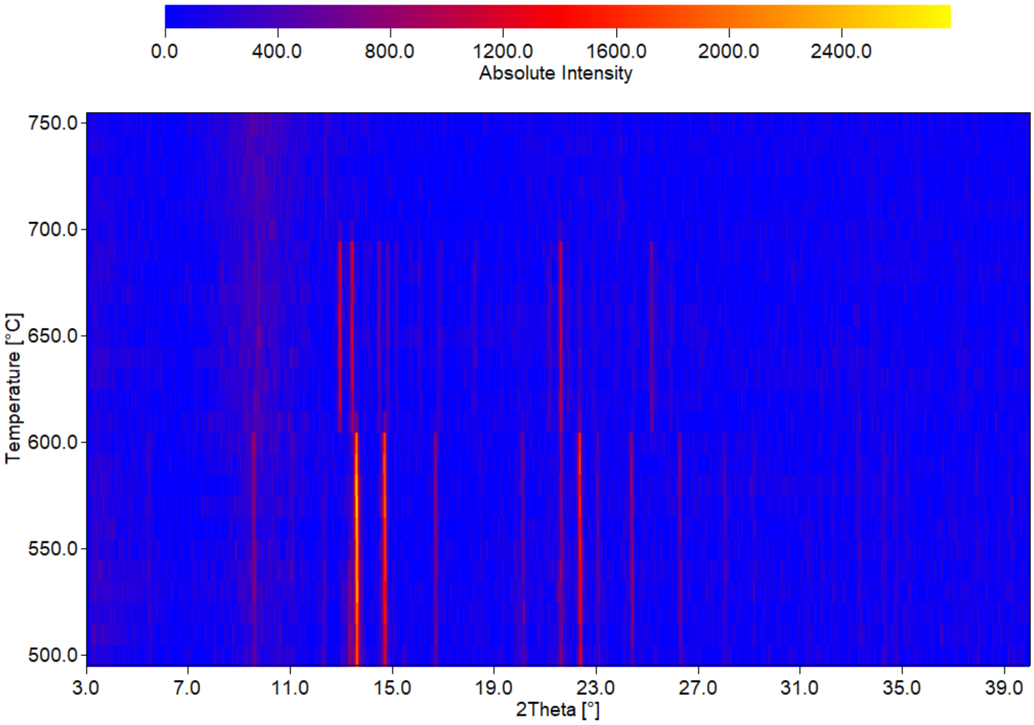

Figure A.18: High temperature powder X-ray diffraction patterns (Mo Kα1) of $BaGe_8As_{14}$ between 773 K and 1023 K with steps of 10 K: Intensities of $BaGe_8As_{14}$ are decreasing for $T > 873$ K.

Table A.25: Powder X-ray diffraction data of $BaGe_8As_{14}$ from Rietveld refinement.

formula	$BaGe_8As_{14}$
space group	$I\bar{4}3m$ (No. 217)
a / Å	10.312605(63)
V_{cell} / Å^3	1096.744(20)
Z	2
$\rho_{X\text{-ray}}$ / g cm^{-3}	5.3518(2)
diffractometer	Stoe Stadi P
radiation type (λ / nm)	Cu Kα1 (1.54056)
T / K	293
μ / mm^{-1}	49.0492(9)
2Θ-range / °	5.000 - 92.420
parameters (incl. side phases)	30
background parameter	12
R_p / R_{wp}	4.524 / 6.788
R_{exp} / R_{Bragg}	2.570 / 2.139
GooF	2.641

A.3 High thermoelectric properties in the sodalite compounds $BaGe_8As_{14}$ and AGe_7As_{15} (A = Rb, Cs)

The temperature dependent values μ and τ were calculated according to formulae (1) and (2) with the elementary charge e and the reduced Planck's constant $\hbar$. V_{DP} was determined according to formulae (3) and (4) with the change in energy ∂E_{edge} in either the valence band maximum *VBM* or the conduction band minimum *CBM* and original and varied lattice parameters a_0 and a.

$$\mu = \frac{2\sqrt{2\pi}e\hbar^4 c_{11}}{3(k_B T)^{3/2} m^{*5/2} V_{DP}^2} \tag{1}$$

$$\tau = \frac{\mu m^*}{e} \tag{2}$$

$$V_{DP} = \frac{\partial E_{edge}}{\partial \alpha} \tag{3}$$

$$\alpha = \frac{a - a_0}{a_0} \tag{4}$$

Table A.26: Detailed single crystal diffraction data of $RbGe_7As_{15}$ (298 K) and $CsGe_7AS_{15}$ (296 K). (**refined as a 2 component inversion twin).

formula	RbGe7As15	CsGe7AS15
space group	I$\bar{4}$3m (No. 217)	
a / Å	10.3642(2)	10.38170(10)
V_{cell} / Å^3	1113.29(6)	1118.94(3)
Z	2	
$\rho_{X\text{-}ray}$ / g cm^{-3}	5.123	5.238
crystal size / mm	0.080 x 0.075 x 0.035	0.068 x 0.044 x 0.031
diffractometer	Bruker D8 VENTURE	
radiation type (λ / nm)	MoKα (0.71073)	
T / K	298	296
μ / mm^{-1}	33.605	32.878
F(000)	1512	1548
Θ-range / °	5.559 – 86.050	5.549 – 86.677
hkl range	± 17	± 18
refl. measured	23455	49600
independent refl.	588	622
parameters	13	15
R_σ / R_{int}	0.0104 / 0.0467	0.0074 / 0.0385
R_1 ($F^2 > 2\sigma(F^2)$) / all	0.0128 / 0.0134	0.0069 / 0.0078
wR_2 ($F^2 > 2\sigma(F^2)$) / all	0.0284 / 0.0285	0.0144 / 0.0147
GooF	1.269	1.221
$\Delta\rho_{max/min}$ / eÅ^{-3}	+0.643 / -0.800	+0.411 / -0.286
Flack	-0.01(2)	0.11(2)**
constraints	4	

Table A.27: Atomic coordinates, equivalent displacement parameters (Å^2) and site occupancy factor (s.o.f.) of $RbGe_7As_{15}$ from single crystal data at 298 K.

atom	Wyckoff	x	y	z	U_{eq}	s.o.f.
Rb1	2*a*	0	0	0	0.0414(4)	1
Ge1	12*d*	1/4	1/2	0	0.00961(8)	1
Ge2	8*c*	0.27777(3)	0.27777(3)	0.27777(3)	0.01149(11)	0.25
As1	24*g*	0.11389(3)	0.11389(3)	0.34412(3)	0.01023(7)	1
As2	8*c*	0.27777(3)	0.27777(3)	0.27777(3)	0.01149(11)	0.75

Table A.28: Anisotropic displacement parameters (Å^2) of $RbGe_7As_{15}$ from single crystal data at 298 K.

atom	U_{11}	U_{22}	U_{33}	U_{23}	U_{13}	U_{12}
Rb1	0.0414(4)	0.0414(4)	0.0414(4)	0	0	0
Ge1	0.01212(18)	0.00835(11)	0.00835(11)	0	0	0
Ge2	0.01149(11)	0.01149(11)	0.01149(11)	0.00085(11)	0.00085(11)	0.00085(11)
As1	0.01086(9)	0.01086(9)	0.00898(13)	0.00026(7)	0.00026(7)	-0.00005(10)
As2	0.01149(11)	0.01149(11)	0.01149(11)	0.00085(11)	0.00085(11)	0.00085(11)

Table A.29: Atomic coordinates, equivalent displacement parameters (Å^2) and site occupancy factor (s.o.f.) of $CsGe_7As_{15}$ from single crystal data at 296 K.

atom	Wyckoff	x	y	z	U_{eq}	s.o.f.
Cs1	2*a*	0	0	0	0.02492(9)	1
Ge1	12*d*	1/4	1/2	0	0.01057(5)	1
Ge2	8*c*	0.22267(2)	0.22267(2)	0.22267(2)	0.01235(6)	0.25
As1	24*g*	0.38611(2)	0.38611(2)	0.15531(2)	0.01100(4)	1
As2	8*c*	0.22267(2)	0.22267(2)	0.22267(2)	0.01235(6)	0.75

Table A.30: Anisotropic displacement parameters (Å^2) of $CsGe_7As_{15}$ from single crystal data at 296 K.

atom	U_{11}	U_{22}	U_{33}	U_{23}	U_{13}	U_{12}
Cs1	0.02492(9)	0.02492(9)	0.02492(9)	0	0	0
Ge1	0.01269(10)	0.00951(6)	0.00951(6)	0	0	0
Ge2	0.01235(6)	0.01235(6)	0.01235(6)	0.00086(6)	0.00086(6)	0.00086(6)
As1	0.01163(5)	0.01163(5)	0.00976(7)	0.00004(4)	0.00004(4)	0.00013(6)
As2	0.01235(6)	0.01235(6)	0.01235(6)	0.00086(6)	0.00086(6)	0.00086(6)

Table A.31: Selected distances (Å) of AGe_7As_{15} (A = Rb, Cs).

atoms	counts	distance (A = Rb)	distance (A = Cs)
*A*1 — As1	12	3.9379(3)	3.9499(2)
*A*1 — Ge2|As2	4	3.9893(3)	4.0040(2)
Ge1 — As1	4	2.4481(3)	2.4484(2)
Ge2|As2 — As1	3	2.4985(3)	2.4494(3)

Table A.32: Detailed single crystal diffraction data of $RbGe_7As_{15}$ at 218, 180, 143 and 102 K.

formula	$RbGe_7As_{15}$			
space group	$I\bar{4}3m$ (No. 217)			
a / Å	10.3582(2)	10.3555(2)	10.3536(2)	10.3497(2)
V_{cell} / Å^3	1111.36(6)	1110.49(6)	1109.88(6)	1108.62(6)
Z	2			
$\rho_{X\text{-ray}}$ / g cm^{-3}	5.132	5.136	5.139	5.145
crystal size / mm	0.080 x 0.075 x 0.035			
diffractometer	Bruker D8 VENTURE			
radiation type (λ / nm)	$Mo_{K\alpha}$ (0.71073)			
T / K	218	180	143	102
μ / mm^{-1}	33.663	33.690	33.708	33.746
F(000)	1512			
Θ-range / °	5.562 - 92.050	5.563 – 93.432	5.564 – 92.914	5.567 – 92.148
hkl range	± 17			
refl. measured	18727	23500	18801	18841
independent refl.	588			
parameters	13			
R_σ / R_{int}	0.0115 / 0.0453	0.0099 / 0.0456	0.0117 / 0.0466	0.0118 / 0.0466
R_1 ($F^2 > 2\sigma(F^2)$) / all	0.0143 / 0.0148	0.0137 / 0.0142	0.0124 / 0.0132	0.0125 / 0.0132
wR_2 ($F^2 > 2\sigma(F^2)$) / all	0.0313 / 0.0314	0.0316 / 0.0317	0.0263 / 0.0264	0.0263 / 0.0265
GooF	1.315	1.271	1.277	1.267
$\Delta\rho_{max/min}$ / eÅ^{-3}	+0.803 / -0.997	+0.810 / -0.911	+0.599 / -0.683	+0.673 / -0.884
Flack	0.03(2)	0.01(2)	0.00(2)	0.02(3)
constraints	4			

Table A.33: Atomic coordinates, equivalent displacement parameters (Å^2) and site occupancy factor (s.o.f.) of $RbGe_7As_{15}$ from single crystal data at 218 K.

atom	Wyckoff	x	y	z	U_{eq}	s.o.f.
Rb1	2*a*	0	0	0	0.0342(4)	1
Ge1	12*d*	1/4	1/2	0	0.00770(9)	1
Ge2	8*c*	0.27784(4)	0.27784(4)	0.27784(4)	0.00932(12)	0.25
As1	24*g*	0.11389(3)	0.11389(3)	0.34404(4)	0.00823(7)	1
As2	8*c*	0.27784(4)	0.27784(4)	0.27784(4)	0.00932(12)	0.75

Table A.34: Anisotropic displacement parameters (Å^2) of $RbGe_7As_{15}$ from single crystal data at 218 K.

atom	U_{11}	U_{22}	U_{33}	U_{23}	U_{13}	U_{12}
Rb1	0.0342(4)	0.0342(4)	0.0342(4)	0	0	0
Ge1	0.0098(2)	0.00666(12)	0.00666(12)	0	0	0
Ge2	0.00932(12)	0.00932(12)	0.00932(12)	0.00075(12)	0.00075(12)	0.00075(12)
As1	0.00872(10)	0.00872(10)	0.00725(14)	0.00020(8)	0.00020(8)	-0.00007(11)
As2	0.00932(12)	0.00932(12)	0.00932(12)	0.00075(12)	0.00075(12)	0.00075(12)

Table A.35: Atomic coordinates, equivalent displacement parameters (Å^2) and site occupancy factor (s.o.f.) of $RbGe_7As_{15}$ from single crystal data at 180 K.

atom	Wyckoff	x	y	z	U_{eq}	s.o.f.
Rb1	2*a*	0	0	0	0.0298(4)	1
Ge1	12*d*	1/4	1/2	0	0.00659(9)	1
Ge2	8*c*	0.22216(4)	0.22216(4)	0.22216(4)	0.00796(11)	0.25
As1	24*g*	0.38611(3)	0.38611(3)	0.15600(4)	0.00703(7)	1
As2	8*c*	0.22216(4)	0.22216(4)	0.22216(4)	0.00796(11)	0.75

Table A.36: Anisotropic displacement parameters (Å^2) of $RbGe_7As_{15}$ from single crystal data at 180 K.

atom	U_{11}	U_{22}	U_{33}	U_{23}	U_{13}	U_{12}
Rb1	0.0298(4)	0.0298(4)	0.0298(4)	0	0	0
Ge1	0.00845(19)	0.00566(12)	0.00566(12)	0	0	0
Ge2	0.00796(11)	0.00796(11)	0.00796(11)	0.00072(11)	0.00072(11)	0.00072(11)
As1	0.00745(9)	0.00745(9)	0.00621(13)	0.00016(7)	0.00016(7)	-0.00010(11)
As2	0.00796(11)	0.00796(11)	0.00796(11)	0.00072(11)	0.00072(11)	0.00072(11)

Table A.37: Atomic coordinates, equivalent displacement parameters (Å^2) and site occupancy factor (s.o.f.) of $RbGe_7As_{15}$ from single crystal data at 143 K.

atom	Wyckoff	x	y	z	U_{eq}	s.o.f.
Rb1	2*a*	0	0	0	0.0258(3)	1
Ge1	12*d*	1/4	1/2	0	0.00579(8)	1
Ge2	8*c*	0.22210(3)	0.22210(3)	0.22210(3)	0.00713(10)	0.25
As1	24*g*	0.38613(2)	0.38613(2)	0.15605(3)	0.00619(6)	1
As2	8*c*	0.22210(3)	0.22210(3)	0.22210(3)	0.00713(10)	0.75

Table A.38: Anisotropic displacement parameters (Å^2) of $RbGe_7As_{15}$ from single crystal data at 143 K.

atom	U_{11}	U_{22}	U_{33}	U_{23}	U_{13}	U_{12}
Rb1	0.0258(3)	0.0258(3)	0.0258(3)	0	0	0
Ge1	0.00729(16)	0.00504(10)	0.00504(10)	0	0	0
Ge2	0.00713(10)	0.00713(10)	0.00713(10)	0.00064(10)	0.00064(10)	0.00064(10)
As1	0.00653(8)	0.00653(8)	0.00553(12)	0.00010(7)	0.00010(7)	0.00001(10)
As2	0.00713(10)	0.00713(10)	0.00713(10)	0.00064(10)	0.00064(10)	0.00064(10)

Table A.39: Atomic coordinates, equivalent displacement parameters (Å^2) and site occupancy factor (s.o.f.) of $RbGe_7As_{15}$ from single crystal data at 102 K.

atom	Wyckoff	x	y	z	U_{eq}	s.o.f.
Rb1	2*a*	0	0	0	0.0206(3)	1
Ge1	12*d*	1/4	1/2	0	0.00458(8)	1
Ge2	8*c*	0.22208(3)	0.22208(3)	0.22208(3)	0.00575(10)	0.25
As1	24*g*	0.38612(2)	0.38612(2)	0.15609(3)	0.00493(6)	1
As2	8*c*	0.22208(3)	0.22208(3)	0.22208(3)	0.00575(10)	0.75

Table A.40: Anisotropic displacement parameters (Å^2) of $RbGe_7As_{15}$ from single crystal data at 102 K.

atom	U_{11}	U_{22}	U_{33}	U_{23}	U_{13}	U_{12}
Rb1	0.0206(3)	0.0206(3)	0.0206(3)	0	0	0
Ge1	0.00597(18)	0.00389(11)	0.00389(11)	0	0	0
Ge2	0.00575(10)	0.00575(10)	0.00575(10)	0.00064(11)	0.00064(11)	0.00064(11)
As1	0.00516(8)	0.00516(8)	0.00447(12)	0.00014(7)	0.00014(7)	-0.00003(10)
As2	0.00575(10)	0.00575(10)	0.00575(10)	0.00064(11)	0.00064(11)	0.00064(11)

Table A.41: Detailed single crystal diffraction data of $CsGe_7As_{15}$ at 218, 180, 143 and 102 K (**refined as a 2 component inversion twin).

formula	$CsGe_7As_{15}$			
space group	$I\bar{4}3m$ (No. 217)			
a / Å	10.3750(3)	10.3722(3)	10.3670(3)	10.3653(2)
V_{cell} / Å^3	1116.77(10)	1115.87(10)	1114.19(10)	1113.64(6)
Z	2			
$\rho_{X\text{-ray}}$ / g cm^{-3}	5.248	5.253	5.260	5.263
crystal size / mm	0.068 x 0.044 x 0.031			
diffractometer	Bruker D8 VENTURE			
radiation type (λ / nm)	$Mo_{K\alpha}$ (0.71073)			
T / K	218	180	143	102
μ / mm^{-1}	32.941	32.968	33.018	33.034
F(000)	1548			
Θ-range / °	5.553 – 87.555	5.554 – 90.813	5.557 – 87.640	5.558 – 87.657
hkl range	± 17			
refl. measured	18105	18086	18162	18091
independent refl.	563			
parameters	14			
R_σ / R_{int}	0.0107 / 0.0418	0.0113 / 0.0429	0.120 / 0.0478	0.0132 / 0.0504
R_1 ($F^2 > 2\sigma(F^2)$) / all	0.0112 / 0.0126	0.0115 / 0.0120	0.0111 / 0.0121	0.0110 / 0.0118
wR_2 ($F^2 > 2\sigma(F^2)$) / all	0.0252 / 0.0256	0.0259 / 0.0260	0.0249 / 0.0252	0.0242 / 0.0243
GooF	1.296	1.275	1.251	1.253
$\Delta\rho_{max/min}$ / eÅ^{-3}	+0.512 / -0.658	+0.503 / -0.727	+0.532 / -0.821	+0.597 / -0.630
Flack**	0.09(4)	0.12(4)	0.09(3)	0.13(3)
constraints	4			

Table A.42: Atomic coordinates, equivalent displacement parameters (Å^2) and site occupancy factor (s.o.f.) of $CsGe_7As_{15}$ from single crystal data at 218 K.

atom	Wyckoff	x	y	z	U_{eq}	s.o.f.
Cs1	2*a*	0	0	0	0.01985(13)	1
Ge1	12*d*	1/4	1/2	0	0.00807(8)	1
Ge2	8*c*	0.22258(3)	0.22258(3)	0.22258(3)	0.00957(9)	0.25
As1	24*g*	0.38609(2)	0.38609(2)	0.15541(3)	0.00850(6)	1
As2	8*c*	0.22258(3)	0.22258(3)	0.22258(3)	0.00957(9)	0.75

Table A.43: Anisotropic displacement parameters (Å^2) of $CsGe_7As_{15}$ from single crystal data at 218 K.

atom	atom	U_{11}	U_{22}	U_{33}	U_{23}	U_{13}
Cs1	0.01985(13)	0.01985(13)	0.01985(13)	0	0	0
Ge1	0.00983(16)	0.00719(10)	0.00719(10)	0	0	0
Ge2	0.00957(9)	0.00957(9)	0.00957(9)	0.00073(10)	0.00073(10)	0.00073(10)
As1	0.00898(8)	0.00898(8)	0.00753(11)	-0.00001(6)	-0.00001(6)	0.00003(10)
As2	0.00957(9)	0.00957(9)	0.00957(9)	0.00073(10)	0.00073(10)	0.00073(10)

Table A.44: **.** Atomic coordinates, equivalent displacement parameters (Å^2) and site occupancy factor (s.o.f.) of $CsGe_7As_{15}$ from single crystal data at 180 K.

atom	Wyckoff	*x*	*y*	*z*	U_{eq}	s.o.f.
Cs1	2*a*	0	0	0	0.01724(13)	1
Ge1	12*d*	1/4	1/2	0	0.00699(8)	1
Ge2	8*c*	0.22252(3)	0.22252(3)	0.22252(3)	0.00838(9)	0.25
As1	24*g*	0.38609(2)	0.38609(2)	0.15545(3)	0.00736(6)	1
As2	8*c*	0.22252(3)	0.22252(3)	0.22252(3)	0.00838(9)	0.75

Table A.45: Anisotropic displacement parameters (Å^2) of $CsGe_7As_{15}$ from single crystal data at 180 K.

atom	atom	U_{11}	U_{22}	U_{33}	U_{23}	U_{13}
Cs1	0.01724(13)	0.01724(13)	0.01724(13)	0	0	0
Ge1	0.00859(16)	0.00619(10)	0.00619(10)	0	0	0
Ge2	0.00838(9)	0.00838(9)	0.00838(9)	0.00066(10)	0.00066(10)	0.00066(10)
As1	0.00777(8)	0.00777(8)	0.00653(11)	-0.00012(6)	-0.00012(6)	0.00008(9)
As2	0.00838(9)	0.00838(9)	0.00838(9)	0.00066(10)	0.00066(10)	0.00066(10)

Table A.46: Atomic coordinates, equivalent displacement parameters (Å^2) and site occupancy factor (s.o.f.) of $CsGe_7As_{15}$ from single crystal data at 143 K.

atom	Wyckoff	*x*	*y*	*z*	U_{eq}	s.o.f.
Cs1	2*a*	0	0	0	0.01474(12)	1
Ge1	12*d*	1/4	1/2	0	0.00615(7)	1
Ge2	8*c*	0.27746(3)	0.27746(3)	0.27746(3)	0.00735(9)	0.25
As1	24*g*	0.11389(2)	0.11389(2)	0.34451(3)	0.00645(6)	1
As2	8*c*	0.27746(3)	0.27746(3)	0.27746(3)	0.00735(9)	0.75

Table A.47: Anisotropic displacement parameters (Å^2) of $CsGe_7As_{15}$ from single crystal data at 143 K.

atom	atom	U_{11}	U_{22}	U_{33}	U_{23}	U_{13}
Cs1	0.01474(12)	0.01474(12)	0.01474(12)	0	0	0
Ge1	0.00748(16)	0.00549(10)	0.00549(10)	0	0	0
Ge2	0.00735(9)	0.00735(9)	0.00735(9)	0.00059(9)	0.00059(9)	0.00059(9)
As1	0.00679(8)	0.00679(8)	0.00576(11)	-0.00002(6)	-0.00002(6)	0.00005(9)
As2	0.00735(9)	0.00735(9)	0.00735(9)	0.00059(9)	0.00059(9)	0.00059(9)

Table A.48: . Atomic coordinates, equivalent displacement parameters (Å^2) and site occupancy factor (s.o.f.) of $CsGe_7As_{15}$ from single crystal data at 102 K.

atom	Wyckoff	*x*	*y*	*z*	U_{eq}	s.o.f.
Cs1	2*a*	0	0	0	0.01158(11)	1
Ge1	12*d*	1/4	1/2	0	0.00501(7)	1
Ge2	8*c*	0.27751(3)	0.27751(3)	0.27751(3)	0.00601(9)	0.25
As1	24*g*	0.11388(2)	0.11388(2)	0.34446(3)	0.00519(6)	1
As2	8*c*	0.27751(3)	0.27751(3)	0.27751(3)	0.00601(9)	0.75

Table A.49: Anisotropic displacement parameters (Å^2) of $CsGe_7As_{15}$ from single crystal data at 102 K.

atom	U_{11}	U_{22}	U_{33}	U_{23}	U_{13}	U_{12}
Cs1	0.01158(11)	0.01158(11)	0.01158(11)	0	0	0
Ge1	0.00611(15)	0.00446(9)	0.00446(9)	0	0	0
Ge2	0.00601(9)	0.00601(9)	0.00601(9)	0.00071(9)	0.00071(9)	0.00071(9)
As1	0.00544(7)	0.00544(7)	0.00469(11)	-0.00003(6)	-0.00003(6)	0.00004(9)
As2	0.00601(9)	0.00601(9)	0.00601(9)	0.00071(9)	0.00071(9)	0.00071(9)

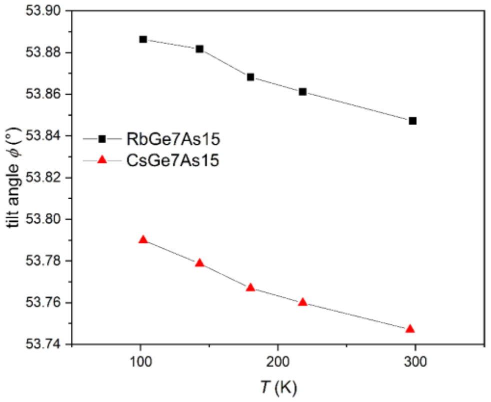

Figure A.19: Tilt angles φ (equation 5) of $RbGe_7As_{15}$ and $CsGe_7As_{15}$ resulting in an over-collapsed framework.

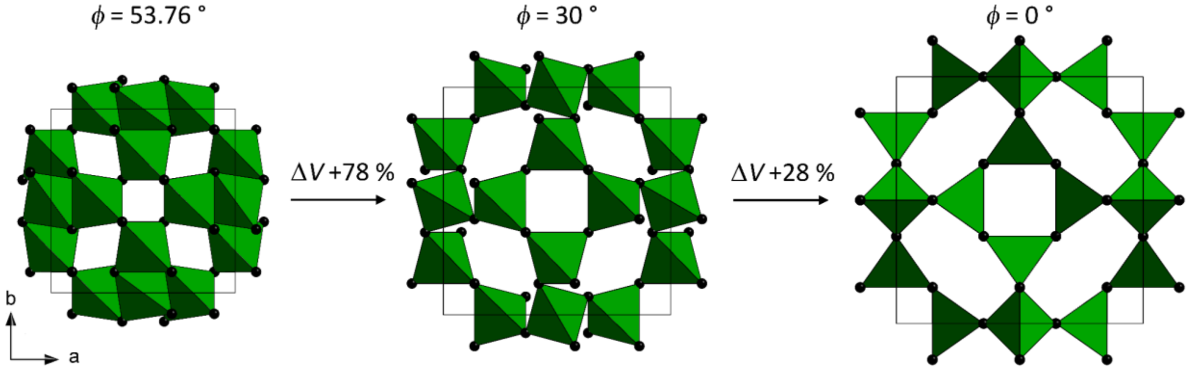

Figure A.20: Over-collapsed Ge-As framework of $CsGe_7As_{15}$ with a tilt angle of φ = 53.76 ° (left). Theoretical structures of $CsGe_7As_{15}$ for a partially-collapsed framework with a tilt angle of 30 ° (middle) and a fully-expanded network with a tilt angle of 0 ° (right). Based on the work of Nyman *et al.*, equations 6-8 were used to calculate the according lattice parameters and coordinates of the As-position.[2]

$$\varphi = \tan^{-1}(z/x) \tag{5}$$

$$a = 2d(\cos\varphi + 1/\sqrt{2}) \tag{6}$$

$$x = \cos\varphi \,/\, 4(\cos\varphi + 1/\sqrt{2}) \tag{7}$$

$$y = \sin\varphi \,/\, 4(\cos\varphi + 1/\sqrt{2}) \tag{8}$$

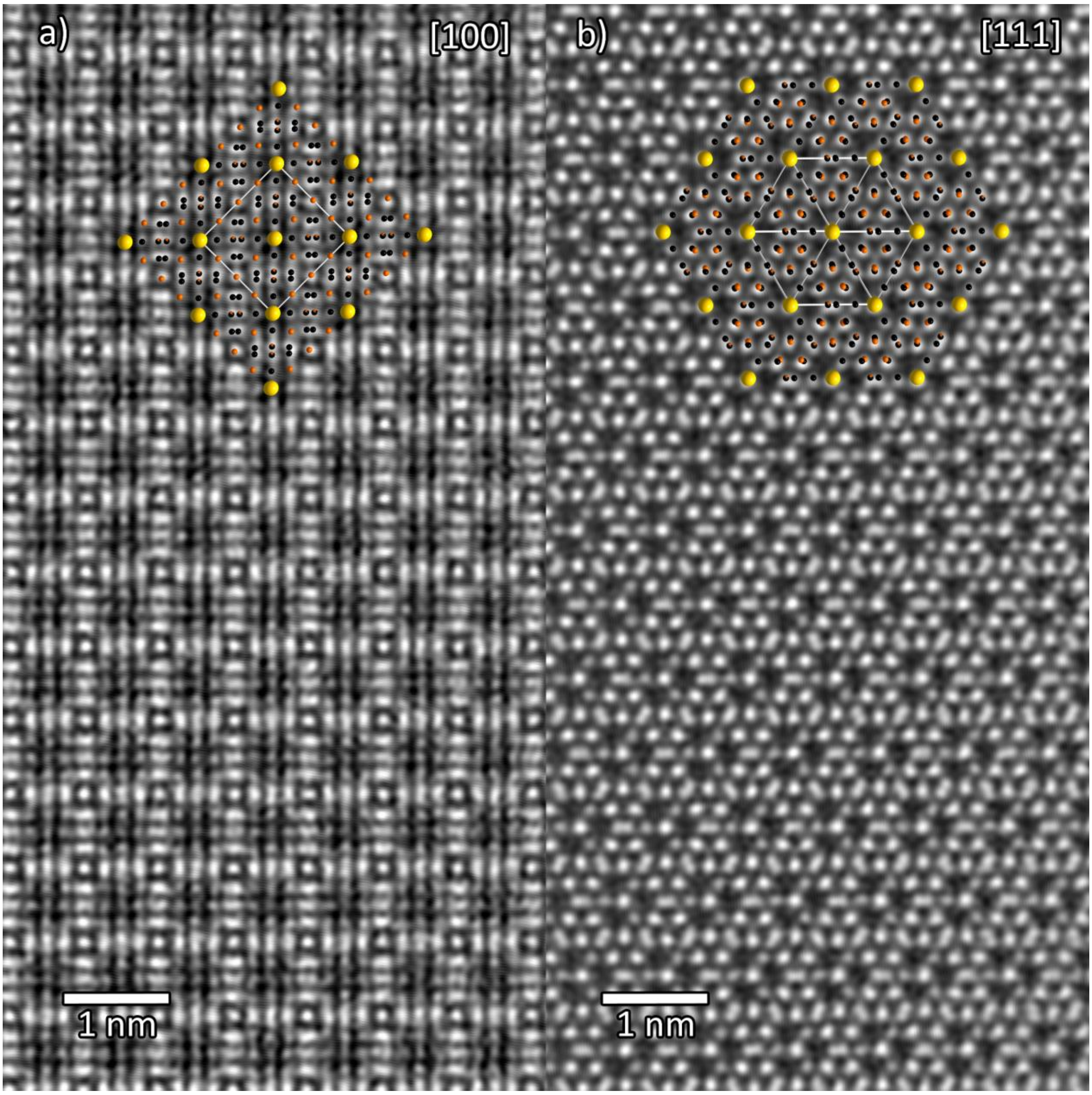

Figure A.21: STEM HAADF image of $RbGe_7As_{15}$ in (a) [100] and (b) [111] direction with structural overlays (Rb: yellow, Ge: brown, As: black) and a resolution of [100]: 1.15 Å and [111]: 1.05 Å.

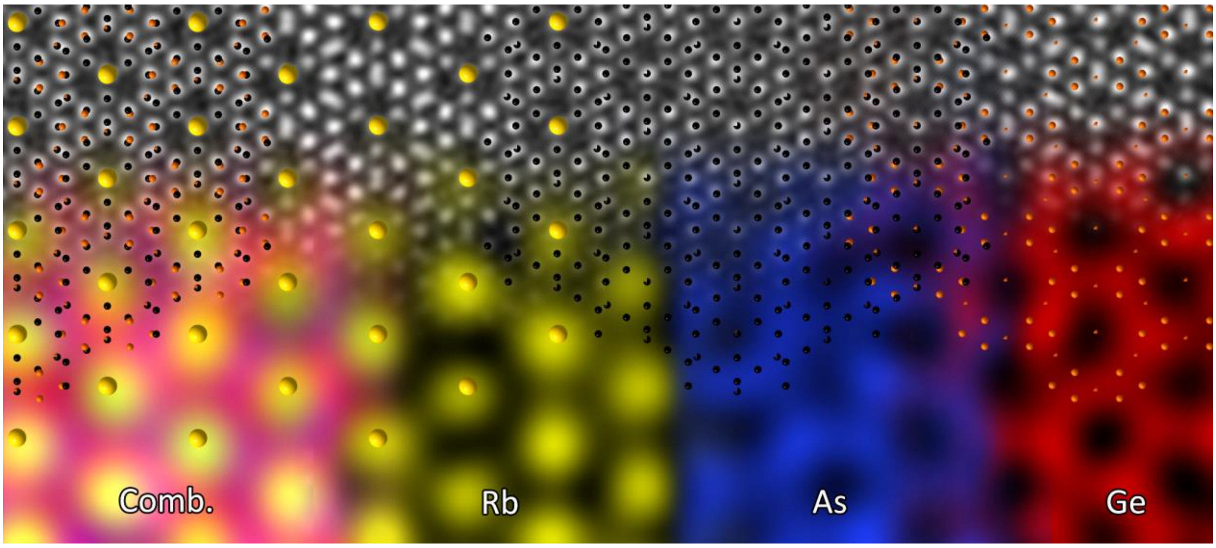

Figure A.22: STEM-HAADF image and high resolution STEM-EDX maps of $RbGe_7As_{15}$ along [111] with structural overlays.

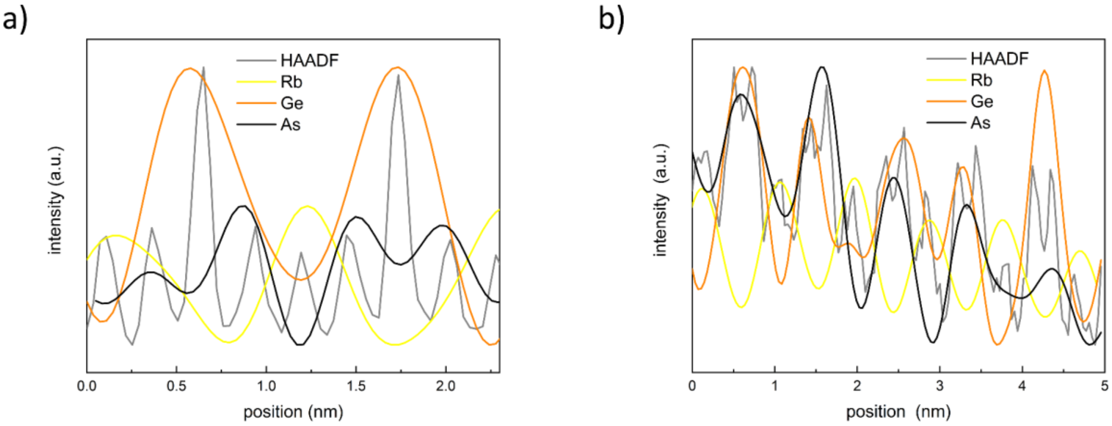

Figure A.23: Linescans of STEM-EDX maps of $RbGe_7As_{15}$ in (a) [100] and (b) [111] direction along (100) and (111) respectively.

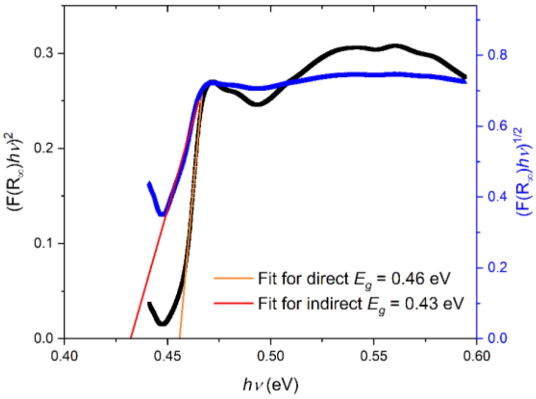

Figure A.24: Tauc plots of a Kubelka Munk converted diffuse reflectance spectra of $CsGe_7As_{15}$ exhibiting an indirect band gap of 0.43 eV and a direct band gap of 0.46 eV.

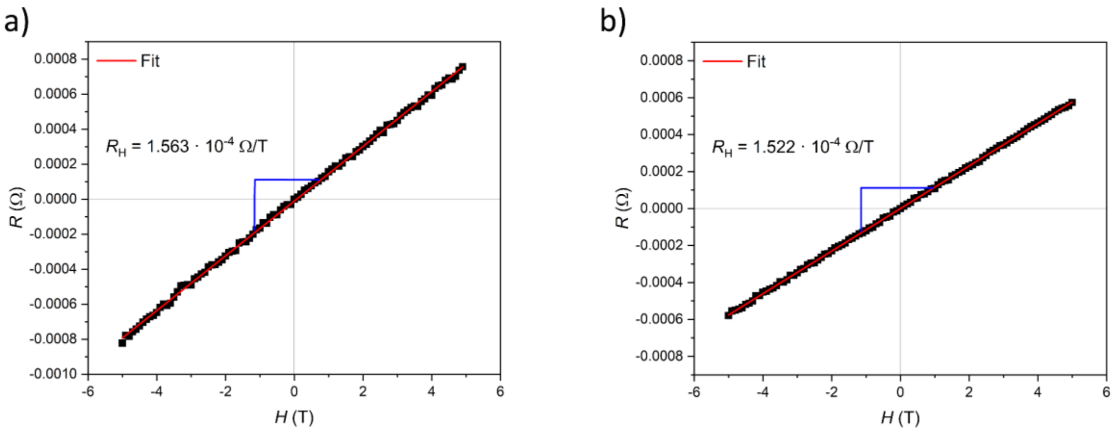

Figure A.25: Hall Effect measurement of (a) $RbGe_7As_{15}$ and (b) $CsGe_7As_{15}$ at 300 K yielding positive Hall resistance values of (a) $1.563 \cdot 10^{-5}$ Ω/T and (b) $1.522 \cdot 10^{-5}$ Ω/T. This yields carrier concentrations of (a) $1.3{\cdot}10^{20}$ cm^{-3} and (b) $8.2{\cdot}10^{19}$ cm^{-3} and mobilities μ of (a) 5.8 cm^{2}V^{-1}s^{-1} (b) 21 cm^{2}V^{-1}s^{-1}.

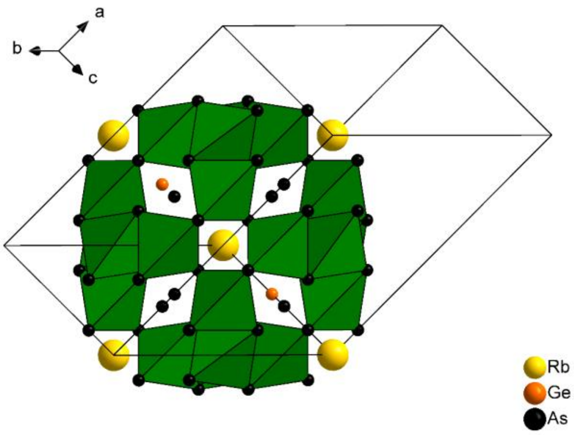

Figure A.26: Unit cell of $RbGe_7As_{15}$ in the symmetry reduced space group *R*3*m* (No. 160) with ordered Ge-As positions.

Table A.50: Calculated structural parameters of **(1)** $RbGe_7As_{15}$ and **(2)** $CsGe_7As_{15}$ in the space group *R*3*m* (PBE **(1)** / PBEsol **(2)**).

Lattice parameter (1) *a* = 14.5068 Å; *c* = 8.8740 Å, (2) *a* = 14.6867 Å; *c* = 8.9803 Å

Atom	Wyckoff	$x_{(1)}$	$y_{(1)}$	$z_{(1)}$	$x_{(2)}$	$y_{(2)}$	$z_{(2)}$
A	3*a*	0	0	0.43413	0	0	0.43827
Ge1	18*c*	0.41688	0.08411	0.26825	0.41691	0.08416	0.26967
Ge2	3*a*	0	0	0.00000	0	0	0.00000
As1	18*c*	0.22706	0.00143	0.20900	0.22791	0.00152	0.20954
As2	9*b*	0.18463	0.81537	0.24957	0.18392	0.81609	0.25176
As3	9*b*	0.48394	0.51606	0.17994	0.48455	0.51544	0.18193
As4	9*b*	0.74316	0.25684	0.14585	0.74353	0.25647	0.14864

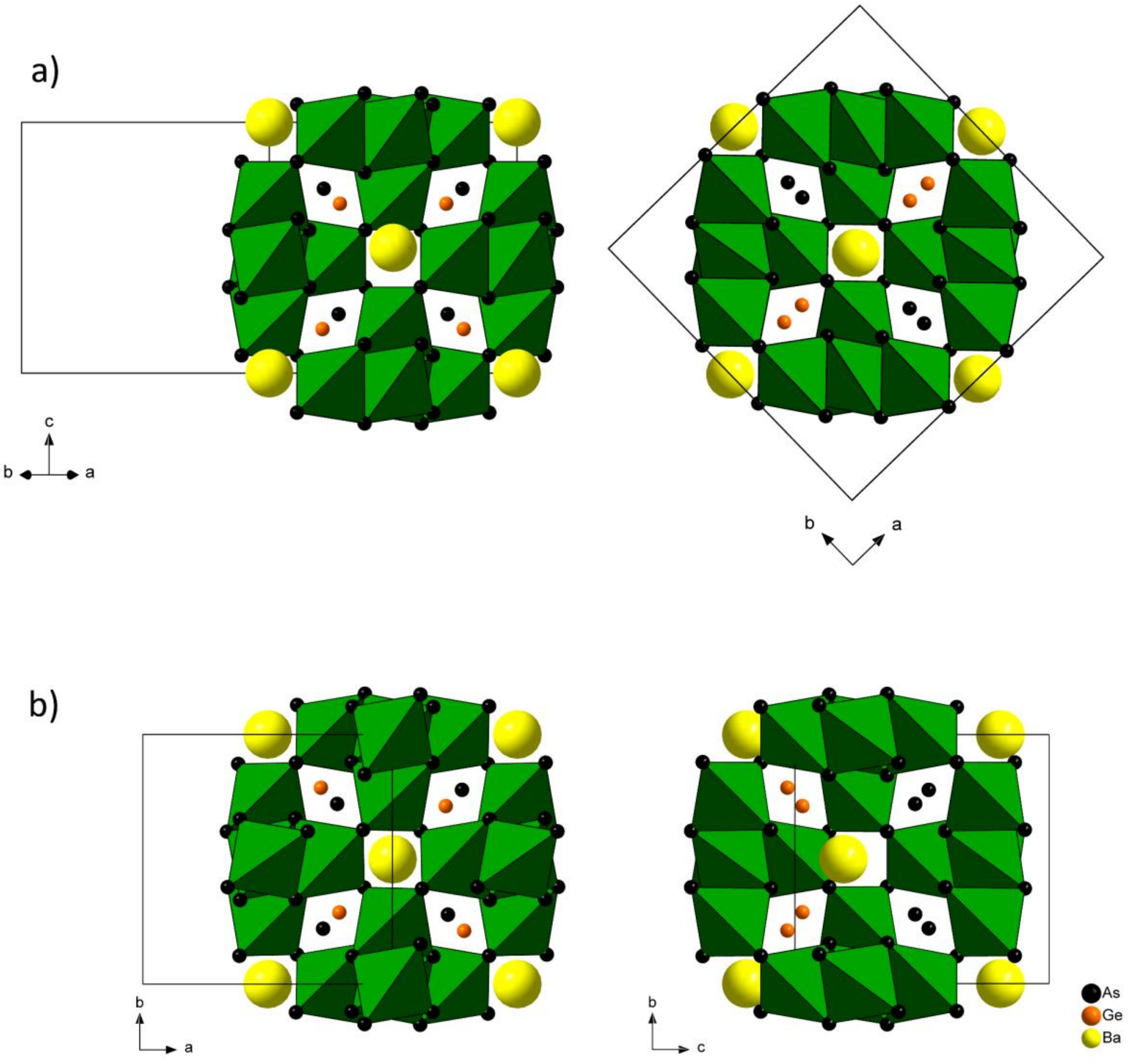

Figure A.27: Unit cells of BaGe$_8$As$_{14}$ in the symmetry reduced space groups (a) *Fmm*2 (no. 42) and (b) $P\bar{4}2_1m$ (no. 113) with ordered Ge-As positions and the Barium shifted off its central position.

Table A.51: Calculated structural parameters of o*F*-BaGe$_8$As$_{14}$ in the space group *Fmm*2 (no. 42) (PBEsol).

Lattice parameters: *a* = 14.4840 Å; *b* = 14.5084 Å; *c* = 10.3896 Å

Atom	Wyckoff	*x*	*y*	*z*
Ba	4*a*	0	0	0
Ge1	16*e*	0.1277	0.1251	0.4573
Ge2	8*d*	0.2147	0	0.1759
Ge3	8*b*	1/4	1/4	0.2355
As1	16*e*	0.1132	0.2253	0.0711
As2	16*e*	0.2752	0.1132	0.343
As3	8*d*	0.3849	0	0.1156
As4	8*c*	0	0.115	0.2999

Table A.52: Calculated parameters of tP-$BaGe_8As_{14}$ in the space group $P\bar{4}2_1m$ (no. 113) (PBEsol).

Lattice parameters: a = 10.2452 Å; c = 10.4476 Å

Atom	Wyckoff	*x*	*y*	*z*
Ba	2*c*	0	1/2	0.19110
Ge1	8*f*	0.24630	0.00080	0.24960
Ge2	4*e*	0.21310	0.71310	0.02970
Ge3	2*b*	0	0	1/2
Ge3	2*a*	0	0	0
As1	8*f*	0.11180	0.16030	0.13460
As2	8*f*	0.16320	0.11060	0.63700
As3	4*e*	0.11320	0.61320	0.59180
As4	4*e*	0.61805	0.11805	0.09520
As5	4*e*	0.72180	0.22180	0.52670

Table A.53: Calculated band gaps of AGe_7As_{15} and oF-/tP-$BaGe_8As_{14}$ with different potentials.

compound	PBEsol	PBE	SCAN
RbGe7As15	0.45	0.42	0.78
CsGe7As15	0.58	0.70	0.96
oF-BaGe8As14	0.28	0.35	0.59
tP-BaGe8As14	0.46	0.53	0.78

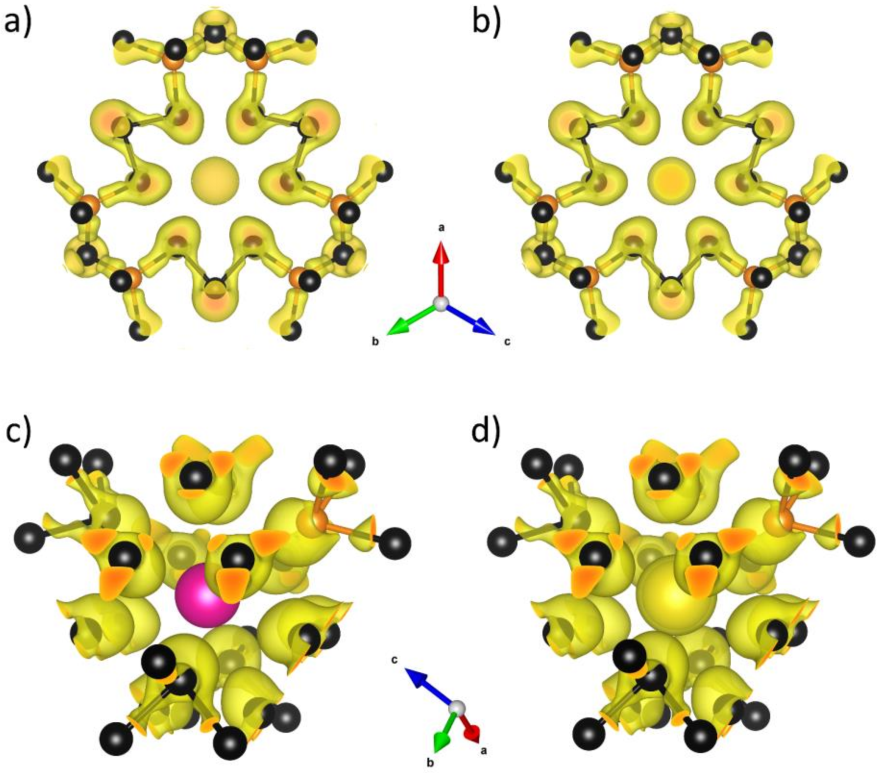

Figure A.28: Electron location function (ELF) of $RbGe_7As_{15}$ (a,d) and $CsGe_7As_{15}$ (b, d) (Isosurfaces at ELF = 0.78). The sodalite framework (a, b) with $GeAs_4$ tetrahedra and $AsAs_3$ units displays a covalent character with electron density located on all drawn bonds. A close-up of the A-coordination sphere displays the lone pairs of either the $GeAs_3$ unit, $AsAs_3$ unit or vertices of the $GeAs_4$ tetrahedra.

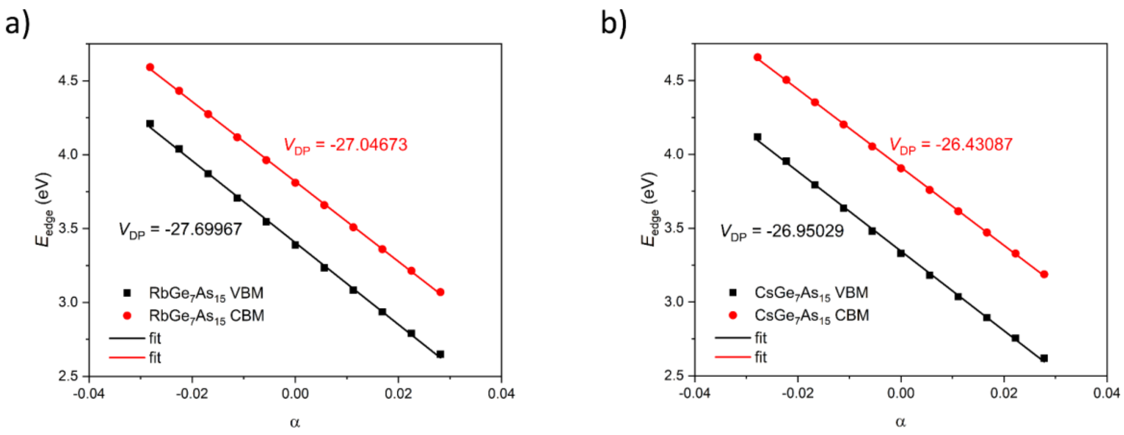

Figure A.29: Change in energy of the valence band maximum *VBM* or the conduction band minimum *CBM* in respect to a relative change of the *a*-axis of (a) $RbGe_7As_{15}$ and (b) $CsGe_7As_{15}$.

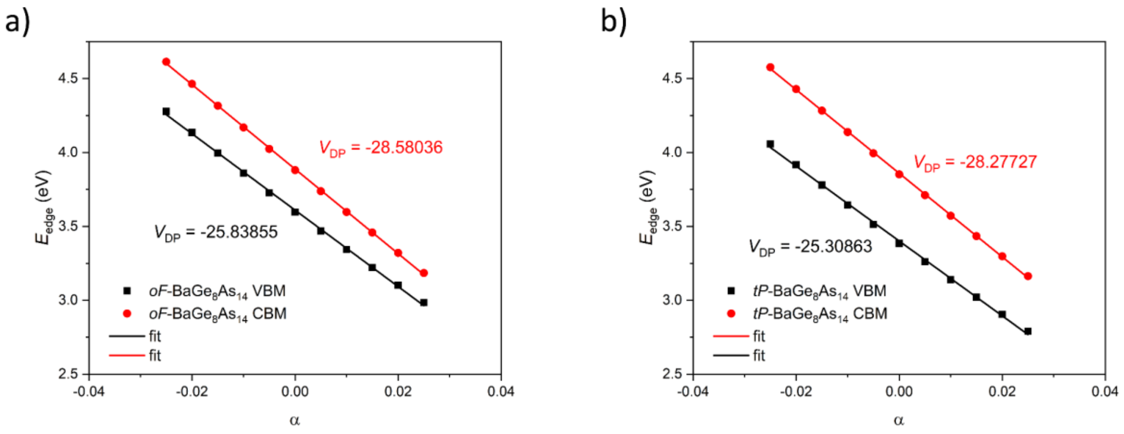

Figure A.30: Change in energy of the valence band maximum *VBM* or the conduction band minimum *CBM* in respect to a relative change of the *a*-axis of (a) *oF*-$BaGe_8As_{14}$ and (b) *tP*-$BaGe_8As_{14}$.

Table A.54: Calculated and experimental electrical conductivity at 300 K and similar carrier concentration.[3]

compound	σ_{DFT} (S/m)	p-doping$_{DFT}$ (cm-3)	σ_{exp} (S/m)	p-doping$_{exp}$ (cm-3)
$RbGe_7As_{15}$	$2.79\cdot10^4$	$1.29585\cdot10^{20}$	$1.23\cdot10^4$	$1.33\cdot10^{20}$
$CsGe_7As_{15}$	$1.80\cdot10^4$	$7.9837\cdot10^{19}$	$2.73\cdot10^4$	$8.20\cdot10^{19}$
oF-$BaGe_8As_{14}$	$1.10\cdot10^5$	$1.57037\cdot10^{20}$	$4.29\cdot10^3$	$1.63\cdot10^{20}$
tP-$BaGe_8As_{14}$	$4.20\cdot10^4$	$1.61242\cdot10^{20}$		

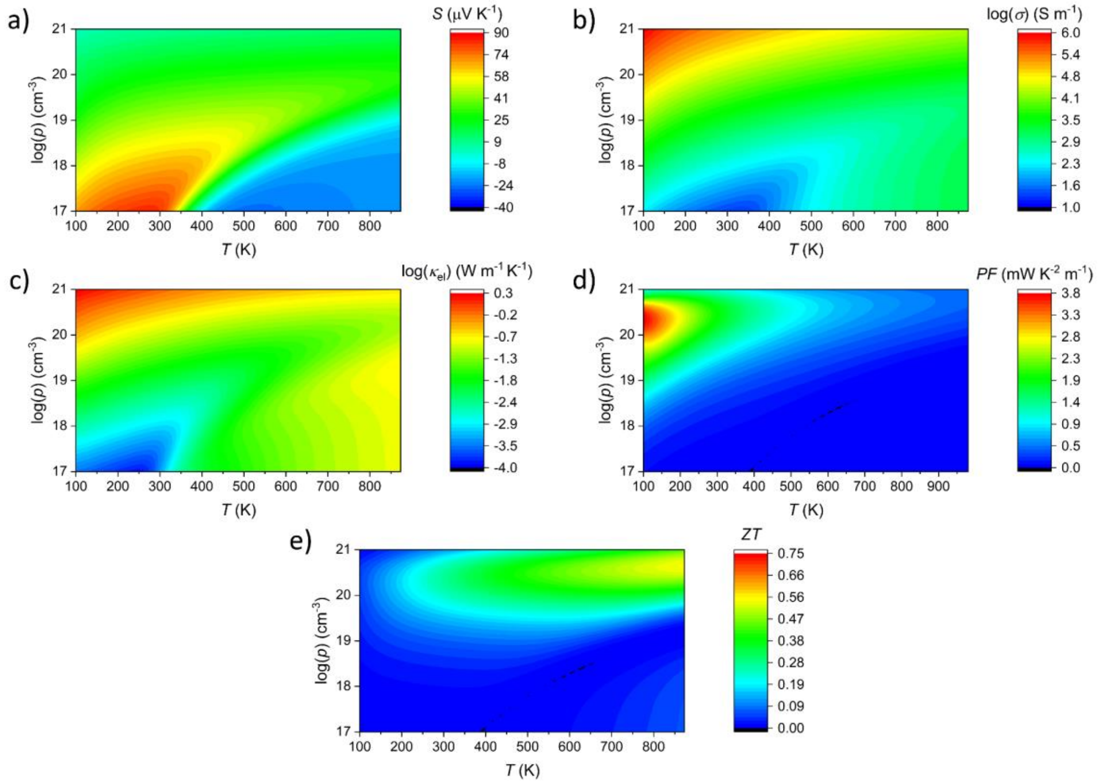

Figure A.31: (a) Seebeck coefficient *S*, (b) electrical conductivity log(*σ*), (c) electronic thermal conductivity log(κ_{el}), (d) Power Factor *PF* and (e) figure of merit *ZT* of *p*-type $RbGe_7As_{15}$ between 100 and 873 K and hole concentrations between $1\cdot10^{17}$ and $1\cdot10^{20}$ cm^{-3}.

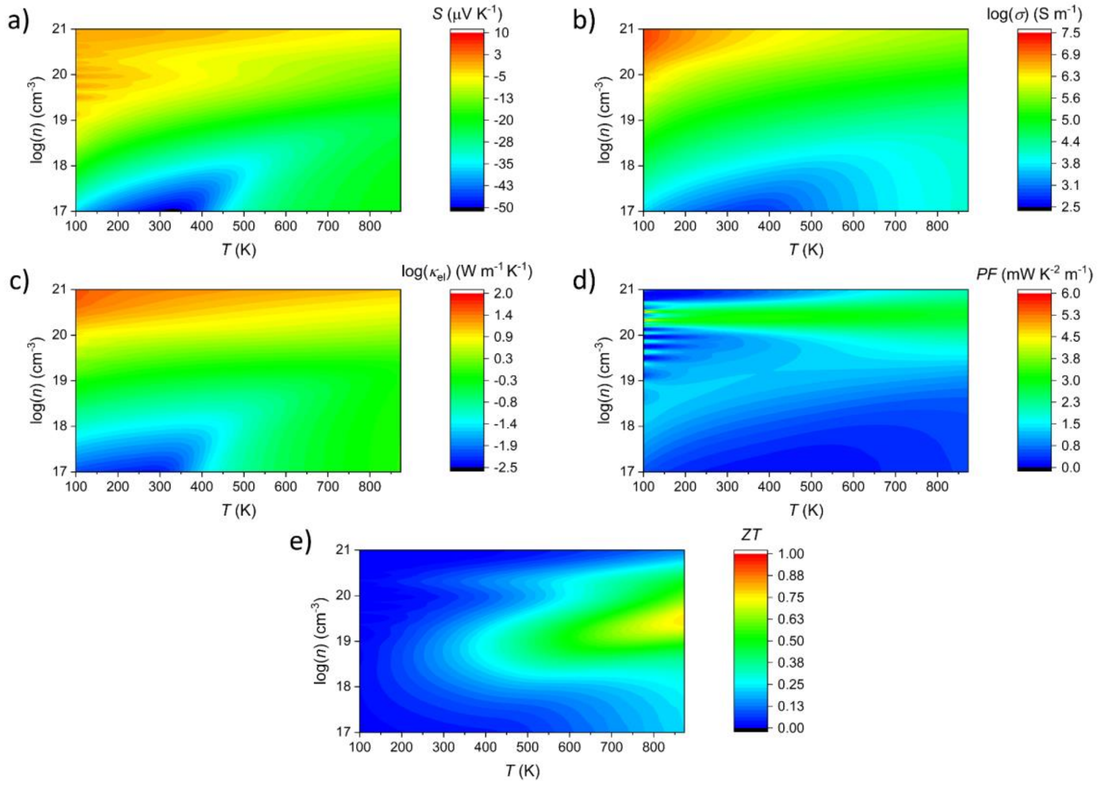

Figure A.32: (a) Seebeck coefficient *S*, (b) electrical conductivity log(*σ*), (c) electronic thermal conductivity log(κ_{el}), (d) Power Factor *PF* and (e) figure of merit *ZT* of *n*-type $RbGe_7As_{15}$ between 100 and 873 K and electron concentrations between $1\cdot10^{17}$ and $1\cdot10^{20}$ cm^{-3}.

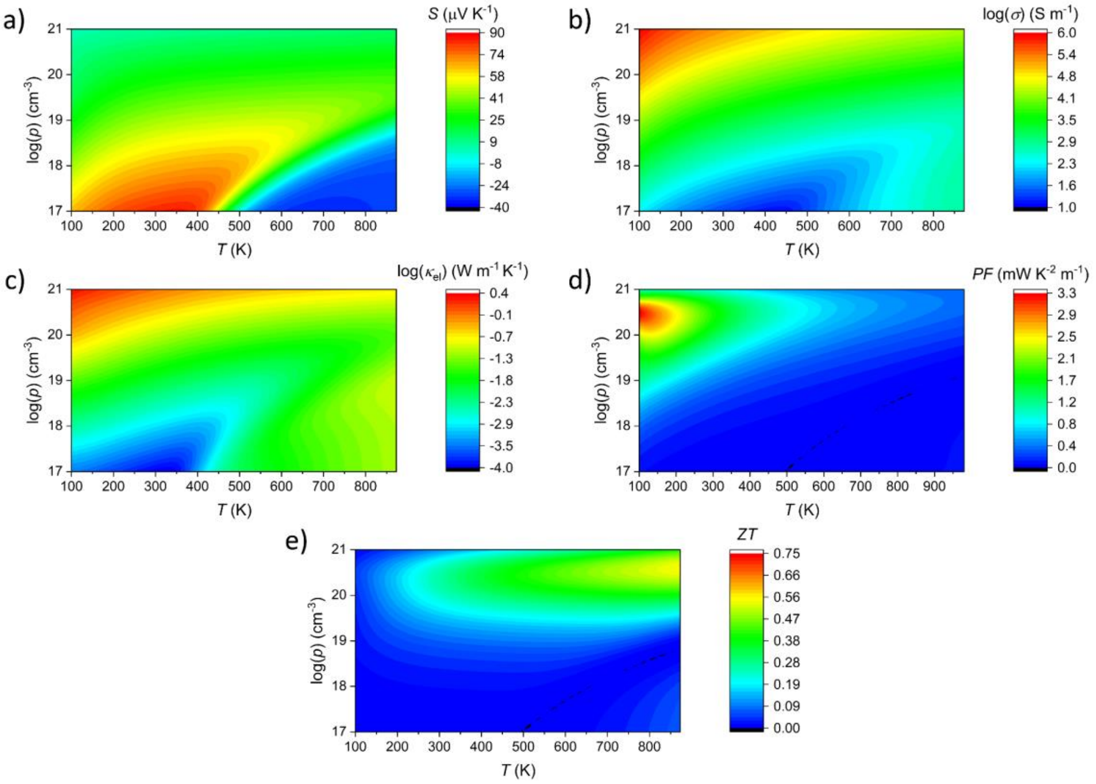

Figure A.33: (a) Seebeck coefficient S, (b) electrical conductivity log(σ), (c) electronic thermal conductivity log(κ_{el}), (d) Power Factor PF and (e) figure of merit ZT of p-type $CsGe_7As_{15}$ between 100 and 873 K and hole concentrations between $1 \cdot 10^{17}$ and $1 \cdot 10^{20}$ cm^{-3}.

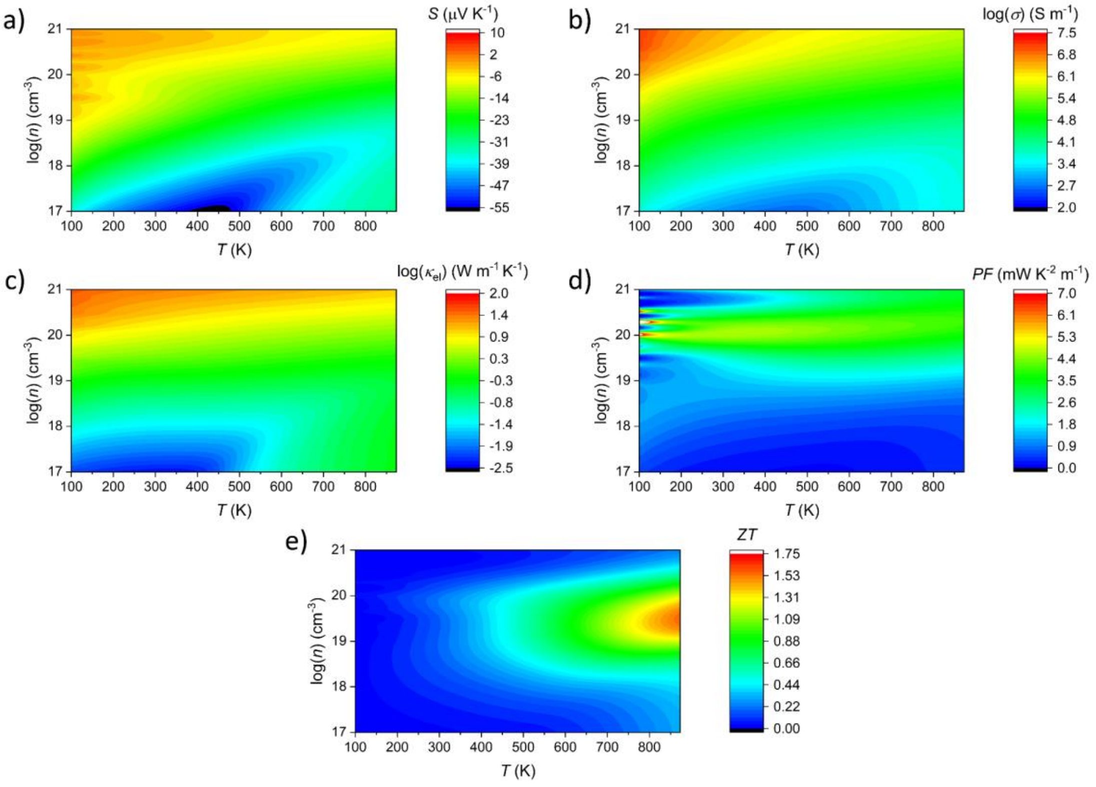

Figure A.34: (a) Seebeck coefficient S, (b) electrical conductivity log(σ), (c) electronic thermal conductivity log(κ_{el}), (d) Power Factor PF and (e) figure of merit ZT of n-type $CsGe_7As_{15}$ between 100 and 873 K and electron concentrations between $1 \cdot 10^{17}$ and $1 \cdot 10^{20}$ cm^{-3}.

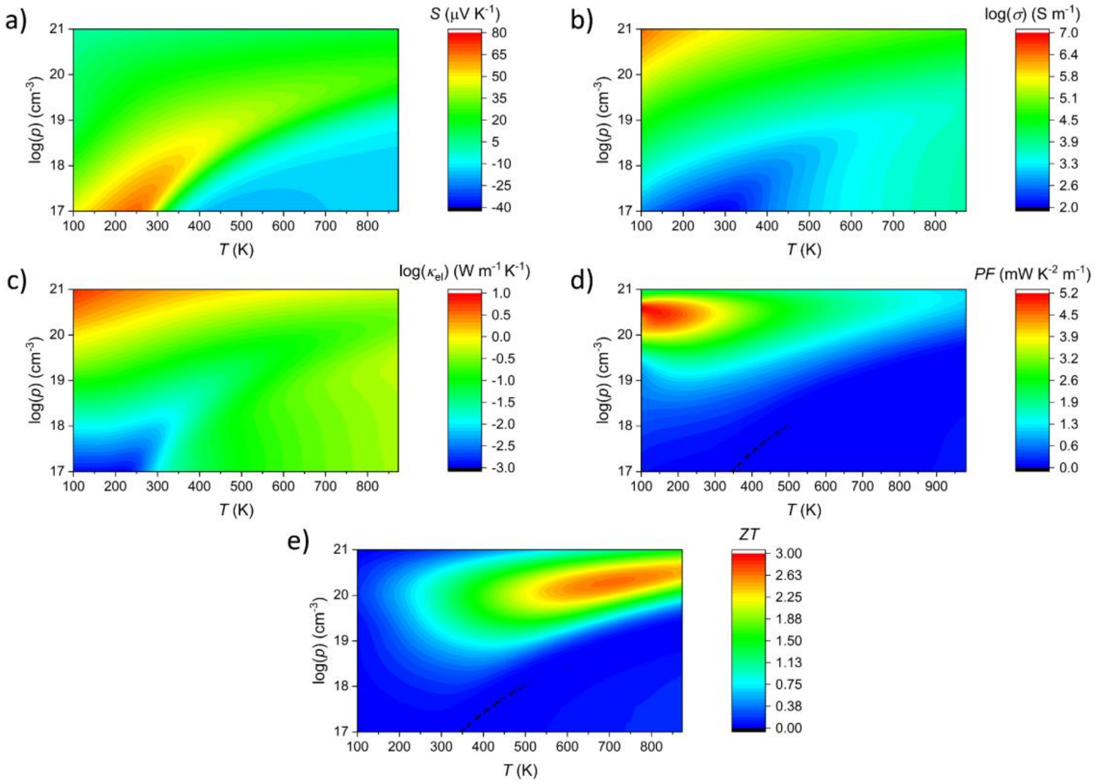

Figure A.35: (a) Seebeck coefficient *S*, (b) electrical conductivity log(σ), (c) electronic thermal conductivity log(κ_{el}), (d) Power Factor *PF* and (e) figure of merit *ZT* of *p*-type *oF*-$\mathrm{BaGe_8As_{16}}$ between 100 and 873 K and hole concentrations between $1\cdot10^{17}$ and $1\cdot10^{20}$ cm^{-3}.

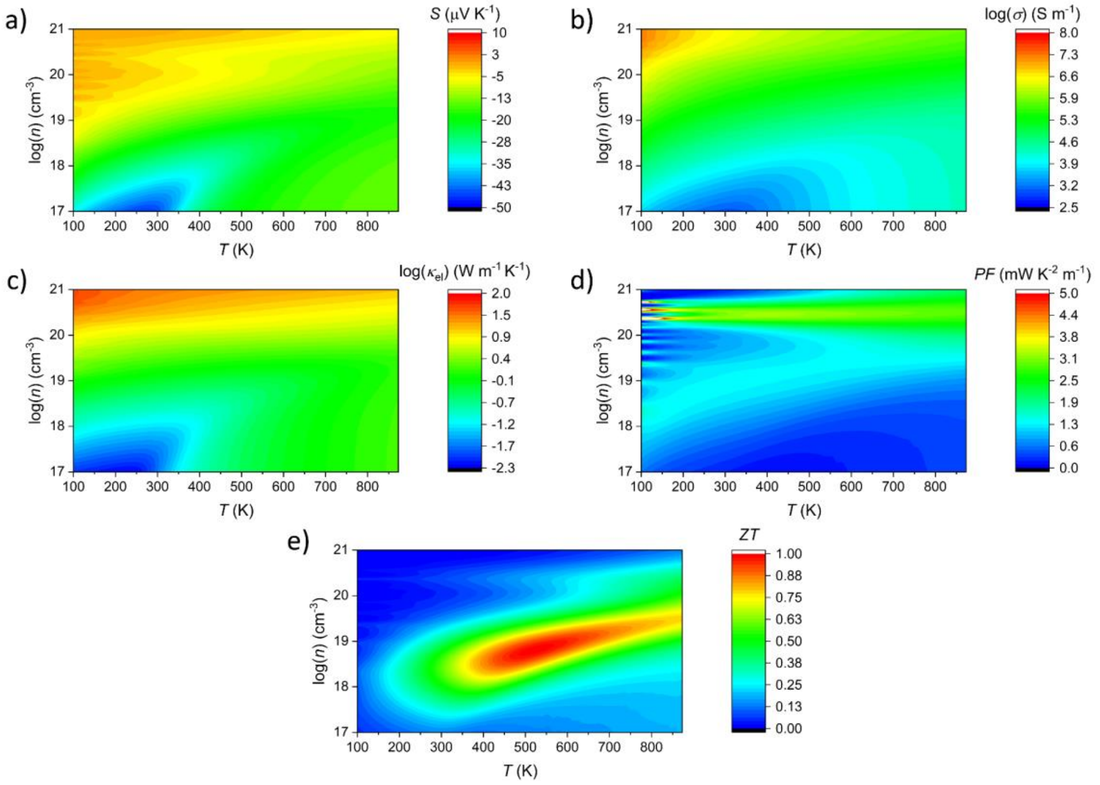

Figure A.36: (a) Seebeck coefficient *S*, (b) electrical conductivity log(σ), (c) electronic thermal conductivity log(κ_{el}), (d) Power Factor *PF* and (e) figure of merit *ZT* of *n*-type *oF*-$\mathrm{BaGe_8As_{16}}$ between 100 and 873 K and electron concentrations between $1\cdot10^{17}$ and $1\cdot10^{20}$ cm^{-3}.

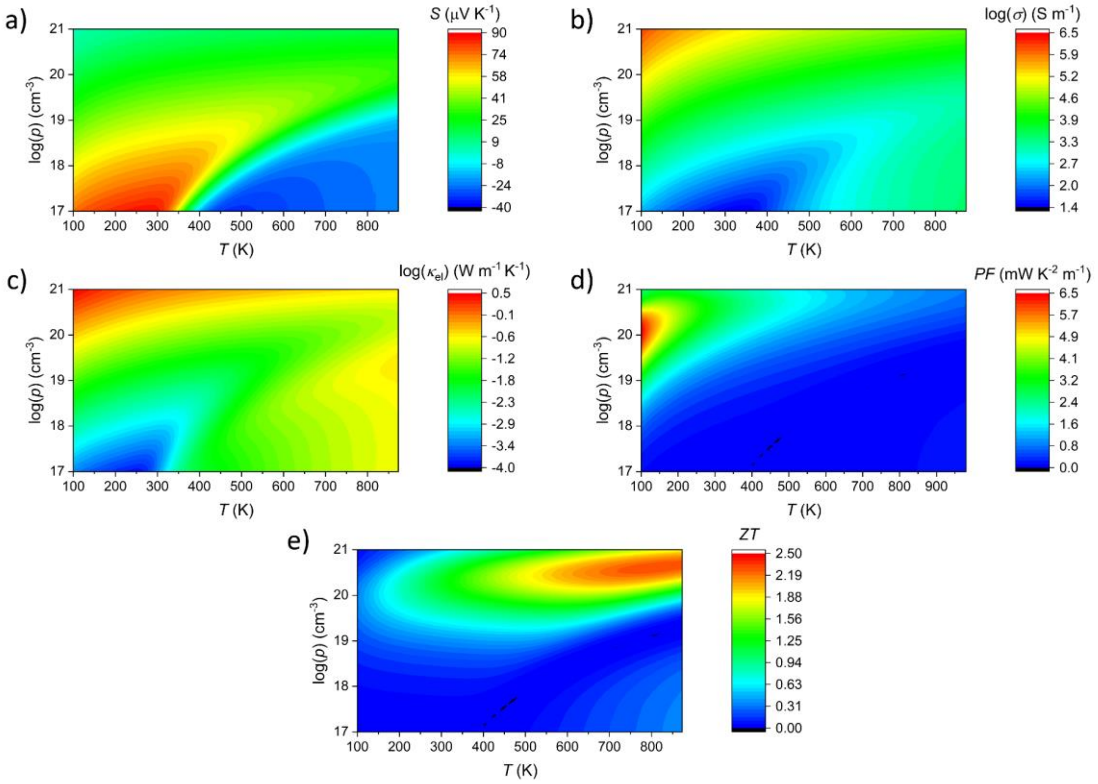

Figure A.37: (a) Seebeck coefficient *S*, (b) electrical conductivity log(σ), (c) electronic thermal conductivity log(κ_{el}), (d) Power Factor *PF* and (e) figure of merit *ZT* of *p*-type *tP*-$BaGe_8As_{16}$ between 100 and 873 K and hole concentrations between $1\cdot10^{17}$ and $1\cdot10^{20}$ cm^{-3}.

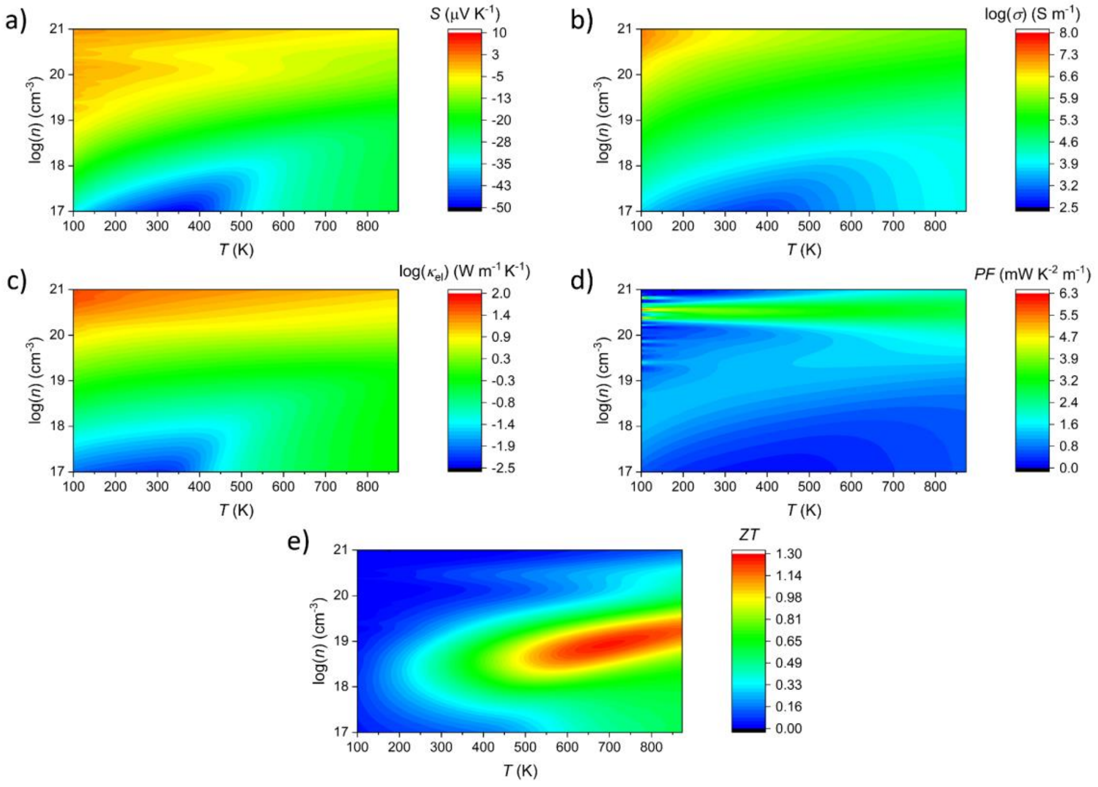

Figure A.38: (a) Seebeck coefficient *S*, (b) electrical conductivity log(σ), (c) electronic thermal conductivity log(κ_{el}), (d) Power Factor *PF* and (e) figure of merit *ZT* of *n*-type *tP*-$BaGe_8As_{16}$ between 100 and 873 K and electron concentrations between $1\cdot10^{17}$ and $1\cdot10^{20}$ cm^{-3}.

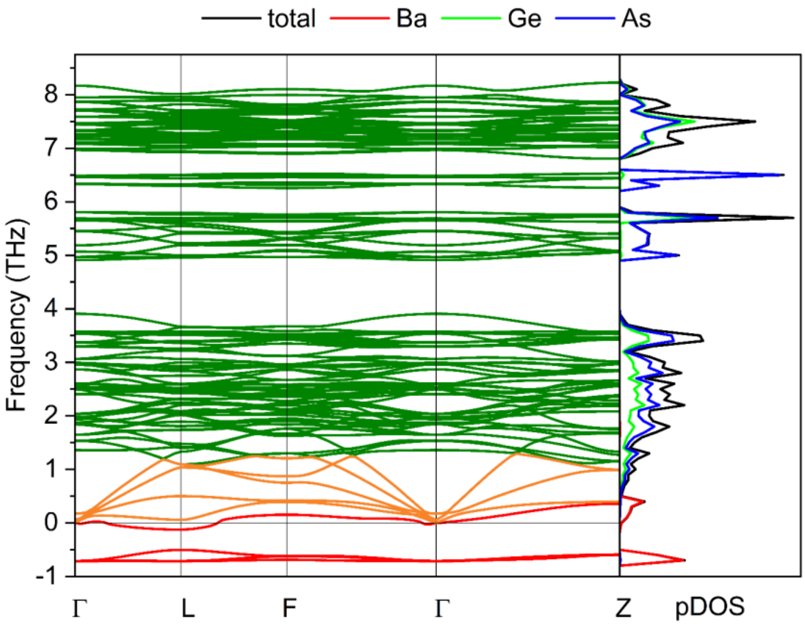

Figure A.39: Calculated phonon spectrum of $BaGe_8As_{14}$-*hR*-1 with optical (green), acoustic (orange) and imaginary (red) modes and the projected phonon DOS (pDOS).

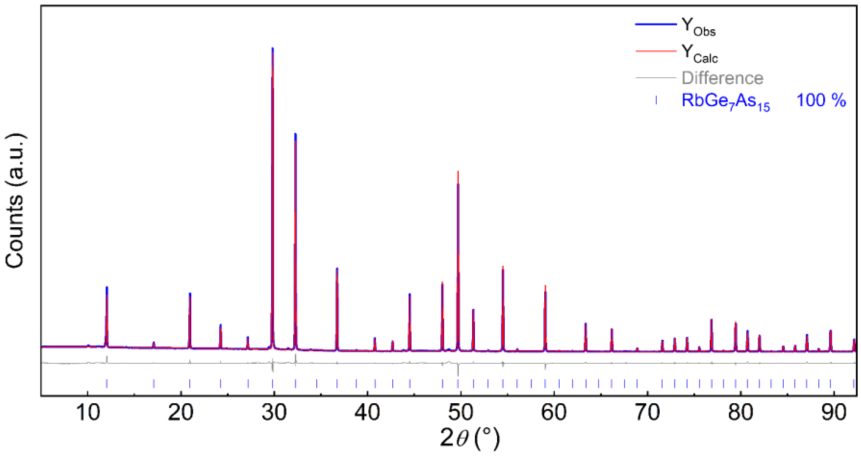

Figure A.40: Powder X-ray diffraction pattern ($Cu_{K\alpha1}$) and Rietveld refinement of $RbGe_7As_{15}$.

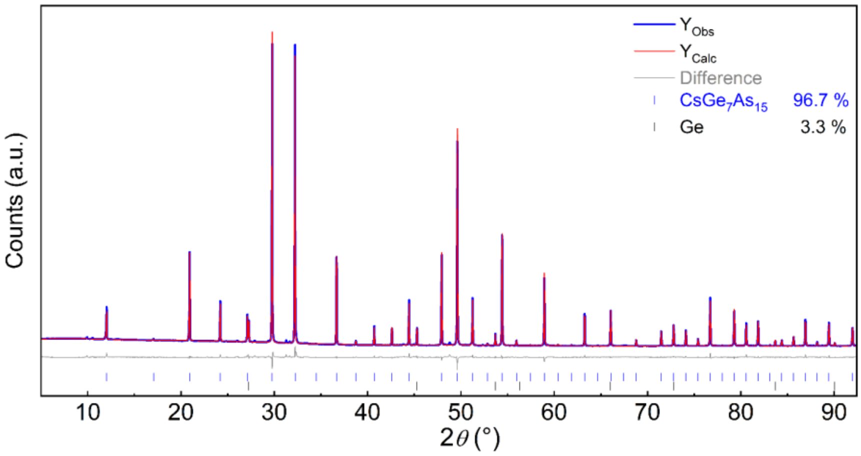

Figure A.41: Powder X-ray diffraction pattern ($Cu_{K\alpha1}$) and Rietveld refinement of $CsGe_7As_{15}$.

Table A.55: Powder X-ray diffraction data of $RbGe_7As_{15}$ and $CsGe_7As_{15}$ from Rietveld refinement.

formula	$RbGe_7As_{15}$	$CsGe_7As_{15}$
space group	$I\bar{4}3m$ (No. 217)	
a / Å	10.370667(46)	10.385859(205)
V_{cell} / Å^3	1115.373(15)	1120.282(66)
Z	2	
$\rho_{X\text{-ray}}$ / g cm^{-3}	5.11475(7)	5.2330(3)
diffractometer	Stoe Stadi P	
radiation type (λ / nm)	$Cu_{K\alpha1}$ (1.54056)	
T / K	293	
μ / mm^{-1}	37.834(5)	47.502(3)
2Θ-range / °	5 - 92.420	5 – 92.420
parameters (incl. side phases)	27	30
background parameter	12	12
R_p / R_{wp}	4.144 / 5.864	3.525 / 5.332
R_{exp} / R_{Bragg}	2.186 / 2.841	1.211 / 2.729
GooF	2.683	4.403

A.4 Supertetrahedral Layers Based on GaAs or InAs

Table A.56: Crystallographic data of $Sr_{15}Ga_{22}As_{32}$, $Eu_{15}Ga_{22}As_{32}$, $Sr_{15}In_{22}As_{32}$, $Eu_{15}In_{22}As_{32}$, $Sr_3Ga_6As_8$ and $Eu_3Ga_6As_8$.

formula	$Sr_{15}Ga_{22}As_{32}$	$Eu_{15}Ga_{22}As_{32}$	$Sr_{15}In_{22}As_{32}$	$Eu_{15}In_{22}As_{32}$	$Sr_3Ga_6As_8$	$Eu_3Ga_6As_8$
space group	$C2/c$ (No. 15)	$C2/c$ (No. 15)	$C2/c$ (No. 15)	$C2/c$ (No. 15)	$C2/c$ (No. 15)	$C2/c$ (No. 15)
a / Å	22.9660 (4)	22.8204 (7)	23.838 (5)	23.703 (2)	22.8363 (13)	22.740 (3)
b / Å	22.9639 (3)	22.8257 (7)	23.818 (4)	23.702 (2)	22.8335 (13)	22.747 (3)
c / Å	19.8929 (3)	19.7972 (6)	20.763 (4)	22.337 (2)	26.8169 (15)	25.505 (3)
β / °	98.2290 (10)	98.2370 (10)	98.244 (6)	113.473 (2)	108.613 (2)	96.393 (2)
V_{cell} / Å^3	10383.3 (3)	10205.8 (5)	11667 (4)	11511 (2)	13251.8 (13)	13111 (3)
Z	6	6	6	6	32	32
$\rho_{X\text{-}Ray}$ / g cm^{-3}	5.033	6.063	5.327	6.235	5.135	5.972
μ / mm^{-1}	35.032	37.581	30.080	32.208	35.004	36.993
Θ-range / °	2.311 - 31.506	2.323 - 24.757	2.428 - 30.034	2.120 - 26.453	2.283 - 27.878	2.277 - 25.681
refl. measured	199392	9028	239129	13073	260459	107875
independent refl.	17301	9028	17058	13073	15797	12444
Parameters	498	478	477	498	273	273
R_σ	0.0356	0.0328	0.0171	0.0372	0.0668	0.0470
R_{int}	0.0719	-	0.0418	-	0.1297	0.0800
R_1 ($F^2 > 2\sigma(F^2)$) / all	0.0365/0.0793	0.0724/0.0926	0.0403/0.0535	0.0553/0.0749	0.1159/0.1884	0.1306/0.1663
wR_2 ($F^2 > 2\sigma(F^2)$) / all	0.0642/0.0765	0.1573/0.1674	0.0853/0.0912	0.1499/0.1640	0.3198/0.3773	0.2890/0.3120
GooF	1.011	1.085	1.044	1.059	1.067	1.177
$\Delta\rho_{max/min}$ / eÅ^{-3}	+1.594/-1.877	+4.783/-4.542	+7.071/-3.141	+6.113/-4.099	+16.374/-5.380	+9.028/-9.518
restraints	1	1	1	1	-	-
twin law	-	-1 0 0 0 -1 0 1/4 0 1	-	-1 0 0 0 -1 0 3/4 0 1	-	-
BASF	-	0.09575	-	0.34734	-	-

Table A.57: Atomic coordinates, equivalent displacement parameters (Å^2) and site occupancy factors (*sof*) of $Sr_{15}Ga_{22}As_{32}$.

atom	Wyckoff	x	y	z	U_{eq}	*sof*
Sr1	8f	0.01099(2)	0.06443(2)	0.57952(3)	0.01144(10)	1
Sr2	8f	0.13730(2)	0.06004(2)	0.07302(3)	0.01070(10)	1
Sr3	8f	0.18075(2)	0.37805(2)	0.42714(3)	0.01073(10)	1
Sr4	8f	0.26150(2)	0.18603(2)	0.07731(3)	0.01125(10)	1
Sr5	8f	0.30453(2)	0.25108(2)	0.42054(3)	0.01137(10)	1
Sr6	8f	0.31207(3)	0.03174(3)	0.23334(3)	0.01690(12)	1
Sr7	8f	0.31421(3)	0.40555(3)	0.26632(3)	0.01666(12)	1
Sr8	8f	0.38566(2)	0.31161(2)	0.08082(3)	0.01111(11)	1
Sr9	8f	0.4123(5)	0.1777(8)	0.2277(4)	0.069(4)	0.174(9)
Sr10	8f	0.4197(2)	0.2660(3)	0.26921(13)	0.075(2)	0.370(6)
Sr11	8f	0.4434(4)	0.1407(4)	0.23067(14)	0.100(3)	0.434(9)
Sr12	8f	0.44572(2)	0.00178(2)	0.07716(3)	0.01112(10)	1
Sr13	8f	0.4589(5)	0.3024(3)	0.26974(19)	0.085(3)	0.271(6)
Sr14	8f	0.57152(2)	0.12577(2)	0.08101(3)	0.01086(10)	1

Ga1	8f	0.01726(3)	0.09631(3)	0.39072(3)	0.00901(12)	1
Ga2	8f	0.01773(3)	0.34228(3)	0.39103(3)	0.00894(12)	1
Ga3	8f	0.03576(3)	0.21920(3)	0.54000(3)	0.01204(13)	1
Ga4	8f	0.10558(3)	0.21888(3)	0.10899(3)	0.00890(12)	1
Ga5	8f	0.10734(3)	0.46497(3)	0.11267(3)	0.01047(13)	1
Ga6	8f	0.12272(3)	0.34213(3)	0.24718(3)	0.00878(13)	1
Ga7	8f	0.12381(3)	0.09568(3)	0.25289(3)	0.00884(13)	1
Ga8	8f	0.14035(3)	0.21931(3)	0.39079(3)	0.00884(12)	1
Ga9	8f	0.16042(3)	0.09387(3)	0.53390(3)	0.01047(12)	1
Ga10	8f	0.22863(3)	0.34372(3)	0.11261(3)	0.01081(13)	1
Ga11	8f	0.24512(3)	0.21877(3)	0.24980(3)	0.00919(12)	1
Ga12	8f	0.26412(3)	0.09379(3)	0.38563(3)	0.01038(13)	1
Ga13	8f	0.28544(3)	0.03131(3)	0.03160(3)	0.01035(12)	1
Ga14	8f	0.35759(3)	0.47207(3)	0.11431(3)	0.01047(13)	1
Ga15	8f	0.41151(3)	0.15675(3)	0.03824(3)	0.01334(13)	1
Ga16	4e	0	0.21904(4)	1/4	0.00823(17)	1
Ga17	4e	0	0.46405(4)	1/4	0.00905(17)	1
Ga18	4e	0	0.97371(4)	1/4	0.00944(17)	1
As1	8f	0.03391(2)	0.40619(3)	0.03436(3)	0.00747(11)	1
As2	8f	0.03670(2)	0.15593(3)	0.03229(3)	0.00714(11)	1
As3	8f	0.05205(2)	0.28021(3)	0.17817(3)	0.00727(11)	1
As4	8f	0.05541(2)	0.03320(3)	0.17792(3)	0.00813(11)	1
As5	8f	0.07009(2)	0.15796(3)	0.32148(3)	0.00756(11)	1
As6	8f	0.07346(2)	0.40516(3)	0.32213(3)	0.00811(11)	1
As7	8f	0.08774(2)	0.03100(2)	0.46297(3)	0.00762(11)	1
As8	8f	0.09008(2)	0.28272(3)	0.46779(3)	0.00703(11)	1
As9	8f	0.10823(2)	0.15562(3)	0.61108(3)	0.01019(11)	1
As10	8f	0.16018(2)	0.53188(2)	0.04008(3)	0.00725(11)	1
As11	8f	0.16042(2)	0.27972(3)	0.03444(3)	0.00762(11)	1
As12	8f	0.17699(2)	0.15460(3)	0.17769(3)	0.00811(11)	1
As13	8f	0.18038(2)	0.40758(3)	0.18641(3)	0.00846(11)	1
As14	8f	0.19495(2)	0.28347(3)	0.32194(3)	0.00787(11)	1
As15	8f	0.19712(2)	0.02998(3)	0.31228(3)	0.00850(12)	1
As16	8f	0.21458(2)	0.15776(3)	0.46299(3)	0.00746(11)	1
As17	8f	0.23267(2)	0.03099(3)	0.60828(3)	0.00885(11)	1
As18	8f	0.28658(2)	0.40540(2)	0.03992(3)	0.00719(11)	1
As19	8f	0.30277(3)	0.28253(3)	0.18469(3)	0.01104(12)	1
As20	8f	0.32032(3)	0.15523(3)	0.31335(3)	0.01047(12)	1
As21	8f	0.35657(2)	0.09284(3)	0.10913(3)	0.00974(11)	1
As22	8f	0.42794(3)	0.40688(3)	0.18646(3)	0.01071(12)	1
As23	8f	0.44498(3)	0.03017(3)	0.31522(3)	0.01085(12)	1
As24	8f	0.48330(3)	0.21863(3)	0.11979(3)	0.01714(13)	1

Table A.58: Anisotropic displacement parameters (Å^2) of $Sr_{15}Ga_{22}As_{32}$.

atom	U_{11}	U_{22}	U_{33}	U_{23}	U_{13}	U_{12}
Sr1	0.0103(3)	0.0114(3)	0.0127(2)	0.0032(2)	0.00196(19)	0.0014(2)

Sr2	0.0103(3)	0.0106(3)	0.0113(2)	-0.0009(2)	0.00204(19)	-0.0007(2)
Sr3	0.0100(3)	0.0109(3)	0.0111(2)	-0.0005(2)	0.00078(19)	0.0005(2)
Sr4	0.0116(3)	0.0102(3)	0.0127(2)	0.0000(2)	0.00424(19)	-0.0009(2)
Sr5	0.0103(2)	0.0102(3)	0.0127(2)	0.0001(2)	-0.00163(19)	0.0010(2)
Sr6	0.0196(3)	0.0203(3)	0.0108(2)	0.0009(2)	0.0021(2)	-0.0017(2)
Sr7	0.0183(3)	0.0197(3)	0.0114(2)	0.0012(2)	0.0002(2)	0.0026(2)
Sr8	0.0103(3)	0.0107(3)	0.0125(2)	-0.0002(2)	0.00246(19)	-0.0016(2)
Sr9	0.080(6)	0.099(9)	0.030(3)	0.013(4)	0.013(3)	-0.052(6)
Sr10	0.072(3)	0.125(5)	0.0241(12)	0.0007(17)	-0.0025(13)	0.058(3)
Sr11	0.162(6)	0.110(4)	0.0234(12)	0.0153(17)	-0.0080(18)	-0.095(4)
Sr12	0.0098(2)	0.0110(3)	0.0124(2)	0.0026(2)	0.00130(19)	-0.0004(2)
Sr13	0.147(8)	0.081(4)	0.0235(18)	0.011(2)	0.005(3)	0.056(5)
Sr14	0.0101(3)	0.0104(3)	0.0120(2)	0.0007(2)	0.00130(19)	-0.0011(2)
Ga1	0.0093(3)	0.0093(3)	0.0084(3)	0.0003(2)	0.0010(2)	0.0006(2)
Ga2	0.0088(3)	0.0094(3)	0.0086(3)	0.0000(2)	0.0009(2)	0.0006(2)
Ga3	0.0103(3)	0.0103(3)	0.0152(3)	0.0010(3)	0.0008(2)	-0.0004(3)
Ga4	0.0090(3)	0.0094(3)	0.0082(3)	-0.0002(2)	0.0009(2)	-0.0007(3)
Ga5	0.0112(3)	0.0111(3)	0.0088(3)	0.0012(2)	0.0004(2)	-0.0015(3)
Ga6	0.0087(3)	0.0097(3)	0.0077(3)	0.0002(2)	0.0005(2)	0.0009(2)
Ga7	0.0089(3)	0.0090(3)	0.0086(3)	0.0002(2)	0.0011(2)	-0.0002(2)
Ga8	0.0087(3)	0.0093(3)	0.0083(3)	-0.0001(2)	0.0002(2)	0.0006(3)
Ga9	0.0099(3)	0.0103(3)	0.0110(3)	0.0006(2)	0.0007(2)	-0.0005(2)
Ga10	0.0112(3)	0.0117(3)	0.0097(3)	-0.0005(2)	0.0021(2)	-0.0020(3)
Ga11	0.0093(3)	0.0106(3)	0.0075(3)	0.0001(2)	0.0006(2)	-0.0004(2)
Ga12	0.0100(3)	0.0115(3)	0.0093(3)	-0.0007(2)	0.0001(2)	0.0010(3)
Ga13	0.0104(3)	0.0102(3)	0.0106(3)	0.0004(2)	0.0018(2)	0.0006(2)
Ga14	0.0114(3)	0.0109(3)	0.0093(3)	-0.0009(2)	0.0019(2)	-0.0013(3)
Ga15	0.0117(3)	0.0124(3)	0.0163(3)	0.0010(3)	0.0033(2)	0.0008(3)
Ga16	0.0080(4)	0.0083(4)	0.0083(4)	0	0.0009(3)	0
Ga17	0.0099(4)	0.0097(4)	0.0075(4)	0	0.0011(3)	0
Ga18	0.0095(4)	0.0105(4)	0.0082(4)	0	0.0006(3)	0
As1	0.0073(3)	0.0080(3)	0.0073(2)	0.0001(2)	0.0014(2)	-0.0008(2)
As2	0.0065(3)	0.0077(3)	0.0070(2)	-0.0001(2)	0.0003(2)	-0.0012(2)
As3	0.0071(3)	0.0076(3)	0.0071(2)	0.0004(2)	0.0011(2)	-0.0004(2)
As4	0.0081(3)	0.0087(3)	0.0074(2)	-0.0005(2)	0.0006(2)	-0.0024(2)
As5	0.0075(3)	0.0083(3)	0.0066(2)	0.0001(2)	0.0002(2)	0.0005(2)
As6	0.0083(3)	0.0088(3)	0.0071(2)	-0.0005(2)	0.0007(2)	0.0019(2)
As7	0.0067(3)	0.0080(3)	0.0078(2)	0.0004(2)	0.0000(2)	0.0006(2)
As8	0.0068(3)	0.0075(3)	0.0066(2)	0.0005(2)	0.0004(2)	0.0014(2)
As9	0.0098(3)	0.0112(3)	0.0091(3)	0.0010(2)	-0.0002(2)	0.0002(2)
As10	0.0075(3)	0.0071(3)	0.0073(2)	-0.0003(2)	0.0014(2)	-0.0006(2)
As11	0.0077(3)	0.0076(3)	0.0075(2)	0.0008(2)	0.0009(2)	-0.0006(2)
As12	0.0083(3)	0.0089(3)	0.0071(2)	-0.0002(2)	0.0012(2)	-0.0020(2)
As13	0.0085(3)	0.0086(3)	0.0083(3)	0.0004(2)	0.0011(2)	-0.0004(2)
As14	0.0077(3)	0.0085(3)	0.0071(2)	-0.0001(2)	0.0003(2)	0.0017(2)
As15	0.0080(3)	0.0092(3)	0.0082(3)	0.0001(2)	0.0009(2)	0.0007(2)
As16	0.0072(3)	0.0076(3)	0.0075(2)	0.0008(2)	0.0006(2)	0.0007(2)
As17	0.0092(3)	0.0097(3)	0.0075(2)	0.0003(2)	0.0007(2)	0.0011(2)

As18	0.0067(3)	0.0074(3)	0.0074(2)	0.0006(2)	0.0006(2)	-0.0009(2)
As19	0.0119(3)	0.0117(3)	0.0101(3)	0.0004(2)	0.0037(2)	-0.0028(2)
As20	0.0096(3)	0.0117(3)	0.0094(3)	0.0006(2)	-0.0009(2)	0.0025(2)
As21	0.0100(3)	0.0105(3)	0.0087(3)	0.0008(2)	0.0014(2)	-0.0002(2)
As22	0.0110(3)	0.0112(3)	0.0098(3)	-0.0019(2)	0.0008(2)	-0.0032(2)
As23	0.0115(3)	0.0111(3)	0.0102(3)	-0.0020(2)	0.0021(2)	0.0029(2)
As24	0.0124(3)	0.0117(3)	0.0278(3)	0.0011(3)	0.0044(2)	0.0014(2)

Table A.59: Atomic coordinates, equivalent displacement parameters (Å^2) and site occupancy factors (*sof*) of $Eu_{15}Ga_{22}As_{32}$.

atom	Wyckoff	*x*	*y*	*z*	U_{eq}	*sof*
Eu1	8f	0.01088(5)	0.06487(5)	0.58035(6)	0.0097(3)	1
Eu2	8f	0.13758(5)	0.05967(5)	0.07337(6)	0.0091(3)	1
Eu3	8f	0.18102(5)	0.37823(5)	0.42681(6)	0.0089(3)	1
Eu4	8f	0.26231(5)	0.18617(5)	0.07840(6)	0.0099(3)	1
Eu5	8f	0.30452(5)	0.25098(5)	0.42016(6)	0.0097(3)	1
Eu6	8f	0.31275(5)	0.03275(5)	0.23472(6)	0.0156(3)	1
Eu7	8f	0.31436(5)	0.40551(6)	0.26504(6)	0.0164(3)	1
Eu8	8f	0.38529(5)	0.31180(5)	0.07981(6)	0.0098(3)	1
Eu9	8f	0.4278(2)	0.2800(3)	0.26860(15)	0.146(3)	0.692(6)
Eu10	8f	0.4395(3)	0.1426(3)	0.23084(19)	0.170(4)	0.558(6)
Eu11	8f	0.44588(5)	0.00202(5)	0.07754(6)	0.0101(3)	1
Eu12	8f	0.57156(5)	0.12579(5)	0.08047(6)	0.0096(3)	1
Ga1	8f	0.01693(10)	0.09572(11)	0.39127(12)	0.0081(5)	1
Ga2	8f	0.01821(10)	0.34264(10)	0.39175(12)	0.0078(5)	1
Ga3	8f	0.03606(10)	0.21906(11)	0.54164(13)	0.0093(5)	1
Ga4	8f	0.10601(10)	0.21841(11)	0.10826(12)	0.0084(5)	1
Ga5	8f	0.10730(11)	0.46499(11)	0.11128(12)	0.0096(5)	1
Ga6	8f	0.12313(10)	0.34283(11)	0.24667(12)	0.0076(5)	1
Ga7	8f	0.12465(10)	0.09515(11)	0.25355(12)	0.0081(5)	1
Ga8	8f	0.14079(10)	0.21967(11)	0.39153(12)	0.0086(5)	1
Ga9	8f	0.16071(10)	0.09368(11)	0.53496(12)	0.0093(5)	1
Ga10	8f	0.22825(10)	0.34440(11)	0.11128(12)	0.0092(5)	1
Ga11	8f	0.24616(10)	0.21891(10)	0.24973(12)	0.0065(5)	1
Ga12	8f	0.26515(10)	0.09428(11)	0.38679(12)	0.0084(5)	1
Ga13	8f	0.28598(11)	0.03132(11)	0.03346(13)	0.0102(5)	1
Ga14	8f	0.35750(11)	0.47145(11)	0.11322(12)	0.0098(5)	1
Ga15	8f	0.41180(10)	0.15684(11)	0.04033(13)	0.0094(5)	1
Ga16	4e	0	0.21920(15)	1/4	0.0077(7)	1
Ga17	4e	0	0.46490(15)	1/4	0.0069(7)	1
Ga18	4e	0	0.97244(15)	1/4	0.0085(7)	1
As1	8f	0.03340(9)	0.40630(10)	0.03268(11)	0.0063(4)	1
As2	8f	0.03689(9)	0.15540(9)	0.03091(11)	0.0055(4)	1
As3	8f	0.05215(9)	0.28033(10)	0.17769(11)	0.0071(5)	1
As4	8f	0.05610(10)	0.03202(10)	0.17794(11)	0.0079(5)	1
As5	8f	0.07028(9)	0.15782(10)	0.32180(11)	0.0059(5)	1
As6	8f	0.07420(9)	0.40606(10)	0.32249(11)	0.0067(5)	1
As7	8f	0.08720(9)	0.03030(10)	0.46436(11)	0.0072(5)	1

As8	8f	0.09075(9)	0.28328(10)	0.46920(11)	0.0062(5)	1
As9	8f	0.10859(10)	0.15556(10)	0.61271(12)	0.0097(5)	1
As10	8f	0.15923(9)	0.53244(10)	0.03802(11)	0.0062(5)	1
As11	8f	0.16060(9)	0.27955(10)	0.03297(11)	0.0075(5)	1
As12	8f	0.17794(9)	0.15391(10)	0.17769(11)	0.0069(5)	1
As13	8f	0.18094(9)	0.40859(9)	0.18579(11)	0.0066(5)	1
As14	8f	0.19580(9)	0.28421(10)	0.32201(11)	0.0066(5)	1
As15	8f	0.19832(9)	0.02954(10)	0.31324(11)	0.0076(5)	1
As16	8f	0.21539(9)	0.15845(10)	0.46435(11)	0.0060(4)	1
As17	8f	0.23328(10)	0.03094(10)	0.61092(11)	0.0088(5)	1
As18	8f	0.28653(9)	0.40498(10)	0.03765(11)	0.0071(5)	1
As19	8f	0.30323(10)	0.28323(10)	0.18349(12)	0.0114(5)	1
As20	8f	0.32204(10)	0.15567(10)	0.31368(12)	0.0107(5)	1
As21	8f	0.35721(10)	0.09293(10)	0.11168(11)	0.0087(5)	1
As22	8f	0.42800(10)	0.40545(10)	0.18624(12)	0.0104(5)	1
As23	8f	0.44479(10)	0.03070(10)	0.31629(12)	0.0103(5)	1
As24	8f	0.48346(10)	0.21877(10)	0.12295(12)	0.0108(5)	1

Table A.60: Anisotropic displacement parameters (Å^2) of $Eu_{15}Ga_{22}As_{32}$.

atom	U_{11}	U_{22}	U_{33}	U_{23}	U_{13}	U_{12}
Eu1	0.0089(6)	0.0102(6)	0.0101(6)	0.0019(5)	0.0012(4)	0.0014(4)
Eu2	0.0087(6)	0.0095(6)	0.0093(6)	-0.0011(5)	0.0023(4)	-0.0002(4)
Eu3	0.0092(6)	0.0086(6)	0.0084(6)	-0.0008(5)	0.0000(4)	0.0005(4)
Eu4	0.0107(6)	0.0094(6)	0.0104(6)	-0.0002(5)	0.0039(5)	-0.0003(4)
Eu5	0.0099(6)	0.0081(6)	0.0106(6)	-0.0003(5)	-0.0005(5)	-0.0001(4)
Eu6	0.0192(6)	0.0188(7)	0.0090(6)	0.0014(5)	0.0027(5)	0.0018(5)
Eu7	0.0187(7)	0.0194(7)	0.0104(6)	0.0017(5)	-0.0003(5)	0.0000(5)
Eu8	0.0095(6)	0.0090(6)	0.0112(6)	0.0002(5)	0.0022(5)	-0.0013(4)
Eu9	0.191(5)	0.223(6)	0.0165(16)	-0.003(2)	-0.009(2)	0.182(5)
Eu10	0.253(8)	0.236(7)	0.0142(19)	0.017(3)	-0.006(3)	-0.225(7)
Eu11	0.0093(6)	0.0093(6)	0.0119(6)	0.0021(5)	0.0019(5)	0.0003(4)
Eu12	0.0089(6)	0.0090(6)	0.0110(6)	0.0002(5)	0.0018(4)	-0.0011(4)
Ga1	0.0107(12)	0.0084(12)	0.0052(12)	-0.0012(10)	0.0010(10)	0.0004(10)
Ga2	0.0102(12)	0.0075(12)	0.0057(12)	0.0000(10)	0.0007(10)	0.0010(9)
Ga3	0.0089(12)	0.0090(12)	0.0094(12)	0.0007(10)	-0.0009(10)	-0.0006(10)
Ga4	0.0085(12)	0.0091(12)	0.0074(12)	0.0005(10)	0.0009(10)	-0.0022(10)
Ga5	0.0111(12)	0.0119(13)	0.0055(12)	0.0018(10)	-0.0002(10)	-0.0033(10)
Ga6	0.0078(12)	0.0095(13)	0.0047(12)	-0.0006(10)	-0.0012(10)	0.0005(9)
Ga7	0.0092(12)	0.0082(12)	0.0068(12)	-0.0001(10)	0.0007(10)	-0.0016(9)
Ga8	0.0089(12)	0.0096(12)	0.0079(12)	0.0002(10)	0.0025(10)	0.0015(10)
Ga9	0.0102(12)	0.0091(12)	0.0082(12)	0.0013(10)	0.0002(10)	-0.0020(10)
Ga10	0.0103(12)	0.0112(13)	0.0063(12)	-0.0020(10)	0.0023(10)	-0.0039(10)
Ga11	0.0074(11)	0.0064(11)	0.0057(12)	0.0006(9)	0.0013(9)	-0.0021(9)
Ga12	0.0093(12)	0.0090(12)	0.0062(12)	-0.0015(10)	-0.0010(10)	0.0001(10)
Ga13	0.0100(12)	0.0118(13)	0.0088(13)	0.0007(10)	0.0013(10)	0.0020(10)
Ga14	0.0118(13)	0.0105(12)	0.0075(12)	-0.0022(10)	0.0028(10)	-0.0029(10)
Ga15	0.0095(12)	0.0083(12)	0.0106(13)	0.0018(10)	0.0025(10)	0.0009(10)

Ga16	0.0105(17)	0.0082(17)	0.0046(17)	0	0.0011(14)	0
Ga17	0.0083(17)	0.0085(17)	0.0040(16)	0	0.0014(13)	0
Ga18	0.0120(18)	0.0089(17)	0.0045(17)	0	0.0007(14)	0
As1	0.0066(10)	0.0057(10)	0.0068(11)	-0.0002(9)	0.0016(9)	0.0011(8)
As2	0.0059(10)	0.0061(10)	0.0046(11)	0.0002(9)	0.0006(8)	-0.0016(8)
As3	0.0072(11)	0.0084(11)	0.0054(11)	0.0006(9)	-0.0004(9)	-0.0008(9)
As4	0.0085(11)	0.0092(11)	0.0058(11)	-0.0019(9)	0.0002(9)	-0.0023(9)
As5	0.0064(11)	0.0053(11)	0.0059(11)	0.0002(9)	0.0002(9)	0.0004(8)
As6	0.0071(11)	0.0074(11)	0.0054(11)	0.0009(9)	0.0005(9)	0.0027(8)
As7	0.0059(11)	0.0073(11)	0.0080(11)	0.0008(9)	-0.0006(9)	0.0013(8)
As8	0.0061(11)	0.0074(11)	0.0055(11)	0.0005(9)	0.0021(9)	0.0020(8)
As9	0.0108(11)	0.0108(11)	0.0070(11)	0.0017(9)	-0.0005(9)	-0.0002(9)
As10	0.0059(11)	0.0082(11)	0.0049(11)	0.0000(9)	0.0016(9)	-0.0010(8)
As11	0.0072(11)	0.0081(11)	0.0076(11)	0.0010(9)	0.0022(9)	-0.0013(9)
As12	0.0063(11)	0.0071(11)	0.0075(11)	-0.0006(9)	0.0014(9)	-0.0014(8)
As13	0.0070(11)	0.0066(11)	0.0067(11)	-0.0001(9)	0.0027(9)	-0.0001(8)
As14	0.0068(11)	0.0078(11)	0.0050(11)	-0.0003(9)	0.0001(9)	0.0016(9)
As15	0.0069(11)	0.0093(11)	0.0063(11)	0.0004(9)	0.0001(9)	-0.0004(9)
As16	0.0051(10)	0.0051(10)	0.0070(11)	0.0015(9)	-0.0017(9)	-0.0002(8)
As17	0.0108(11)	0.0099(11)	0.0058(11)	0.0004(9)	0.0014(9)	-0.0002(9)
As18	0.0086(11)	0.0061(11)	0.0070(11)	0.0007(9)	0.0025(9)	-0.0004(9)
As19	0.0144(12)	0.0115(12)	0.0094(12)	-0.0002(10)	0.0055(10)	-0.0044(9)
As20	0.0115(11)	0.0130(12)	0.0069(11)	-0.0005(10)	-0.0015(9)	0.0043(9)
As21	0.0120(11)	0.0100(11)	0.0046(11)	0.0007(9)	0.0025(9)	-0.0012(9)
As22	0.0110(12)	0.0103(12)	0.0102(12)	-0.0030(10)	0.0021(9)	-0.0041(9)
As23	0.0128(12)	0.0103(12)	0.0076(11)	-0.0038(9)	0.0013(9)	0.0035(9)
As24	0.0096(11)	0.0101(11)	0.0129(12)	0.0004(10)	0.0018(9)	-0.0021(9)

Table A.61: Atomic coordinates, equivalent displacement parameters (Å^2) and site occupancy factors (*sof*) of $Sr_{15}In_{22}As_{32}$.

atom	Wyckoff	*x*	*y*	*z*	U_{eq}	*sof*
Sr1	8f	0.01119(3)	0.06716(3)	0.58087(3)	0.01200(12)	1
Sr2	8f	0.13902(3)	0.05850(3)	0.07616(3)	0.01117(11)	1
Sr3	8f	0.18206(3)	0.37957(3)	0.42398(3)	0.01113(11)	1
Sr4	8f	0.26478(3)	0.18632(3)	0.08038(3)	0.01195(12)	1
Sr5	8f	0.30710(3)	0.25108(3)	0.41927(3)	0.01208(12)	1
Sr6	8f	0.31302(4)	0.03376(4)	0.23551(4)	0.02440(16)	1
Sr7	8f	0.31687(4)	0.40377(4)	0.26425(4)	0.02429(16)	1
Sr8	8f	0.38650(3)	0.31026(3)	0.07918(3)	0.01222(12)	1
Sr9	8f	0.42718(11)	0.14738(11)	0.23628(7)	0.0670(8)	0.638(3)
Sr10	8f	0.43100(11)	0.28913(11)	0.26377(7)	0.0671(8)	0.614(3)
Sr11	8f	0.44637(3)	0.00474(3)	0.08026(3)	0.01186(12)	1
Sr12	8f	0.57002(3)	0.12671(3)	0.07901(3)	0.01214(12)	1
In1	8f	0.01593(2)	0.09297(2)	0.39309(2)	0.01121(9)	1
In2	8f	0.01941(2)	0.34490(2)	0.39288(2)	0.01101(9)	1
In3	8f	0.03543(2)	0.21977(2)	0.54208(2)	0.01171(9)	1
In4	8f	0.10807(2)	0.46730(2)	0.10955(2)	0.01189(9)	1
In5	8f	0.10836(2)	0.21707(2)	0.10715(2)	0.01111(9)	1

In6	8f	0.12639(2)	0.34563(2)	0.24662(2)	0.01097(9)	1
In7	8f	0.12753(2)	0.09177(2)	0.25394(2)	0.01086(9)	1
In8	8f	0.14359(2)	0.22059(2)	0.39320(2)	0.01119(9)	1
In9	8f	0.16097(2)	0.09376(2)	0.53820(2)	0.01079(9)	1
In10	8f	0.23102(2)	0.34430(2)	0.10954(2)	0.01196(9)	1
In11	8f	0.25017(2)	0.21874(2)	0.25022(2)	0.00981(9)	1
In12	8f	0.26703(2)	0.09316(2)	0.39063(2)	0.01201(9)	1
In13	8f	0.28621(2)	0.03137(2)	0.03841(2)	0.01071(9)	1
In14	8f	0.35688(2)	0.46931(2)	0.10938(2)	0.01204(9)	1
In15	8f	0.41236(2)	0.15726(2)	0.04131(2)	0.01194(9)	1
In16	4e	0	0.21881(3)	1/4	0.01224(12)	1
In17	4e	0	0.46894(3)	1/4	0.01002(12)	1
In18	4e	0	0.96867(3)	1/4	0.01015(12)	1
As1	8f	0.03075(3)	0.41068(3)	0.02930(3)	0.00959(12)	1
As2	8f	0.03992(3)	0.15182(3)	0.02749(3)	0.00919(12)	1
As3	8f	0.05356(3)	0.28142(3)	0.17686(3)	0.01069(12)	1
As4	8f	0.05914(3)	0.02671(3)	0.17515(3)	0.01040(12)	1
As5	8f	0.07172(3)	0.15613(3)	0.32327(3)	0.01051(12)	1
As6	8f	0.07765(3)	0.41105(3)	0.32493(3)	0.01030(12)	1
As7	8f	0.08505(3)	0.02629(3)	0.47020(3)	0.00959(12)	1
As8	8f	0.09464(3)	0.28642(3)	0.47249(3)	0.00914(12)	1
As9	8f	0.15447(3)	0.53549(3)	0.02932(3)	0.00914(12)	1
As10	8f	0.16440(3)	0.27703(3)	0.02929(3)	0.00972(12)	1
As11	8f	0.18297(3)	0.15038(3)	0.17536(3)	0.01032(12)	1
As12	8f	0.18669(3)	0.41340(3)	0.18627(3)	0.01146(13)	1
As13	8f	0.20141(3)	0.28719(3)	0.32514(3)	0.01043(12)	1
As14	8f	0.20285(3)	0.02399(3)	0.31452(3)	0.01146(13)	1
As15	8f	0.22003(3)	0.16122(3)	0.47018(3)	0.00969(12)	1
As16	8f	0.26658(3)	0.46864(3)	0.38176(3)	0.01074(12)	1
As17	8f	0.28914(3)	0.40081(3)	0.02929(3)	0.00902(12)	1
As18	8f	0.30935(3)	0.28281(3)	0.18213(3)	0.01264(13)	1
As19	8f	0.32690(3)	0.15473(3)	0.31777(3)	0.01264(13)	1
As20	8f	0.35880(3)	0.09400(3)	0.11804(3)	0.01078(12)	1
As21	8f	0.39151(3)	0.34375(3)	0.38226(3)	0.01092(12)	1
As22	8f	0.42755(3)	0.40036(3)	0.18244(3)	0.01287(13)	1
As23	8f	0.44446(3)	0.03663(3)	0.31805(3)	0.01261(13)	1
As24	8f	0.48415(3)	0.21861(3)	0.12449(4)	0.01402(13)	1

Table A.62: Anisotropic displacement parameters (Å^2) of $Sr_5In_{22}As_{32}$.

atom	U_{11}	U_{22}	U_{33}	U_{23}	U_{13}	U_{12}
Sr1	0.0122(3)	0.0120(3)	0.0120(3)	0.0026(2)	0.0022(2)	0.0012(2)
Sr2	0.0118(3)	0.0115(3)	0.0107(3)	-0.0013(2)	0.0030(2)	-0.0014(2)
Sr3	0.0110(3)	0.0113(3)	0.0108(3)	-0.0012(2)	0.0004(2)	0.0012(2)
Sr4	0.0126(3)	0.0121(3)	0.0119(3)	-0.0006(2)	0.0041(2)	-0.0013(2)
Sr5	0.0112(3)	0.0124(3)	0.0120(3)	-0.0002(2)	-0.0004(2)	0.0009(2)
Sr6	0.0306(4)	0.0297(4)	0.0132(3)	0.0022(3)	0.0045(3)	0.0005(3)
Sr7	0.0287(4)	0.0301(4)	0.0130(3)	0.0024(3)	-0.0005(3)	-0.0001(3)

Sr8	0.0122(3)	0.0117(3)	0.0132(3)	-0.0006(2)	0.0034(2)	-0.0018(2)
Sr9	0.0924(17)	0.0994(18)	0.0064(6)	-0.0033(8)	-0.0023(7)	0.0143(13)
Sr10	0.0988(18)	0.0957(18)	0.0060(7)	-0.0039(8)	0.0052(8)	-0.0090(14)
Sr11	0.0120(3)	0.0117(3)	0.0118(3)	0.0023(2)	0.0014(2)	-0.0011(2)
Sr12	0.0115(3)	0.0118(3)	0.0129(3)	0.0014(2)	0.0012(2)	-0.0016(2)
In1	0.0120(2)	0.0116(2)	0.0102(2)	0.00085(16)	0.00192(16)	0.00179(16)
In2	0.0115(2)	0.0116(2)	0.0099(2)	-0.00042(16)	0.00143(16)	0.00180(16)
In3	0.00960(19)	0.0100(2)	0.0153(2)	0.00147(17)	0.00096(16)	0.00009(16)
In4	0.0133(2)	0.0126(2)	0.0096(2)	0.00123(16)	0.00120(16)	-0.00205(17)
In5	0.0118(2)	0.0118(2)	0.0100(2)	-0.00019(16)	0.00226(16)	-0.00184(16)
In6	0.0117(2)	0.0118(2)	0.0094(2)	0.00009(16)	0.00177(16)	0.00116(16)
In7	0.0115(2)	0.0116(2)	0.0094(2)	0.00026(16)	0.00120(16)	-0.00103(16)
In8	0.0116(2)	0.0118(2)	0.0101(2)	-0.00004(16)	0.00111(16)	0.00151(16)
In9	0.01048(19)	0.0107(2)	0.0112(2)	0.00010(16)	0.00169(16)	-0.00060(16)
In10	0.0128(2)	0.0137(2)	0.0097(2)	-0.00037(16)	0.00264(16)	-0.00244(17)
In11	0.01057(19)	0.0109(2)	0.00788(19)	-0.00019(15)	0.00104(15)	-0.00013(16)
In12	0.0122(2)	0.0137(2)	0.0099(2)	-0.00041(16)	0.00080(16)	0.00207(17)
In13	0.01069(19)	0.0107(2)	0.0108(2)	0.00013(16)	0.00179(16)	0.00069(16)
In14	0.0135(2)	0.0130(2)	0.0097(2)	-0.00082(16)	0.00195(16)	-0.00198(17)
In15	0.01062(19)	0.0100(2)	0.0159(2)	0.00184(17)	0.00414(16)	0.00049(16)
In16	0.0128(3)	0.0125(3)	0.0114(3)	0	0.0019(2)	0
In17	0.0109(3)	0.0112(3)	0.0080(3)	0	0.0014(2)	0
In18	0.0109(3)	0.0111(3)	0.0085(3)	0	0.0016(2)	0
As1	0.0104(3)	0.0104(3)	0.0083(3)	0.0004(2)	0.0026(2)	-0.0013(2)
As2	0.0096(3)	0.0101(3)	0.0078(3)	0.0003(2)	0.0009(2)	-0.0016(2)
As3	0.0110(3)	0.0114(3)	0.0098(3)	-0.0001(2)	0.0015(2)	-0.0007(2)
As4	0.0118(3)	0.0113(3)	0.0082(3)	-0.0009(2)	0.0019(2)	-0.0034(2)
As5	0.0108(3)	0.0114(3)	0.0093(3)	0.0000(2)	0.0013(2)	0.0003(2)
As6	0.0110(3)	0.0114(3)	0.0083(3)	-0.0003(2)	0.0008(2)	0.0032(2)
As7	0.0100(3)	0.0097(3)	0.0087(3)	0.0003(2)	0.0000(2)	0.0012(2)
As8	0.0100(3)	0.0099(3)	0.0076(3)	0.0008(2)	0.0017(2)	0.0016(2)
As9	0.0104(3)	0.0095(3)	0.0078(3)	-0.0001(2)	0.0022(2)	-0.0012(2)
As10	0.0104(3)	0.0102(3)	0.0086(3)	0.0010(2)	0.0015(2)	-0.0010(2)
As11	0.0113(3)	0.0115(3)	0.0083(3)	-0.0005(2)	0.0019(2)	-0.0035(2)
As12	0.0115(3)	0.0123(3)	0.0106(3)	0.0001(2)	0.0017(2)	-0.0007(2)
As13	0.0110(3)	0.0118(3)	0.0083(3)	-0.0006(2)	0.0007(2)	0.0032(2)
As14	0.0118(3)	0.0117(3)	0.0108(3)	0.0002(2)	0.0013(2)	0.0006(2)
As15	0.0101(3)	0.0103(3)	0.0086(3)	0.0017(2)	0.0013(2)	0.0016(2)
As16	0.0119(3)	0.0122(3)	0.0081(3)	0.0000(2)	0.0016(2)	0.0020(2)
As17	0.0097(3)	0.0095(3)	0.0078(3)	0.0008(2)	0.0012(2)	-0.0011(2)
As18	0.0134(3)	0.0149(3)	0.0102(3)	0.0014(2)	0.0036(2)	-0.0030(3)
As19	0.0122(3)	0.0152(3)	0.0101(3)	0.0017(2)	0.0000(2)	0.0031(3)
As20	0.0120(3)	0.0118(3)	0.0088(3)	0.0005(2)	0.0021(2)	-0.0020(2)
As21	0.0116(3)	0.0118(3)	0.0092(3)	0.0005(2)	0.0009(2)	0.0019(2)
As22	0.0144(3)	0.0130(3)	0.0107(3)	-0.0018(2)	-0.0001(2)	-0.0033(3)
As23	0.0152(3)	0.0131(3)	0.0100(3)	-0.0017(2)	0.0033(2)	0.0026(3)
As24	0.0122(3)	0.0123(3)	0.0177(3)	0.0002(3)	0.0029(3)	-0.0004(3)

Table A.63: Atomic coordinates, equivalent displacement parameters (Å^2) and site occupancy factors (*sof*) of Eu$_{15}$In$_{22}$As$_{32}$.

atom	Wyckoff	*x*	*y*	*z*	U_{eq}	*sof*
Eu1	8f	0.02710(5)	0.06459(5)	0.57890(5)	0.0121(2)	1
Eu2	8f	0.09580(5)	0.05716(5)	0.41937(5)	0.0122(2)	1
Eu3	8f	0.09605(5)	0.50407(4)	0.07714(5)	0.0109(2)	1
Eu4	8f	0.14994(5)	0.18824(5)	0.58077(5)	0.0121(2)	1
Eu5	8f	0.18972(7)	0.02846(6)	0.26339(6)	0.0250(3)	1
Eu6	8f	0.22291(5)	0.37596(5)	0.08065(5)	0.0122(2)	1
Eu7	8f	0.22519(5)	0.18279(4)	0.42287(5)	0.0114(2)	1
Eu8	8f	0.32084(7)	0.15955(6)	0.26361(5)	0.0264(3)	1
Eu9	8f	0.34412(5)	0.25238(5)	0.07895(5)	0.0118(2)	1
Eu10	8f	0.4086(7)	0.3997(10)	0.2329(5)	0.129(9)	0.261(13)
Eu11	8f	0.4336(5)	0.4116(4)	0.2358(3)	0.060(3)	0.391(12)
Eu12	8f	0.4372(4)	0.2844(6)	0.2640(4)	0.066(4)	0.344(13)
Eu13	8f	0.4529(12)	0.2609(7)	0.2665(7)	0.124(9)	0.254(13)
Eu14	8f	0.46842(5)	0.13011(5)	0.08070(5)	0.0118(2)	1
In1	8f	0.05166(8)	0.47047(7)	0.39406(7)	0.0117(3)	1
In2	8f	0.05517(7)	0.21699(6)	0.39372(7)	0.0105(3)	1
In3	8f	0.07281(8)	0.09427(6)	0.10885(7)	0.0113(3)	1
In4	8f	0.07313(7)	0.34540(6)	0.10634(8)	0.0113(3)	1
In5	8f	0.12602(7)	0.21647(6)	0.24679(7)	0.0095(3)	1
In6	8f	0.12841(7)	0.47034(6)	0.25407(8)	0.0109(3)	1
In7	8f	0.18069(7)	0.34152(6)	0.39401(7)	0.0107(3)	1
In8	8f	0.19721(8)	0.21860(7)	0.10910(7)	0.0124(3)	1
In9	8f	0.19736(7)	0.03002(7)	0.60844(7)	0.0115(3)	1
In10	8f	0.25109(6)	0.34374(7)	0.25044(9)	0.0115(3)	1
In11	8f	0.26603(8)	0.03095(7)	0.45993(7)	0.0109(3)	1
In12	8f	0.32118(8)	0.09356(7)	0.10844(8)	0.0131(3)	1
In13	8f	0.36079(8)	0.40522(7)	0.04316(6)	0.0111(3)	1
In14	8f	0.39139(8)	0.15651(7)	0.45938(6)	0.0103(3)	1
In15	8f	0.48361(7)	0.28227(7)	0.04272(7)	0.0108(3)	1
In16	4e	0	0.09249(8)	1/4	0.0072(4)	1
In17	4e	0	0.34355(12)	1/4	0.0143(4)	1
In18	4e	0	0.59433(9)	1/4	0.0115(4)	1
As1	8f	0.01463(10)	0.41145(9)	0.47348(10)	0.0085(4)	1
As2	8f	0.02448(11)	0.15024(9)	0.47195(10)	0.0087(4)	1
As3	8f	0.03554(11)	0.28061(10)	0.17693(10)	0.0115(4)	1
As4	8f	0.03849(11)	0.02422(9)	0.18179(11)	0.0122(5)	1
As5	8f	0.09041(12)	0.40587(12)	0.32441(10)	0.0123(4)	1
As6	8f	0.09666(10)	0.15054(9)	0.32514(10)	0.0091(4)	1
As7	8f	0.09900(10)	0.02679(9)	0.02731(10)	0.0087(4)	1
As8	8f	0.11012(10)	0.28523(9)	0.02766(10)	0.0089(4)	1
As9	8f	0.15136(10)	0.27447(9)	0.47321(10)	0.0084(4)	1
As10	8f	0.16545(10)	0.41207(9)	0.17514(11)	0.0110(5)	1
As11	8f	0.17116(10)	0.14869(9)	0.18574(10)	0.0106(5)	1
As12	8f	0.22148(10)	0.27468(9)	0.32514(10)	0.0101(4)	1
As13	8f	0.22304(10)	0.09830(9)	0.52831(11)	0.0092(4)	1

As14	8f	0.23342(10)	0.16149(9)	0.02712(10)	0.0084(4)	1
As15	8f	0.28063(11)	0.03889(10)	0.18547(11)	0.0128(5)	1
As16	8f	0.29415(11)	0.28030(10)	0.18200(11)	0.0140(5)	1
As17	8f	0.29865(12)	0.09382(11)	0.37949(8)	0.0104(4)	1
As18	8f	0.32637(11)	0.46861(10)	0.12025(10)	0.0105(4)	1
As19	8f	0.34464(11)	0.40786(10)	0.31851(11)	0.0138(5)	1
As20	8f	0.35906(10)	0.03758(9)	0.02803(10)	0.0090(4)	1
As21	8f	0.41038(11)	0.16289(10)	0.18134(11)	0.0151(5)	1
As22	8f	0.42431(11)	0.21938(10)	0.37995(10)	0.0110(4)	1
As23	8f	0.45413(12)	0.34366(11)	0.12736(9)	0.0141(4)	1
As24	8f	0.45882(10)	0.03668(10)	0.32521(11)	0.0122(5)	1

Table A.64: Anisotropic displacement parameters (Å^2) of Eu$_5$In$_{22}$As$_{32}$.

atom	U_{11}	U_{22}	U_{33}	U_{23}	U_{13}	U_{12}
Eu1	0.0106(5)	0.0117(5)	0.0114(5)	0.0015(4)	0.0018(4)	-0.0020(4)
Eu2	0.0112(5)	0.0115(5)	0.0119(5)	0.0030(4)	0.0026(4)	-0.0003(4)
Eu3	0.0106(5)	0.0116(5)	0.0099(5)	0.0011(4)	0.0032(4)	0.0021(4)
Eu4	0.0097(5)	0.0116(5)	0.0116(5)	0.0007(4)	0.0007(4)	-0.0009(4)
Eu5	0.0288(7)	0.0302(6)	0.0140(6)	0.0034(5)	0.0066(5)	0.0021(6)
Eu6	0.0132(5)	0.0127(5)	0.0114(5)	0.0003(4)	0.0058(4)	0.0008(4)
Eu7	0.0099(5)	0.0107(5)	0.0114(5)	0.0010(4)	0.0019(4)	-0.0013(4)
Eu8	0.0274(7)	0.0336(6)	0.0130(5)	-0.0014(6)	0.0027(6)	-0.0005(6)
Eu9	0.0108(5)	0.0125(5)	0.0120(5)	0.0011(4)	0.0045(4)	0.0019(4)
Eu10	0.054(7)	0.33(2)	0.017(4)	0.045(7)	0.024(5)	0.116(10)
Eu11	0.049(5)	0.102(5)	0.016(2)	-0.015(2)	0.000(3)	0.050(4)
Eu12	0.073(5)	0.087(7)	0.011(3)	0.016(4)	-0.012(3)	-0.061(5)
Eu13	0.28(2)	0.069(9)	0.013(5)	-0.022(5)	0.046(8)	-0.106(11)
Eu14	0.0103(5)	0.0137(5)	0.0107(5)	0.0021(4)	0.0034(4)	0.0019(4)
In1	0.0117(8)	0.0126(7)	0.0091(7)	-0.0004(6)	0.0025(6)	-0.0022(6)
In2	0.0097(7)	0.0104(7)	0.0097(7)	-0.0007(6)	0.0021(6)	-0.0029(6)
In3	0.0112(8)	0.0117(7)	0.0086(7)	-0.0007(6)	0.0014(6)	0.0031(6)
In4	0.0107(8)	0.0120(8)	0.0100(7)	0.0004(6)	0.0029(6)	0.0020(6)
In5	0.0091(6)	0.0099(6)	0.0079(6)	-0.0002(6)	0.0017(6)	-0.0018(6)
In6	0.0088(7)	0.0123(6)	0.0089(6)	-0.0002(6)	0.0006(6)	0.0011(7)
In7	0.0106(7)	0.0109(7)	0.0095(7)	-0.0004(6)	0.0027(6)	-0.0020(6)
In8	0.0119(8)	0.0149(7)	0.0094(7)	0.0006(6)	0.0033(7)	0.0030(6)
In9	0.0100(7)	0.0124(7)	0.0094(7)	0.0017(6)	0.0011(6)	-0.0030(6)
In10	0.0120(7)	0.0125(6)	0.0082(6)	0.0013(5)	0.0021(6)	0.0009(7)
In11	0.0103(7)	0.0108(7)	0.0106(7)	0.0000(6)	0.0031(6)	0.0000(6)
In12	0.0128(8)	0.0154(8)	0.0092(8)	0.0023(6)	0.0025(7)	0.0046(7)
In13	0.0111(7)	0.0089(6)	0.0143(6)	-0.0014(7)	0.0063(7)	-0.0005(5)
In14	0.0096(7)	0.0093(6)	0.0111(6)	-0.0001(6)	0.0030(7)	0.0008(5)
In15	0.0087(7)	0.0089(6)	0.0146(7)	0.0014(6)	0.0043(6)	-0.0004(6)
In16	0.0068(9)	0.0071(9)	0.0066(9)	0	0.0014(7)	0
In17	0.0130(10)	0.0132(8)	0.0138(9)	0	0.0023(10)	0
In18	0.0118(11)	0.0119(10)	0.0089(10)	0	0.0020(9)	0
As1	0.0072(10)	0.0107(10)	0.0066(10)	-0.0002(8)	0.0017(8)	-0.0009(8)

As2	0.0109(11)	0.0061(10)	0.0084(10)	-0.0005(8)	0.0031(9)	-0.0023(9)
As3	0.0102(11)	0.0112(10)	0.0116(10)	0.0000(9)	0.0026(9)	-0.0012(9)
As4	0.0169(11)	0.0093(10)	0.0108(10)	-0.0024(8)	0.0061(9)	0.0033(9)
As5	0.0106(11)	0.0139(10)	0.0114(9)	0.0002(10)	0.0032(10)	0.0001(8)
As6	0.0083(10)	0.0088(10)	0.0063(10)	0.0000(8)	-0.0011(8)	-0.0040(8)
As7	0.0077(10)	0.0079(10)	0.0087(10)	0.0008(8)	0.0016(8)	0.0018(9)
As8	0.0076(10)	0.0107(10)	0.0067(10)	-0.0007(8)	0.0010(8)	0.0006(9)
As9	0.0099(11)	0.0066(10)	0.0079(10)	-0.0020(8)	0.0029(9)	-0.0028(8)
As10	0.0089(11)	0.0135(10)	0.0088(11)	-0.0007(8)	0.0017(9)	0.0030(9)
As11	0.0082(11)	0.0115(10)	0.0103(10)	-0.0008(8)	0.0017(8)	-0.0009(9)
As12	0.0093(10)	0.0108(10)	0.0069(10)	-0.0008(8)	-0.0003(9)	-0.0033(9)
As13	0.0093(11)	0.0085(10)	0.0091(11)	-0.0014(8)	0.0030(9)	-0.0025(8)
As14	0.0069(10)	0.0096(10)	0.0071(9)	-0.0004(8)	0.0009(9)	0.0016(9)
As15	0.0113(11)	0.0150(11)	0.0095(10)	0.0007(9)	0.0013(9)	0.0003(9)
As16	0.0126(11)	0.0176(11)	0.0124(11)	-0.0028(9)	0.0058(9)	0.0010(9)
As17	0.0112(10)	0.0113(8)	0.0074(8)	0.0005(9)	0.0023(10)	-0.0016(7)
As18	0.0108(10)	0.0105(9)	0.0093(10)	-0.0005(8)	0.0031(9)	0.0004(9)
As19	0.0134(11)	0.0166(11)	0.0082(11)	-0.0018(8)	0.0008(9)	-0.0031(9)
As20	0.0076(10)	0.0097(10)	0.0077(10)	0.0004(8)	0.0010(9)	0.0006(9)
As21	0.0145(12)	0.0151(11)	0.0106(11)	0.0039(9)	-0.0004(9)	0.0057(10)
As22	0.0100(10)	0.0107(10)	0.0099(10)	-0.0008(9)	0.0013(9)	-0.0025(9)
As23	0.0133(10)	0.0119(8)	0.0173(9)	-0.0001(10)	0.0062(10)	0.0007(8)
As24	0.0120(11)	0.0146(11)	0.0087(10)	-0.0014(8)	0.0027(9)	-0.0058(9)

Table A.65: Atomic coordinates and isotropic displacement parameters (Å^2) of $Sr_3Ga_6As_8$.

atom	Wyckoff	*x*	*y*	*z*	U_{iso}
Sr1	8f	0.02419(11)	0.06496(11)	0.55957(9)	0.0069(5)
Sr2	8f	0.14996(11)	0.06077(10)	0.05947(9)	0.0063(5)
Sr3	8f	0.16680(11)	0.37780(11)	0.44040(9)	0.0070(5)
Sr4	8f	0.27470(11)	0.18578(10)	0.06025(9)	0.0062(5)
Sr5	8f	0.27659(12)	0.40639(12)	0.32027(10)	0.0124(5)
Sr6	8f	0.29269(11)	0.25173(10)	0.44053(9)	0.0070(5)
Sr7	8f	0.35129(12)	0.03276(12)	0.18314(10)	0.0134(5)
Sr8	8f	0.39916(11)	0.31019(11)	0.06029(9)	0.0072(5)
Sr9	8f	0.40179(12)	0.27982(12)	0.31737(10)	0.0136(5)
Sr10	8f	0.45835(11)	0.00211(10)	0.06011(9)	0.0065(5)
Sr11	8f	0.47331(14)	0.15625(14)	0.17896(11)	0.0197(6)
Sr12	8f	0.58285(11)	0.12657(11)	0.06014(9)	0.0067(5)
Ga1	8f	0.00096(13)	0.09398(13)	0.08722(11)	0.0067(6)
Ga2	8f	0.00280(14)	0.34351(13)	0.08861(11)	0.0072(6)
Ga3	8f	0.04034(13)	0.21888(12)	0.52507(11)	0.0057(5)
Ga4	8f	0.04206(13)	0.21822(13)	0.19541(11)	0.0052(6)
Ga5	8f	0.04296(14)	0.03020(14)	0.69798(12)	0.0088(6)
Ga6	8f	0.04437(13)	0.46605(13)	0.20101(11)	0.0064(6)
Ga7	8f	0.08155(13)	0.34240(14)	0.30222(11)	0.0063(6)
Ga8	8f	0.08285(13)	0.09408(13)	0.30434(11)	0.0053(6)
Ga9	8f	0.12296(14)	0.21865(14)	0.41272(12)	0.0101(6)

Ga10	8f	0.12684(14)	0.22012(14)	0.08837(11)	0.0081(6)
Ga11	8f	0.12766(13)	0.46848(13)	0.09001(11)	0.0075(6)
Ga12	8f	0.16589(13)	0.09302(13)	0.52570(11)	0.0070(6)
Ga13	8f	0.16623(14)	0.09486(14)	0.19772(12)	0.0081(6)
Ga14	8f	0.16769(14)	0.34388(13)	0.19932(11)	0.0073(6)
Ga15	8f	0.20630(13)	0.21857(13)	0.30282(12)	0.0069(6)
Ga16	8f	0.24767(13)	0.09233(13)	0.41160(11)	0.0077(6)
Ga17	8f	0.25194(13)	0.34366(13)	0.08971(11)	0.0079(6)
Ga18	8f	0.29078(13)	0.03156(13)	0.02491(11)	0.0077(6)
Ga19	8f	0.29180(13)	0.21887(13)	0.20019(11)	0.0040(6)
Ga20	8f	0.29432(14)	0.46881(14)	0.19940(11)	0.0079(6)
Ga21	8f	0.32925(14)	0.09445(13)	0.29975(11)	0.0071(6)
Ga22	8f	0.37605(14)	0.46928(13)	0.08863(11)	0.0076(6)
Ga23	8f	0.41529(13)	0.15607(13)	0.02488(11)	0.0064(6)
Ga24	8f	0.41870(13)	0.34522(13)	0.20048(11)	0.0043(6)
As1	8f	0.04119(11)	0.15645(12)	0.35987(9)	0.0029(5)
As2	8f	0.04150(12)	0.40783(12)	0.35845(10)	0.0065(5)
As3	8f	0.04181(12)	0.40813(12)	0.02967(10)	0.0043(5)
As4	8f	0.04427(12)	0.15584(11)	0.02925(10)	0.0041(5)
As5	8f	0.08194(12)	0.02977(12)	0.47084(10)	0.0052(5)
As6	8f	0.08409(12)	0.28275(11)	0.47092(10)	0.0039(5)
As7	8f	0.08460(12)	0.28190(12)	0.14193(10)	0.0033(5)
As8	8f	0.08506(12)	0.03024(12)	0.14010(10)	0.0055(5)
As9	8f	0.12284(12)	0.15633(13)	0.25014(10)	0.0064(6)
As10	8f	0.12463(12)	0.15664(12)	0.58405(10)	0.0064(5)
As11	8f	0.13028(12)	0.40781(12)	0.25569(10)	0.0035(5)
As12	8f	0.16525(12)	0.03115(12)	0.35756(10)	0.0060(5)
As13	8f	0.16596(12)	0.53204(12)	0.02984(10)	0.0046(5)
As14	8f	0.16780(12)	0.28233(12)	0.36025(10)	0.0058(5)
As15	8f	0.16841(12)	0.28028(12)	0.02941(10)	0.0051(5)
As16	8f	0.20936(12)	0.15716(12)	0.47086(10)	0.0048(5)
As17	8f	0.21003(12)	0.40603(13)	0.14406(10)	0.0062(5)
As18	8f	0.21066(12)	0.15526(12)	0.14151(10)	0.0056(5)
As19	8f	0.24964(12)	0.02819(11)	0.24428(10)	0.0030(5)
As20	8f	0.25096(12)	0.03048(11)	0.58422(10)	0.0050(5)
As21	8f	0.25382(11)	0.28458(11)	0.25578(9)	0.0005(5)
As22	8f	0.29223(12)	0.15724(12)	0.35857(10)	0.0047(5)
As23	8f	0.29295(12)	0.40476(11)	0.02984(10)	0.0042(5)
As24	8f	0.33589(12)	0.27977(12)	0.14253(10)	0.0053(5)
As25	8f	0.37401(11)	0.40499(12)	0.25556(10)	0.0034(5)
As26	8f	0.37482(12)	0.09329(11)	0.08377(10)	0.0048(5)
As27	8f	0.37793(13)	0.15611(13)	0.25016(11)	0.0091(6)
As28	8f	0.41646(12)	0.03320(12)	0.35718(10)	0.0061(5)
As29	8f	0.46028(12)	0.40529(12)	0.14144(10)	0.0054(5)
As30	8f	0.50028(12)	0.21878(11)	0.08390(10)	0.0051(5)
As31	4e	0	0.03292(17)	1/4	0.0061(8)
As32	4e	0	0.27964(16)	1/4	0.0026(7)
As33	4e	0	0.53492(19)	1/4	0.0110(8)

As34	4e	0	0.77819(18)	1/4	0.0083(8)

Table A.66: Atomic coordinates and isotropic displacement parameters (Å^2) of $Eu_3Ga_6As_8$.

atom	Wyckoff	*x*	*y*	*z*	U_{iso}
Eu1	8f	0.00548(8)	0.06454(8)	0.56019(7)	0.0069(4)
Eu2	8f	0.07211(8)	0.50250(8)	0.05951(7)	0.0073(4)
Eu3	8f	0.11950(8)	0.05980(8)	0.44058(7)	0.0064(4)
Eu4	8f	0.13038(8)	0.18920(8)	0.56024(7)	0.0072(4)
Eu5	8f	0.19764(8)	0.37699(8)	0.05948(7)	0.0065(4)
Eu6	8f	0.24502(8)	0.18529(8)	0.44048(7)	0.0071(4)
Eu7	8f	0.25871(9)	0.03132(9)	0.32001(8)	0.0146(5)
Eu8	8f	0.32198(8)	0.25185(8)	0.06018(7)	0.0070(4)
Eu9	8f	0.36873(9)	0.40395(9)	0.18420(8)	0.0149(5)
Eu10	8f	0.38515(9)	0.15838(9)	0.31609(8)	0.0142(5)
Eu11	8f	0.44671(8)	0.12719(8)	0.06012(7)	0.0071(4)
Eu12	8f	0.49097(10)	0.28143(10)	0.17837(9)	0.0184(5)
Ga1	8f	0.04224(19)	0.34251(18)	0.08593(16)	0.0083(8)
Ga2	8f	0.04280(18)	0.09266(18)	0.08795(15)	0.0062(8)
Ga3	8f	0.05519(18)	0.21855(18)	0.19476(15)	0.0068(8)
Ga4	8f	0.05597(17)	0.03002(18)	0.69923(15)	0.0048(8)
Ga5	8f	0.05655(18)	0.46720(18)	0.19726(15)	0.0056(8)
Ga6	8f	0.06893(18)	0.09402(18)	0.30165(16)	0.0070(8)
Ga7	8f	0.06954(17)	0.34372(17)	0.30549(14)	0.0038(8)
Ga8	8f	0.08297(17)	0.21960(17)	0.41388(15)	0.0052(8)
Ga9	8f	0.08346(18)	0.47000(18)	0.41229(16)	0.0072(8)
Ga10	8f	0.16703(18)	0.03020(18)	0.58853(16)	0.0065(8)
Ga11	8f	0.16716(17)	0.21927(17)	0.08688(15)	0.0045(8)
Ga12	8f	0.18071(17)	0.34470(17)	0.19691(15)	0.0047(8)
Ga13	8f	0.18087(17)	0.09443(17)	0.19872(15)	0.0048(8)
Ga14	8f	0.19321(18)	0.46845(18)	0.30096(16)	0.0078(8)
Ga15	8f	0.19375(18)	0.21990(18)	0.30266(16)	0.0083(8)
Ga16	8f	0.20795(18)	0.34367(18)	0.41269(16)	0.0068(8)
Ga17	8f	0.27751(19)	0.03080(18)	0.47350(16)	0.0088(8)
Ga18	8f	0.29244(18)	0.09307(18)	0.08846(15)	0.0069(8)
Ga19	8f	0.30507(18)	0.21857(18)	0.20021(15)	0.0071(8)
Ga20	8f	0.31681(18)	0.34337(18)	0.30078(16)	0.0069(8)
Ga21	8f	0.34680(18)	0.40645(17)	0.02641(15)	0.0055(8)
Ga22	8f	0.43030(18)	0.09292(18)	0.20057(16)	0.0074(8)
Ga23	8f	0.47187(18)	0.28221(18)	0.02702(16)	0.0070(8)
Ga24	8f	0.59762(19)	0.15616(18)	0.02638(16)	0.0083(8)
As1	8f	0.01369(15)	0.28112(15)	0.36067(13)	0.0008(7)
As2	8f	0.01497(17)	0.03029(17)	0.35932(14)	0.0071(8)
As3	8f	0.02662(15)	0.40798(16)	0.47157(13)	0.0032(7)
As4	8f	0.02945(17)	0.15455(17)	0.47228(15)	0.0092(8)
As5	8f	0.09547(16)	0.02878(16)	0.02865(14)	0.0032(7)
As6	8f	0.09912(15)	0.28259(15)	0.02806(13)	0.0008(7)
As7	8f	0.10942(16)	0.09621(16)	0.64171(13)	0.0035(7)

As8	8f	0.11170(16)	0.15541(15)	0.14182(14)	0.0033(7)
As9	8f	0.11359(15)	0.40752(15)	0.13930(13)	0.0026(7)
As10	8f	0.12322(15)	0.28060(16)	0.24974(13)	0.0019(7)
As11	8f	0.13028(17)	0.02841(18)	0.25545(15)	0.0093(8)
As12	8f	0.13873(17)	0.40740(17)	0.35884(14)	0.0072(8)
As13	8f	0.14132(17)	0.15474(17)	0.36029(15)	0.0079(8)
As14	8f	0.15443(16)	0.28041(16)	0.47219(14)	0.0049(7)
As15	8f	0.22068(15)	0.09507(15)	0.52806(13)	0.0022(7)
As16	8f	0.22418(15)	0.15809(15)	0.02816(13)	0.0004(7)
As17	8f	0.23659(17)	0.03151(16)	0.14239(14)	0.0060(7)
As18	8f	0.23733(16)	0.28307(16)	0.14087(14)	0.0041(7)
As19	8f	0.25239(16)	0.40968(16)	0.24459(14)	0.0038(7)
As20	8f	0.25394(17)	0.15323(17)	0.25654(14)	0.0068(8)
As21	8f	0.26603(16)	0.27849(16)	0.35915(13)	0.0037(7)
As22	8f	0.29252(16)	0.46788(16)	0.08555(13)	0.0035(7)
As23	8f	0.33317(16)	0.09413(16)	0.41402(14)	0.0043(7)
As24	8f	0.34821(18)	0.03313(18)	0.02809(15)	0.0105(8)
As25	8f	0.36393(18)	0.15907(17)	0.14196(16)	0.0109(8)
As26	8f	0.37184(17)	0.03383(17)	0.25585(15)	0.0087(8)
As27	8f	0.37764(16)	0.28205(17)	0.25000(14)	0.0063(8)
As28	8f	0.41680(17)	0.34440(16)	0.08600(15)	0.0075(8)
As29	8f	0.48867(16)	0.03373(16)	0.14182(14)	0.0052(7)
As30	8f	0.54194(17)	0.21859(17)	0.08596(15)	0.0079(8)
As31	4e	0	0.1595(2)	1/4	0.0039(10)
As32	4e	0	0.4056(2)	1/4	0.0010(9)
As33	4e	0	0.6604(3)	1/4	0.0131(12)
As34	4e	0	0.9020(2)	1/4	0.0043(10)

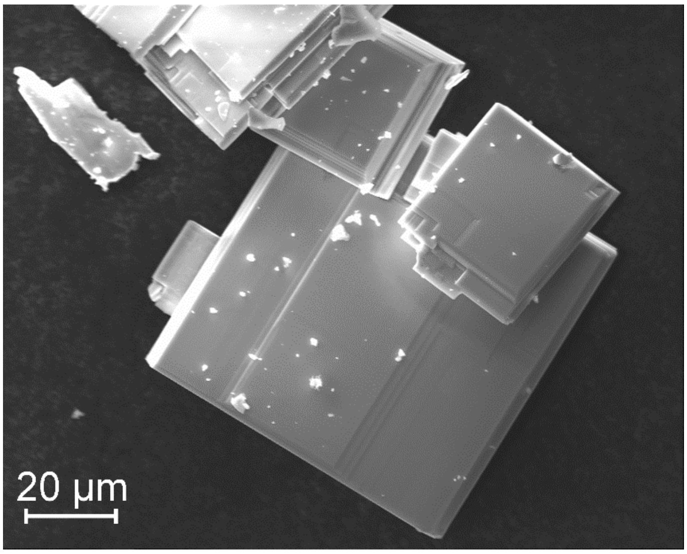

Figure A.42: SEM-image of plate-like $Sr_3Ga_6As_8$ crystals.

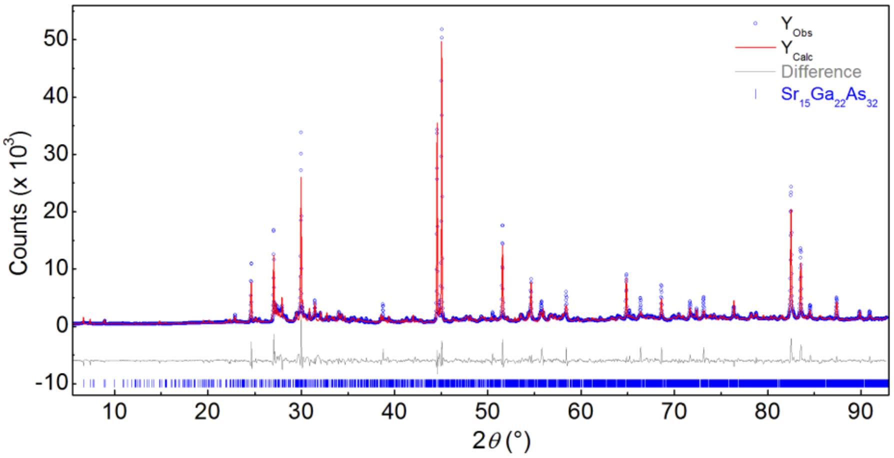

Figure A.43: X-ray powder diffraction pattern (Y_{obs}, Cu Kα), Rietveld fit (Y_{calc}) and difference curve (grey) of $Sr_{15}Ga_{22}As_{32}$.

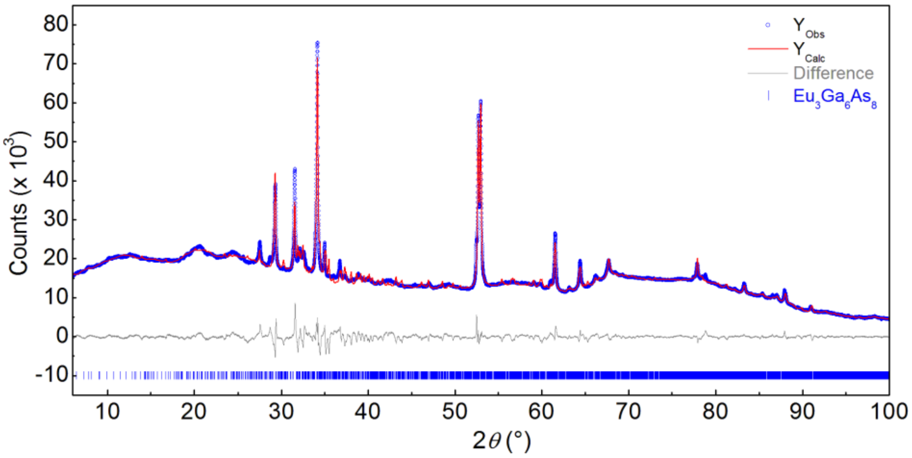

Figure A.44: X-ray powder diffraction pattern (Y_{obs}, Co Kα), Rietveld fit (Y_{calc}) and difference curve (grey) of $Eu_{15}Ga_{22}As_{32}$.

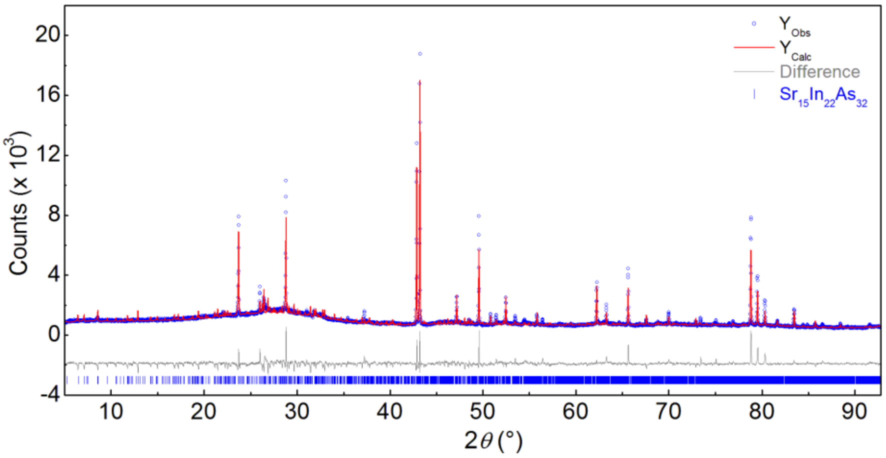

Figure A.45: X-ray powder diffraction pattern (Y_{obs}, Cu Kα), Rietveld fit (Y_{calc}) and difference curve (grey) of $Sr_{15}In_{22}As_{32}$.

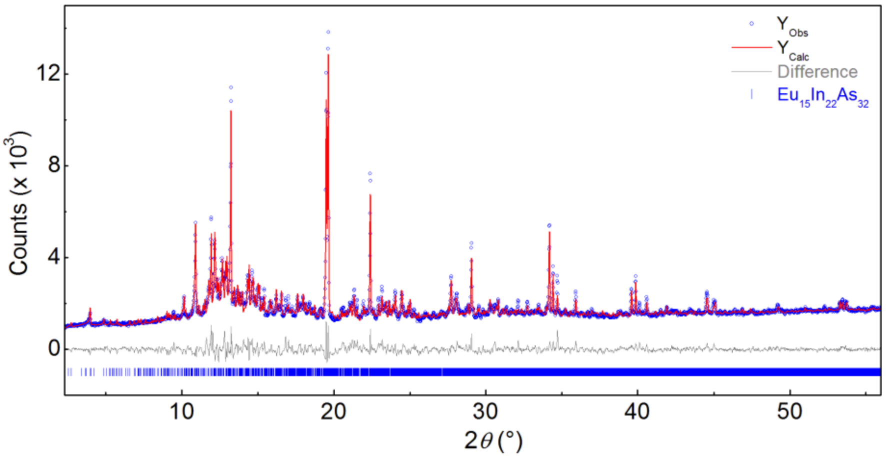

Figure A.46: X-ray powder diffraction pattern (Y_{obs}, Mo Kα), Rietveld fit (Y_{calc}) and difference curve (grey) of $Eu_{15}In_{22}As_{32}$.

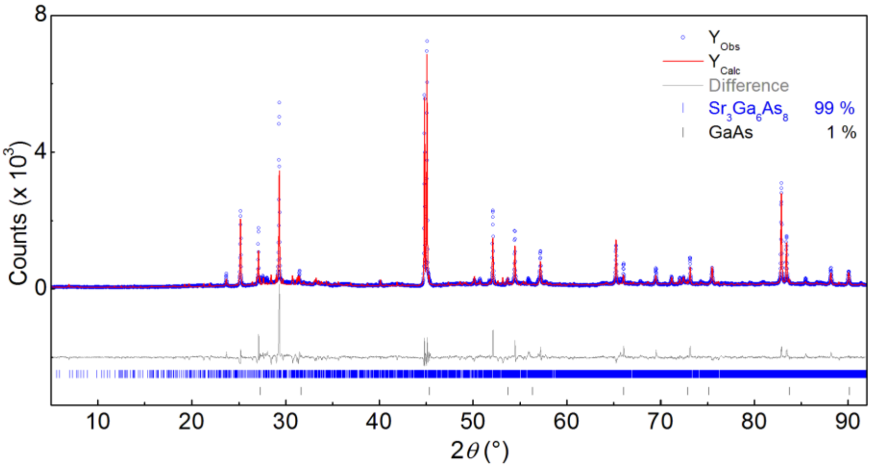

Figure A.47: X-ray powder diffraction pattern (Y_{obs}, Cu Kα), Rietveld fit (Y_{calc}) and difference curve (grey) of $Sr_3Ga_6As_8$.

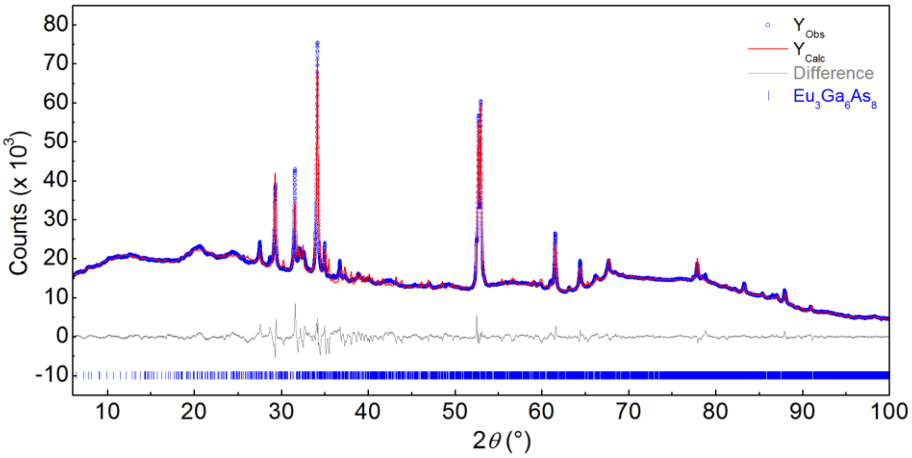

Figure A.48: X-ray powder diffraction pattern (Y_{obs}, Co Kα), Rietveld fit (Y_{calc}) and difference curve (grey) of $Eu_3Ga_6As_8$.

Table A.67: EDX results of $M_{15}Tr_{22}As_{32}$ and $M_3Ga_6As_8$.

Formula	*M* (at.-%)	*Tr* (at.-%)	As (at.-%)
$M_{15}Tr_{22}As_{32}$ (calc.)	21.74	31.88	46.38
$Sr_{15}Ga_{22}As_3$	21(1)	33(1)	46(1)
$Eu_{15}Ga_{22}As_{32}$	21.9(7)	32(1)	46(1)
$Sr_{15}In_{22}As_{32}$	21.1(8)	32(1)	46(1)
$Eu_{15}In_{22}As_{32}$	21.4(8)	33.3(5)	45.3(8)
$M_3Ga_6As_8$ (calc.)	17.65	35.29	47.06
$Sr_3Ga_6As_8$	17.2(9)	34.9(9)	48(1)
$Eu_3Ga_6As_8$	17.8(7)	35.0(9)	47(1)

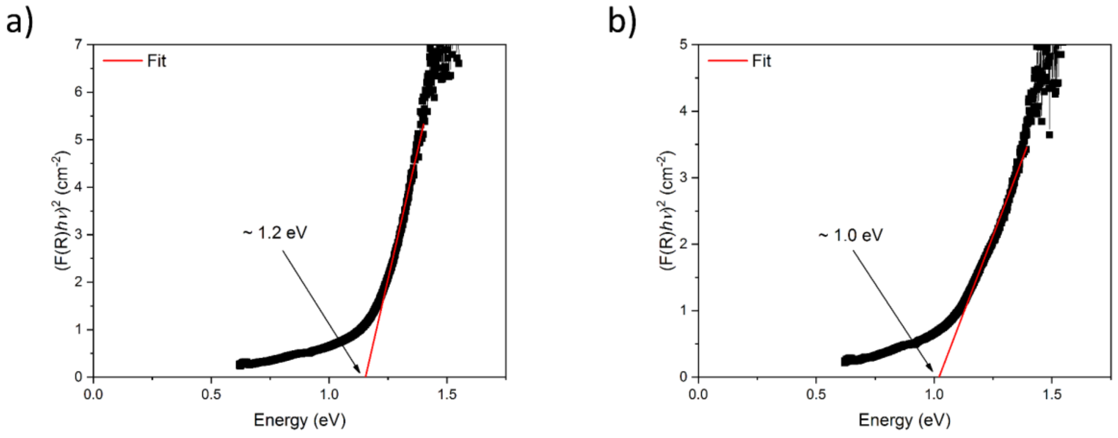

Figure A.49: UV-Vis-NIR measurement of (a) $Sr_{15}Ga_{22}As_{32}$ and (b) $Eu_{15}Ga_{22}As_{32}$.

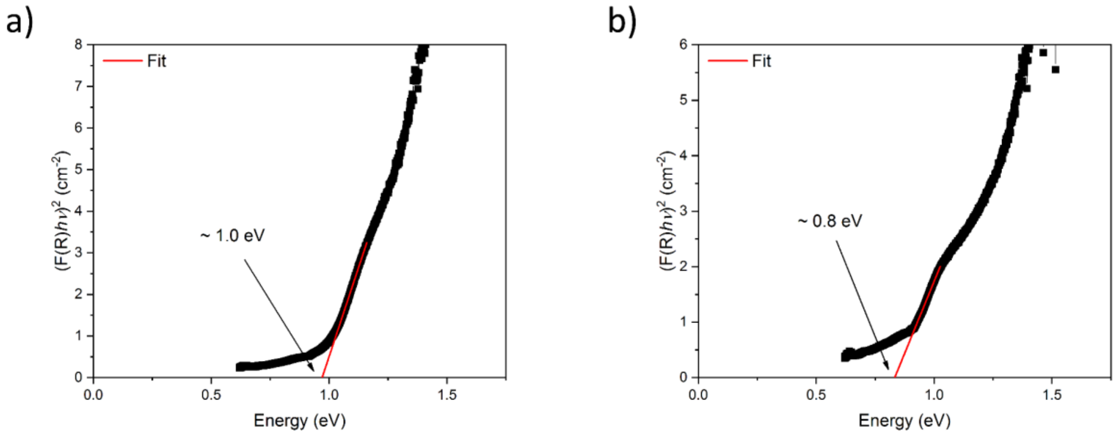

Figure A.50: UV-Vis-NIR measurement of (a) $Sr_{15}In_{22}As_{32}$ and (b) $Eu_{15}In_{22}As_{32}$.

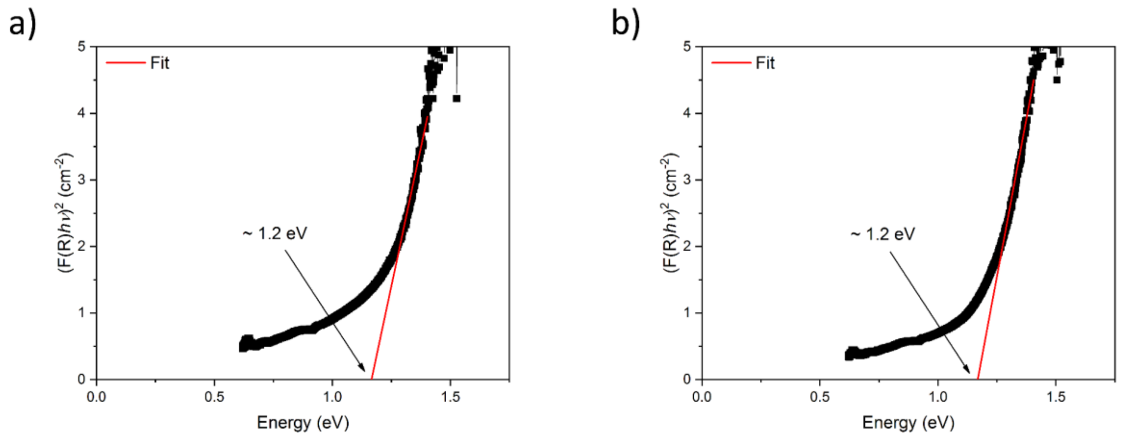

Figure A.51: UV-Vis-NIR measurement of (a) $Sr_3Ga_6As_8$ and (b) $Eu_3Ga_6As_8$.

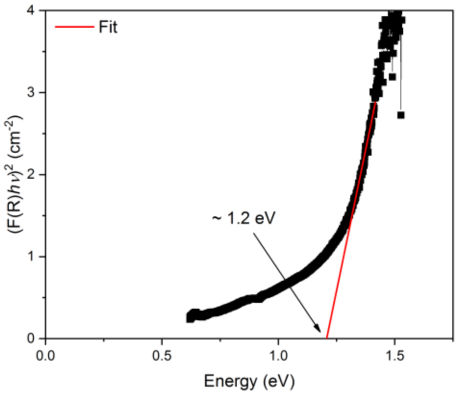

Figure A.52: UV-Vis-NIR measurement of GaAs.

Table A.68: Optical band gaps E_g, electrical resistivity ρ, charge carrier density N and Hall mobility μ at 300 K and 400 K of $M_{15}Tr_{22}As_{32}$, $M_3Ga_6As_8$, GaAs[4-8] and InAs.[7, 9-11]

Formula	E_g (eV)	ρ_{300K} (Ωcm)	ρ_{400K} (Ωcm)	N_{300K} (cm^{-3})	N_{400K} (cm^{-3})	μ_{300K} (cm^{2}V^{-1}s^{-1})	μ_{400K} (cm^{2}V^{-1}s^{-1})
$Sr_{15}Ga_{22}As_{32}$	1.2	1.6	1.0	$1.6\cdot10^{18}$	$5.0\cdot10^{18}$	2.6	1.3
$Eu_{15}Ga_{22}As_{32}$	1.0	1.7	1.4	$1.8\cdot10^{19}$	$3.2\cdot10^{19}$	0.2	0.1
$Sr_{15}In_{22}As_{32}$	1.0	$1.1\cdot10^{-2}$	$1.0\cdot10^{-2}$	$1.3\cdot10^{18}$	$1.3\cdot10^{18}$	453	468
$Eu_{15}In_{22}As_{32}$	0.8	3.4	2.5	$1.1\cdot10^{18}$	$3.8\cdot10^{18}$	1.7	0.7
$Sr_3Ga_6As_8$	1.2	5.0	2.6	$1.3\cdot10^{18}$	$4.6\cdot10^{18}$	0.9	0.5
$Eu_3Ga_6As_8$	1.2	2.2	1.3	$1.2\cdot10^{18}$	$4.6\cdot10^{18}$	2.4	1.0
$GaAs_{\text{intr.}}$	1.42	$3.3\cdot10^{8}$		$2.1\cdot10^{6}$		400	
$GaAs_{\text{doped}}$	1.2–1.7	$5.6\cdot10^{-3}$		$8.12\cdot10^{18}$		131	
$InAs_{\text{intr.}}$	0.36	0.13		$1\cdot10^{15}$		500	
$InAs_{\text{doped}}$	0.29–0.57	$1\cdot10^{-3}$		$1\cdot10^{18}$		10000	

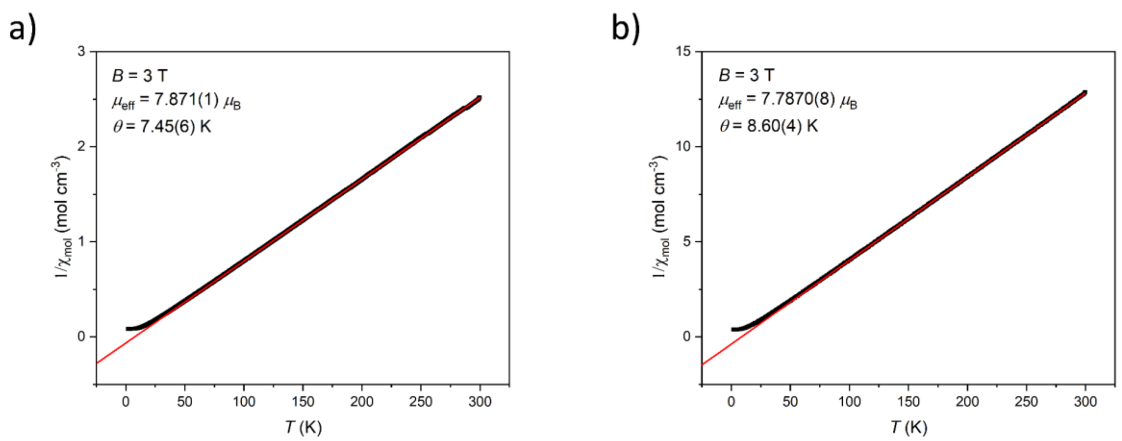

Figure A.53: Inverse susceptibility of (a) $Eu_{15}Ga_{22}As_{32}$ and (b) $Eu_3Ga_6As_8$ with a Curie-Weiss-fit (red).

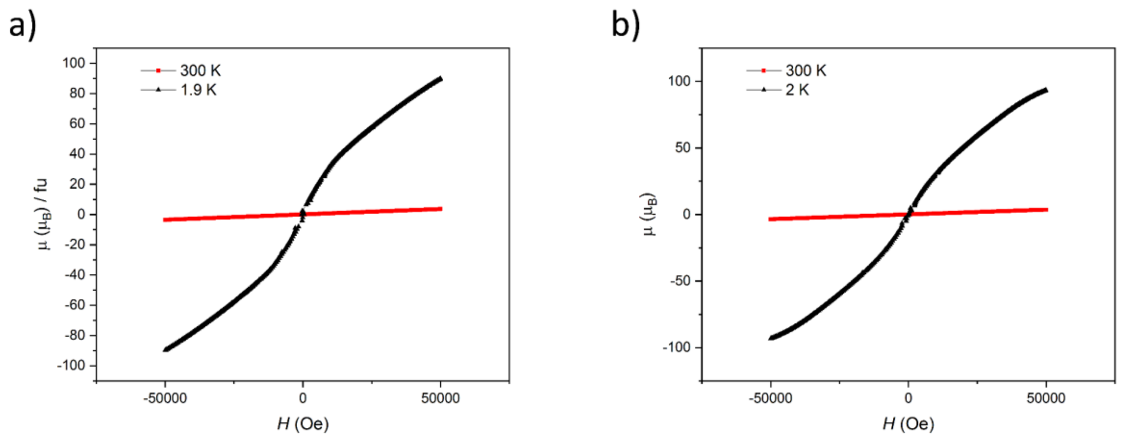

Figure A.54: Magnetization isotherms of (a) $Eu_{15}Ga_{22}As_{32}$ and (b) $Eu_{15}In_{22}As_{32}$ at 300 K (red) and 1.9 K (black).

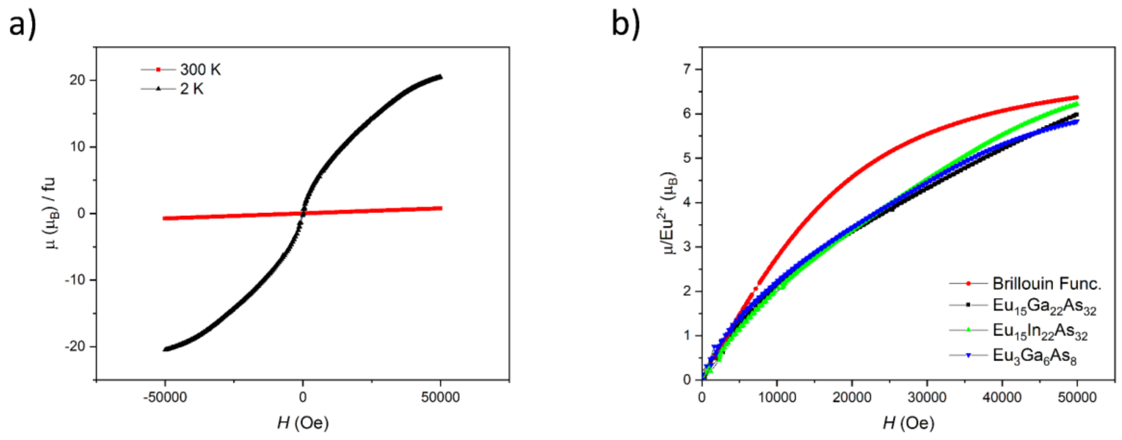

Figure A.55: (a) Magnetization isotherms of $Eu_3Ga_6As_8$ at 300 K (red) and 2 K (black). (b) Magnetization isotherms of $Eu_{15}Ga_{22}As_{32}$, $Eu_{15}In_{22}As_{32}$ and $Eu_3Ga_6As_8$ at 2 K and a Brillouin Function for $J = 7/2$.

A.5 New layered supertetrahedral compounds T2-*M*SiAs$_2$, T3-*M*GaSiAs$_3$ and polytypic T4-*M*$_4$Ga$_5$SiAs$_9$ (*M* = Sr, Eu)

Table A.69: Atomic coordinates, isotropic thermal parameter B_{iso} and site occupancy factors (*sof*) of SrSiAs$_2$ from Rietveld refinement.

atom	Wyckoff	*x*	*y*	*z*	B_{iso}	*sof*
Sr1	8*f*	0.4705(8)	0.3246(12)	0.0949(7)	1.5	1
Sr2	8*f*	0.2817(8)	0.068(1)	0.4033(8)	1.5	1
Si1	8*f*	0.108(2)	0.185(3)	0.175(2)	0.7	1
Si2	8*f*	0.134(2)	0.435(3)	0.327(2)	0.7	1
As1	8*f*	0.0100(7)	0.336(1)	0.4095(8)	0.7	1
As2	8*f*	0.2228(8)	0.070(1)	0.0920(8)	0.7	1
As3	8*f*	0.2581(7)	0.320(1)	0.2536(8)	0.7	1
As4	4*e*	0	0.067(2)	1/4	0.7	1
As5	4*e*	0	0.577(2)	1/4	0.7	1

Table A.70: Atomic coordinates, isotropic thermal parameter B_{iso} and site occupancy factors (*sof*) of EuSiAs$_2$ from Rietveld refinement.

atom	Wyckoff	*x*	*y*	*z*	B_{iso}	*sof*
Eu1	8*f*	0.2947(7)	0.0605(6)	0.4011(5)	0.7	1
Eu2	8*f*	0.4698(7)	0.3187(6)	0.1030(5)	0.7	1
Si1	8*f*	0.112(3)	0.197(3)	0.166(3)	0.7	1
Si2	8*f*	0.127(3)	0.403(2)	0.324(3)	0.7	1
As1	8*f*	0.022(1)	0.316(1)	0.387(1)	0.7	1
As2	8*f*	0.226(1)	0.028(1)	0.093(1)	0.7	1
As3	8*f*	0.240(1)	0.306(1)	0.2303(9)	0.7	1
As4	4*e*	0	0.062(2)	1/4	0.7	1
As5	4*e*	0	0.590(2)	1/4	0.7	1

Table A.71: Atomic coordinates, isotropic thermal parameter B_{iso} and site occupancy factors (*sof*) of SrGaSiAs$_3$ from Rietveld refinement.

atom	Wyckoff	*x*	*y*	*z*	B_{iso}	*sof*
Sr1	8*f*	0.3236(9)	0.432(1)	0.0772(3)	1.5	1
Sr2	8*f*	0.5680(8)	0.1760(9)	0.0753(3)	1.5	1
Ga1	8*f*	0.044(2)	0.319(2)	0.3841(6)	1	0.28(2)
Ga2	8*f*	0.204(2)	0.069(2)	0.1112(7)	1	0.14(3)
Ga3	8*f*	0.247(1)	0.3140(2)	0.2504(4)	1	0.79(3)
Ga4	4*e*	0	0.063(2)	1/4	1	0.76(4)
Ga5	4*e*	0	0.566(2)	1/4	1	0.82(4)
Si1	8*f*	0.044(2)	0.319(2)	0.3841(6)	1	0.72(2)
Si2	8*f*	0.204(2)	0.069(2)	0.1112(7)	1	0.86(3)
Si3	8*f*	0.247(1)	0.314(2)	0.2504(4)	1	0.21(3)
Si4	4*e*	0	0.063(2)	1/4	1	0.24(4)
Si5	4*e*	0	0.566(2)	1/4	1	0.18(4)

As1	8*f*	0.0690(1)	0.190(1)	0.0418(3)	1	1
As2	8*f*	0.1070(1)	0.439(1)	0.1736(6)	1	1
As3	8*f*	0.152(1)	0.182(1)	0.3245(6)	1	1
As4	8*f*	0.2927(9)	0.088(1)	0.5486(4)	1	1
As5	8*f*	0.360(1)	0.1909(1)	0.1738(6)	1	1
As6	8*f*	0.403(1)	0.434(1)	0.3253(6)	1	1

Table A.72: Atomic coordinates, isotropic thermal parameter B_{iso} and site occupancy factors (*sof*) of EuGaSiAs$_3$ from Rietveld refinement.

atom	Wyckoff	*x*	*y*	*z*	B_{iso}	*sof*
Eu1	8*f*	0.317(2)	0.418(2)	0.0745(6)	1	1
Eu2	8*f*	0.575(2)	0.188(2)	0.0822(6)	1	1
Ga1	8*f*	0.050(2)	0.315(3)	0.380(1)	0.7	0.28(5)
Ga2	8*f*	0.190(2)	0.072(3)	0.113(1)	0.7	0.15(5)
Ga3	8*f*	0.249(3)	0.314(3)	0.251(1)	0.7	0.98(9)
Ga4	4*e*	0	0.066(4)	0.25	0.7	0.55(1)
Ga5	4*e*	0	0.567(4)	0.25	0.7	0.63(9)
Si1	8*f*	0.050(2)	0.315(3)	0.380(1)	0.7	0.72(5)
Si2	8*f*	0.190(2)	0.072(3)	0.113(1)	0.7	0.85(5)
Si3	8*f*	0.249(3)	0.314(3)	0.251(1)	0.7	0.02(9)
Si4	4*e*	0	0.066(4)	0.25	0.7	0.45(1)
Si5	4*e*	0	0.567(4)	0.25	0.7	0.37(9)
As1	8*f*	0.052(4)	0.162(3)	0.042(1)	0.7	1
As2	8*f*	0.096(4)	0.062(4)	0.669(1)	0.7	1
As3	8*f*	0.106(4)	0.440(4)	0.1623(9)	0.7	1
As4	8*f*	0.143(4)	0.186(4)	0.3206(1)	0.7	1
As5	8*f*	0.311(4)	0.075(3)	0.551(1)	0.7	1
As6	8*f*	0.356(4)	0.192(4)	0.180(1)	0.7	1

Table A.73: Atomic coordinates, equivalent displacement parameters (Å^2) and site occupancy factors (*sof*) of *tI*-Sr$_4$Ga$_5$SiAs$_9$ from single crystal data.

atom	Wyckoff	*x*	*y*	*z*	U_{eq}	*sof*
Sr1	16*h*	0	0.0796(2)	0.17078(4)	0.0154(4)	1
Sr2	16*f*	0.1656(1)	0	0	0.0062(3)	1
Sr3	8*e*	0	1/4	0.82728(6)	0.0211(7)	1
Sr4	8*d*	0	0	1/2	0.0062(4)	1
Ga1	32*i*	0.1678(1)	0.0834(1)	0.09302(4)	0.0067(3)	0.8333
Ga2	16*h*	0	0.0828(2)	0.40860(5)	0.0045(4)	0.8333
Ga3	16*h*	0	0.0832(2)	0.27166(5)	0.0055(4)	0.8333
Ga4	8*e*	0	1/4	0.02238(7)	0.0039(5)	0.8333
Si1	32*i*	0.1678(1)	0.0834(1)	0.09302(4)	0.0067(3)	0.1667
Si2	16*h*	0	0.0828(2)	0.40860(5)	0.0045(4)	0.1667
Si3	16*h*	0	0.0832(2)	0.27166(5)	0.0055(4)	0.1667
Si4	8*e*	0	1/4	0.02238(7)	0.0039(5)	0.1667
As1	32*i*	0.33199(9)	0.0760(1)	0.05554(3)	0.0057(3)	1
As2	16*h*	0	0.0753(2)	0.05627(4)	0.0061(4)	1
As3	16*h*	0	0.0910(2)	0.62181(4)	0.0062(4)	1

As4	16*h*	0	0.5835(1)	0.23364(4)	0.0054(4)	1
As5	16*g*	0.1609(1)	0.4109(1)	7/8	0.0087(4)	1
As6	8*e*	0	1/4	0.23337(6)	0.0065(5)	1
As7	4*b*	0	1/4	3/8	0.0053(6)	1

Table A.74: Anisotropic displacement parameters (Å^2) of of *tI*-$Sr_4Ga_5SiAs_9$ from single crystal data.

atom	U_{11}	U_{22}	U_{33}	U_{23}	U_{13}	U_{12}
Sr1	0.0286(1)	0.0058(7)	0.0118(8)	0.0006(6)	0	0
Sr2	0.0029(6)	0.0067(7)	0.0090(6)	-0.0017(5)	0	0
Sr3	0.047(2)	0.005(1)	0.011(1)	0	0	0
Sr4	0.0047(9)	0.006(1)	0.0084(9)	0.0018(7)	0	0
Ga1	0.0066(7)	0.0066(7)	0.0070(6)	0.0008(5)	-0.0009(5)	-0.0001(6)
Ga2	0.0038(8)	0.0048(9)	0.0048(8)	0.0001(6)	0	0
Ga3	0.0083(9)	0.0017(8)	0.0065(8)	-0.0002(7)	0	0
Ga4	0.005(1)	0.003(1)	0.004(1)	0	0	0
Si1	0.0066(7)	0.0066(7)	0.0070(6)	0.0008(5)	-0.0009(5)	-0.0001(6)
Si2	0.0038(8)	0.0048(9)	0.0048(8)	0.0001(6)	0	0
Si3	0.0083(9)	0.0017(8)	0.0065(8)	-0.0002(7)	0	0
Si4	0.005(1)	0.003(1)	0.004(1)	0	0	0
As1	0.0017(5)	0.0111(6)	0.0044(5)	-0.0003(4)	-0.0007(4)	-0.0004(5)
As2	0.0027(7)	0.0101(8)	0.0054(7)	-0.0004(6)	0	0
As3	0.0042(7)	0.0062(8)	0.0082(7)	0.0000(6)	0	0
As4	0.0055(7)	0.0047(7)	0.0061(7)	0.0003(5)	0	0
As5	0.0058(5)	0.0058(5)	0.0145(8)	-0.0029(4)	0.0029(4)	-0.0009(6)
As6	0.007(1)	0.006(1)	0.007(1)	0	0	0
As7	0.0034(9)	0.0034(9)	0.009(1)	0	0	0

Table A.75: Atomic coordinates, equivalent displacement parameters (Å^2) and site occupancy factors (*sof*) of *mC*-$Eu_4Ga_5SiAs_9$ from single crystal data.

atom	Wyckoff	*x*	*y*	*z*	U_{eq}	*sof*
Eu1	8*f*	0.08409(2)	0.41646(2)	0.00101(2)	0.01168(4)	1
Eu2	8*f*	0.16630(2)	0.16608(2)	0.49904(2)	0.01166(4)	1
Eu3	8*f*	0.32079(2)	0.45559(2)	0.15991(2)	0.01852(5)	1
Eu4	8*f*	0.35113(2)	0.12741(2)	0.34065(2)	0.01893(5)	1
Eu5	8*f*	0.48399(2)	0.29169(2)	0.15364(2)	0.02409(6)	1
Eu6	4*c*	1/4	1/4	0	0.01163(6)	1
Eu7	4*a*	0	0	0	0.01167(6)	1
Ga1	8*f*	0.04927(3)	0.20789(3)	0.04245(2)	0.01024(9)	0.86
Ga2	8*f*	0.07234(3)	0.04166(3)	0.18583(3)	0.00991(9)	0.8067
Ga3	8*f*	0.07253(3)	0.37594(3)	0.18191(2)	0.00878(9)	0.86
Ga4	8*f*	0.09554(3)	0.20785(3)	0.31799(2)	0.00897(9)	0.86
Ga5	8*f*	0.11916(3)	0.37625(3)	0.45832(2)	0.00991(9)	0.8332
Ga6	8*f*	0.21610(3)	0.04100(3)	0.04271(2)	0.00977(9)	0.86
Ga7	8*f*	0.23941(3)	0.20857(3)	0.18574(2)	0.00996(9)	0.8067
Ga8	8*f*	0.26069(3)	0.37441(3)	0.31434(3)	0.0102(1)	0.8067
Ga9	8*f*	0.40652(3)	0.04175(3)	0.18565(3)	0.01033(9)	0.8067
Si1	8*f*	0.04927(3)	0.20789(3)	0.04245(2)	0.01024(9)	0.14

Si2	8*f*	0.07234(3)	0.04166(3)	0.18583(3)	0.00991(9)	0.1933
Si3	8*f*	0.07253(3)	0.37594(3)	0.18191(2)	0.00878(9)	0.14
Si4	8*f*	0.09554(3)	0.20785(3)	0.31799(2)	0.00897(9)	0.14
Si5	8*f*	0.11916(3)	0.37625(3)	0.45832(2)	0.00991(9)	0.1668
Si6	8*f*	0.21610(3)	0.04100(3)	0.04271(2)	0.00977(9)	0.14
Si7	8*f*	0.23941(3)	0.20857(3)	0.18574(2)	0.00996(9)	0.1933
Si8	8*f*	0.26069(3)	0.37441(3)	0.31434(3)	0.0102(1)	0.1933
Si9	8*f*	0.40652(3)	0.04175(3)	0.18565(3)	0.01033(9)	0.1933
As1	8*f*	0.02020(3)	0.46377(3)	0.39006(2)	0.01040(8)	1
As2	8*f*	0.02641(3)	0.11986(3)	0.38945(2)	0.01019(8)	1
As3	8*f*	0.13920(3)	0.04636(3)	0.61142(2)	0.01037(8)	1
As4	8*f*	0.14868(3)	0.29493(3)	0.11055(2)	0.01019(8)	1
As5	8*f*	0.17047(2)	0.46348(3)	0.24300(2)	0.00998(8)	1
As6	8*f*	0.17317(2)	0.11988(3)	0.25734(2)	0.00983(8)	1
As7	8*f*	0.19528(3)	0.28862(3)	0.39003(2)	0.01048(8)	1
As8	8*f*	0.28520(2)	0.04132(3)	0.46363(2)	0.01043(8)	1
As9	8*f*	0.31496(3)	0.12944(3)	0.11130(2)	0.01041(8)	1
As10	8*f*	0.34079(3)	0.29148(3)	0.25013(2)	0.01215(8)	1
As11	8*f*	0.38010(2)	0.37565(3)	0.03430(2)	0.00983(8)	1
As12	8*f*	0.54759(3)	0.20800(3)	0.03372(2)	0.01002(8)	1
As13	4*e*	0	0.29186(4)	1/4	0.0080(1)	1
As14	4*e*	0	0.63236(4)	1/4	0.0123(1)	1
As15	4*e*	0	0.95083(4)	1/4	0.0120(1)	1

Table A.76: Anisotropic displacement parameters (Å^2) of of mC-Eu$_4$Ga$_5$SiAs$_9$ from single crystal data.

atom	U_{11}	U_{22}	U_{33}	U_{23}	U_{13}	U_{12}
Eu1	0.01111(9)	0.01067(9)	0.01348(9)	0.00109(7)	0.00251(7)	0.00129(7)
Eu2	0.01050(9)	0.01075(9)	0.01344(9)	0.00069(7)	0.00075(7)	-0.00106(7)
Eu3	0.0213(1)	0.0211(1)	0.0132(1)	-0.00091(8)	0.00266(8)	0.01136(9)
Eu4	0.0212(1)	0.0216(1)	0.0137(1)	-0.00085(9)	0.00111(8)	-0.01189(9)
Eu5	0.0304(1)	0.0305(1)	0.0111(1)	0.00004(9)	0.00151(9)	0.0206(1)
Eu6	0.0110(1)	0.0107(1)	0.0136(1)	0.0005(1)	0.0033(1)	0.0011(1)
Eu7	0.0107(1)	0.0105(1)	0.0137(1)	-0.0014(1)	0.0014(1)	0.0010(1)
Ga1	0.0102(2)	0.0106(2)	0.0099(2)	-0.0002(2)	0.0014(2)	0.0021(2)
Ga2	0.0102(2)	0.0100(2)	0.0096(2)	-0.0001(2)	0.0017(2)	0.0003(2)
Ga3	0.0090(2)	0.0090(2)	0.0083(2)	-0.0004(2)	0.0011(2)	0.0005(2)
Ga4	0.0092(2)	0.0092(2)	0.0086(2)	-0.0002(2)	0.0014(2)	-0.0004(2)
Ga5	0.0102(2)	0.0100(2)	0.0095(2)	0.0002(2)	0.0013(2)	-0.0022(2)
Ga6	0.0100(2)	0.0100(2)	0.0093(2)	-0.0001(2)	0.0012(2)	0.0016(2)
Ga7	0.0103(2)	0.0099(2)	0.0097(2)	-0.0002(2)	0.0015(2)	0.0001(2)
Ga8	0.0104(2)	0.0101(2)	0.0100(2)	-0.0005(2)	0.0013(2)	-0.0003(2)
Ga9	0.0100(2)	0.0109(2)	0.0099(2)	0.0001(2)	0.0006(2)	0.0002(2)
Si1	0.0102(2)	0.0106(2)	0.0099(2)	-0.0002(2)	0.0014(2)	0.0021(2)
Si2	0.0102(2)	0.0100(2)	0.0096(2)	-0.0001(2)	0.0017(2)	0.0003(2)
Si3	0.0090(2)	0.0090(2)	0.0083(2)	-0.0004(2)	0.0011(2)	0.0005(2)
Si4	0.0092(2)	0.0092(2)	0.0086(2)	-0.0002(2)	0.0014(2)	-0.0004(2)
Si5	0.0102(2)	0.0100(2)	0.0095(2)	0.0002(2)	0.0013(2)	-0.0022(2)

Si6	0.0100(2)	0.0100(2)	0.0093(2)	-0.0001(2)	0.0012(2)	0.0016(2)
Si7	0.0103(2)	0.0099(2)	0.0097(2)	-0.0002(2)	0.0015(2)	0.0001(2)
Si8	0.0104(2)	0.0101(2)	0.0100(2)	-0.0005(2)	0.0013(2)	-0.0003(2)
Si9	0.0100(2)	0.0109(2)	0.0099(2)	0.0001(2)	0.0006(2)	0.0002(2)
As1	0.0115(2)	0.0113(2)	0.0085(2)	-0.0003(2)	0.0019(1)	-0.0043(1)
As2	0.0109(2)	0.0113(2)	0.0082(2)	0.0002(2)	0.0006(1)	-0.0038(1)
As3	0.0114(2)	0.0118(2)	0.0078(2)	0.0004(2)	0.0008(1)	-0.0031(2)
As4	0.0112(2)	0.0114(2)	0.0080(2)	0.0005(2)	0.0014(1)	0.0038(1)
As5	0.0093(2)	0.0094(2)	0.0111(2)	-0.0004(2)	0.0010(1)	-0.0000(1)
As6	0.0094(2)	0.0093(2)	0.0109(2)	-0.0004(1)	0.0019(1)	-0.0000(1)
As7	0.0114(2)	0.0114(2)	0.0085(2)	0.0006(2)	0.0008(1)	-0.0038(2)
As8	0.0111(2)	0.0108(2)	0.0094(2)	0.0000(2)	0.0014(1)	-0.0002(1)
As9	0.0119(2)	0.0118(2)	0.0076(2)	0.0004(2)	0.0014(1)	0.0031(2)
As10	0.0108(2)	0.0107(2)	0.0150(2)	-0.0010(2)	0.0020(2)	-0.0001(1)
As11	0.0104(2)	0.0104(2)	0.0086(2)	0.0002(1)	0.0010(1)	0.0006(1)
As12	0.0105(2)	0.0109(2)	0.0087(2)	-0.0001(2)	0.0015(1)	0.0006(1)
As13	0.0078(2)	0.0080(2)	0.0081(2)	0	0.0011(2)	0
As14	0.0106(3)	0.0110(3)	0.0152(3)	0	0.0012(2)	0
As15	0.0106(3)	0.0111(3)	0.0145(3)	0	0.0025(2)	0

Table A.77: Atomic coordinates, isotropic displacement parameters B_{iso} and site occupancy factors (*sof*) of *mC*-$Sr_4Ga_5SiAs_9$ from Rietveld refinement.

atom	Wyckoff	*x*	*y*	*z*	B_{iso}	*sof*
Sr1	8*f*	0.072(2)	0.401(2)	0.018(2)	0.7	1
Sr2	8*f*	0.167(2)	0.164(2)	0.499(2)	0.7	1
Sr3	8*f*	0.307(2)	0.459(2)	0.140(1)	0.7	1
Sr4	8*f*	0.359(2)	0.133(2)	0.371(2)	0.7	1
Sr5	8*f*	0.481(2)	0.293(2)	0.100(1)	0.7	1
Sr6	4*c*	0.25	0.25	0	0.7	1
Sr7	4*a*	0	0	0	0.7	1
Ga1	8*f*	0.04928	0.20790	0.04244	0.7	0.8067
Ga2	8*f*	0.07233	0.04166	0.18582	0.7	0.8332
Ga3	8*f*	0.07254	0.37594	0.18192	0.7	0.8067
Ga4	8*f*	0.09554	0.20785	0.31800	0.7	0.86
Ga5	8*f*	0.11916	0.37626	0.45832	0.7	0.86
Ga6	8*f*	0.21611	0.04100	0.04272	0.7	0.86
Ga7	8*f*	0.23940	0.20857	0.18574	0.7	0.8067
Ga8	8*f*	0.26069	0.37440	0.31434	0.7	0.8067
Ga9	8*f*	0.40652	0.04175	0.18565	0.7	0.86
Si1	8*f*	0.04928	0.20790	0.04244	0.7	0.1933
Si2	8*f*	0.07233	0.04166	0.18582	0.7	0.1668
Si3	8*f*	0.07254	0.37594	0.18192	0.7	0.1933
Si4	8*f*	0.09554	0.20785	0.31800	0.7	0.14
Si5	8*f*	0.11916	0.37626	0.45832	0.7	0.14
Si6	8*f*	0.21611	0.04100	0.04272	0.7	0.14
Si7	8*f*	0.23940	0.20857	0.18574	0.7	0.1933
Si8	8*f*	0.26069	0.37440	0.31434	0.7	0.1933
Si9	8*f*	0.40652	0.04175	0.18565	0.7	0.14

As1	8*f*	0.021(2)	0.127(2)	0.386(2)	0.7	1
As2	8*f*	0.027(2)	0.468(2)	0.390(2)	0.7	1
As3	8*f*	0.131(2)	0.054(2)	0.644(2)	0.7	1
As4	8*f*	0.137(2)	0.284(2)	0.126(2)	0.7	1
As5	8*f*	0.160(3)	0.450(2)	0.247(2)	0.7	1
As6	8*f*	0.174(2)	0.115(2)	0.240(2)	0.7	1
As7	8*f*	0.181(2)	0.281(2)	0.393(2)	0.7	1
As8	8*f*	0.191(2)	0.518(2)	0.024(2)	0.7	1
As9	8*f*	0.314(2)	0.145(2)	0.136(2)	0.7	1
As10	8*f*	0.340(2)	0.292(2)	0.248(2)	0.7	1
As11	8*f*	0.392(2)	0.368(2)	0.037(2)	0.7	1
As12	8*f*	0.558(2)	0.218(2)	0.037(2)	0.7	1
As13	4*e*	0	0.303(3)	1/4	0.7	1
As14	4*e*	0	0.628(3)	1/4	0.7	1
As15	4*e*	0	0.941(3)	1/4	0.7	1

Table A.78: Atomic coordinates, isotropic displacement parameters B_{iso} and site occupancy factors (*sof*) of *tI*-$Eu_4Ga_5SiAs_9$ from Rietveld refinement.

atom	Wyckoff	*x*	*y*	*z*	B_{iso}	*sof*
Eu1	16*h*	0	0.082(4)	0.1740(7)	0.7	1
Eu2	16*f*	0.167(4)	0	0	0.7	1
Eu3	8*e*	0	1/4	0.805(1)	0.7	1
Eu4	8*d*	0	0	1/2	0.7	1
Ga1	32*i*	0.16788	0.08340	0.09308	0.7	0.8333
Ga2	16*h*	0	0.08276	0.40857	0.7	0.8333
Ga3	16*h*	0	0.08331	0.27169	0.7	0.8333
Ga4	8*e*	0	1/4	0.0224	0.7	0.8333
Si1	32*i*	0.16788	0.08340	0.09308	0.7	0.1667
Si2	16*h*	0	0.08276	0.40857	0.7	0.1667
Si3	16*h*	0	0.08331	0.27169	0.7	0.1667
Si4	8*e*	0	1/4	0.0224	0.7	0.1667
As1	32*i*	0.330(4)	0.075(5)	0.0555(9)	0.7	1
As2	16*h*	0	0.067(8)	0.0567(1)	0.7	1
As3	16*h*	0	0.083(8)	0.628(1)	0.7	1
As4	16*h*	0	0.582(7)	0.233(2)	0.7	1
As5	16*g*	0.16077	0.41077	7/8	0.7	1
As6	8*e*	0	1/4	0.237(2)	0.7	1
As7	4*b*	0	1/4	3/8	0.7	1

Table A.79: Electrical resistivity *ρ*, charge carrier density *N* and Hall mobility *μ* at *T* = 300 and 400 K of $Sr_4Ga_5SiAs_9$ and $Eu_4Ga_5SiAs_9$.

Formula	ρ_{300K} (Ω cm)	ρ_{400K} (Ω cm)	N_{300K} (cm^{-3})	N_{400K} (cm^{-3})	μ_{300K} (cm^2 V^{-1} s^{-1})	μ_{400K} (cm^2 V^{-1} s^{-1})
$Sr_4Ga_5SiAs_9$	5.70	2.68	$1.7\cdot10^{18}$	$2.2\cdot10^{18}$	0.66	1.1
$Eu_4Ga_5SiAs_9$	0.74	0.38	$6.1\cdot10^{18}$	$1.5\cdot10^{18}$	1.4	1.1

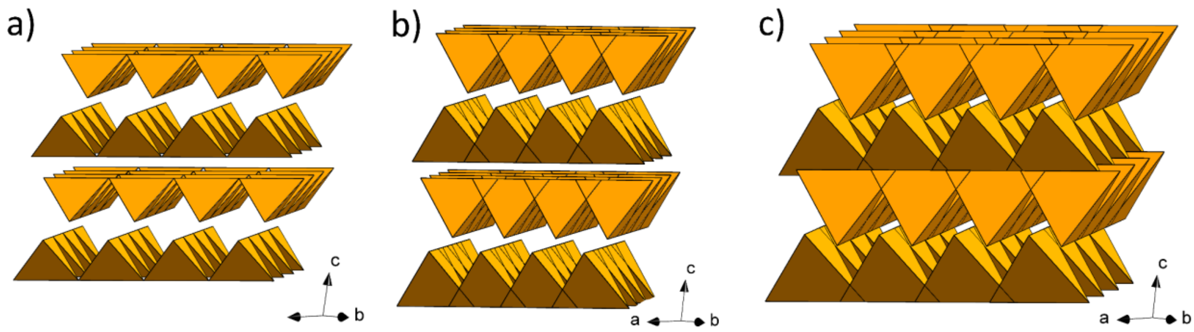

Figure A.56: (a) Layered structure of *M*SiAs$_2$ with a saw tooth-like arrangement. Each tetrahedron represents one T2 supertedrahedron. (b) Layered structure of *M*GaSiAs$_3$ with a saw tooth-like arrangement. Each tetrahedron represents one T3 supertedrahedron. (c) Layered structure of *mC*-*M*$_4$Ga$_5$SiAs$_9$ with a saw tooth-like arrangement. Each tetrahedron represents one T4 supertedrahedron.

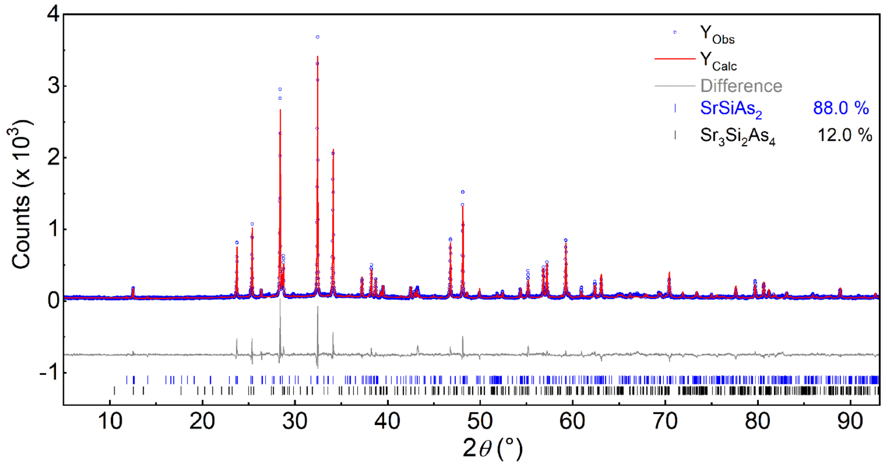

Figure A.57: X-ray powder diffraction pattern (Y$_{obs}$, Cu Kα), Rietveld fit (Y$_{calc}$) and difference curve (grey) of SrSiAs$_2$ and Sr$_3$Si$_2$As$_2$ as a side phase.

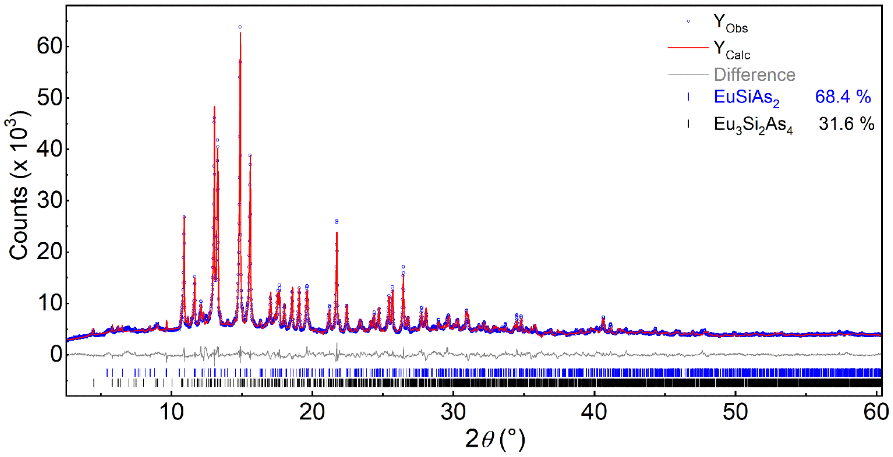

Figure A.58: X-ray powder diffraction pattern (Y$_{obs}$, Mo Kα), Rietveld fit (Y$_{calc}$) and difference curve (grey) of EuSiAs$_2$ and Eu$_3$Si$_2$As$_2$ as a side phase.

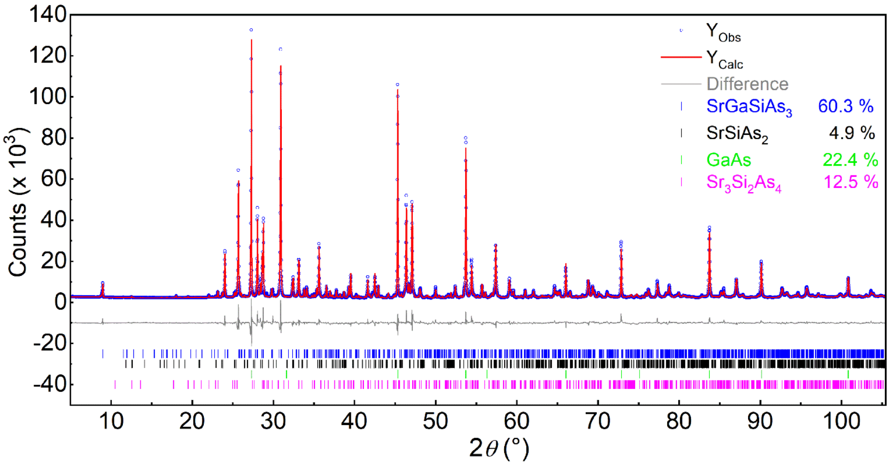

Figure A.59: X-ray powder diffraction pattern (Y_{obs}, Cu Kα), Rietveld fit (Y_{calc}) and difference curve (grey) of $SrGaSiAs_3$ and $SrSiAs_2$, GaAs and $Sr_3Si_2As_2$ as side phases.

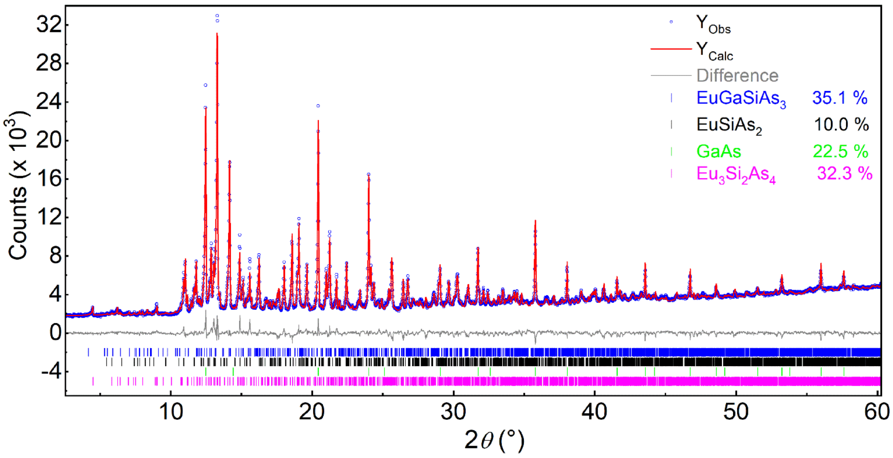

Figure A.60: X-ray powder diffraction pattern (Y_{obs}, Mo Kα), Rietveld fit (Y_{calc}) and difference curve (grey) of $EuGaSiAs_3$ and $EuSiAs_2$, GaAs and $Eu_3Si_2As_2$ as side phases.

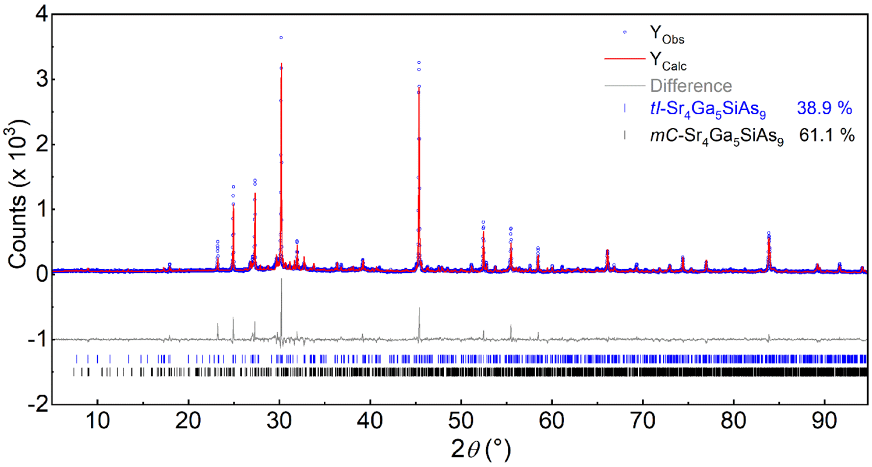

Figure A.61: X-ray powder diffraction pattern (Y_{obs}, Cu Kα), Rietveld fit (Y_{calc}) and difference curve (grey) of $Sr_4Ga_5SiAs_9$.

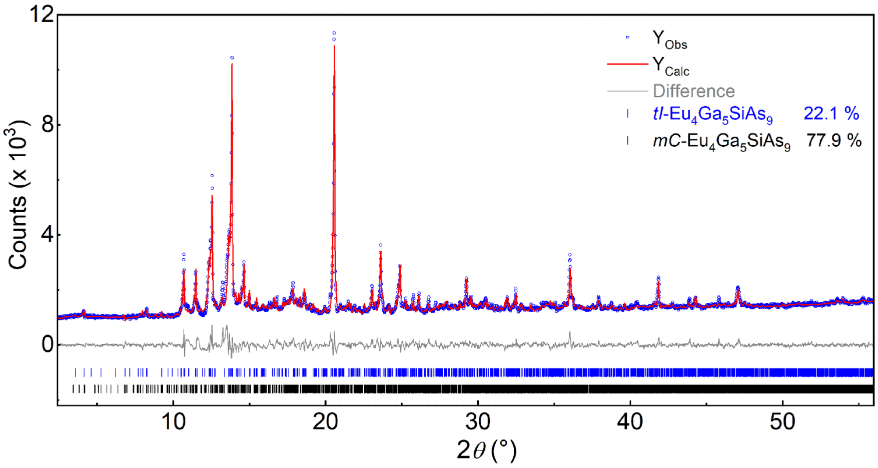

Figure A.62: X-ray powder diffraction pattern (Y_{obs}, Mo Kα), Rietveld fit (Y_{calc}) and difference curve (grey) of $Eu_4Ga_5SiAs_9$.

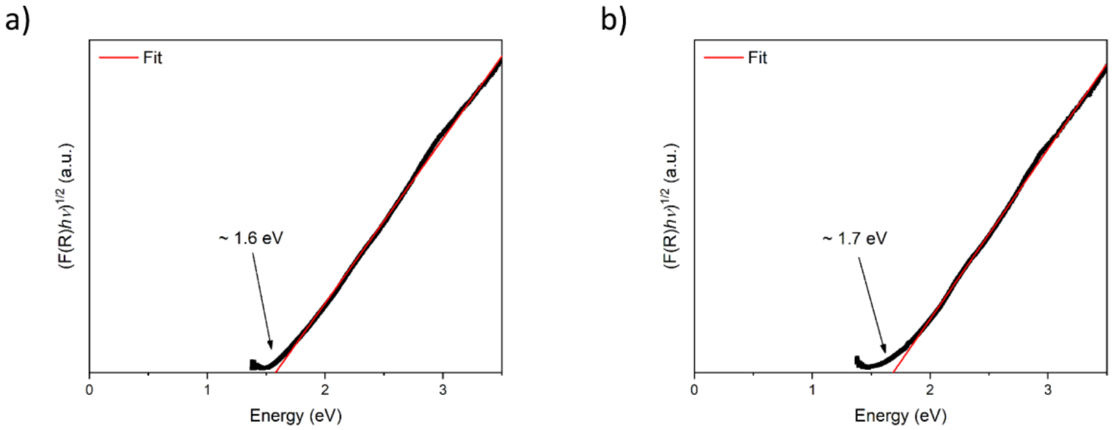

Figure A.63: Tauc plots of UV/Vis spectra of (a) $Sr_4Ga_5SiAs_9$ and (b) $Eu_4Ga_5SiAs_9$.

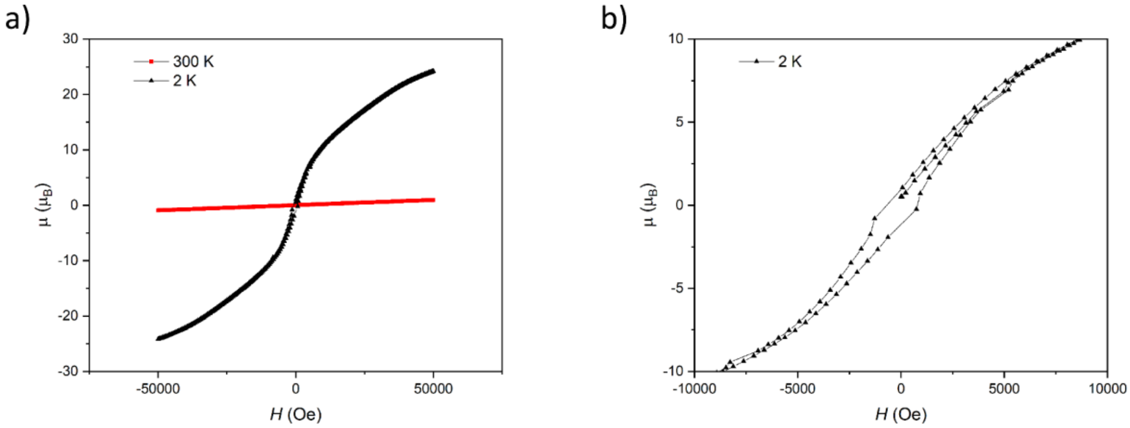

Figure A.64: (a) Magnetization isotherm of $Eu_4Ga_5SiAs_9$ at $T = 300$ K (red) and 2 K (black) per formula unit and (b) an excerpt of the isotherm at $T = 2$ K between -10 and 10 kOe (1 kOe = 7.96×10^4 A m^{-1}).

A.6 High-pressure synthesis and crystal structure of $SrGa_4As_4$

Table A.80: Detailed single crystal data of $SrGa_4As_4$.

formula	$SrGa_4As_4$
space group	$P3_221$ (No. 154)
a / Å	6.3615(1)
c / Å	16.5792(2)
V_{cell} / Å^3	581.05(2)
Z	3
$\rho_{X\text{-}Ray}$ / g·cm^{-3}	5.711
crystal size / mm	0.10 x 0.05 x 0.05
diffractometer	Bruker D8 Quest
radiation type (λ / nm)	Mo Kα
T / K	293
μ / mm^{-1}	37.42
F(000)	882
Θ-range / °	3.7-30.4
hkl range	h ≤ ±8; k ≤ ±8; l ≤ ±21
refl. measured	14966
independent refl.	928
parameters	52
R_σ / R_{int}	0.0135 / 0.0337
R_1 ($F^2 > 2\sigma(F^2)$) / all	0.0116 / 0.0120
wR_2 ($F^2 > 2\sigma(F^2)$) / all	0.0253 / 0.0254
GooF	1.172
$\Delta\rho_{max/min}$ / eÅ^{-3}	+0.51 / -0.69
Absolute structure	Flack x determined using 340 quotients $[(I^+) - (I^-)]/[(I^+) + (I^-)]$
Absolute structure parameter	-0.024(11)

Table A.81: Atomic coordinates, equivalent displacement parameters (Å^2) and site occupancy factors (*sof*) of $SrGa_4As_4$

atom	Wyckoff	*x*	*y*	*z*	U_{eq}	*sof*
Sr1	3b	0.52374 (8)	0	1/6	0.01264 (11)	1
Ga1A	6c	0.8090 (7)	0.9427 (8)	0.8779 (2)	0.0120 (4)	0.5
Ga1B	6c	0.8516 (7)	0.9303 (8)	0.8920 (2)	0.0175 (5)	0.5
Ga2	6c	0.27470 (8)	0.54448 (7)	0.00800 (2)	0.00988 (9)	1
As1	6c	0.50915 (7)	0.49019 (6)	0.11634 (2)	0.00817 (8)	1
As2	6c	0.86593 (6)	0.17439 (6)	0.00577 (2)	0.00838 (8)	1

Table A.82: Anisotropic displacement parameters (Å^2) of $SrGa_4As_4$ from single crystal data.

atom	U_{11}	U_{22}	U_{33}	U_{23}	U_{13}	U_{12}
Sr1	0.01406 (18)	0.0121 (2)	0.0111 (2)	0.00605 (12)	0.00104 (9)	0.00209 (17)
Ga1A	0.0136 (10)	0.0079 (6)	0.0131 (10)	0.0044 (6)	0.0032 (6)	0.0001 (6)
Ga1B	0.0184 (13)	0.0080 (7)	0.0206 (13)	0.0025 (7)	0.0107 (9)	−0.0018 (8)
Ga2	0.0105 (2)	0.00988 (18)	0.01119 (18)	0.00654 (16)	−0.00233 (16)	−0.00109 (14)
As1	0.00767 (16)	0.00801 (17)	0.00862 (16)	0.00376 (14)	−0.00032 (13)	0.00041 (12)
As2	0.00712 (16)	0.00890 (17)	0.00970 (17)	0.00444 (14)	0.00033 (13)	0.00055 (13)

Table A.83: Selected distances (Å) in $SrGa_4As_4$.

atoms	distance (Å)	atoms	distance (Å)
Sr1—As2	3.2665 (4)	Ga1A—As1^{xii}	2.477 (4)
Sr1—As2^{i}	3.2666 (4)	Ga1A—As2^{xiii}	2.503 (4)
Sr1—As1^{i}	3.2739 (4)	Ga1A—Ga1B^{xiv}	2.5444 (13)
Sr1—As1	3.2739 (4)	Ga1A—Ga1A^{xiv}	2.572 (8)
Sr1—As1^{ii}	3.3048 (4)	Ga1A—As1^{xv}	2.694 (2)
Sr1—As1^{iii}	3.3048 (4)	Ga1B—As2^{xiii}	2.415 (4)
Sr1—Ga1B^{iv}	3.312 (4)	Ga1B—As1^{xii}	2.515 (4)
Sr1—Ga1B^{v}	3.312 (4)	Ga1B—Ga1B^{xiv}	2.542 (8)
Sr1—Ga1A^{vi}	3.346 (4)	Ga1B—As2^{xvi}	2.845 (2)
Sr1—Ga1A^{vii}	3.346 (4)	Ga2—As2^{viii}	2.4384 (5)
Sr1—Ga2^{viii}	3.3505 (4)	Ga2—As1	2.4668 (5)
Sr1—Ga2^{ix}	3.3506 (4)	Ga2—As2^{xvii}	2.4868 (5)
Sr1—As2^{x}	3.4560 (4)	Ga2—As1^{viii}	2.5470 (5)
Sr1—As2^{xi}	3.4560 (4)	Ga2—Ga2^{viii}	2.9844 (8)

Symmetry codes: (i) x−y, −y, −z+1/3; (ii) x, y−1, z; (iii) x−y+1, −y+1, −z+1/3; (iv) y, x−1, −z+1; (v) −x+y+1, −x+1, z−2/3; (vi) y−1, x−1, −z+1; (vii) −x+y, −x+1, z−2/3; (viii) y, x, −z; (ix) −x+y, −x, z+1/3; (x) y, x−1, −z; (xi) −x+y+1, −x+1, z+1/3; (xii) y, x, −z+1; (xiii) x, y+1, z+1; (xiv) −x+2, −x+y+1, −z+5/3; (xv) −y+1, x−y+1, z+2/3; (xvi) y+1, x, −z+1; (xvii) x−1, y, z; (xviii) −y+1, x−y, z+2/3; (xix) −y, x−y, z+2/3; (xx) −y, x−y, z−1/3; (xxi) x, y+1, z; (xxii) −y+1, x−y, z−1/3; (xxiii) x, y−1, z−1; (xxiv) x+1, y, z; (xxv) −y+1, x−y−1, z−1/3; (xxvi) x+1, y+1, z.

Table A.84: Selected angles (°) in $SrGa_4As_4$.

atoms	angle (°)	atoms	angle (°)
As2—Sr1—As2^{i}	120.45 (2)	Ga1A^{xiv}—Ga1B—As2^{xvi}	89.08 (12)
As2—Sr1—As1^{i}	134.533 (8)	As2^{xiii}—Ga1B—Sr1^{xviii}	142.90 (10)
As2^{i}—Sr1—As1^{i}	78.453 (9)	As1^{xii}—Ga1B—Sr1^{xviii}	67.51 (9)
As2—Sr1—As1	78.453 (9)	Ga1B^{xiv}—Ga1B—Sr1^{xviii}	67.43 (7)
As2^{i}—Sr1—As1	134.533 (8)	Ga1A^{xiv}—Ga1B—Sr1^{xviii}	72.45 (15)
As1^{i}—Sr1—As1	119.39 (2)	As2^{xvi}—Ga1B—Sr1^{xviii}	63.55 (6)
As2—Sr1—As1^{ii}	79.285 (11)	As2^{xiii}—Ga1B—Sr1^{xv}	67.96 (9)
As2^{i}—Sr1—As1^{ii}	74.128 (11)	As1^{xii}—Ga1B—Sr1^{xv}	137.34 (9)
As1^{i}—Sr1—As1^{ii}	66.217 (5)	Ga1B^{xiv}—Ga1B—Sr1^{xv}	68.95 (7)
As1—Sr1—As1^{ii}	150.471 (11)	Ga1A^{xiv}—Ga1B—Sr1^{xv}	64.32 (16)
As2—Sr1—As1^{iii}	74.128 (11)	As2^{xvi}—Ga1B—Sr1^{xv}	119.38 (13)
As2^{i}—Sr1—As1^{iii}	79.284 (11)	Sr1^{xviii}—Ga1B—Sr1^{xv}	136.38 (13)
As1^{i}—Sr1—As1^{iii}	150.470 (11)	As2^{xiii}—Ga1B—Sr1^{xix}	100.06 (10)
As1—Sr1—As1^{iii}	66.217 (5)	As1^{xii}—Ga1B—Sr1^{xix}	39.58 (5)
As1^{ii}—Sr1—As1^{iii}	124.89 (2)	Ga1B^{xiv}—Ga1B—Sr1^{xix}	118.30 (16)

As2—Sr1—Ga1B$^{\mathrm{iv}}$	51.25 (5)
As2$^{\mathrm{i}}$—Sr1—Ga1B$^{\mathrm{iv}}$	73.07 (5)
As1$^{\mathrm{i}}$—Sr1—Ga1B$^{\mathrm{iv}}$	109.71 (7)
As1—Sr1—Ga1B$^{\mathrm{iv}}$	126.49 (6)
As1$^{\mathrm{ii}}$—Sr1—Ga1B$^{\mathrm{iv}}$	44.67 (7)
As1$^{\mathrm{iii}}$—Sr1—Ga1B$^{\mathrm{iv}}$	81.77 (7)
As2—Sr1—Ga1B$^{\mathrm{v}}$	73.07 (5)
As2$^{\mathrm{i}}$—Sr1—Ga1B$^{\mathrm{v}}$	51.25 (5)
As1$^{\mathrm{i}}$—Sr1—Ga1B$^{\mathrm{v}}$	126.49 (6)
As1—Sr1—Ga1B$^{\mathrm{v}}$	109.71 (7)
As1$^{\mathrm{ii}}$—Sr1—Ga1B$^{\mathrm{v}}$	81.77 (7)
As1$^{\mathrm{iii}}$—Sr1—Ga1B$^{\mathrm{v}}$	44.67 (7)
Ga1B$^{\mathrm{iv}}$—Sr1—Ga1B$^{\mathrm{v}}$	45.14 (14)
As2—Sr1—Ga1A$^{\mathrm{vi}}$	111.75 (6)
As2$^{\mathrm{i}}$—Sr1—Ga1A$^{\mathrm{vi}}$	123.12 (5)
As1$^{\mathrm{i}}$—Sr1—Ga1A$^{\mathrm{vi}}$	48.02 (5)
As1—Sr1—Ga1A$^{\mathrm{vi}}$	74.76 (5)
As1$^{\mathrm{ii}}$—Sr1—Ga1A$^{\mathrm{vi}}$	95.97 (6)
As1$^{\mathrm{iii}}$—Sr1—Ga1A$^{\mathrm{vi}}$	138.60 (6)
Ga1B$^{\mathrm{iv}}$—Sr1—Ga1A$^{\mathrm{vi}}$	135.24 (5)
Ga1B$^{\mathrm{v}}$—Sr1—Ga1A$^{\mathrm{vi}}$	174.30 (10)
As2—Sr1—Ga1A$^{\mathrm{vii}}$	123.12 (5)
As2$^{\mathrm{i}}$—Sr1—Ga1A$^{\mathrm{vii}}$	111.75 (6)
As1$^{\mathrm{i}}$—Sr1—Ga1A$^{\mathrm{vii}}$	74.76 (5)
As1—Sr1—Ga1A$^{\mathrm{vii}}$	48.02 (5)
As1$^{\mathrm{ii}}$—Sr1—Ga1A$^{\mathrm{vii}}$	138.60 (6)
As1$^{\mathrm{iii}}$—Sr1—Ga1A$^{\mathrm{vii}}$	95.97 (7)
Ga1B$^{\mathrm{iv}}$—Sr1—Ga1A$^{\mathrm{vii}}$	174.30 (10)
Ga1B$^{\mathrm{v}}$—Sr1—Ga1A$^{\mathrm{vii}}$	135.23 (5)
Ga1A$^{\mathrm{vi}}$—Sr1—Ga1A$^{\mathrm{vii}}$	45.20 (14)
As2—Sr1—Ga2$^{\mathrm{viii}}$	43.223 (9)
As2$^{\mathrm{i}}$—Sr1—Ga2$^{\mathrm{viii}}$	161.548 (17)
As1$^{\mathrm{i}}$—Sr1—Ga2$^{\mathrm{viii}}$	118.760 (14)
As1—Sr1—Ga2$^{\mathrm{viii}}$	45.205 (10)
As1$^{\mathrm{ii}}$—Sr1—Ga2$^{\mathrm{viii}}$	105.550 (10)
As1$^{\mathrm{iii}}$—Sr1—Ga2$^{\mathrm{viii}}$	86.374 (9)
Ga1B$^{\mathrm{iv}}$—Sr1—Ga2$^{\mathrm{viii}}$	93.55 (5)
Ga1B$^{\mathrm{v}}$—Sr1—Ga2$^{\mathrm{viii}}$	110.30 (5)
Ga1A$^{\mathrm{vi}}$—Sr1—Ga2$^{\mathrm{viii}}$	75.33 (5)
Ga1A$^{\mathrm{vii}}$—Sr1—Ga2$^{\mathrm{viii}}$	81.05 (6)
As2—Sr1—Ga2$^{\mathrm{ix}}$	161.548 (17)
As2$^{\mathrm{i}}$—Sr1—Ga2$^{\mathrm{ix}}$	43.223 (9)
As1$^{\mathrm{i}}$—Sr1—Ga2$^{\mathrm{ix}}$	45.205 (10)
As1—Sr1—Ga2$^{\mathrm{ix}}$	118.759 (14)
As1$^{\mathrm{ii}}$—Sr1—Ga2$^{\mathrm{ix}}$	86.374 (9)
As1$^{\mathrm{iii}}$—Sr1—Ga2$^{\mathrm{ix}}$	105.549 (10)
Ga1B$^{\mathrm{iv}}$—Sr1—Ga2$^{\mathrm{ix}}$	110.30 (5)
Ga1B$^{\mathrm{v}}$—Sr1—Ga2$^{\mathrm{ix}}$	93.55 (5)
Ga1A$^{\mathrm{xiv}}$—Ga1B—Sr1$^{\mathrm{xix}}$	125.48 (7)
As2$^{\mathrm{xvi}}$—Ga1B—Sr1$^{\mathrm{xix}}$	138.21 (12)
Sr1$^{\mathrm{xviii}}$—Ga1B—Sr1$^{\mathrm{xix}}$	101.86 (10)
Sr1$^{\mathrm{xv}}$—Ga1B—Sr1$^{\mathrm{xix}}$	98.42 (5)
As2$^{\mathrm{xiii}}$—Ga1B—Sr1$^{\mathrm{xiii}}$	30.22 (6)
As1$^{\mathrm{xii}}$—Ga1B—Sr1$^{\mathrm{xiii}}$	86.93 (10)
Ga1B$^{\mathrm{xiv}}$—Ga1B—Sr1$^{\mathrm{xiii}}$	155.24 (14)
Ga1A$^{\mathrm{xiv}}$—Ga1B—Sr1$^{\mathrm{xiii}}$	146.47 (15)
As2$^{\mathrm{xvi}}$—Ga1B—Sr1$^{\mathrm{xiii}}$	80.65 (8)
Sr1$^{\mathrm{xviii}}$—Ga1B—Sr1$^{\mathrm{xiii}}$	128.07 (9)
Sr1$^{\mathrm{xv}}$—Ga1B—Sr1$^{\mathrm{xiii}}$	93.16 (8)
Sr1$^{\mathrm{xix}}$—Ga1B—Sr1$^{\mathrm{xiii}}$	80.08 (6)
As2$^{\mathrm{viii}}$—Ga2—As1	127.996 (19)
As2$^{\mathrm{viii}}$—Ga2—As2$^{\mathrm{xvii}}$	101.790 (19)
As1—Ga2—As2$^{\mathrm{xvii}}$	107.308 (18)
As2$^{\mathrm{viii}}$—Ga2—As1$^{\mathrm{viii}}$	112.107 (18)
As1—Ga2—As1$^{\mathrm{viii}}$	100.790 (19)
As2$^{\mathrm{xvii}}$—Ga2—As1$^{\mathrm{viii}}$	104.987 (18)
As2$^{\mathrm{viii}}$—Ga2—Ga2$^{\mathrm{viii}}$	160.190 (16)
As1—Ga2—Ga2$^{\mathrm{viii}}$	54.718 (14)
As2$^{\mathrm{xvii}}$—Ga2—Ga2$^{\mathrm{viii}}$	94.821 (13)
As1$^{\mathrm{viii}}$—Ga2—Ga2$^{\mathrm{viii}}$	52.245 (14)
As2$^{\mathrm{viii}}$—Ga2—Sr1$^{\mathrm{xx}}$	66.554 (14)
As1—Ga2—Sr1$^{\mathrm{xx}}$	164.526 (19)
As2$^{\mathrm{xvii}}$—Ga2—Sr1$^{\mathrm{xx}}$	70.850 (14)
As1$^{\mathrm{viii}}$—Ga2—Sr1$^{\mathrm{xx}}$	65.805 (12)
Ga2$^{\mathrm{viii}}$—Ga2—Sr1$^{\mathrm{xx}}$	109.825 (18)
As2$^{\mathrm{viii}}$—Ga2—Sr1$^{\mathrm{xxi}}$	65.922 (13)
As1—Ga2—Sr1$^{\mathrm{xxi}}$	62.098 (13)
As2$^{\mathrm{xvii}}$—Ga2—Sr1$^{\mathrm{xxi}}$	126.697 (18)
As1$^{\mathrm{viii}}$—Ga2—Sr1$^{\mathrm{xxi}}$	128.043 (18)
Ga2$^{\mathrm{viii}}$—Ga2—Sr1$^{\mathrm{xxi}}$	112.066 (16)
Sr1$^{\mathrm{xx}}$—Ga2—Sr1$^{\mathrm{xxi}}$	131.844 (12)
As2$^{\mathrm{viii}}$—Ga2—Sr1$^{\mathrm{xvii}}$	94.008 (14)
As1—Ga2—Sr1$^{\mathrm{xvii}}$	87.434 (14)
As2$^{\mathrm{xvii}}$—Ga2—Sr1$^{\mathrm{xvii}}$	33.956 (10)
As1$^{\mathrm{viii}}$—Ga2—Sr1$^{\mathrm{xvii}}$	137.041 (15)
Ga2$^{\mathrm{viii}}$—Ga2—Sr1$^{\mathrm{xvii}}$	105.802 (10)
Sr1$^{\mathrm{xx}}$—Ga2—Sr1$^{\mathrm{xvii}}$	97.358 (11)
Sr1$^{\mathrm{xxi}}$—Ga2—Sr1$^{\mathrm{xvii}}$	93.202 (9)
As2$^{\mathrm{viii}}$—Ga2—Sr1	154.513 (14)
As1—Ga2—Sr1	29.480 (10)
As2$^{\mathrm{xvii}}$—Ga2—Sr1	84.221 (13)
As1$^{\mathrm{viii}}$—Ga2—Sr1	89.655 (14)
Ga2$^{\mathrm{viii}}$—Ga2—Sr1	37.413 (11)
Sr1$^{\mathrm{xx}}$—Ga2—Sr1	137.673 (13)
Sr1$^{\mathrm{xxi}}$—Ga2—Sr1	90.483 (9)
Sr1$^{\mathrm{xvii}}$—Ga2—Sr1	77.087 (5)

Ga1A^{vi}—Sr1—Ga2^{ix}	81.05 (6)
Ga1A^{vii}—Sr1—Ga2^{ix}	75.33 (5)
Ga2^{viii}—Sr1—Ga2^{ix}	154.42 (2)
As2—Sr1—As2^{x}	69.230 (6)
As2^{i}—Sr1—As2^{x}	150.543 (8)
As1^{i}—Sr1—As2^{x}	76.839 (11)
As1—Sr1—As2^{x}	72.738 (10)
As1^{ii}—Sr1—As2^{x}	81.367 (9)
As1^{iii}—Sr1—As2^{x}	129.115 (8)
Ga1B^{iv}—Sr1—As2^{x}	100.60 (6)
Ga1B^{v}—Sr1—As2^{x}	140.87 (6)
Ga1A^{vi}—Sr1—As2^{x}	43.14 (7)
Ga1A^{vii}—Sr1—As2^{x}	76.71 (7)
Ga2^{viii}—Sr1—As2^{x}	42.823 (9)
Ga2^{ix}—Sr1—As2^{x}	120.222 (14)
As2—Sr1—As2^{xi}	150.543 (8)
As2^{i}—Sr1—As2^{xi}	69.230 (6)
As1^{i}—Sr1—As2^{xi}	72.738 (10)
As1—Sr1—As2^{xi}	76.839 (11)
As1^{ii}—Sr1—As2^{xi}	129.114 (8)
As1^{iii}—Sr1—As2^{xi}	81.366 (9)
Ga1B^{iv}—Sr1—As2^{xi}	140.87 (6)
Ga1B^{v}—Sr1—As2^{xi}	100.60 (6)
Ga1A^{vi}—Sr1—As2^{xi}	76.71 (7)
Ga1A^{vii}—Sr1—As2^{xi}	43.14 (7)
Ga2^{viii}—Sr1—As2^{xi}	120.222 (14)
Ga2^{ix}—Sr1—As2^{xi}	42.823 (9)
As2^{x}—Sr1—As2^{xi}	117.382 (19)
As1^{xii}—Ga1A—As2^{xiii}	114.84 (16)
As1^{xii}—Ga1A—Ga1B^{xiv}	119.2 (2)
As2^{xiii}—Ga1A—Ga1B^{xiv}	121.43 (16)
As1^{xii}—Ga1A—Ga1A^{xiv}	127.04 (14)
As2^{xiii}—Ga1A—Ga1A^{xiv}	112.61 (17)
Ga1B^{xiv}—Ga1A—Ga1A^{xiv}	8.82 (9)
As1^{xii}—Ga1A—As1^{xv}	87.94 (10)
As2^{xiii}—Ga1A—As1^{xv}	107.20 (13)
Ga1B^{xiv}—Ga1A—As1^{xv}	95.81 (13)
Ga1A^{xiv}—Ga1A—As1^{xv}	99.49 (15)
As1^{xii}—Ga1A—Sr1^{xv}	151.81 (10)
As2^{xiii}—Ga1A—Sr1^{xv}	70.77 (10)
Ga1B^{xiv}—Ga1A—Sr1^{xv}	72.42 (16)
Ga1A^{xiv}—Ga1A—Sr1^{xv}	67.40 (7)
As1^{xv}—Ga1A—Sr1^{xv}	64.59 (7)
As1^{xii}—Ga1A—Sr1^{xviii}	64.22 (9)
As2^{xiii}—Ga1A—Sr1^{xviii}	128.43 (8)
Ga1B^{xiv}—Ga1A—Sr1^{xviii}	63.92 (16)
Ga1A^{xiv}—Ga1A—Sr1^{xviii}	68.55 (7)
As1^{xv}—Ga1A—Sr1^{xviii}	123.83 (13)

As2^{viii}—Ga2—Sr1^{xxii}	123.013 (14)
As1—Ga2—Sr1^{xxii}	78.871 (13)
As2^{xvii}—Ga2—Sr1^{xxii}	117.500 (15)
As1^{viii}—Ga2—Sr1^{xxii}	22.713 (10)
Ga2^{viii}—Ga2—Sr1^{xxii}	37.772 (10)
Sr1^{xx}—Ga2—Sr1^{xxii}	88.357 (8)
Sr1^{xxi}—Ga2—Sr1^{xxii}	111.288 (14)
Sr1^{xvii}—Ga2—Sr1^{xxii}	141.184 (8)
Sr1—Ga2—Sr1^{xxii}	73.220 (6)
Ga2—As1—Ga1A^{xii}	114.64 (6)
Ga2—As1—Ga1B^{xii}	105.91 (6)
Ga1A^{xii}—As1—Ga1B^{xii}	9.02 (9)
Ga2—As1—Ga2^{viii}	73.038 (18)
Ga1A^{xii}—As1—Ga2^{viii}	96.32 (10)
Ga1B^{xii}—As1—Ga2^{viii}	96.14 (9)
Ga2—As1—Ga1A^{vii}	98.03 (9)
Ga1A^{xii}—As1—Ga1A^{vii}	141.90 (4)
Ga1B^{xii}—As1—Ga1A^{vii}	147.27 (17)
Ga2^{viii}—As1—Ga1A^{vii}	112.22 (9)
Ga2—As1—Sr1	128.755 (16)
Ga1A^{xii}—As1—Sr1	102.71 (6)
Ga1B^{xii}—As1—Sr1	111.12 (6)
Ga2^{viii}—As1—Sr1	68.989 (12)
Ga1A^{vii}—As1—Sr1	67.39 (9)
Ga2—As1—Sr1^{xxi}	76.628 (13)
Ga1A^{xii}—As1—Sr1^{xxi}	73.33 (8)
Ga1B^{xii}—As1—Sr1^{xxi}	67.82 (8)
Ga2^{viii}—As1—Sr1^{xxi}	139.977 (16)
Ga1A^{vii}—As1—Sr1^{xxi}	97.23 (9)
Sr1—As1—Sr1^{xxi}	150.472 (11)
Ga2—As1—Sr1^{xvii}	65.908 (13)
Ga1A^{xii}—As1—Sr1^{xvii}	161.16 (10)
Ga1B^{xii}—As1—Sr1^{xvii}	156.82 (8)
Ga2^{viii}—As1—Sr1^{xvii}	101.547 (13)
Ga1A^{vii}—As1—Sr1^{xvii}	32.12 (9)
Sr1—As1—Sr1^{xvii}	89.333 (9)
Sr1^{xxi}—As1—Sr1^{xvii}	89.018 (12)
Ga1B^{xxiii}—As2—Ga2^{viii}	109.16 (6)
Ga1B^{xxiii}—As2—Ga2^{xxiv}	107.80 (10)
Ga2^{viii}—As2—Ga2^{xxiv}	111.741 (17)
Ga1B^{xxiii}—As2—Ga1A^{xxiii}	8.97 (10)
Ga2^{viii}—As2—Ga1A^{xxiii}	100.47 (6)
Ga2^{xxiv}—As2—Ga1A^{xxiii}	110.18 (10)
Ga1B^{xxiii}—As2—Ga1B^{iv}	88.49 (12)
Ga2^{viii}—As2—Ga1B^{iv}	133.38 (9)
Ga2^{xxiv}—As2—Ga1B^{iv}	102.40 (9)
Ga1A^{xxiii}—As2—Ga1B^{iv}	96.31 (10)
Ga1B^{xxiii}—As2—Sr1	127.93 (10)

Sr1^{xv}—Ga1A—Sr1^{xviii}	135.95 (13)
As1^{xii}—Ga1A—Sr1^{xix}	44.97 (5)
As2^{xiii}—Ga1A—Sr1^{xix}	105.82 (11)
Ga1B^{xiv}—Ga1A—Sr1^{xix}	127.80 (7)
Ga1A^{xiv}—Ga1A—Sr1^{xix}	135.48 (17)
As1^{xv}—Ga1A—Sr1^{xix}	46.51 (6)
Sr1^{xv}—Ga1A—Sr1^{xix}	107.02 (6)
Sr1^{xviii}—Ga1A—Sr1^{xix}	104.00 (10)
As1^{xii}—Ga1A—Sr1^{xiii}	85.55 (10)
As2^{xiii}—Ga1A—Sr1^{xiii}	29.68 (6)
Ga1B^{xiv}—Ga1A—Sr1^{xiii}	149.64 (10)
Ga1A^{xiv}—Ga1A—Sr1^{xiii}	140.99 (16)
As1^{xv}—Ga1A—Sr1^{xiii}	102.85 (10)
Sr1^{xv}—Ga1A—Sr1^{xiii}	94.16 (9)
Sr1^{xviii}—Ga1A—Sr1^{xiii}	120.80 (7)
Sr1^{xix}—Ga1A—Sr1^{xiii}	81.80 (6)
As2^{xiii}—Ga1B—As1^{xii}	116.66 (16)
As2^{xiii}—Ga1B—Ga1B^{xiv}	125.23 (17)
As1^{xii}—Ga1B—Ga1B^{xiv}	117.83 (16)
As2^{xiii}—Ga1B—Ga1A^{xiv}	116.7 (2)
As1^{xii}—Ga1B—Ga1A^{xiv}	126.56 (18)
Ga1B^{xiv}—Ga1B—Ga1A^{xiv}	8.90 (9)
As2^{xiii}—Ga1B—As2^{xvi}	80.20 (9)
As1^{xii}—Ga1B—As2^{xvi}	102.75 (11)
Ga1B^{xiv}—Ga1B—As2^{xvi}	93.10 (15)
Ga2^{viii}—As2—Sr1	70.223 (14)
Ga2^{xxiv}—As2—Sr1	120.879 (15)
Ga1A^{xxiii}—As2—Sr1	128.03 (10)
Ga1B^{iv}—As2—Sr1	65.20 (9)
Ga1B^{xxiii}—As2—Sr1^{xxii}	71.67 (8)
Ga2^{viii}—As2—Sr1^{xxii}	73.974 (13)
Ga2^{xxiv}—As2—Sr1^{xxii}	66.325 (12)
Ga1A^{xxiii}—As2—Sr1^{xxii}	66.09 (8)
Ga1B^{iv}—As2—Sr1^{xxii}	151.44 (9)
Sr1—As2—Sr1^{xxii}	143.341 (12)
Ga1B^{xxiii}—As2—Sr1^{xxv}	21.56 (6)
Ga2^{viii}—As2—Sr1^{xxv}	128.411 (14)
Ga2^{xxiv}—As2—Sr1^{xxv}	103.930 (14)
Ga1A^{xxiii}—As2—Sr1^{xxv}	30.44 (6)
Ga1B^{iv}—As2—Sr1^{xxv}	68.27 (8)
Sr1—As2—Sr1^{xxv}	120.158 (9)
Sr1^{xxii}—As2—Sr1^{xxv}	88.418 (8)
Ga1B^{xxiii}—As2—Sr1^{xxvi}	139.37 (9)
Ga2^{viii}—As2—Sr1^{xxvi}	97.627 (13)
Ga2^{xxiv}—As2—Sr1^{xxvi}	32.041 (11)
Ga1A^{xxiii}—As2—Sr1^{xxvi}	142.22 (10)
Ga1B^{iv}—As2—Sr1^{xxvi}	94.88 (8)
Sr1—As2—Sr1^{xxvi}	89.306 (7)
Sr1^{xxii}—As2—Sr1^{xxvi}	87.812 (8)
Sr1^{xxv}—As2—Sr1^{xxvi}	130.398 (9)

Symmetry codes: (i) *x*−*y*, −*y*, −*z*+1/3; (ii) *x*, *y*−1, *z*; (iii) *x*−*y*+1, −*y*+1, −*z*+1/3; (iv) *y*, *x*−1, −*z*+1; (v) −*x*+*y*+1, −*x*+1, *z*−2/3; (vi) *y*−1, *x*−1, −*z*+1; (vii) −*x*+*y*, −*x*+1, *z*−2/3; (viii) *y*, *x*, −*z*; (ix) −*x*+*y*, −*x*, *z*+1/3; (x) *y*, *x*−1, −*z*; (xi) −*x*+*y*+1, −*x*+1, *z*+1/3; (xii) *y*, *x*, −*z*+1; (xiii) *x*, *y*+1, *z*+1; (xiv) −*x*+2, −*x*+*y*+1, −*z*+5/3; (xv) −*y*+1, *x*−*y*+1, *z*+2/3; (xvi) *y*+1, *x*, −*z*+1; (xvii) *x*−1, *y*, *z*; (xviii) −*y*+1, *x*−*y*, *z*+2/3; (xix) −*y*, *x*−*y*, *z*+2/3; (xx) −*y*, *x*−*y*, *z*−1/3; (xxi) *x*, *y*+1, *z*; (xxii) −*y*+1, *x*−*y*, *z*−1/3; (xxiii) *x*, *y*−1, *z*−1; (xxiv) *x*+1, *y*, *z*; (xxv) −*y*+1, *x*−*y*−1, *z*−1/3; (xxvi) *x*+1, *y*+1, *z*.

A.7 CSD Numbers

Table A.85: Compounds featured in this thesis and their according deposition numbers (CSD-XXXXXXX). Crystallographic information files (CIF) are provided free of charge by the joint Cambridge Crystallographic Data Centre and Fachinformationszentrum Karlsruhe Access Structures service www.ccdc.cam.ac.uk/structures.

Compound	Deposition Number	single crystal- (SC) / powder-(P) data
$SrGe_8As_{10}$	2010143	SC
$BaGe_8As_{10}$	2010144	SC
$BaGe_7P_{12}$	2010142	P
$BaGe_8As_{14}$ (293 K)	2015241	SC
$BaGe_8As_{14}$ (218 K)	2017129	SC
$BaGe_8As_{14}$ (189 K)	2017128	SC
$BaGe_8As_{14}$ (143 K)	2017127	SC
$BaGe_8As_{14}$ (103 K)	2017126	SC
$RbGe_7As_{15}$ (298 K)	2078539	SC
$RbGe_7As_{15}$ (218 K)	2078538	SC
$RbGe_7As_{15}$ (180 K)	2078537	SC
$RbGe_7As_{15}$ (143 K)	2078542	SC
$RbGe_7As_{15}$ (102 K)	2078536	SC
$CsGe_7As_{15}$ (296 K)	2078535	SC
$CsGe_7As_{15}$ (218 K)	2078542	SC
$CsGe_7As_{15}$ (180 K)	2078540	SC
$CsGe_7As_{15}$ (143 K)	2078533	SC
$CsGe_7As_{15}$ (102 K)	2078534	SC
T5-$Sr_{15}Ga_{22}As_{32}$	1913218	SC
T5-$Eu_{15}Ga_{22}As_{32}$	1913213	SC
T5-$Sr_{15}In_{22}As_{32}$	1913215	SC
T5-$Eu_{15}In_{22}As_{32}$	1913216	SC
T6-$Sr_3Ga_6As_8$	1913217	SC
T6-$Eu_3Ga_6As_8$	1913214	SC
T2-$SrSiAs_2$	1971148	P
T2-$EuSiAs_2$	1971150	P
T3-$SrGaSiAs_3$	1971151	P
T3-$EuGaSiAs_3$	1971154	P
T4-*mC*-$Sr_4Ga_5SiAs_9$	1971149	P
T4-*mC*-$Eu_4Ga_5SiAs_9$	1971152	SC
T4-*tI*-$Sr_4Ga_5SiAs_9$	1971155	SC
T4-*tI*-$Eu_4Ga_5SiAs_9$	1971153	P
$SrGa_4As_4$	1957548	SC

References

[1] L. Solymar, D. Walsh, R. R. Syms, *Electrical properties of materials*, Oxford university press, **2014**.

[2] H. Nyman, B. G. Hyde, *Acta Crystallographica Section A* **1981**, *37*, 11-17.

[3] V. Weippert, T. Chau, K. Witthaut, L. Eisenburger, D. Johrendt, *Chem. Commun.* **2021**, *57*, 1332 -1335.

[4] H. C. Casey, D. D. Sell, K. W. Wecht, *J. Appl. Phys.* **1975**, *46*, 250-257.

[5] R. Bhat, P. S. Dutta, S. Guha, *J. Cryst. Growth* **2008**, *310*, 1910-1916.

[6] Y. I. Diakite, S. D. Traore, Y. Malozovsky, B. Khamala, L. Franklin, D. Bagayoko, *J. Mod. Phys.* **2016**, *8*, 531-546.

[7] M. Levinshtein, S. Rumyantsev, M. Shur, *Handbook Series on Semiconductor Parameters, Vol. 1*, 1 ed., World Scientific Pub Co Inc, Singapore, **1996**.

[8] M. Sharmin, S. Choudhury, N. Akhtar, T. Begum, *J. Bangladesh Acad. Sci.* **2012**, *36*, 97-107.

[9] T. C. Harman, H. L. Goering, A. C. Beer, *Phys. Rev.* **1956**, *104*, 1562-1564.

[10] F. Oswald, in *Z. Naturforsch., A: Phys. Sci., Vol. 10*, **1955**, p. 927.

[11] F. Stern, R. M. Talley, *Phys. Rev.* **1955**, *100*, 1638-1643.

A.8 Scientific contributions

Publications within this thesis

Mixed Valence and Unusual Germanium Coordination in $SrGe_8As_{10}$, $BaGe_8As_{10}$, and $BaGe_7P_{12}$

Valentin Weippert, Thanh Chau, Kristian Witthaut and Dirk Johrendt

Inorganic Chemistry **2020**, *20*, 15447-15453.

V. Weippert: Conceptualization: Lead; Formal analysis: Lead; Investigation: Lead; Validation: Lead; Visualization: Lead; Writing – original draft: Lead; Writing –review & editing: Equal. **T. Chau**: Conceptualization: Equal; Formal analysis: Equal; Investigation: Equal; Validation: Equal; Visualization: Supporting; Writing – original draft: Supporting. **K. Witthaut**: Conceptualization: Supporting; Formal analysis: Supporting; Investigation: Supporting; Validation: Equal; Visualization: Supporting; Writing – original draft: Supporting. **D. Johrendt**: Conceptualization: Supporting; Validation: Supporting; Funding acquisition: Lead; Project administration: Lead; Resources: Lead; Supervision: Lead; Writing – original draft: Supporting; Writing – review & editing: Equal.

$BaGe_8As_{14}$: a semiconducting sodalite type compound

Valentin Weippert, Thanh Chau, Kristian Witthaut, Lucien Eisenburger and Dirk Johrendt

Chemical Communications **2021**, *57*, 1332-1335.

V. Weippert: Conceptualization: Lead; Formal analysis: Lead; Investigation: Lead; Validation: Lead; Visualization: Lead; Writing – original draft: Lead; Writing –review & editing: Equal. **T. Chau**: Conceptualization: Equal; Formal analysis: Equal; Investigation: Equal; Validation: Equal; Visualization: Supporting; Writing – original draft: Supporting. **K. Witthaut**: Conceptualization: Equal; Formal analysis: Equal; Investigation: Equal; Validation: Equal; Visualization: Supporting; Writing – original draft: Supporting. **L. Eisenburger**: Formal analysis: Supporting; Investigation: Supporting; Validation: Supporting; Visualization: Supporting; Writing – original draft: Supporting. **D. Johrendt**: Conceptualization: Equal; Validation: Supporting; Funding acquisition: Lead; Project administration: Lead; Resources: Lead; Supervision: Lead; Visualization: Supporting; Writing – original draft: Supporting; Writing – review & editing: Equal.

High thermoelectric properties in the sodalite compounds $BaGe_8As_{14}$ and $A$$Ge_7As_{15}$ (A = Rb, Cs)

Valentin Weippert, Kristian Witthaut, Monika Pointner, Lucien Eisenburger and Dirk Johrendt

submitted

V. Weippert: Conceptualization: Lead; Formal analysis: Lead; Investigation: Lead; Validation: Lead; Visualization: Lead; Writing – original draft: Lead; Writing –review & editing: Equal. **K. Witthaut**: Conceptualization: Equal; Formal analysis: Supporting; Investigation: Equal; Validation: Equal; Visualization: Supporting; Writing – original draft: Supporting. **M. Pointner**: Formal analysis: Supporting; Investigation: Equal; Validation: Supporting; Visualization: Supporting; Writing – original draft: Supporting. **L. Eisenburger**: Formal analysis: Supporting; Investigation: Supporting; Validation: Supporting; Visualization: Supporting. **D. Johrendt**: Conceptualization: Equal; Formal analysis: Supporting; Validation: Supporting; Funding acquisition: Lead; Project administration: Lead; Resources: Lead; Supervision: Lead; Writing – original draft: Supporting; Writing – review & editing: Equal.

Supertetrahedral Layers Based on GaAs or InAs

Valentin Weippert, Arthur Haffner, Alexis Stamatopoulos and Dirk Johrendt

Journal of the American Chemical Society **2019**, *141*, 11245-11252.

V. Weippert: Conceptualization: Lead; Formal analysis: Lead; Investigation: Lead; Validation: Lead; Visualization: Lead; Writing – original draft: Lead; Writing –review & editing: Equal. **A. Haffner**: Conceptualization: Supporting; Formal analysis: Supporting; Investigation: Supporting; Validation: Supporting; Writing – original draft: Supporting. **A. Stamatopoulos**: Formal analysis: Supporting; Investigation: Supporting; **D. Johrendt**: Conceptualization: Equal; Formal analysis: Equal; Validation: Supporting; Funding acquisition: Lead; Project administration: Lead; Resources: Lead; Supervision: Lead; Visualization: Equal; Writing – original draft: Equal; Writing – review & editing: Equal.

New layered supertetrahedral compounds T2-MSiAs$_2$, T3-MGaSiAs$_3$ and polytypic T4-M_4Ga$_5$SiAs$_9$ (M = Sr, Eu)

Valentin Weippert, Arthur Haffner and Dirk Johrendt

Zeitschrift für Naturforschung B **2020**, *75*, 983-989.

V. Weippert: Conceptualization: Lead; Formal analysis: Lead; Investigation: Lead; Validation: Lead; Visualization: Lead; Writing – original draft: Lead; Writing –review & editing: Equal. **A. Haffner**: Conceptualization: Supporting; Formal analysis: Supporting; Investigation: Supporting; **D. Johrendt**: Conceptualization: Equal; Validation: Supporting; Funding acquisition: Lead; Project administration: Lead; Resources: Lead; Supervision: Lead; Writing – original draft: Supporting; Writing – review & editing: Equal.

High-pressure synthesis and crystal structure of SrGa$_4$As$_4$

Valentin Weippert and Dirk Johrendt

Acta Crysallographica Section E **2019**, *75*, 1643-1645.

V. Weippert: Conceptualization: Lead; Formal analysis: Lead; Investigation: Lead; Validation: Lead; Visualization: Lead; Writing – original draft: Lead; Writing –review & editing: Equal. **D. Johrendt**: Conceptualization: Equal; Validation: Supporting; Funding acquisition: Lead; Project administration: Lead; Resources: Lead; Supervision: Lead; Writing – original draft: Supporting; Writing – review & editing: Equal.

Publications beyond this thesis

Polymorphism of Ba_2SiP_4

Arthur Haffner, Valentin Weippert and Dirk Johrendt

Zeitschrift für anorganische und allgemeine Chemie **2020**, *646*, 120-124.

V. Weippert: Formal analysis: Supporting; Investigation: Supporting; Validation: Supporting.

The Phosphidosilicates $SrSi_7P_{10}$ and $BaSi_7P_{10}$

Arthur Haffner, Valentin Weippert and Dirk Johrendt

Zeitschrift für anorganische und allgemeine Chemie **2020**, *647*, 326-330.

V. Weippert: Formal analysis: Supporting; Investigation: Supporting; Validation: Supporting.

Tailoring the properties of 3d transition metal complexes with different *N*-cycloalkyl-substituted tetrazoles

Vanessa Braun, Maximilian H. H. Wurzenberger, Valentin Weippert and Jörg Stierstorfer

New Journal of Chemistry **2021**, *45*, 11042-11050.

V. Weippert: Formal analysis: Supporting; Investigation: Supporting; Validation: Supporting; Writing – original draft: Supporting; Writing – review & editing: Supporting.

NH_4F Provides Synthetic Access to $Sc_5P_{12}N_{23}O_3$ and $Ti_5P_{12}N_{24}O_2$ from Refractory Nitrides ScN and TiN.

Lucien Eisenburger, Valentin Weippert, Oliver Oeckler and Wolfgang Schnick

submitted

V. Weippert: Formal analysis: Supporting; Investigation: Supporting; Validation: Supporting; Writing – original draft: Supporting; Writing – review & editing: Supporting.

Conference Contributions

BaF($Al_{0.5}Li_{0.5}$)As [*talk*]

Valentin Weippert and Dirk Johrendt

47. Hirschegg-Festkörpersymposium, Hirschegg, Austria, **2018**.

verdünnte Halbleiter [*talk*]

Valentin Weippert and Dirk Johrendt

4. Obergurgl-Seminar-Festkörperchemie, Obergurgl, Austria, **2019**.

Die Welt braucht mehr Supertetraeder [*talk*]

Valentin Weippert and Dirk Johrendt

5. Obergurgl-Seminar-Festkörperchemie, Obergurgl, Austria, **2020**.